Rational design of next-generation filovirus vaccines with glycoprotein stabilization, nanoparticle display, and glycan modification

Yi-Zong Lee[1#], Yi-Nan Zhang[1#], Maddy L. Newby[2], Garrett Ward[1], Keegan Braz Gomes[3], Sarah Auclair[1], Connor DesRoberts[1], Joel D. Allen[2], Andrew B. Ward[1], Robyn L. Stanfield[1], Linling He[1], Max Crispin[2], Ian A. Wilson[1,4], and Jiang Zhu[1,3,5]*

[1]Department of Integrative Structural and Computational Biology, The Scripps Research Institute, La Jolla, CA 92037, USA

[2]School of Biological Sciences, Highfield Campus, University of Southampton, Southampton, SO17 1BJ, UK

[3]Uvax Bio, LLC, Newark, DE 19702, USA

[4]Skaggs Institute for Chemical Biology, The Scripps Research Institute, La Jolla, CA 92037, USA

[5]Department of Immunology and Microbiology, The Scripps Research Institute, La Jolla, CA 92037, USA

[#] These authors contributed equally to this work

* Corresponding author

JZ: Phone (858) 784-8157; Email: jiang@scripps.edu

ABSTRACT (200 WORD LIMIT)

Filoviruses pose a significant threat to human health with frequent outbreaks and high mortality. Although two vector-based vaccines are available for Ebola virus, a broadly protective filovirus vaccine remains elusive. In this study, we evaluate a general strategy for stabilizing glycoprotein (GP) structures of Ebola, Sudan, and Bundibugyo ebolaviruses and Ravn marburgvirus. A 3.2 Å-resolution crystal structure provides atomic details for the redesigned Ebola virus GP, and cryo-electron microscopy reveals how a pan-ebolavirus neutralizing antibody targets a conserved site on the Sudan virus GP (3.13 Å-resolution), in addition to a low-resolution model of antibody-bound Ravn virus GP. A self-assembling protein nanoparticle (SApNP), I3-01v9, is redesigned at the *N*-terminus to allow the optimal surface display of filovirus GP trimers. Following detailed *in vitro* characterization, the lymph node dynamics of Sudan virus GP and GP-presenting SApNPs are investigated in a mouse model. Compared with soluble GP trimer, SApNPs show ~112 times longer retention in lymph node follicles, up-to-28 times greater presentation on follicular dendritic cell dendrites, and up-to-3 times stronger germinal center reactions. Functional antibody responses induced by filovirus GP trimers and SApNPs bearing wildtype and modified glycans are assessed in mice. Our study provides a foundation for next-generation filovirus vaccine development.

ONE-SENTENCE SUMMARY

Filovirus glycoproteins and nanoparticles were rationally designed and characterized *in vitro* and *in vivo* to aid filovirus vaccine development.

41 **INTRODUCTION**

42 The first case of human infection with filovirus was documented in 1967 in Marburg and Frankfurt,
43 Germany, where laboratory workers were infected with the subsequently named Marburg virus
44 (MARV) by nonhuman primates (NHPs) imported from Africa (*1*). The largest filovirus outbreak
45 in history was caused by Ebola virus (EBOV), which was first identified in 1976 in Zaire in Central
46 Africa (*2, 3*). Approximately 28,600 cases were reported during this outbreak, which resulted in
47 11,325 deaths between 2013 and 2016 (*4*). Both MARV and EBOV cause viral hemorrhagic fever
48 (VHF) in humans, with a case fatality rate of up to 90% (*5, 6*). Filoviruses can be classified into
49 five genera, including *Ebolavirus* and *Marburgvirus (7, 8)*. The *Ebolavirus* genus comprises three
50 pathogenic species, including EBOV, Bundibugyo virus (BDBV), and Sudan virus (SUDV), and
51 three species that are non-pathogenic or rarely infect humans. The *Marburgvirus* genus contains a
52 single species with two members, MARV and Ravn virus (RAVV). The single-stranded, negative-
53 sense RNA genome of filoviruses encodes the nucleoprotein, virion proteins, glycoprotein (GP),
54 and RNA-polymerase, among others. As a class I viral fusion protein (*9-12*), functional GP is a
55 trimer of heterodimers responsible for filovirus attachment, entry, and membrane fusion (*13*). GP
56 is recognized by the host immune system during natural infection (*14-16*), and thus represents the
57 main target for the development of prophylactic vaccines and antibody therapeutics (*17-20*).

58 Substantial progress has been made in filovirus research (*21*). First, a greater understanding
59 of filovirus pathogenesis and its mechanism of infection has been achieved (*22-24*). Niemann-Pick
60 C1 (NPC1) was identified as the endosomal receptor for filovirus entry, suggesting that NPC1
61 inhibitors may have antiviral potential (*25-27*). Second, neutralizing antibodies (NAbs) have now
62 been established as effective therapeutics to treat filovirus infections (*28-31*). Compared with a
63 monoclonal antibody (mAb) cocktail, ZMapp (*32*), which showed early promise (*33*), REGN-EB3

64 (a three-mAb cocktail (*34*)) and mAb114 (*35*) proved to be more efficacious against EBOV in a
65 randomized controlled trial (*36*). The 2013-2016 EBOV outbreak led to an enduring campaign for
66 antibody discovery against filoviruses (*37*). Panels of mAbs were isolated from human survivors
67 and immunized animals, revealing multiple sites of vulnerability on GP (*15, 16, 35, 38-53*). At the
68 peak of this effort, the Viral Hemorrhagic Fever Immunotherapeutic Consortium analyzed 171
69 mAbs targeting diverse GP epitopes: base, glycan cap, fusion loop, GP1/core, GP1/head, GP1/2,
70 heptad repeat 2 (HR2), and mucin (*54*). Third, x-ray crystallography and cryo-electron microscopy
71 (EM) have been used to determine high-resolution structures of filovirus GP bound to the NPC1
72 receptor (*27*), small-molecule ligands (*55-57*), and mAbs (*15, 38, 39, 41, 42, 46, 48-51, 58, 59*).
73 Notably, negative-stain EM (nsEM) offers a useful tool for validating GP structures and mapping
74 mAb epitopes (*16, 40, 45-47, 52-54*). These GP complex structures have provided insights into the
75 molecular mechanism of filovirus neutralization and facilitated the development of antibody
76 therapeutics and vaccines (*17, 60, 61*). Fourth, two viral vector-based EBOV vaccines have been
77 approved for human use thus far. ERVEBO (*62*) is a single-dose vaccine based on the recombinant
78 vesicular stomatitis virus (rVSV) expressing the EBOV GP, while Zabdeno/Mvabea (*63*) utilizes
79 a two-dose, heterologous regimen administering an Adenovirus 26 (Ad26) expressing the EBOV
80 GP followed by a modified Vaccina Ankara (MVA) virus expressing multiple filovirus GPs. Other
81 EBOV vaccines that utilize DNA (*64*) and viral vectors (*65-70*) have been tested in humans. Recent
82 efforts have been directed toward mRNA, protein, and nanoparticle (NP) platforms (*71-74*).

83 Despite this rapid advancement, critical innovations are still needed for next-generation
84 filovirus vaccine development (*75*). Although the correlates of protection remained unclear (*76*),
85 an in-depth B cell analysis revealed diverse yet convergent polyclonal NAb responses induced by
86 the rVSV-ZEBOV vaccine in a Phase 1 trial (*77*). A follow-up study elucidated how NAbs from

87 multiple subjects utilized the same germline genes to target the receptor binding site on GP (*78*).
88 These results highlighted the central role of GP as a vaccine antigen for eliciting protective NAbs.
89 For more than a decade, antibody-guided, structure-based antigen design has been the focus of
90 vaccine development for several important targets, such as type-1 human immunodeficiency virus
91 (HIV-1) (*79-82*) and respiratory syncytial virus (RSV) (*83*). Rational designs have been proposed
92 for stabilization of the HIV-1 envelope (Env) (*84-86*) and RSV fusion (F) (*87-90*) proteins in their
93 prefusion state. After preclinical assessment, many of these vaccine designs have been advanced
94 to human trials (*91, 92*), with two products approved for RSV prevention in older adults (*93*). So
95 far, however, only two studies reported rational designs of stabilized filovirus GP with limited *in*
96 *vivo* data (*94, 95*). Most recently, Xu et al. proposed an immunofocusing GP design by engineering
97 additional *N*-linked glycans (*73*). Notably, almost all current filovirus vaccine candidates (*96*) are
98 based on wildtype GP with a highly variable mucin-like domain (MLD), which shields conserved
99 NAb epitopes and facilitates immune evasion (*97, 98*). As a vaccine antigen, the MLD-deleted GP
100 (GPΔmuc) should in principle be more effective in NAb elicitation than wildtype GP but has not
101 been evaluated in humans. In addition to the GP form, the delivery platform may be crucial for
102 vaccine-induced immunity. Although viral vectors appeared to be a preferable platform with the
103 licensure of two EBOV vaccines, mRNA vaccines may provide an alternative given their widely
104 acclaimed success in the COVID-19 vaccine campaign (*99, 100*). In the realm of protein vaccines,
105 NPs have become an increasingly recognized delivery platform due to their virus-like size, shape,
106 surface display, and ability to induce strong and durable NAb responses (*101-106*). Two EBOV
107 GP-presenting NP vaccines were recently reported (*73, 95*) but have not been evaluated in animal
108 challenge models. Finally, engineering the glycan component of vaccine candidates may prove to
109 be an important step in their development. The enzymatic trimming of *N*-glycans was previously

110 shown to enhance NAb responses for influenza hemagglutinin (HA) or stem, SARS-CoV-2 spike,
111 and HIV-1 Env vaccines (*107-110*). It is unclear whether the same strategy is applicable to filovirus
112 GP, which is also heavily glycosylated with up to 17 glycans on the surface.

113 In our previous study, we stabilized EBOV GP with mutations in the $HR1_C$ bend and HR2
114 stalk and displayed one of two lead designs, termed GPΔmuc-WL^2P^2, on self-assembling protein
115 nanoparticles (SApNPs) as EBOV vaccine candidates (*95*). Here, we first extended the GPΔmuc-
116 WL^2P^2 and WL^2P^4 construct designs from EBOV to SUDV and BDBV and determined a crystal
117 structure for EBOV GPΔmuc-WL^2P^4 at 3.2 Å-resolution. We also obtained a 3.13 Å cryo-EM
118 model for SUDV GPΔmuc-WL^2P^4 bound to CA45 Fab. The nearly identical backbones of SUDV
119 and EBOV GPΔmuc-WL^2P^4 suggest a widely applicable design to stabilize ebolavirus GPs. We
120 then displayed EBOV, SUDV, and BDBV GPΔmuc-WL^2P^4 trimers on SApNPs derived from E2p
121 and I3-01v9, the latter of which was computationally redesigned at the *N*-terminus. A similar
122 design strategy was applied to RAVV GP, resulting in a promising trimer construct termed
123 GPΔmuc-P^2CT. Next, we investigated the lymph node delivery and immunological responses for
124 ebolavirus vaccines, using SUDV GPΔmuc-WL^2P^4 trimer and SApNPs as examples, at the intra-
125 organ, intercellular, and intracellular levels in mice. Compared with soluble trimers, large SApNPs
126 showed prolonged retention and presentation on follicular dendritic cell (FDC) dendrites and more
127 robust and durable germinal center (GC) reactions in lymph node follicles. Lastly, we immunized
128 mice with various filovirus GP vaccines to evaluate their antibody responses. RAVV GPΔmuc-
129 P^2CT trimer elicited detectable cross-ebolavirus NAbs, but not vice versa. Both multivalent display
130 and glycan modification were found to impact the immunogenicity of GP-based filovirus vaccines.
131 Notably, increasing the mannose content of the GP glycan shield exerted a positive effect on NAb
132 responses. These findings should facilitate future filovirus vaccine development.

133 **RESULTS**

134 **A universal design strategy for ebolavirus GP stabilization**

135 GPs within the *Ebolavirus* genus share considerable sequence and structural similarities (*58, 111*).
136 These viral GPs consist of functionally conserved structural components, such as GP1, MLD,
137 internal fusion loop (IFL), GP2, which contains the heptad repeat 1 (HR1) and HR2 regions, and
138 transmembrane domain (TMD). Recently, we stabilized EBOV GPΔmuc with a T577P (P^2) or
139 L579P (P^4) mutation in the $HR1_C$ bend, a W615L mutation at the neck of the HR2 stalk, and an
140 HR2 C-terminal extension (D632 to D637) (*95*) (**Fig. 1a**). A foldon motif was appended to the
141 HR2 stalk C-terminus in trimer but not SApNP constructs. The modified EBOV GPΔmuc trimers
142 exhibited superior structural and thermal stability compared with the wildtype GP construct.

143 Here, we applied the same design principles to SUDV and BDBV GPs and characterized
144 the two constructs, GPΔmuc-WL^2P^2 and -WL^2P^4, for all three ebolaviruses (**Fig. S1a**). Following
145 a similar protocol (*95*), all six GPΔmuc constructs were transiently expressed in HEK293F cells
146 and purified using two different methods. In addition to an immobilized nickel affinity (Nickel)
147 chromatography column, pan-ebolavirus NAbs ADI-15878 (*112*) and CA45 (*113*) were produced
148 in the immunoglobulin G (IgG) form in ExpiCHO cells and used to prepare immunoaffinity
149 chromatography (IAC) columns. The IAC method was established in our previous study, where
150 the mAb100 and mAb114 (*35*) columns were used to purify EBOV GP trimers and SApNPs (*95*).
151 The IAC/Nickel-purified ebolavirus GP was then characterized by size-exclusion chromatography
152 (SEC) on a Superdex 200 column after ADI-15878 (**Fig. 1b)** and CA45 (**Fig. S1b**) purification.
153 All SEC profiles showed an aggregation peak around ~8 ml and a consistent trimer peak at ~11
154 ml, with little hint of dimer or monomer peaks. The Nickel column generated higher aggregation
155 peaks for EBOV and SUDV GPs than both IAC columns (**Fig. S1b**). Between the two tested

156 broadly neutralizing antibodies (bNAbs), ADI-15878 appeared to be more effective at capturing
157 diverse ebolavirus GPs than CA45, indicated by substantially higher ultraviolet absorbance at 280
158 nm (UV_{280}) for the eluted protein (**Fig. 1b** and **S1b**). Our results suggest that ADI-15878 provides
159 a universal, tag-free IAC method for purifying ebolavirus GP. Blue native polyacrylamide gel
160 electrophoresis (BN-PAGE) confirmed that the SEC fractions around ~11 ml were indeed
161 GPΔmuc trimers, with bands on the native gel corresponding to their theoretical molecular weights
162 (**Fig. 1c**). Next, differential scanning calorimetry (DSC) was used to assess the thermostability of
163 ebolavirus GP trimers. For EBOV, while GPΔmuc-WL^2P^2 showed two denaturing states at melting
164 temperatures (T_m) of 60.9ºC and 67.7ºC, GPΔmuc-WL^2P^4 had a widened peak with a single T_m of
165 64.4ºC (**Fig. 1d**), consistent with our previous findings (*95*). By comparison, all four SUDV and
166 BDBV GPΔmuc trimers generated similar DSC curves with a single denaturing state and a narrow
167 range of T_m values (62.9-63.6ºC). Notably, among the three ebolaviruses, SUDV GPΔmuc trimers
168 showed the highest T_{onset} (54.8ºC and 56.0ºC), followed by EBOV and BDBV GPΔmuc trimers
169 (50.1-54.2ºC). Based on the biochemical and biophysical data, GPΔmuc-WL^2P^4 was selected as a
170 candidate for the pan-ebolavirus GP design and subjected to further experimental validation.

171 A glycan shield is utilized by the HIV-1 Env spike as a major defense mechanism to evade
172 host NAb responses (*108*). Similarly, ebolavirus GPs have a glycan cap to shield the receptor
173 binding site (*95*), in addition to a heavily glycosylated MLD, which is removed in GPΔmuc. Thus,
174 glycans play a critical role in evading or mediating antibody interactions with the GP. To generate
175 site-specific glycosylation profiles, the three ebolavirus GPΔmuc-WL^2P^4 proteins were digested
176 with trypsin, chymotrypsin, and α-lytic protease to generate glycopeptides each containing a single
177 *N*-linked glycan site. Site-specific composition and occupancy were determined by analyzing these
178 glycopeptides using liquid chromatography-mass spectrometry (LC-MS), as previously described

179 (*108*). All glycosylation sites on the three ebolavirus GPΔmuc-WL^{2}P^4 proteins present complex-
180 type glycans except for N563 and N257, where mixed forms were detected. Specifically, the N563
181 site contains ~30% of oligomannose-type glycans for EBOV and ~60% for both SUDV and BDBV,
182 whereas the N257 site has ~15% of oligomannose-type glycans for EBOV (**Fig. 1e** and **Fig. S1c**).
183 Due to technical limitations, accurate assessment of the glycan compositions could not be achieved
184 for all glycosylation sites.

185 Negative-stain EM (nsEM) was used to characterize structures of ebolavirus GPΔmuc-
186 WL^{2}P^4 trimers, either alone or in complex with bNAb ADI-15878 (**Fig. S1d**). For EBOV and
187 BDBV, crystal structures of wildtype GPΔmuc trimer in complex with ADI-15878 (Protein Data
188 Bank [PDB] IDs: 7JPH (*95*), 6EA7, and 6EA5 (*111*)) were used for fitting three-dimensional (3D)
189 EM reconstructions, whereas for SUDV, the GPΔmuc and ADI-15878 structures obtained from
190 two different complexes (PDB IDs: 3S88 (*58*) and 6DZM (*112*)) were fitted separately (**Fig. 1f**
191 and **Figs. S1e-g**). Overall, the low-resolution nsEM models of three ebolavirus GPΔmuc trimers
192 shared a three-lobed chalice shape consistent with the native-like GPΔmuc structure, albeit missing
193 densities associated with the HR2 stalk. The nsEM models of ADI-15878-bound GPΔmuc trimer
194 were highly similar among the three ebolaviruses, revealing an epitope formed across two GP
195 protomers overlapping the conserved regions of the IFL and HR1 in GP2 (*47, 112*).

196 The antigenicity of six stabilized ebolavirus GPΔmuc trimers was assessed against pan-
197 ebolavirus bNAbs CA45 (*46*), ADI-15878, ADI-15946 (*114*), and BDBV-289 (*51*), along with a
198 marburgvirus NAb, MR78 (*39*). In the enzyme-linked immunosorbent assay (ELISA), the proline
199 mutation in HR1c (P^2 or P^4) appeared to have no influence on antibody binding (**Fig. 1g** and **Fig.**
200 **S1h**). Among the four pan-ebolavirus bNAbs, ADI-15946 and BDBV-289 showed the lowest
201 binding affinity for SUDV GPΔmuc trimers, 2.5 to 6-fold weaker than those for EBOV and BDBV

202 GPΔmuc trimers, indicated by the half maximal effective concentration (EC_{50}). The NHP-derived
203 bNAb, CA45, yielded 1.5- to 2.5-fold lower EC_{50} values in ELISA binding to EBOV compared
204 with SUDV and BDBV GPΔmuc trimers. The negative control, MR78, exhibited no detectable
205 binding to any of ebolavirus GPΔmuc trimers. The results from biolayer interferometry (BLI) were
206 largely consistent with the ELISA data (**Fig. 1h** and **Fig. S1i**). Among the six ebolavirus GPs,
207 CA45 bound to EBOV GPΔmuc trimers with the highest signals, whereas ADI-15946 and BDBV-
208 289 interacted least favorably with SUDV GPΔmuc trimers. BLI showed negligible to no binding
209 signals between ebolavirus GPΔmuc trimers and the marburgvirus NAb, MR78.

210 **Structural characterization of ligand-free and antibody-bound ebolavirus GPΔmuc trimers**

211 Previously, we determined the crystal structure of EBOV GPΔmuc-WL^2P^2 (*95*). Here, we sought
212 to obtain atomic details for the more stable EBOV GPΔmuc-WL^2P^4. To this end, EBOV GPΔmuc-
213 WL^2P^4 was transiently expressed in HEK293S cells and purified by IAC (mAb100) and SEC as
214 previously described (*95*) (**Fig. S2a**). EBOV GPΔmuc-WL^2P^4 was crystallized under a similar
215 condition to GPΔmuc-WL^2P^2, resulting in similar crystal packing with a P321 space group (**Table**
216 **S1**). The final structure was determined at a resolution of 3.2 Å. Each asymmetric unit contained
217 one GP protomer, with the glycan cap atop the GP1 and the belt-forming IFL of the GP2 clearly
218 recognizable from the densities (**Fig. 2a**). Three GP1-GP2 heterodimers assembled into a chalice-
219 shaped trimer in the crystal lattice, with three GP2 subunits forming a base that cradles the three
220 outward-facing GP1 lobes (**Fig. S2b**). Four *N*-linked glycans, N228, N257, N563, and N618, were
221 identified in the crystal structure. The most complete carbohydrate chain was obtained for N563
222 (revealing electron density for $Man_4GlcNAc_2$), which is part of the ADI-15878 epitope in HR1a
223 (*111*), whereas a single *N*-acetylglucosamine (GlcNAc) was visible at the other three sites. EBOV
224 GPΔmuc-WL^2P^4 showed a nearly identical backbone to GPΔmuc-WL^2P^2, with a global Cα root-

225 mean-square deviation (RMSD) of 0.48 Å calculated for 243 matching Cα atoms and a local Cα-
226 RMSD of 0.68 Å for the HR1c bend after fitting the protomer structure (**Fig. 2a** and **Fig. S2c**). In
227 GPΔmuc-WL^{2}P^4, the amine group of the K95 sidechain formed hydrogen bonds with the backbone
228 carbonyl groups of L573 and T576 (~3.0 Å), which were absent in GPΔmuc-WL^{2}P^2. These two
229 interprotomer hydrogen bonds stabilized the GPΔmuc-WL^{2}P^4 trimer from its center, resulting in
230 higher thermostability compared with GPΔmuc-WL^{2}P^2. This was also supported by the EBOV
231 GPΔmuc-WL^2 structure (PDB ID: 7JPI), which contained the K95-L573 and K95-T576 hydrogen
232 bonds (2.7 and 2.9 Å, respectively). The structural analysis is consistent with the DSC data, where
233 EBOV GPΔmuc-WL^{2}P^4 showed a single denaturing state with a T_m of 64.4°C (*95*).

234 Cryo-EM plays an important role in understanding how viral GPs interact with antibodies
235 (*115-117*). Several cryo-EM models have been reported for EBOV and BDBV GPs (*42, 51, 112*),
236 but only two crystal structures (*58, 118*) and no cryo-EM models are available for SUDV GP. Here,
237 we determined a cryo-EM structure for SUDV GPΔmuc-WL^{2}P^4 in complex with CA45 Fab. The
238 SUDV GP was transiently expressed in HEK293F cells and purified using an IAC (ADI-15878)
239 column, prior to complexation with CA45 Fab and SEC on a Superose 6 16/600 GL column (**Fig.
240 S2d**). The complex fraction at ~72 ml was imaged on a Krios G4 transmission electron microscope
241 with the data processed in CryoSPARC (*119*) (see Methods) (**Fig. S2e**). A resolution of 3.13 Å
242 was obtained for the final reconstruction, in which the SUDV GPΔmuc-WL^{2}P^4 trimer flanked by
243 three CA45 Fabs could be recognized from the density map (**Fig. 2b**). The glycan cap and GP2
244 stalk only became partially visible when the density was relaxed beyond 4.0 Å (**Fig. S2e**). Crystal
245 structures of EBOV GPΔmuc-WL^{2}P^2 (PDB ID: 7JPH) (*95*) and CA45 variable domains (PDB ID:
246 6EAY) (*113*) were used as the initial model for EM fitting, followed by manual refinement. The
247 final model of SUDV GPΔmuc-WL^{2}P^4 lacking the glycan cap and GP2 stalk was superposed onto

248 the crystal structure of EBOV GPΔmuc-WL^{2}P^4, showing a Cα-RMSD of 0.66 Å for 154 matching
249 Cα atoms (**Fig. S2f**, left). The three HR1$_C$ bends of SUDV GPΔmuc-WL^{2}P^4 were superposed onto
250 those of EBOV GPΔmuc-WL^{2}P^4 and BDBV GPΔmuc (PDB ID: 7KFE) (*51*), with Cα-RMSDs of
251 0.34 and 0.53 Å for the 24 matching Cα atoms, respectively (**Fig. 2c**, right). Compared with the
252 crystal structure of EBOV GPΔmuc/CA45 complex (PDB ID: 6EAY) (*113*), cryo-EM revealed a
253 nearly identical CA45 binding mode and epitope in the SUDV GPΔmuc-WL^{2}P^4/CA45 complex,
254 with a Cα-RMSD of 0.69 Å for 147 matching Cα atoms after superposition of a single GP/CA45
255 component between the two complexes (**Fig. S2f**, right). Specifically, the CA45-GP2 interface
256 was stabilized by a backbone hydrogen bond formed between CA45 HC-Y32 and GP2-E545 (~3.3
257 Å) and a sidechain salt bridge between CA45 HC-D101 carboxyl and GP2-H595 imidazole groups
258 (~4.0 Å), as well as hydrogen bonds between the CA45 LC-Y49 sidechain and GP2-N550
259 backbone (~3.4 Å) and between the CA45 LC-N53 sidechain and GP2-N550 backbone (~2.6 Å)
260 (**Fig. 2c**). Although the interpretation of these interactions may be limited by the resolution of the
261 cryo-EM structure, similar interactions were identified in the previous 3.7 Å-resolution crystal
262 structure of EBOV GPΔmuc in complex with CA45 Fab (PDB ID: 6EAY) (**Fig. S2g**) (*113*),
263 including those between CA45 HC-Y32 and GP2-E545 (~3.2 Å), between CA45 HC-D101 and
264 GP2-H549 (~3.9 Å), and the same CA45 LC-GP2 pairs with nearly identical lengths.

265 **Rational design and basic characterization of ebolavirus GPΔmuc-presenting nanoparticles**

266 Previously, we redesigned the I3-01v9 SApNP to achieve optimal display of monomeric antigens
267 (*120*). In the resulting I3-01v9a scaffold, the *N*-termini formed a triangle of 43.9 Å (**Fig. 3a**, left).
268 Here, we further modified I3-01v9a to accommodate trimeric antigens with a narrow stalk, such
269 as filovirus GPs (see Methods). After removing the first 4 amino acids (aa) of I3-01v9a, we fused
270 a 9-aa helix to the truncated I3-01v9a *N*-terminal helix with a 4-aa turn. The resulting model was

271 computationally optimized first in structure and then in sequence to generate two new I3-01v9
272 scaffolds, termed I3-01v9b/c (**Fig. S3a**), in which the *N*-termini form a triangle of 12.9 Å (**Fig. 3a**,
273 right). The trimeric forms of I3-01v9b/c, termed I3-01v9b/c-T, were generated by interrupting the
274 particle-forming interface based on the structure of the aldolase (PDB ID: 1VLW) from which I3-
275 01 was derived. Two "scaffolded" EBOV GP constructs, termed GPΔmuc-WL^{2}P^4-I3-01v9b/c-T,
276 were designed to validate whether the I3-01v9b/c *N*-termini can accommodate the GP2 stalk (**Fig.**
277 **S3b**). Both constructs were transiently expressed in HEK293S cells, purified using a mAb100
278 column, and analyzed by SEC (**Fig. S3c**). The trimer fractions were validated by BN-PAGE (**Fig.**
279 **S3d**) before the nsEM analysis, which yielded two-dimensional (2D) classes corresponding to
280 native-like GPΔmuc-WL^{2}P^4 trimers anchored to I3-01v9b/c-T (**Figs. S3e** and **S3f**). The GP2 stalk,
281 although indiscernible in EM, was likely well-formed as the GPΔmuc trimer displayed the classic
282 chalice shape (**Fig. 3b** and **Fig. S3g**). Computational modeling suggested that EBOV GPΔmuc-
283 WL^{2}P^4-I3-01v9b would form a particle of 49.1 nm diameter measured for GP1-T269 (**Fig. 3c**).

284 Six SApNP constructs, with EBOV, SUDV, and BDBV GPΔmuc-WL^{2}P^4 displayed on the
285 E2p and I3-01v9b scaffolds (**Fig. S3h**), were transiently expressed in ExpiCHO cells and purified
286 by IAC using an ADI-15878 column and SEC using a Superose 6 increase 10/300 GL SEC column.
287 All constructs showed a peak at ~8.7 ml corresponding to assembled protein particles (**Fig. 3d**).
288 For EBOV and BDBV, a greater yield was noted for the GPΔmuc-WL^{2}P^4-presenting E2p SApNPs,
289 but for SUDV, an opposite pattern was observed, with I3-01v9b showing a higher particle peak in
290 SEC. The structural integrity of SApNPs was validated by nsEM (**Fig. 3e**). Most EM micrographs
291 contained well-formed protein particles displaying an array of GP trimers on the outer surface. The
292 particle size distribution was analyzed in solution using dynamic light scattering (DLS) (**Fig. 3f**).
293 For EBOV GPΔmuc-WL^{2}P^4-presenting SApNPs, E2p and I3-01v9b were sized at 55.7 and 84.0

294 nm, respectively (**Fig. 3f**). The unusually large I3-01v9b "particle size" from DLS might be caused
295 by SApNP aggregation, although this form was not frequently observed in nsEM. For SUDV and
296 BDBV GPΔmuc-WL^{2}P^4-presenting SApNPs, the particle size was in the range of 61.1-71.9 and
297 51.3-53.8 nm, respectively. The notable variation in particle size might be attributed to the intrinsic
298 structural flexibility of the glycan cap, which could have a significant impact on the measurement
299 of hydrodynamic radius in DLS. Site-specific glycosylation profiles were generated for SUDV
300 GPΔmuc-presenting SApNPs (**Fig. 3g** and **Fig. S3i**). An increase in oligomannose-type glycans
301 was observed for SApNPs compared with soluble trimers. In both SUDV GPΔmuc trimers and
302 their SApNPs, N563 carried predominantly oligomannose-type glycans (**Fig. 3g**).

303 The antigenicity of ebolavirus GPΔmuc-WL^{2}P^4-presenting SApNPs was assessed against
304 the same antibody panel. In ELISA, SApNPs exhibited largely similar antibody-binding patterns
305 to soluble trimers (**Fig. 3h** and **Fig. S3j**). For example, SUDV SApNPs bound less favorably to
306 ADI-15946 and BDBV-289 compared with EBOV and BDBV SApNPs, with 5.0- to 16.8-fold
307 higher EC_{50} values. SUDV GPΔmuc-WL^{2}P^4 E2p outperformed I3-01v9b with greater affinities
308 for both bNAbs, with 1.4- to 1.9-fold lower EC_{50} values. A similar pattern was also found in SUDV
309 GPΔmuc-WL^{2}P^4-presenting SApNPs binding to CA45, with a 2.5-fold difference in EC_{50} between
310 the two NP scaffolds. Interestingly, an opposite trend was observed for EBOV and BDBV SApNPs,
311 with I3-01v9b binding more tightly than E2p in most cases. BLI revealed a somewhat different
312 antigenic profile (**Fig. 3i** and **Fig. S3k**). Most notably, SUDV and BDBV SApNPs exhibited
313 greater signals in their binding to ADI-15878 and ADI-15946 than EBOV SApNPs, while SUDV
314 SApNPs bound most weakly to BDBV-289 among the three ebolaviruses. For each ebolavirus GP,
315 the binding signals against each bNAb were mostly similar between E2p and I3-01v9b, except in

316 the cases of SUDV SApNPs against CA45 and BDBV SApNPs against CA45 and BDBV-289,
317 where the difference between the two NP scaffolds was evident.

318 In this study, we displayed a stabilized GPΔmuc-WL^{2}P^4 trimer on two SApNP scaffolds,
319 E2p and a newly designed I3-01v9b, for three representative ebolaviruses. While SEC, nsEM, and
320 DLS were used to assess their purity and particle properties, which were largely comparable to our
321 HIV-1 Env trimer-presenting SApNPs (*108*), glycan and antigenic profiling revealed some unique
322 patterns associated only with SApNPs (e.g., a higher proportion of oligomannose-type glycans).

323 ***In vitro* effect of glycan modification on ebolavirus GPΔmuc trimers and SApNPs**

324 Previously, we investigated the effect of glycan modification on rationally designed HIV-1 Env
325 trimer and SApNP vaccines (*108*). Adding kifunensine (Kif) to ExpiCHO culture media, which
326 induced oligomannose-type glycosylation, neither enhanced nor reduced NAb elicitation, whereas
327 glycan trimming by endoglycosidase H (endo H) significantly improved NAb responses, indicated
328 by a high vaccine responder rate (*108*). The benefit of glycan trimming has also been reported for
329 influenza hemagglutinin (HA) and SARS-CoV-2 spike vaccines (*107, 109*). It is thus imperative
330 to examine how glycan modification may affect filovirus vaccines *in vivo*. However, these glycan-
331 modified filovirus GP immunogens first needed to be generated and characterized *in vitro*.

332 Here, we adopted a similar strategy (*108*) to generate ebolavirus GPΔmuc trimers that carry
333 either oligomannose-only glycans or a single layer of mono-*N*-acetylglucosamine (mono-GlcNAc)
334 glycans. EBOV and SUDV GPΔmuc-WL^{2}P^4 were transiently expressed in HEK293F cells in the
335 presence of Kif, which resulted in oligomannose-only glycans, and purified using an ADI-15878
336 column followed by SEC. The SEC profiles showed a trimer peak at ~10.7 ml, similar to wildtype
337 trimers (**Fig. 4a**). SEC-purified, Kif-treated GPΔmuc (e.g., 1 mg) was treated with endo H (termed
338 Kif/Endo H), which resulted in mono-GlcNAc stumps, with the enzyme removed by SEC. The

339 SEC profiles showed a trimer peak at ~11.1 ml and an endo H peak at ~13.9 ml (**Fig. 4a**). Sodium
340 dodecyl sulfate (SDS)-PAGE and BN-PAGE confirmed that Kif/Endo H-treated GPΔmuc had a
341 lower molecular weight than wildtype and Kif-treated GPΔmuc (**Fig. S4a**). DSC revealed a
342 differential effect of glycan modification on GPΔmuc thermostability (**Fig. 4b**). The Kif-treated
343 EBOV GPΔmuc-WL^{2}P^4 trimer displayed two denaturing states, with T_{m1} at 58.2ºC and T_{m2} at
344 64.3ºC. Endo H treatment further reduced T_{m1} and T_{m2} by 5.2ºC and 2.6ºC, respectively. In contrast,
345 the Kif-treated SUDV GPΔmuc-WL^{2}P^4 trimer remained thermostable, showing the same T_m
346 (63.6ºC) as the wildtype trimer with T_{onset} measured at 54.7ºC. Endo H treatment slightly reduced
347 T_m to 62.6ºC and initiated unfolding at a lower T_{onset} of 48.9ºC. Antigenicity was assessed using
348 the same antibody panel. In the ELISA (**Fig. 4c and Fig. S4b**), endo H treatment improved trimer
349 binding to CA45, ADI-15878, and ADI-15946, which access a quaternary epitope near the base
350 with few glycan contacts, but reduced trimer binding to BDBV-289, which targets the glycan cap,
351 with glycans at N238 and N268 being part of the epitope. However, their differences in EC_{50} were
352 small (1.5- to 1.9-fold) and not ebolavirus-specific. In the BLI analysis, glycan-modified trimers
353 generated slightly higher binding signals than wildtype trimers (**Fig. 4d** and **Fig. S4c**). Glycan
354 modification appeared to only have a modest impact on the biochemical, biophysical, and antigenic
355 properties of stabilized ebolavirus GPΔmuc trimers except thermostability for EBOV.

356 We next characterized glycan-modified GPΔmuc-WL^{2}P^4-presenting SApNPs. For SUDV,
357 both E2p and I3-01v9 SApNPs were included in this analysis, but for EBOV, only the E2p scaffold
358 was tested due to the low yield of I3-01v9b SApNP. Notably, an N655D mutation was introduced
359 to eliminate an *N*-glycan site at the base of the SUDV GP2 stalk that may hinder SApNP assembly.
360 A design variant termed SUDV GPΔmuc-WL^{2}P^4-PD will be used hereafter (**Fig. S4d**). EBOV and
361 SUDV SApNPs were transiently expressed in ExpiCHO cells with Kif and purified by IAC (ADI-

362 15878) and SEC. SEC-purified, Kif-treated SApNP was trimmed by endo H and further purified
363 by SEC. The SEC profiles contained a peak at ~8.5-9.0 ml corresponding to SApNPs and, after
364 endo H treatment, a peak at ~16.8 ml corresponding to endo H (**Fig. 4e**). The structural integrity
365 of glycan-modified EBOV and SUDV GPΔmuc SApNPs was validated by nsEM (**Fig. 4e**). SDS-
366 PAGE confirmed that Kif/Endo H-treated SApNPs had a lower molecular weight than Kif-treated
367 SApNPs (**Fig. S4e**). Given the low yield of EBOV SApNPs, only SUDV SApNPs were subjected
368 to glycan profiling and antigenic characterization. Site-specific glycan profiles confirmed that all
369 complex glycans in SUDV GPΔmuc were now replaced by oligomannose-type glycans in the Kif-
370 treated material (**Fig. 4f** and **Fig. S4f**). As expected, the N655 glycan was absent in the N655D
371 mutant construct. In the ELISA (**Fig. 4g** and **Fig. S4g**), the antigenic profiles of SApNPs appeared
372 to be largely consistent with those of trimers, with a more pronounced difference in EC_{50} between
373 Kif and Kif/Endo H-treated materials (1.0- to 7.9-fold) observed for CA45, ADI-15878, and ADI-
374 15946 (**Fig. 4g** and **Fig. S4g**). In the BLI analysis, all pan-ebolavirus bNAbs showed higher
375 binding signals to Kif/Endo H-treated SApNPs, which only had a layer of mono-GlcNAc stumps
376 on the GP trimer (**Fig. 4h** and **Fig. S4h**). In summary, these results suggested that glycan trimming
377 may allow better antibody access to the conserved GP epitopes on the SApNP surface.

378 **Rational design of a prefusion-stabilized RAVV GPΔmuc trimer**

379 RAVV is one of the two known members of the *Marburgvirus* genus in the filovirus family (*39,*
380 *48*). Similar to ebolavirus GPs, RAVV GP also contains GP1 with a heavily glycosylated MLD
381 and GP2 (**Fig. 5a**). Here, we applied a similar strategy to design a prefusion-stabilized RAVV GP
382 trimer based on an MLD-deleted GP construct (ΔN257-T425), termed GPΔmuc. Other mutations,
383 such as T578P and E580P (P^2 and P^4, respectively) in the HR1c bend and E631F/Q632V at the C-
384 terminus (termed CT), were introduced to create five RAVV GP constructs: 1) GPΔTM (truncation

385 at 637), 2) GPΔmuc, 3) GPΔmuc-P^2, 4) GPΔmuc-P^4, and 5) GPΔmuc-P^2CT, all with a C-terminal
386 foldon motif and His_6 tag (**Fig. S5a**). All RAVV GP constructs were transiently expressed in
387 ExpiCHO cells and purified using a Nickel column followed by SEC. Both GPΔTM and GPΔmuc
388 constructs produced a low yield that contained multiple GP species including aggregate (~9-10
389 ml), trimer (~10.5 ml), dimer (~13.6 ml), and monomer (~14.7) (**Fig. 5b**). The P^2 mutation in HR1c
390 substantially improved the SEC profiles of various GPΔmuc constructs, showing a predominant
391 trimer peak at ~10.5 ml as well as visible dimer and monomer peaks. In contrast, the P^4 mutation
392 caused significant aggregation, indicated by a peak at ~8.63 ml (**Fig. S5b**). The GPΔmuc-P^2CT
393 construct demonstrated an optimal SEC profile, with an equivalent yield to GPΔmuc-P^2 but less
394 dimer/monomer content. MARV NAbs MR78 and MR191 (*48*), when used in IAC purification,
395 failed to capture GPΔmuc-P^2 and GPΔmuc-P^2CT (**Fig. S5c**). Nonetheless, distinct trimer bands
396 were discernible on the SDS-PAGE gel after Nickel/SEC purification (**Fig. 5c** and **Fig. S5d**). In
397 DSC, we observed two denaturing states for GPΔmuc-P^2 at 51.0ºC and 60.0ºC and three denaturing
398 states for GPΔmuc-P^2CT at 54.5ºC, 58.3ºC, and 66.6ºC (**Fig. 5d**). The CT mutation appeared to
399 improve the trimer thermostability at the cost of creating a new unfolding intermediate.

400 The lead RAVV GPΔmuc design, GPΔmuc-P^2CT, was complexed with MR78 for nsEM
401 analysis (**Fig. 5e** and **Fig. S5e**). We hypothesized that if the nsEM model, albeit at a low resolution,
402 matched the crystal structure (PDB ID: 5UQY), then it would not only validate our rational design
403 but also provide evidence for the correct presentation of a conserved neutralizing epitope. Indeed,
404 the 2D classifications showed well-formed RAVV GPΔmuc/MR78 complexes (**Fig. S5e**). The
405 crystal structure could be fitted into the nsEM density map (**Fig. 5e**, left). Notably, our nsEM
406 model also superposed well with a previous nsEM model of the RAVV GPΔmuc/MR78 complex
407 (**Fig. 5e**, right). The site-specific glycan analysis showed distinct patterns compared to ebolavirus

408 GPs (**Fig. 5f** and **Fig. S5f**). Specifically, four *N*-glycan sites at N94, N171, N219, and N564 were
409 mainly oligomannose-type, whereas N190, N202, and N487 presented either oligomannose- or
410 complex-type glycans. Two sites, N475 and N619, presented predominantly complex-type glycans.
411 In the ELISA (**Fig. 5g** and **Fig. S5g**), RAVV GPΔmuc-P^2- and GPΔmuc-P^2CT trimers bound to
412 MR78 and MR191 with similar EC_{50} values. The BLI data were largely consistent with the ELISA
413 data (**Fig. 5h** and **Fig. S5h**). RAVV GPΔmuc-P^2CT was displayed on E2p and I3-01v9b SApNPs,
414 which were assessed by nsEM following ExpiCHO expression and IAC purification (**Fig. S5i**).
415 Protein NPs were not observed in any nsEM micrographs. Taken together, our results indicate that
416 GPΔmuc-P^2CT provides a native-like, prefusion-stabilized design for marburgvirus GP vaccine
417 development, but its multivalent display on SApNPs may require further optimization.

418 **Distribution, trafficking, and retention of SUDV GPΔmuc trimers and trimer-presenting**
419 **SApNPs in lymph nodes**

420 In our previous studies, we observed a positive correlation between the thermostability of a viral
421 antigen (i.e., T_m) to be displayed on E2p or I3-01v9 SApNPs and the retention time of resulting
422 SApNP vaccine antigens in lymph node follicles (*108, 120, 121*). In this study, we hypothesized
423 that SUDV GPΔmuc-presenting SApNPs may behave *in vivo* similarly to HIV-1 Env-presenting
424 SApNPs, as their trimeric antigens exhibited comparable T_m values (~63-66°C). Following our
425 previously established protocol (*108, 120, 121*), we immunized mice with SUDV GPΔmuc-WL^2P^4
426 trimer and SApNPs (both E2p and I3-01v9b included) to investigate their interaction with cellular
427 components in lymph nodes and analyze vaccine-induced immunological responses.

428 To induce a robust humoral response, vaccine antigens must be transported through the
429 lymphatic system, accumulate in lymph node follicles, and effectively engage with B cell receptors
430 (BCRs) to stimulate B cell activation (*122-125*). We first examined the distribution of E2p and I3-

431 01v9b SApNPs in lymph nodes. We intradermally administered SApNPs to mice via footpads (4
432 footpads, 10 μg/footpad). The brachial and popliteal sentinel lymph nodes were isolated from both
433 sides of the body of the mouse 12 h after a single-dose injection for immunohistological studies.
434 Four NAbs, ADI-15878 (*111*), ADI-15946 (*114*), CA45 (*113*), and mAb100 (*126*), were used to
435 stain lymph node sections for antigen detection (**Fig. S6a**). Overall, the immunostaining images
436 from CA45 demonstrated the best signal-to-noise ratio. Based on these data, CA45 was selected
437 to study the distribution and trafficking of SUDV GPΔmuc-based vaccines in lymph nodes.
438 Consistent with our previous studies of SARS-CoV-2 spike (*121*), HIV-1 Env (*108*), and influenza
439 M2ex3 (*120*) SApNPs, SUDV GPΔmuc-presenting E2p and I3-01v9b SApNPs accumulated in the
440 centers of lymph node follicles (**Figs. 6a** and **b**, images on the left; schematics on the right).

441 We next assessed the trafficking and retention patterns of SUDV GPΔmuc-WL^{2}P^4 trimer
442 and SApNPs in lymph node follicles over a period of 8 weeks after a single-dose injection (4
443 footpads, 10 μg/footpad) (**Fig. 6c**). Histological images showed that all SUDV immunogens were
444 transported into lymph nodes and accumulated in the subcapsular sinus within 2 h (**Fig. 6c**). While
445 the soluble trimer was transported into lymph node follicles within 2 h and completely cleared by
446 48 h, both E2p and I3-01v9b SApNPs appeared in follicles at 2 h, achieved peak accumulation at
447 48 h, and were retained in follicles over a period of 8 weeks (**Fig. 6c**). Next, the CA45-stained area
448 was quantified in a time-dependent manner, demonstrating a ~112-times longer retention for the
449 E2p and I3-01v9b SApNPs compared with the soluble trimer (**Figs. 6c** and **d**). The area under the
450 curve (AUC) indicated that the exposure of SUDV GPΔmuc presented on the SApNP surface is
451 14-28 times higher than the same antigen in a soluble trimer form (**Fig. 6e**). The two large SApNPs
452 displaying 20 GPΔmuc trimers also showed 19-33 times greater accumulation compared with the
453 soluble GPΔmuc trimer at 48 h (**Fig. 6f**). These findings are consistent with our previous studies

454 (*108, 120, 121*), where individual antigens were cleared from follicles within 48 h, whereas large
455 antigen-presenting SApNPs exhibited prolonged follicular retention lasting for 2-8 weeks. Notably,
456 the retention time of SUDV GPΔmuc SApNPs fell in the same range as HIV-1 Env SApNPs and
457 influenza M2ex3 SApNPs, all of which yielded a T_m value greater than 62°C, supporting our
458 hypothesis that antigen thermostability (T_m) correlates with SApNP retention.

459 FDCs are resident stromal cells that form a network structure in lymph node follicles and
460 play an essential role in antigen retention and presentation to stimulate B cell responses (*122-124,*
461 *127*). FDC networks retain soluble antigens, immune complexes, viruses, and bacteria on their
462 surfaces and dendrites to induce GC initiation and maintenance (*128-130*). Our previous studies
463 demonstrated that FDC networks are the major follicular components to retain SARS-CoV-2 spike,
464 HIV-1 Env, and influenza M2ex3 SApNPs (*108, 120, 121*). To test whether this would be the case
465 for SUDV GPΔmuc SApNPs, we isolated sentinel lymph nodes at the peak of accumulation (48 h)
466 and subsequent timepoints (2 h to 8 weeks) after intradermal administration (**Fig. 6g** and **Figs.**
467 **S6b-g**). Lymph node sections were stained with NAb CA45 (white) (*113*) for SUDV GPΔmuc,
468 anti-CD21 antibodies (green) for FDCs, and anti-CD169 antibodies (red) for subcapsular sinus
469 macrophages. The immunofluorescent signals of SUDV GPΔmuc SApNPs colocalized well with
470 FDC ($CD21^+$) networks at 48 h (**Fig. 6g**), thus confirming our hypothesis.

471 **Interaction of SUDV GPΔmuc SApNPs with FDCs and phagocytic cells in lymph nodes**

472 FDC networks form a reservoir in lymph node follicles for antigen sequestration, alignment, and
473 presentation to effectively crosslink BCRs, activate naive B cells, and stimulate GC reactions (*122-*
474 *124, 131*). Our previous transmission electron microscopy (TEM) analysis indicated that FDC
475 networks retained SARS-CoV-2 spike and HIV-1 Env SApNPs on their cell surface and dendrites
476 through interactions with complement protein 3 (C3) and complement receptor 2 (CR2) (*108, 121*).

477 Here, we visualized the interface between FDC dendrites and B cells to understand how FDC
478 networks present SUDV GPΔmuc SApNPs adjuvanted with aluminum phosphate (AP) to engage
479 B cells. To this end, we injected adjuvanted E2p and I3-01v9b SApNPs into the mouse hind
480 footpads (2 footpads, 50 μg/footpad). Fresh popliteal sentinel lymph nodes were isolated 2, 12,
481 and 48 h after a single injection. The lymph node tissues were sectioned and processed for TEM
482 analysis. TEM images revealed the expected, characteristic morphology of long FDC dendrites
483 interacting with B cells in lymph node follicles (**Figs. 7a-c**). Intact SUDV GPΔmuc E2p and I3-
484 01v9b SApNPs (round-shaped granules, yellow arrows) were aligned on FDC dendrites and B cell
485 surfaces at all timepoints, and AP particles appeared not to colocalize with SApNPs (**Figs. 7a-c**
486 and **Fig. S7a-f**). These results illustrated how FDC networks collect and present vaccine antigens
487 (i.e., SUDV GPΔmuc SApNPs) and use their long dendrites to maximize interactions between
488 antigens and BCRs. At the later timepoints (12 and 48 h), SUDV GPΔmuc SApNPs were also
489 found to be inside endolysosomes of B cells (**Figs. S7c** and **e**).

490 Phagocytic cell populations, such as macrophages and dendritic cells, take up and process
491 vaccine antigens to facilitate adaptive immune responses (*125, 132, 133*). These innate immune
492 cells, located in the subcapsular sinus and medullary sinus of lymph nodes, can capture vaccine
493 antigens, transport them to migrating B cells, and eventually deposit them on FDCs through a
494 complement-dependent transport mechanism (*123, 124, 134-138*). In this study, we assessed the
495 interaction between phagocytic cells and AP-adjuvanted SApNPs. SUDV GPΔmuc-presenting
496 E2p and I3-01v9b SApNPs were found to be either on the surface or inside endolysosomes of
497 phagocytic cells (**Figs. 7d** and **e** and **Figs. S7g-l**), consistent with our previous findings for SARS-
498 CoV-2 spike and HIV-1 Env SApNPs (*108, 121*). AP particles tended to aggregate in the
499 extracellular matrix (ECM) 2 h after the injection (**Fig. 7f** and **Fig. S7m**). Both I3-01v9b SApNPs

500 and AP particles were also observed inside endolysosomes of phagocytic cells at all timepoints
501 (**Fig. 7g** and **Figs. S7n-p**). Overall, E2p and I3-01v9b SApNPs were associated with FDC
502 networks, B cells, and phagocytic cells with a similar trend. FDC networks retained SApNPs on
503 the cell dendrites and presented native antigens to B cells in lymph node follicles. A substantial
504 amount of SApNPs was processed inside endolysosomes of phagocytic cells with AP adjuvant.

505 **Assessment of GC reactions induced by SUDV GPΔmuc trimers and SApNPs in lymph nodes**

506 In lymph node follicles, GCs are the places where B cell somatic hypermutation, selection, affinity
507 maturation, and class switching occur (*128, 139, 140*). GC reactions lead to the formation of
508 immune memory and development of NAb responses upon vaccination (*122, 125*). As the essential
509 components supporting GC initiation and maintenance, FDC networks and T follicular helper (T_{fh})
510 cells present vaccine antigens and stimulate B cells, respectively (*141-143*). Here, we hypothesized
511 that SUDV GPΔmuc SApNPs can be retained by FDC networks for a longer period and thus induce
512 more robust and long-lived GC reactions in lymph node follicles compared with the soluble trimers.
513 We first characterized GC reactions induced by I3-01v9b after a single-dose injection (4 footpads,
514 10 μg/footpad). Using a previously established protocol (*108, 120, 121*), vaccine-induced GC B
515 cells ($GL7^+$, red) and T_{fh} cells ($CD4^+$ $Bcl6^+$, co-labeled with cyan and red) in lymph nodes were
516 assessed by immunohistological analysis. Robust GCs were formed and attached to FDC networks
517 ($CD21^+$, green), with well-organized dark zone (DZ) and light zone (LZ) compartments in B cell
518 follicles (B220+, blue) (**Fig. 8a**, left). T_{fh} cells were observed in the LZ of GCs, sustaining the
519 process of B cell affinity maturation (**Fig. 8a**, right). We then applied this immunohistological
520 assessment to the SUDV GPΔmuc trimer and SApNPs (both E2p and I3-01v9b) 2, 5, and 8 weeks
521 after a single-dose injection (**Fig. 8b** and **Figs. S8a-c**) and 2 and 5 weeks after the boost (**Fig. 8c**
522 and **Figs. S8d** and **e**). We quantified GC reactions using two metrics: GC/FDC ratio (the frequency

523 of GCs associated with FDC networks) and size of GCs (occupied area in follicles) as previously
524 described (*108, 120, 121*). All three SUDV GPΔmuc immunogens induced robust GCs, with the
525 I3-01v9b SApNP group showing the largest GCs 2 weeks after a single-dose vaccination (**Fig. 8b**
526 and **Fig. S8a**). While the GC/FDC ratio after a single trimer dose decreased significantly over 8
527 weeks, the two SApNPs induced long-lived GCs with high GC/FDC ratios (above 50%) lasting
528 for 8 weeks (**Fig. 8b**). The sizes of GCs declined over time in both trimer and SApNP groups (**Figs.**
529 **8b** and **d**). For all vaccine groups, robust GCs were restored after the boost, and the GC/FDC ratio
530 of the GPΔmuc trimer group remained similar (all above 75%) to the two SApNP groups (**Fig. 8c**).
531 Overall, the two SApNPs generated larger GCs than the soluble trimer, 1.3 to 2.5 times larger after
532 one dose (**Figs. 8b** and **d**) and 1.4 to 1.8 times larger after the boost (**Figs. 8c** and **e**).

533 Next, we assessed GC reactions using flow cytometry. We intradermally immunized mice
534 with three vaccines and isolated the sentinel lymph nodes 2, 5, and 8 weeks after a single-dose
535 injection (**Fig. 8f** and **Fig. S9**) and 2 and 5 weeks after the boost injection (**Fig. 8g**) (4 footpads,
536 10 μg/injection). Fresh lymph node tissues were disaggregated into a single-cell suspension and
537 stained with an antibody cocktail. The GC reactions were quantified based on the percentage and
538 number of GC B and T_{fh} cells (**Fig. S9**). The I3-01v9b SApNP group yielded the highest percentage
539 and number of GC B cells 2 weeks after a single-dose injection (**Fig. 8f**), consistent with the
540 immunohistological analysis. Among all the vaccine groups, GC B cells declined over time while
541 T_{fh} remained steady for 8 weeks. A boost improved both the frequency and number of GC B cells
542 and T_{fh} cells (**Fig. 8g**). Notably, GC B and T_{fh} cells induced by I3-01v9b SApNP remained at a
543 relatively high level over 8 weeks after a boost injection. Compared with the soluble trimer, the
544 E2p and I3-01v9b SApNPs elicited 1.8/2.4-3.3 times more GC B cells and 1.5-1.8/2.4-3.2 times
545 more T_{fh} cells 8 weeks after the single-dose/boost injection, respectively (**Figs. 8f** and **g**). In

546 summary, the two SUDV GPΔmuc SApNPs generated more robust and long-lived GC reactions
547 than the soluble GPΔmuc trimer, leading to more potent and durable humoral immune responses.

548 **Antibody responses induced by rationally designed filovirus GPΔmuc vaccines in mice**

549 We assessed the immunogenicity of rationally designed filovirus GPΔmuc constructs, both trimers
550 and SApNPs (E2p and I3-01v9b), in mice (**Fig. 9a**). The filovirus antigen (10 μg) was adjuvanted
551 with aluminum hydroxide (AH) and a Toll-like receptor 9 (TLR9) agonist (CpG ODN 1826). Mice
552 were immunized intraperitoneally at weeks 0, 3, 9, and 15 with an interval of 6 weeks between the
553 second and third doses and the third and fourth doses. Blood serum was collected 2 weeks after
554 each immunization for serological analysis. The EBOV vaccine-induced serum binding antibody
555 (bAb) responses were determined by ELISA using an EBOV GPΔmuc-WL^{2}P^4(1TD0) antigen (**Fig.**
556 **9b** and **Figs. S10a** and **b**). Notably, the use of 1TD0, and not foldon, as the trimerization motif
557 allowed us to detect only GPΔmuc-specific bAb responses. Overall, EBOV GPΔmuc E2p SApNP
558 elicited the highest bAb titers at all four timepoints, showing 8.2- and 5.3-fold higher EC_{50} values
559 than the soluble trimer at weeks 2 and 5, respectively. All vaccine groups reached plateaued EC_{50}
560 titers after three immunizations at week 11. EBOV GPΔmuc I3-01v9b SApNP yielded an identical
561 EC_{50} titer of 182253 to its E2p counterpart at week 11, 2.5-fold higher than the EC_{50} titers elicited
562 by the soluble trimer. The sera after four vaccine doses at week 17 were assessed against a SUDV
563 GPΔmuc-WL^{2}P^4(1TD0) antigen (**Fig. 9c** and **Fig. S10c**). Similarly, EBOV GPΔmuc E2p SApNP
564 elicited the highest EC_{50} titer of 32585, which was 3.5-fold higher than the soluble trimer. Cross-
565 reactive bAb responses were also tested against a RAVV GPΔmuc-P^{2}CT(1TD0) antigen (**Fig. 9d**
566 and **Fig. S10d**). Both E2p and I3-01v9b SApNP groups demonstrated significantly higher serum
567 binding signals, indicated by absorbance at 450 nm (A450), than the soluble trimer group. Serum
568 NAb responses were evaluated using a filovirus pseudoparticle (pp) neutralization assay (*35*), with

569 the 50% inhibitory dilution (ID_{50}) values calculated for comparison. Here, the week-2 sera were
570 used as a negative control in the longitudinal serum NAb analysis. None of the EBOV GPΔmuc
571 vaccines elicited any NAb response at week 2, but ID_{50} titers were detected at weeks 5, 11, and 17
572 and continued to increase when tested against an EBOV-Makona pseudovirus (**Fig. 9e** and **Figs.**
573 **S10e** and **f**). Consistent with the bAb titers, EBOV GPΔmuc E2p SApNP produced the highest
574 NAb titers at all timepoints, although no statistical significance was observed in a cross-group
575 comparison. The week-17 mouse sera were also assessed using a SUDV-Gulu pseudovirus assay
576 (**Fig. 9f** and **Fig. S10g**). EBOV GPΔmuc E2p SApNP yielded the highest EC_{50} titer of 761 among
577 all vaccine groups. Notably, the EBOV GPΔmuc trimer group elicited the highest EC_{50} titer of
578 2759 at week 17 against a BDBV-Uganda pseudovirus, which was 4.5- and 4.9-fold higher than
579 E2p and I3-01v9b SApNPs, respectively (**Fig. 9g** and **Fig. S10h**).

580 We assessed SUDV vaccine-induced serum bAb responses by ELISA against a SUDV
581 GPΔmuc-WL^2P^4(1TD0) antigen (**Fig. 9h** and **Figs. S10i** and **j**). Consistent with the bAb responses
582 elicited by EBOV vaccines, SUDV GPΔmuc E2p SApNP yielded the highest EC_{50} titers of 871,
583 82910, and 307187 at weeks 2, 5 and 11, respectively, 12.4-, 4.5-, and 5.7-fold higher than the
584 soluble trimer. The EC_{50} titers in both E2p and I3-01v9 SApNP groups plateaued after three doses
585 at week 11, whereas the soluble trimer group reached a peak of 102959 after four doses at week
586 17, which was still slightly lower than the two SApNP groups. These results correlated well with
587 the GC reactions generated by SUDV GPΔmuc trimer and SApNPs (**Fig. 8**). The week-17 sera
588 were then evaluated against an EBOV GPΔmuc-WL^2P^4(1TD0) antigen (**Fig. 9i** and **Fig. S10k**).
589 SUDV GPΔmuc-presenting E2p and I3-01v9b SApNPs elicited EC_{50} titers of 27290 and 25446,
590 which were 2.6- and 2.4-fold higher than the soluble GPΔmuc trimer. We tested cross-reactive
591 bAb responses using week-17 sera against a RAVV GPΔmuc-P^2CT(1TD0) antigen (**Fig. 9j** and

592 **Fig. S10l**). The E2p and I3-01v9b SApNP groups demonstrated significantly higher serum binding
593 signals (A450) than the soluble trimer group. Next, we assessed SUDV GPΔmuc vaccine-induced
594 autologous NAb responses in a SUDV-Gulu pseudovirus assay. Similarly, the week-2 sera were
595 used as a negative control in the longitudinal SUDV neutralization assays. None of the vaccines
596 elicited a detectable NAb response at week 2 except for one mouse in the E2p group, but the ID_{50}
597 titers were detectable at weeks 5, 11, and 17 and plateaued at week 11 after three doses (**Fig. 9k**
598 and **Figs. S10m** and **n**). Overall, SUDV GPΔmuc trimer and SApNP vaccines showed comparable
599 EC_{50} titers in the range of 1329-4628 at each timepoint after two doses. The week-17 mouse sera
600 were tested against EBOV-Makona (**Fig. 9l** and **Fig. S10o**) and BDBV-Uganda (**Fig. 9m** and **Fig.**
601 **S10p**) pseudoviruses. No statistical significance was found between the SUDV trimer and SApNP
602 groups in their cross-NAb responses, measured by ID_{50} titers, against EBOV and BDBV.

603 Lastly, we assessed RAVV GPΔmuc trimer-induced serum bAb responses in ELISA using
604 a RAVV GPΔmuc-P^2CT(1TD0) antigen (**Fig. 9n** and **Fig. S10q**). Similar to EBOV and SUDV
605 GPΔmuc trimers, RAVV GPΔmuc trimer generated a strong bAb response after two doses, with
606 the peak EC_{50} titer of 362215 at week 5. We tested cross-reactive bAb responses using week-17
607 sera against two ebolavirus antigens, EBOV GPΔmuc-WL^2P^4(1TD0) (**Fig. 9o** and **Fig. S10r**) and
608 SUDV GPΔmuc-WL^2P^4(1TD0) (**Fig. 9p** and **Fig. S10s**). Low bAb titers, indicated by absorbance
609 (A450) values, were observed for SUDV GPΔmuc in most mice. Vaccine-induced NAb responses
610 were evaluated against pseudotyped MARV-Angola and ebolaviruses using purified IgG and
611 week-17 sera, respectively (**Fig. 9q** and **Figs. S10t** and **u**). Notably, mouse IgG was purified to
612 eliminate nonspecific serum background in the MARV pseudovirus assay (**Fig. S10t**, left), and in
613 this assay, the neutralization potency was measured by the 50% inhibitory concentration (IC_{50}).
614 To summarize, the RAVV GPΔmuc trimer group yielded IC_{50} values of 30.9-148.4 μg/ml with a

615 geometric mean of 70.2 μg/ml when IgG was tested against MARV-Angola. To be consistent with
616 EBOV and SUDV vaccines, RAVV GPΔmuc trimer-induced sera were tested against EBOV-
617 Makona, SUDV-Gulu, and BDBV-Uganda in pseudovirus assays. Despite the positive signals in
618 serum (**Fig. S10u**), IgG neutralization is likely needed to confirm this critical finding.

619 **Antibody responses induced by glycan-modified filovirus GPΔmuc vaccines in mice**

620 We assessed the immunogenicity of filovirus GPΔmuc vaccines with oligomannose-rich (Kif) and
621 trimmed (Kif/endo H) glycans in mice (**Fig. 10a**). We utilized the same immunization protocol as
622 in our previous vaccine studies (*95, 108, 144, 145*), which differed from the longer-interval (6
623 weeks) regimen used for wildtype GPΔmuc vaccines (**Fig. 9a**). Here, mice were immunized at
624 weeks 0, 3, 6, and 9 with an interval of 3 weeks between two adjacent doses via the intraperitoneal
625 route. The injection dose contained 10 μg of glycan-modified antigen formulated with 100 μl of
626 CpG/AH adjuvant, resulting in a final volume of 200 μl. Blood serum was collected 2 weeks after
627 each dose and the EC_{50} titers were plotted longitudinally for comparison.

628 We first assessed glycan-modified EBOV GPΔmuc trimer-induced serum bAb responses
629 by ELISA against an EBOV GPΔmuc-WL^2P^4(1TD0) antigen (**Fig. 10b** and **Figs. S11a** and **b**).
630 Among the three groups, the glycan-trimmed EBOV GPΔmuc trimer elicited the lowest EC_{50} titers
631 at all three timepoints, while Kif-treated EBOV GPΔmuc trimer yield the highest EC_{50} titers, 212
632 and 42360 at weeks 2 and 5, respectively. In terms of EC_{50} titers, the Kif-treated group was 2.2-
633 and 6.2-fold higher at week 2 and 1.2- and 2.1-fold higher at week 5 than the wildtype and trimmed
634 groups, respectively. All trimer groups reached the peak of EC_{50} titers after three doses. Following
635 a similar trend, the Kif-treated EBOV GPΔmuc-E2p SApNP group showed the highest bAb titers
636 at all three timepoints (**Fig. 10c** and **Figs. S11a** and **b**). The bAb responses appeared to plateau at

637 week 5, with Kif-treated EBOV GPΔmuc-E2p SApNP showing the highest EC_{50} titer of 300502,
638 1.5- and 3.2-fold higher than its wildtype and glycan-trimmed counterparts, respectively. Wildtype
639 and Kif-treated EBOV GPΔmuc I3-01v9 SApNPs induced comparable bAb responses, reaching
640 peak EC_{50} titers after three doses (**Fig. 10d** and **Figs. S11a** and **b**). We next assessed NAb
641 responses induced by glycan-modified EBOV GPΔmuc vaccines against EBOV-Makona. Overall,
642 the Kif-treated vaccines were the best performers, while the glycan-trimmed vaccines induced the
643 lowest NAb responses at all three timepoints (**Fig. 10e-g** and **Figs. S11c** and **d**). Specifically, Kif-
644 treated EBOV GPΔmuc trimer yielded an ID_{50} titer of 449 at week 5, 1.5- and 1.9-fold higher than
645 its wildtype and glycan-trimmed counterparts, respectively (**Fig. 10e**). Kif-treated EBOV GPΔmuc
646 E2p SApNP elicited an ID_{50} titer of 1459 at week 5, 2.3- and 4.1-fold higher than its wildtype and
647 glycan-trimmed counterparts, respectively (**Fig. 10f**). A similar pattern was noted for the I3-01v9b
648 SApNP groups (**Fig. 10g**). Our results thus demonstrated the beneficial effect of an oligomannose-
649 rich glycan shield on bAb and NAb responses induced by EBOV GPΔmuc vaccines.

650 We assessed glycan-modified SUDV GPΔmuc trimer-induced serum bAb responses by
651 ELISA against a SUDV GPΔmuc-WL^2P^4(1TD0) antigen (**Fig. 10h** and **Figs. S11e** and **f**). At all
652 three timepoints, Kif-treated SUDV GPΔmuc trimer elicited the highest bAb titers, whereas
653 glycan-trimmed elicited the lowest bAb titers, similar to EBOV. Regardless of glycan modification,
654 all vaccine groups reached peak EC_{50} titers after three doses. Kif-treated SUDV GPΔmuc trimer
655 elicited the highest EC_{50} titers, 425 and 150326 at weeks 2 and 5, respectively. In terms of EC_{50}
656 titers, Kif-treated SUDV GPΔmuc trimer was 6.1- and 13.3-fold higher at week 2 and 8.2- and
657 27.6-fold higher at week 5 than its wildtype and glycan-trimmed counterparts, respectively.
658 Similarly, for both SUDV GPΔmuc E2p and I3-01v9b SApNPs, the Kif-treated groups showed

659 the highest bAb responses at weeks 2 and 5 (**Figs. 10i** and **j** and **Figs. S11e** and **f**). In addition, for
660 both SApNPs, Kif treatment led to plateaued EC_{50} titers after two doses at week 5, whereas the
661 wildtype and glycan-trimmed groups required three doses to reach their EC_{50} titers at week 8. Kif-
662 treated SUDV GPΔmuc E2p and I3-01v9b SApNP elicited the highest EC_{50} titers of 329358 and
663 271692 at week 5, respectively, 2.1- and 6.9-fold higher than their wildtype counterparts and 2.3-
664 and 5.7-fold higher than their glycan-trimmed counterparts, respectively. We then evaluated NAb
665 responses induced by glycan-modified SUDV GPΔmuc vaccines against SUDV-Gulu. All three
666 SUDV GPΔmuc trimer groups reached peak ID_{50} titers after three doses (**Fig. 10k** and **Figs. S11g**
667 and **h**). The Kif-treated SUDV GPΔmuc trimer group showed the highest ID_{50} titer of 3652 at week
668 5, 2.7- and 2.2-fold higher than its wildtype and glycan-trimmed counterparts, respectively (**Fig.**
669 **10k**). Three E2p SApNPs showed comparable ID_{50} titers, indicating a limited impact of glycan
670 modification on NAb responses (**Fig. 10l**). Among the I3-01v9 SApNP groups, Kif-treated I3-
671 01v9b SApNP elicited the highest ID_{50} titer of 4041 at week 8, 2.9- and 3.2-fold higher than its
672 wildtype and glycan-trimmed counterparts, respectively (**Fig. 10m**).

673 Lastly, we assessed glycan-trimmed RAVV GPΔmuc trimer-induced serum bAb responses
674 by ELISA against a wildtype RAVV GPΔmuc-P^2CT(1TD0) antigen (**Fig. 10n** and **Figs. S11i** and
675 **j**). The wildtype trimer group achieved the peak EC_{50} titer of 362215 after two doses, whereas the
676 glycan-trimmed trimer group required three doses to reach the highest EC_{50} titer, 446121. Overall,
677 no significant difference was found between the two groups at any timepoint. We also compared
678 NAb responses induced by the wildtype and glycan-trimmed RAVV GPΔmuc vaccines using
679 purified IgG against pseudotyped MARV-Angola and ebolaviruses (**Fig. 10o** and **Fig. S10k**). In
680 terms of MARV-Angola neutralization, the two trimer groups showed similar IC_{50} values in the
681 range of 25.9-191.6 μg/ml. In terms of ebolavirus neutralization, mouse IgG was tested against

682 EBOV-Makona, SUDV-Gulu, and BDBV-Uganda. Indeed, both RAVV GPΔmuc trimers elicited
683 cross-ebolavirus NAbs, with the wildtype being more effective than the glycan-trimmed trimers.
684 IgG neutralization against lymphocytic choriomeningitis virus pseudoparticles (LCMV-pps) was
685 tested in a negative control assay, in which nonspecific activity was not detected.

686 Our results illustrated the importance of NP display and glycan modification for filovirus
687 vaccine immunogenicity in a mouse model. Overall, the Kif-treated GPΔmuc SApNPs elicited the
688 strongest bAb and NAb responses. However, due to the differences in our immunization protocols
689 (e.g., injection intervals), more *in vivo* studies are needed to confirm our results. Another important
690 finding is the induction of cross-ebolavirus NAbs by RAVV GPΔmuc-P^2CT, shown at both serum
691 and IgG levels (**Fig. 9q** right and **Fig. 10o**), suggesting a more immunogenetic nature of this
692 marburgvirus GP and its potential as a pan-filovirus vaccine antigen.

693 **DISCUSSION**

694 Filoviruses are a major cause of lethal VHF in humans and NHPs (*5, 6*). Viral GP mediates cell
695 entry by initiating attachment and membrane fusion (*13*). Structures of filovirus GP bound to NAbs
696 from human survivors demonstrate that GP harbors neutralizing epitopes and is the main target of
697 vaccine development (*17-20*). Two vector-based EBOV vaccines are now available for human use
698 after rVSV-ZEBOV (ERVEBO) (*62*) and a two-dose formula (Zabdeno + Mvabea) (*63*) were
699 approved by the U.S. FDA in 2019 and the European Commission in 2020, respectively. However,
700 no vaccines exist to prevent VHF caused by other filoviruses. In the past decade, a structure-based
701 rational approach has emerged and proven useful in accelerating vaccine development for RSV,
702 as well as the more challenging HIV-1 (*83, 84, 86, 87*). Like other class-I viral fusion proteins,
703 filovirus GP is metastable in its wildtype form (*94, 95*). As a result, filovirus vaccines that express
704 wildtype GP may not elicit an optimal immune response. Two recent studies explored potential

705 causes of filovirus GP metastability and stabilized the MLD-deleted GPΔmuc trimer in a native-
706 like conformation as vaccine antigens (*94, 95*). While native-like GP trimers remained the focus
707 of filovirus vaccines, protein NPs began to be assessed as a more effective platform for vaccine
708 delivery (*73, 95*). Glycan trimming was reported to improve NAb responses for influenza, HIV-1,
709 and SARS-CoV-2 vaccines (*107-109*), suggesting a general strategy for viral GP-based vaccines.
710 However, GP stabilization, NP display, and glycan modification have yet to be explored in a
711 systematic manner for diverse filoviruses in the context of rational vaccine design.

712 We previously reported that the HR2 stalk and HR1c bend in GP2 contributed to EBOV
713 GP metastability, and a W615L mutation and C-terminal extension (targeting HR2) in combination
714 with a proline mutation at T577 or L579 (targeting HR1c) resulted in a stable GPΔmuc trimer that
715 can be produced in mammalian cells with high yield and homogeneity (*95*). In the present study,
716 we sought to extend rational GP design to SUDV and BDBV in the *Ebolavirus* genus and RAVV
717 in the *Marburgvirus* genus to facilitate vaccine development to counter future filovirus outbreaks,
718 as highlighted by the U.S. Biomedical Advanced Research and Development Authority (BARDA)
719 (*75, 146, 147*). For GPs from these two filovirus genera, while the same GP2 elements (i.e., HR1c
720 and HR2 stalk) cause metastability, solutions to stabilize these proteins appear to be different. For
721 EBOV, SUDV, and BDBV, a comparative analysis of GPΔmuc-WL^2P^2 and -WL^2P^4 constructs
722 revealed a more favorable thermostability profile for P^4 but little difference in trimer yield, purity,
723 and antigenicity between P^2 and P^4. The crystal structure of EBOV GPΔmuc-WL^2P^4 elucidated
724 the stabilizing effect of an interprotomer hydrogen bond (R130-A575), while the cryo-EM model
725 of SUDV GPΔmuc-WL^2P^4 captured the atomic details of GP-CA45 interactions, thus confirming
726 that GPΔmuc-WL^2P^4 is a general design to stabilize ebolavirus GP in a native-like conformation
727 for immune recognition. For RAVV, the P^2 (T578P) construct showed substantially higher trimer

728 yield than its P^4 (E580P) counterpart, with a double mutation (E631F/Q632V) toward the base of
729 the HR2 stalk further improving trimer stability, resulting in a GPΔmuc-P^2CT design. Notably, the
730 W615L mutation used to stabilize ebolavirus GP was adopted from MARV GP (*95*), whereas here
731 the E631F/Q632V mutation used to stabilize marburgvirus GP was introduced from EBOV GP,
732 suggesting that filoviruses may have evolved distinct mechanisms to control metastability through
733 either a widened neck (for ebolaviruses) or a charged tail (for marburgviruses) within the coiled-
734 coil HR2 stalk. Our findings also suggest that other class-I viral GPs may contain triggers of
735 metastability within their stalks, such as RSV fusion and SARS-CoV-2 spike proteins.

736 We previously focused our NP design efforts on the interior, incorporating an inner shell
737 of locking domains and a core of helper T-cell epitopes (*95*). The resulting "multilayered" E2p
738 and I3-01v9 SApNPs were used to present EBOV, SARS-CoV-2, HIV-1, and influenza antigens
739 (*95, 108, 120, 144, 148*). We also observed that EBOV GP and RSV F (*95, 149*), both containing
740 a coiled-coil stalk, but not HIV-1 Env (*86, 150*) dissociated into monomers without a C-terminal
741 trimerization motif, suggesting that NPs with small, rigid anchoring sites may be more suitable for
742 displaying such GP trimers with extended stalks. Compared with E2p, which has a small triangular
743 anchoring site (9 Å) on the NP surface (*151*), I3-01v9 *N*-termini form a large spacing of 50.5 Å
744 (*150*), which may destabilize EBOV and other filovirus GPs on the NP surface. To address this
745 issue, we redesigned I3-01v9 using a previously created I3-01v9a variant (*120*) as the template.
746 An *N*-terminal helix was generated and packed against the protein core *in silico*, resulting in I3-
747 01v9b/c. When the I3-01v9b/c-T variants were used as "scaffolds" to present EBOV GPΔmuc-
748 WL^2P^4, the resulting constructs showed native-like GP structures in EM. However, it is worth
749 noting that while all three ebolavirus GPΔmuc-WL^2P^4 trimers were successfully displayed on E2p
750 and I3-01v9b SApNPs, a similar attempt with RAVV GPΔmuc-P^2CT produced low yield and

751 aggregation. It is plausible that certain regions within RAVV GP might interact with the NP
752 backbone and consequently cause misfolding. Nonetheless, our results suggest that I3-01v9b/c can
753 now be used to display filovirus GP as well as other viral GPs, such as RSV F and SARS-CoV-2
754 spike, with greater trimer stability. Glycan modification adds another dimension to rational vaccine
755 design (*108*), but the biochemical, biophysical, structural, and antigenic properties must be
756 reevaluated. Here, the glycan-trimmed GPΔmuc trimers showed lower T_m values than wildtype
757 and Kif-treated oligomannose-rich GPΔmuc trimers. Similar to our previous HIV-1 study (*108*),
758 glycan trimming improved NAb epitope recognition for both trimers and SApNPs. However, the
759 improved *in vitro* antigenicity may not necessarily correlate with *in vivo* immunogenicity.

760 In recent studies, we established a vaccine strategy in which a detailed mechanistic analysis
761 was performed to characterize *in vivo* behaviors of immunogens to provide potential explanations
762 for the NAb results from vaccination (*108, 120, 121*). In the analysis of SUDV GPΔmuc vaccine
763 constructs, multivalent display of GPΔmuc trimers on SApNPs allowed stronger interactions with
764 FDC networks, B cells, and phagocytic cells in lymph nodes. The size and intrinsic thermostability
765 of SApNPs enhanced vaccine retention and presentation in lymph node follicles (over 8 weeks),
766 in addition to more robust and durable GC reactions, compared with the soluble GPΔmuc trimer.
767 The nearly identical trafficking and retention patterns observed for SApNPs presenting SUDV
768 GPΔmuc, HIV-1 Env (*108*), and influenza M2ex3 (*120*), which differ significantly in their glycan
769 profiles, confirm our previous conclusion that glycans may not be critical for the follicular
770 localization of NP vaccines in lymph nodes (*108*). Collectively, our current and previous studies
771 suggest that NP size and antigen thermostability may be determining factors in behaviors of these
772 NPs in lymph nodes (*108, 120, 121*). Mouse immunization sheds light on antibody responses to
773 various filovirus vaccines. Overall, the NAb responses tracked well with the bAb responses in the

774 longitudinal serum analysis. Among wildtype vaccines, EBOV and SUDV GPΔmuc-presenting
775 E2p SApNPs elicited the highest EC_{50} and ID_{50} titers at most timepoints, consistent with robust
776 GC reactions induced by E2p in the lymph node analysis. The two glycan modification strategies,
777 however, showed somewhat unexpected results. Glycan-trimmed trimers and SApNPs elicited the
778 lowest EC_{50} and ID_{50} titers at all timepoints, whereas Kif-treated, oligomannose-rich immunogens
779 induced the most potent bAb and NAb responses at most timepoints. This pattern was opposite to
780 that seen in the previous influenza HA/stem, SARS-CoV-2 spike, and HIV-1 Env vaccine studies,
781 in which glycan trimming improved the breadth and potency of vaccine-induced NAb responses
782 (*107-110*). Although the causes for this discrepancy remain unclear, our results suggest that there
783 may not be a general glycan strategy that fits all viral GP vaccines.

784 Our future research will focus on several directions. First, antibodies induced by GPΔmuc
785 trimers and SApNPs, both wildtype and glycan-modified, need to be isolated and mapped onto the
786 GP surface to determine how SApNP display improves NAb function, as demonstrated for SARS-
787 CoV-2 (*121*), how cross-NAbs recognize diverse GPs, and how glycan modification alters epitope
788 targeting. Second, the impact of glycan modification on vaccine-induced NAb responses requires
789 more in-depth studies. While it remains to be seen whether enriched oligomannose content can
790 improve NAb elicitation for other viral GP vaccines, approaches that produce different glycan
791 profiles may be readily tested for filovirus vaccine constructs. Non-mammalian systems, such as
792 engineered fungal (*152, 153*) and insect (*154*) cell lines, may generate shorter oligomannose-type
793 glycans with distinct glycoforms, reducing the complexity of chemical-based glycan modification.
794 Third, strategies for achieving pan-filovirus protection may warrant investigation. Although our
795 EBOV or SUDV GPΔmuc SApNPs can elicit cross-ebolavirus NAb responses, their combined use
796 with an optimized marburgvirus GP immunogen may be required to generate a pan-filovirus bNAb

797 response. Given the cross-ebolavirus NAb response induced by the RAVV GPΔmuc-P^2CT trimer,
798 efforts may also be directed to the multivalent display of this GPΔmuc trimer on SApNPs to further
799 improve the breadth and potency of this bNAb-like response. Lastly, filovirus challenge in mice
800 or guinea pigs will provide critical information on protection, allowing selected vaccine constructs
801 to be advanced to evaluation in an NHP immunization/challenge model.

802 **METHODS**

803 **Construct design, expression, and purification of filovirus GP immunogens**

804 For ebolaviruses, the amino acid sequences of EBOV GP (Mayinga strain, GenBank Accession:
805 NP_066246) with a T42A substitution, SUDV GP (Gulu strain, GenBank Accession: AAU43887),
806 and BDBV GP (R4386L strain, GenBank Accession: AYI50307) were used to design GPΔmuc
807 trimers (**Fig. S1a**) and SApNPs (**Fig. S3h**). Of note, an N637D mutation was later introduced to
808 the SUDV GPΔmuc-WL^2P^4 construct to eliminate a potential *N*-linked glycosylation site at N637
809 due to the enzymatic site "AS" between the GP and SApNP backbone. For marburgviruses, the
810 amino acid sequence of RAVV GP (Ravn-87 strain, GenBank Accession: ABE27071) was used
811 to design GPΔTM and various GPΔmuc trimers (**Fig. S5a**).

812 Rationally designed EBOV, SUDV, and BDBV GPΔmuc trimers were transiently
813 expressed in HEK293F cells as previously described (*95*). Briefly, HEK293F cells were thawed
814 and suspended in FreeStyle 293 Expression Medium (Life Technologies, Carlsbad, CA) and
815 placed in a shaker incubator at 37°C at 135 rotations per minute (rpm) with 8% CO_2. When the
816 cells reached a density of 2.0×10^6/ml, the cells were diluted to a concentration of 1.0×10^6/ml in
817 1 L of FreeStyle 293 Expression Medium for transfection using a polyethyleneimine (PEI)
818 (Polysciences) transfection protocol. In brief, 900 μg of expression plasmid in 25 ml of Opti-MEM
819 transfection medium (Life Technologies, Carlsbad, CA) was mixed with 5 ml of PEI-MAX

820 (1.0 mg/ml) in 25 ml of Opti-MEM and incubated for 30 min at room temperature. Next, the
821 HEK293F cells were transfected with the DNA-PEI-MAX mixture and incubated in a shaker
822 incubator at 37°C at 135 rpm with 8% CO_2. Kifunensine (10 mg/L, Tocris Bioscience) was added
823 at the time of transfection to inhibit α-mannosidase I to generate oligomannose-type glycans. Five
824 days after transfection, supernatants containing the target protein were harvested, clarified by
825 centrifugation at 1126 × g for 22 min, and filtered through a 0.45 µm filter (Thermo Scientific).
826 Ebolavirus GP was purified using an ADI-15878 antibody column except for the crystallographic
827 analysis of EBOV GPΔmuc-WL^2P^4 and nsEM analysis of EBOV GPΔmuc-WL^2P^4-I3-01v9b/c-T,
828 where an mAb100 antibody column was used. Ebolavirus GP was eluted three times each with 5
829 ml of 0.2 M glycine (pH 2.2), neutralized with 0.5 ml of 2 M Tris-Base (pH 9.0), and buffer-
830 exchanged into phosphate-buffered saline (PBS; pH 7.2). The IAC-purified ebolavirus GP was
831 further purified by SEC using a Superdex 200 Increase 10/300 GL column (Cytiva).

832 RAVV GPΔmuc trimers and all ebolavirus GPΔmuc-presenting SApNPs were produced
833 in ExpiCHO cells (Thermo Fisher). Briefly, ExpiCHO cells were thawed and incubated in
834 ExpiCHO Expression Medium (Thermo Fisher) in a shaker incubator at 37°C at 135 rpm with 8%
835 CO_2. When the cells reached a density of 10×10^6/ml, ExpiCHO Expression Medium was added
836 to adjust the cell density to 6×10^6/ml for transfection. The ExpiFectamine CHO/plasmid DNA
837 complexes were prepared for 100-ml transfection in ExpiCHO cells following the manufacturer's
838 instructions. Kifunensine (10 mg/L, Tocris Bioscience) was added at the time of ExpiCHO
839 transfection to inhibit α-mannosidase I to generate oligomannose-type glycans. For these
840 constructs, 100 µg of plasmid and 320 µl of ExpiFectamine CHO reagent were mixed in 7.7 ml of
841 cold OptiPRO™ medium (Thermo Fisher). After the first feed on day 1, ExpiCHO cells were
842 cultured in a shaker incubator at 33°C at 115 rpm with 8% CO_2 according to the Max Titer protocol

843 with an additional feed on day 5 (Thermo Fisher). Culture supernatants were harvested 13–14 days
844 after transfection, clarified by centrifugation at 3724 × g for 25 min, and filtered using a 0.45 µm
845 filter (Thermo Fisher). RAVV GPΔmuc trimers were purified using Ni Sepharose excel resin
846 (Nickel, Cytiva), and the bound protein was eluted twice, each with 15 ml of 0.5 M imidazole, and
847 then exchanged into Tris-buffered saline (TBS; pH 7.2). Ebolavirus GPΔmuc-presenting SApNPs
848 were purified using an ADI-15878 antibody column, eluted three times each with 5 ml of 0.2 M
849 glycine (pH 2.2), neutralized with 0.5 ml of 2 M Tris-Base (pH 9.0), and buffer-exchanged into
850 PBS (pH 7.2). The Nickel-purified RAVV GPΔmuc trimer and all ebolavirus GPΔmuc-presenting
851 SApNPs were further polished by SEC using a Superdex 200 Increase 10/300 GL column (Cytiva)
852 and a Superose 6 Increase 10/300 GL column (Cytiva), respectively. Selected SEC fractions were
853 pooled, aliquoted, and frozen in liquid nitrogen or at -80 ºC until use.

854 **Expression and purification of neutralizing antibodies (NAbs)**

855 Antibodies in the IgG form were transiently expressed in ExpiCHO cells (Thermo Fisher). At 12-
856 14 days post-transfection, the cells were centrifuged at 3,724 × g for 25 min, with the supernatants
857 filtered using a 0.45-µm filter (Millipore). IgGs were purified using protein A affinity resin
858 (Cytiva) and eluted in 0.3 M citric acid (pH 3.0). The elution was immediately titrated to a neutral
859 pH of 7.0 by the addition of 2 M Tris-base (pH 9.0). The eluate was concentrated and exchanged
860 into PBS using an Amicon 10 kDa filter (Millipore). The IgG concentration was quantified by
861 UV_{280} absorption with theoretical extinction coefficients.

862 **Glycan trimming by endo H treatment and enzyme removal**

863 The protocol for endo H treatment and removal was reported in our previous study (*108*). Briefly,
864 the surface glycans of filovirus GPΔmuc trimers and SApNPs were trimmed by endoglycosidase
865 H (Endo-Hf), a fusion of endo H and MBP (NEB, catalog no. P0703L), by mixing 1 mg of antigen

866 with 200 µl of 10× GlycoBuffer 3, 250 µl of endo H, and H_2O (if necessary) to make a 2 ml reaction.
867 The mixture was incubated at room temperature (25°C) for 5 h to facilitate enzymatic processing
868 of the GP glycans. After incubation, the mixtures were passed through a Superdex 200 increase
869 10/300 GL column (for trimers) and Superose 6 increase 10/300 GL column (for SApNPs) to
870 remove the MBP-tagged endo H. Notably, to enable glycan trimming by endo H, the filovirus
871 GPΔmuc trimers and SApNPs must be expressed in the presence of kifunensine. Previously, the
872 amylose resin (NEB, catalog no. E8021S) was used to remove residual endo Hf from the SEC-
873 purified HIV-1 Env trimer and SApNPs (*108*). Notably, this additional step of endo H removal
874 was not included in the present study to preserve vaccine antigens for animal studies. The SEC-
875 purified fractions were pooled aliquoted, and frozen in liquid nitrogen or at -80 ºC until use.

876 **SDS-PAGE and BN-PAGE**

877 Filovirus GPΔmuc trimers and SApNPs were analyzed by sodium dodecyl sulfate-polyacrylamide
878 gel electrophoresis (SDS-PAGE) and blue native-polyacrylamide gel electrophoresis (BN-PAGE).
879 The proteins were mixed with loading dye and loaded on a 10% Tris-Glycine Gel (Bio-Rad) or a
880 4-12% Bis-Tris NativePAGE gel (Life Technologies). For SDS-PAGE under reducing conditions,
881 the proteins were mixed with 6× Laemmli SDS sample buffer (Thermo Scientific) and boiled for
882 5 min at 100°C. SDS-PAGE gels were run for 25 min at 250 V using SDS running buffer (Bio-
883 Rad). SDS-PAGE gels were stained with InstantBlue (Abcam). For BN-PAGE, the proteins were
884 mixed with 4× native dye and loaded on a BN-PAGE gel. The gel was run for 2–2.5 h at 150 V
885 with NativePAGE running buffer (Life Technologies) according to the manufacturer's instructions.
886 The BN-PAGE gels were stained using Coomassie Brilliant Blue R-250 (Bio-Rad) and destained
887 using a solution of 6% ethanol and 3% glacial acetic acid.

888 **Differential scanning calorimetry (DSC)**

889 Melting temperature (T_m) and other thermal parameters of filovirus GPΔmuc trimers purified by
890 an IAC or Nickel column followed by SEC were obtained using a MicroCal PEAQ-DSC Man
891 instrument (Malvern). Briefly, the purified protein in PBS buffer was diluted to 0.5-5 μM. Melting
892 was probed at a scan rate of 60°C/h from 20°C to 100°C. Data processing, including buffer
893 correction, normalization, and baseline subtraction, was conducted using MicroCal PEAQ-DSC
894 software. Gaussian fitting was performed using GraphPad Prism 10.3.1 software.

895 **Site-specific glycan analysis**

896 To generate site-specific glycan profiles, 100 μg aliquots of each antigen were denatured for 1 h
897 in 50 mM Tris/HCl, pH 8.0 containing 6 M urea and 5 mM dithiothreitol (DTT). Next, antigen
898 samples were reduced and alkylated by adding 20 mM iodoacetamide (IAA) and incubated for 1
899 h in the dark, followed by 1h of incubation with 20 mM DTT to eliminate residual IAA. The
900 alkylated antigen samples were buffer-exchanged into 50 mM Tris/HCl, pH 8.0 using Vivaspin
901 columns (10 kDa), and three of the aliquots were digested separately overnight using trypsin (Mass
902 Spectrometry Grade, Promega), chymotrypsin (Mass Spectrometry Grade, Promega) or alpha lytic
903 protease (Sigma Aldrich) at a ratio of 1:30 (w/w). The next day, the peptides were dried and
904 extracted using an Oasis HLB μElution Plate (Waters).

905 The peptides were dried again, resuspended in 0.1% formic acid, and analyzed by nanoLC-
906 electrospray ionization MS with an Ultimate 3000 HPLC (Thermo Fisher Scientific) system
907 coupled to an Orbitrap Eclipse mass spectrometer (Thermo Fisher Scientific) using stepped higher
908 energy collision-induced dissociation (HCD) fragmentation. Peptides were separated using an
909 EasySpray PepMap RSLC C18 column (75 μm × 75 cm). A trapping column (PepMap 100 C18
910 3μM 75μM × 2cm) was used in line with liquid chromatography (LC) prior to separation with the
911 analytical column. The LC conditions were as follows: 280-minute linear gradient consisting of 4-

912 32% acetonitrile in 0.1% formic acid over 260 minutes followed by 20 minutes of alternating 76%
913 acetonitrile in 0.1% formic acid and 4% ACN in 0.1% formic acid, used to ensure all the sample
914 had eluted from the column. The flow rate was set to 300 nl/min. The spray voltage was set to 2.7
915 kV and the temperature of the heated capillary was set to 40 °C. The ion transfer tube temperature
916 was set to 275 °C. The scan range was 375−1500 m/z. The stepped HCD collision energies were
917 set to 15%, 25%, and 45% and the MS2 for each energy was combined. Precursor and fragment
918 detection were performed using an Orbitrap at a resolution of MS^1 = 120,000 and MS^2 = 30,000.
919 The AGC target for MS1 was set to standard and injection time set to auto which involves the
920 system setting the two parameters to maximize sensitivity while maintaining cycle time. Full LC
921 and MS methodology can be extracted from the appropriate Raw file using XCalibur FreeStyle
922 software or upon request.

923 Glycopeptide fragmentation data were extracted from the raw file using Byos 4.6 (Protein
924 Metrics). The glycopeptide fragmentation data were evaluated manually for each glycopeptide;
925 the peptide was scored as true-positive when the correct b and y fragment ions were observed
926 along with oxonium ions corresponding to the glycan identified. The MS data was searched using
927 the Protein Metrics 38 insect N-glycan library. The relative amounts of each glycan at each site as
928 well as the unoccupied proportion were determined by comparing the extracted chromatographic
929 areas for different glycotypes with an identical peptide sequence. All charge states for a single
930 glycopeptide were summed. The precursor mass tolerance was set at 4 ppm and 10 ppm for
931 fragments. A 1% false discovery rate (FDR) was applied. The relative amounts of each glycan at
932 each site as well as the unoccupied proportion were determined by comparing the extracted ion
933 chromatographic areas for different glycopeptides with an identical peptide sequence. Glycans
934 were categorized according to the composition detected.

935 HexNAc(2)Hex(9−3) was classified as M9 to M3. Any of these structures containing a
936 fucose were categorized as fucosylated mannose (FM). Complex-type glycans were classified
937 according to the number of HexNAc subunits and the presence or absence of fucose. Core glycans
938 refer to truncated structures smaller than M3. As this fragmentation method does not provide
939 linkage information, compositional isomers are grouped.

940 **Biolayer interferometry**

941 Antigenic profiles of filovirus GPΔmuc trimers and SApNPs were measured using Octet RED96
942 (FortéBio, Pall Life Sciences) against a panel of antibodies, including five pan-ebolavirus NAbs
943 and two marburgvirus NAbs, all in the IgG form. All assays were performed with agitation set to
944 1000 rpm in FortéBio 1× kinetic buffer. The final volume for all solutions was 200 µl per well.
945 Assays were performed at 30 °C in solid black 96-well plates (Geiger Bio-One). For all antigens,
946 5 µg/ml antibody in 1× kinetic buffer was loaded onto the surface of anti-human Fc Capture
947 Biosensors (AHC) for 300 s. Next, a 2-fold concentration gradient of antigen, starting at 500 nM
948 for trimers and 10 nM for SApNPs, was used in a dilution series of six. A 60-s biosensor baseline
949 step was applied before the analysis of association of the antibody on the biosensor to the antigen
950 in solution for 200 s. Dissociation of the interaction was followed for 300 s. The correction of
951 baseline drift was performed by subtracting the mean value of shifts recorded for a sensor loaded
952 with antibody but not incubated with antigen, and for a sensor without antibody but incubated with
953 antigen. Octet data were processed by FortéBio's data acquisition software (version 8.1). Peak
954 signals at the highest antigen concentration were summarized in a matrix and color-coded
955 accordingly to allow comparisons between different constructs. Experimental data for each
956 antigen-antibody pair were fitted with the binding equations describing a 1:1 interaction, and three

957 datasets that showed the optimal fitting were then grouped to determine the K_{on} and K_D values.
958 The antibody-antigen binding curve was plotted using GraphPad Prism 10.3.1 software.

959 **Enzyme-linked immunosorbent assay (ELISA)**

960 Costar 96-well, high-binding, flat-bottom, half-area plates (Corning) were first coated with 50 µl
961 of PBS containing 0.1 µg of the appropriate filovirus GPΔmuc trimer or SApNP antigen protein.
962 The plates were incubated overnight at 4 °C and then washed five times with PBST wash buffer
963 containing PBS and 0.05% (v/v) Tween 20. Each well was then blocked for 1 h at RT with 150 µl
964 of blocking buffer consisting of 4% w/v blotting-grade blocker (Bio-Rad) in PBS. Next, the plates
965 washed five times with PBST wash buffer. To evaluate antibody binding to the coating antigens,
966 antibodies were diluted in blocking buffer to a maximum concentration of 10 µg/ml followed by
967 a 10-fold dilution series. For each antibody dilution, a total volume of 50 µl was added to the
968 appropriate wells. For serum sample analysis, mouse sera were diluted 40-fold in blocking buffer
969 and subjected to a 10-fold dilution series. For each sample dilution, a total volume of 50 µl was
970 added to the wells. Each plate was incubated for 1 h at room temperature and then washed five
971 times with PBST wash buffer. For secondary antibody binding, a 1:5000 dilution of goat anti-
972 human IgG antibody (Jackson ImmunoResearch Laboratories) or for mouse sample analysis, a
973 1:3000 dilution of horseradish peroxidase (HRP)-conjugated goat anti-mouse IgG antibody
974 (Jackson ImmunoResearch Laboratories) was prepared in PBST wash buffer, with 50 µl of diluted
975 secondary antibody added to each well. The plates were incubated for 1 h at room temperature and
976 then washed six times with PBST wash buffer. Lastly, the wells were developed with 50 µl of
977 3,3',5,5'-tetramethylbenzidine (Life Sciences) for 3-5 min before the reaction was stopped with
978 50 µl of 2 N sulfuric acid. The plates were then immediately read on a BioTek Synergy plate reader
979 at a wavelength of 450 nm. EC_{50} values were then calculated from full curves using GraphPad

980 Prism 10.3.1 software. When OD_{450} absorbance values were lower than 0.5, the EC_{50} values were
981 set to 10 μg/ml in **Figs. 1g**, **3h**, **4c** and **4h** to facilitate EC_{50} plotting and comparison.

982 **Protein crystallization and data collection**

983 EBOV GPΔmuc-WL^2P^4 was transiently expressed in HEK293S cells using the same procedure as
984 in HEK293F cells, followed by mAb100 and SEC purification. The mAb100/SEC-purified EBOV
985 GPΔmuc-WL^2P^4 trimer at a 9.3 mg/ml concentration was used for crystallization experiments
986 following the sitting drop vapor diffusion method using an automated CrystalMation robotic
987 system (Rigaku) at 20°C at The Scripps Research Institute (*155*). The reservoir solution consisted
988 of 12% PEG-6000 (*v/v*) and 0.1 M sodium citrate-citric acid (pH 4.51). Diffraction-quality crystals
989 were obtained after 2 weeks of incubation at 20°C. The crystal was cryoprotected with a well
990 solution containing 25% (*v/v*) ethylene glycol, mounted on a nylon loop, and flash cooled in liquid
991 nitrogen. Diffraction data were collected at Stanford Synchrotron Radiation Lightsource (SSRL)
992 beamline 12-1 and processed with HKL-2000 (*156*). Diffraction data were indexed in P321.

993 **Structure determination and refinement**

994 The crystal structure of EBOV GPΔmuc-WL^2P^4 was determined by molecular replacement using
995 Phaser-MR from Phenix (version 1.19.2-4158) with the coordinates of the previously reported
996 EBOV GPΔmuc-WL^2P^2 structure (PDB ID: 7JPH) (*95*) as a search model. Polypeptide chains
997 were manually adjusted into electron density using Coot (*157*), refined with phenix-refine (*158*),
998 and validated using the wwPDB Validation System (*159*). Carbohydrates were further validated
999 using Privateer in CCP4i (*160*) before and after refinement. The final data processing and
1000 refinement statistics are described in **Table S1**. All images for crystal structures shown in the
1001 figures were generated using PyMOL 2.3.4 software. Notably, due to the weak electron density,
1002 structural model was not built for residues K633-D637 in the GP2 stalk region of EBOV GPΔmuc-

1003 WL^2P^4, as well as the C-terminal foldon trimerization motif, leaving an apparent gap in crystal
1004 packing when visualizing the GP structure within the electron density map.

1005 **Negative-stain electron microscopy (nsEM)**

1006 The nsEM analysis of filovirus GPΔmuc trimers, their antibody-bound complexes, and GPΔmuc-
1007 presenting SApNPs, was performed by the Core Microscopy Facility at The Scripps Research
1008 Institute. Briefly, samples were prepared at a concentration of 0.008 and 0.01 mg/ml, respectively.
1009 Carbon-coated copper grids (400 mesh) were glow-discharged, and 8 µl of each sample was then
1010 adsorbed for 2 min. Next, excess samples were removed, and grids were negatively stained with
1011 2% uranyl formate for 2 min. Excess stain was wicked away and the grids were allowed to dry.
1012 Trimer samples were analyzed at 120 kV with a Talos L120C transmission electron microscope
1013 (Thermo Fisher), and images were acquired using a CETA 16 M CMOS camera under 73,000×
1014 magnification at a resolution of 1.93 Å/pixel and defocus of 0.5-2 µm. For SApNP samples, the
1015 images were collected under 52,000× magnification. The resulting pixel size at the specimen plane
1016 was 2.05 Å, and the defocus was set to −1.50 µm. Computational analysis of the images was
1017 performed using the high-performance computing core facility at The Scripps Research Institute.
1018 Briefly, the nsEM images were converted to the MRC format by EMAN2 (*161*) for further
1019 processing by CryoSPARC 4.3.0 (*119*). Micrographs were contrast-transfer function (CTF)-
1020 corrected by patch CTF estimation. Particles were selected using a Blob/template picker and later
1021 extracted with a box size of 130 pixels for 2D classification, with 50 and 230 Å used as the
1022 minimum and maximum particle sizes in blob picking. 3D models were generated by *ab initio*
1023 reconstruction and optimized by heterogeneous and homogeneous refinement. All nsEM and fitted
1024 structure images were generated by UCSF Chimera (*162*) and Chimera X (*163-165*).

1025 **Cryo-electron microscopy (cryo-EM) for SUDV GP-CA45 complexes**

1026 The SUDV GPΔmuc-WL^{2}P^4 construct was expressed in HEK293F cells and purified using an
1027 ADI-15878 column. The eluate was then mixed with CA45 Fab at a 1:1.5 molar ratio. The mixture
1028 was further purified using a Superose 6 Increase 10/300 GL column and the complex fractions
1029 were pooled. Cryo-EM grid preparation and image collection were performed at the UC San Diego
1030 Cryo-EM Facility. Vitrification was carried out using a Vitrobot Mark IV (FEI) equilibrated to 4ºC
1031 and 100% humidity. The Quantifoil Cu 1.2/1.3 300 grid was plasma cleaned by Solarus II (Gatan)
1032 with a mixture of Ar/O_2 for 10 s. After plasma cleaning, the grid was blotted on one side with 3.5
1033 µl of the SUDV GPΔmuc-WL^{2}P^4/CA45 Fab complex at a concentration of 0.55 mg/ml for 4 s and
1034 then frozen in liquid ethane. The frozen grid was stored in liquid nitrogen until image collection.
1035 Cryo-EM data were collected on a Krios G4 (Thermo Fisher) operated at 200 keV with a Falcon
1036 4 camera and Selectris-X energy filter (Thermo Fisher). Automated data collection was performed
1037 using Smart EPU software (Thermo Fisher). Images were collected under 130,000× magnification,
1038 resulting in a pixel size of 0.89 Å, with the defocus range set between -1 and -2.5 µm. All datasets
1039 were processed by CryoSPARC 3.3 software. Movie frames were aligned using "Patch Motion
1040 Correction," and CTF estimations were performed by "Patch CTF Estimation" (**Fig. S2d**). Particle
1041 picking was performed by "Blob Picking" with the particle size set to 100-350 Å, and particles
1042 were extracted using a box size of 360 pixels. After 2D classification, the selected classes were
1043 used as an input for "Template Picking" and extracted using a box size of 360 pixels. After multiple
1044 2D classifications, 249,139 particles were selected for building 3D volume models. The function
1045 "Ab-Initio Reconstruction" in CryoSPARC was used to generate three starting reference models
1046 for "Heterologous Refinement". The particles derived from the largest cluster (163,924 particles)
1047 were used for "Homogeneous Refinement" using a focusing mask and C3 symmetry. The refined
1048 model was then subjected to "3D Classification," resulting in 10 models, of which the cluster

1049 associated with the most complete model (41,233 particles) was used for another around of "Ab-
1050 Initio Reconstruction." The model obtained from this smaller set was further optimized using
1051 "Non-uniform Refinement" and "Local Refinement" using 163,924 particles and a focusing mask.
1052 The final GSFSC resolution was 3.13 Å, and the final structural model was built using the crystal
1053 structures of EBOV GPΔmuc-WL^{2}P^2 (PDB ID: 7JPH) (*95*) and EBOV GPΔmuc-bound CA45 Fab
1054 (PDB ID: 6EAY) (*113*) as templates. After fitting into the density map using Chimera X (*163-*
1055 *165*), the resulting complex underwent real-space refinement in Phenix (*158*), manual refinement
1056 by Coot (*157*), and again real-space refinement in Phenix (*158*). Statistical details of the final cryo-
1057 EM structure are shown in **Table S2**, with the coordinates and 3D density map deposited in Protein
1058 Data Bank (PDB) and Electron Microscopy Data Bank (EMDB), respectively.

1059 **Rational design of trimer-presenting I3-01v9b/c SApNP scaffolds**

1060 Previously, we redesigned the I3-01v9 scaffold to optimize the NP display of monomeric antigens
1061 (*120*). In the resulting I3-01v9a SApNP, the *N*-terminal helix was extended so that its first residue
1062 is just above the NP surface. Here, we redesigned the I3-01v9a scaffold to optimize the NP display
1063 of trimeric antigens with a long coiled-coil stalk (**Fig. S3**). First, the 11-aa *N*-terminal helix in I3-
1064 01v9a was truncated to 7 aa. Then, a 13-aa helix-turn fragment (9-aa helix + 4-aa turn, all alanine)
1065 was fused to the 7-aa *N*-terminal helix of the modified I3-01v9a such that the new 9-aa *N*-terminal
1066 helix from the fused fragment packed within the groove of two helices that are part of the I3-01
1067 core. The 9-aa helix in this fragment was from the structure of a human transcription factor (PDB
1068 ID: 6G6L). Next, four mutations were introduced to the I3-01 core helices to remove their steric
1069 clashes with the new *N*-terminal helix. Iterative modular optimization (IMO) (*166*) was used to
1070 relax the helix-turn backbone, which was then subjected to the CONCOORD structure sampling
1071 program (*167*) to generate 1000 slightly perturbed backbone conformations. An ensemble-based

1072 protein design program (*86, 145*) was used to predict the optimal sequence for the 9-aa *N*-terminal
1073 helix within the fragment using Cα and Cβ-based RAPDF (*168*) scoring functions. The 4-aa turn
1074 was set to "GSGS" during the protein design process. The I3-01v9b design was selected by
1075 combining data from both scoring functions, and a second design I3-01v9c was obtained by
1076 mutating the turn from "GSGS" to "GPPS" to increase its rigidity. An I3-01v9b structural model
1077 was built after further backbone relaxation using IMO with a minimum perturbation angle. The
1078 distance between the *N*-termini of the I3-01v9b/c trimer (I3-01v9b/c-T) model was 43.9 Å. EBOV
1079 GPΔmuc-WL^{2}P^4-I3-01v9b/c-T constructs (**Fig. S3b**) were designed for experimental validation
1080 with transient expression in HEK293F cells followed by structural validation by nsEM.

1081 **Dynamic Light Scattering (DLS)**

1082 Particle size distributions of ebolavirus GPΔmuc trimer-presenting SApNPs were obtained using
1083 a Zetasizer Ultra instrument (Malvern). Briefly, ADI-15878/SEC-purified SApNPs produced from
1084 ExpiCHO cells were diluted to 0.2 mg/ml in 1× PBS buffer, after which 30 µl of the prepared
1085 sample was added to a quartz batch cuvette (Malvern, catalog no. ZEN2112). Particle size was
1086 measured at 25°C using back scattering mode. Data processing was performed on the Zetasizer
1087 particle size analyzer using Ultra instrument software. The resulting particle size distribution was
1088 plotted using GraphPad Prism 10.3.1 software.

1089 **Mouse immunization and sample collection**

1090 We utilized similar mouse immunization protocols from our previous studies (*108, 120, 121*). The
1091 Association for the Assessment and Accreditation of Laboratory Animal Care (AAALAC)
1092 guidelines were followed throughout all animal experiments. The animal protocols were approved
1093 by the Institutional Animal Care and Use Committee (IACUC) of The Scripps Research Institute.
1094 Six-to-8-week-old female BALB/c mice were purchased from The Jackson Laboratory and housed

1095 in ventilated cages in environmentally controlled rooms at 20°C with 50% humidity under a 12
1096 h/12 h light-dark cycle. In the mechanistic analysis of vaccine transport and induced immune
1097 responses in lymph nodes, mice were intradermally inoculated via four footpads using a 29-gauge
1098 insulin needle under 3% isoflurane anesthesia with oxygen. The injection dose was 80 µl of antigen
1099 and AP adjuvant mix containing 40 µg of vaccine antigen per mouse or 10 µg per footpad. In the
1100 first immunogenicity study, mice were injected at weeks 0, 3, 9, and 15, with an extended interval
1101 of 6 weeks between the second and third doses and third and fourth doses, via the intraperitoneal
1102 (i.p.) route. In the second immunogenicity study, our standard screening regimen (*108, 120, 121,*
1103 *148*) was used with mice injected at weeks 0, 3, 6, and 9 with an interval of 3 weeks. The injecting
1104 dose was 200 µl of antigen/adjuvant mix containing 10 µg of vaccine antigen and 100 µl of
1105 adjuvant including 40 µg/50 µl of CpG (oligonucleotide 1826, a TLR9 agonist from InvivoGen)
1106 adsorbed onto 50 µl of AH (InvivoGen). Blood samples were collected 2 weeks after each injection
1107 through the retro-orbital sinus using heparinized capillary tubes. Samples were spun at 12000 rpm
1108 for 10 min to separate serum (top layer) and the rest of the whole blood layer. Upon heat
1109 inactivation at 56°C for 30 min, serum was spun at 12000 rpm for 10 min to remove precipitates.
1110 For the last timepoint, the rest of the whole blood layer was diluted with an equal volume of PBS
1111 and then overlaid on 4.5 ml of Ficoll in a 15 ml SepMate tube (STEMCELL Technologies) and
1112 spun at 1200 rpm for 10 min at 20°C to separate peripheral blood mononuclear cells (PBMCs).
1113 Cells were washed once in PBS and then resuspended in 1 ml of ACK Red Blood Cell lysis buffer
1114 (Lonza). After washing with PBS, PBMCs were resuspended in 1 ml of freezing media (10%
1115 dimethyl sulfoxide [DMSO]/90% fetal calf serum [FCS]). Two weeks after the last bleed, spleens
1116 were harvested and ground against a 70-µm cell strainer (BD Falcon) to release splenocytes into a
1117 cell suspension. Splenocytes were centrifuged, washed in PBS, treated with 5 ml of ACK lysing

1118 buffer (Lonza), and frozen with 3 ml of freezing media (10% DMSO/90% FCS). Serum samples
1119 from week 11 in the second study were purified using a CaptureSelect™ IgG-Fc (Multispecies)
1120 Affinity Matrix (Thermo Scientific) following the manufacturer's instructions. Purified IgG from
1121 individual mice was analyzed in filovirus-pp assays to determine vaccine-induced NAb responses.

1122 **Histology, immunostaining, and imaging for lymph node tissues**

1123 To study vaccine distribution, trafficking, retention, cellular interaction, and GC reactions in
1124 sentinel lymph nodes, SUDV GPΔmuc trimer and SApNPs (E2p and I3-01v9b) adjuvanted with
1125 AP were intradermally injected into four mouse footpads. A similar protocol was reported in our
1126 previous studies (*108, 120, 121*). In brief, the injection dose consisted of 80 µl of antigen and
1127 adjuvant mix that contained 40 µg of filovirus antigen (10 µg/footpad, 40 µg/mouse). Mice were
1128 euthanized at 2 h to 8 weeks after a single-dose injection. Fresh sentinel lymph nodes were
1129 collected and merged into the frozen section compound (VWR International, catalog no. 95057-
1130 838). Lymph node sample molds were merged into liquid nitrogen and stored at -80°C before
1131 shipping to The Centre for Phenogenomics (Toronto, Canada). Lymph node tissues were cut into
1132 8 µm thick sections using a cryostat (Cryostar NX70). The primary antibody was applied on lymph
1133 node sections and incubated overnight at 4 °C. After washing with TBS containing 0.1% Tween-
1134 20 (TBST), biotin or fluorophore-conjugated secondary antibodies were utilized on the sections
1135 and tissue samples were incubated at 25 °C for 1 h. Lymph node sections were stained with NAbs
1136 ADI-15878 (*111*), ADI-15946 (*114*), CA45 (*113*), or mAb100 (*126*) (1:100) and biotinylated goat
1137 anti-human secondary antibody (Abcam, catalog no. ab7152, 1:300), followed by streptavidin-
1138 horseradish peroxidase (HRP) reagent (Vectastain Elite ABC-HRP Kit, Vector, catalog no. PK-
1139 6100) and ImmPACT diaminobenzidine (DAB; Vector, catalog no. SK-4105).

1140 To study interactions between SUDV GPΔmuc immunogens and cellular components in
1141 lymph nodes, FDCs were labeled using anti-CD21 primary antibody (Abcam, catalog no. ab75985,
1142 1:1800), followed by anti-rabbit secondary antibody conjugated with Alexa Fluor 555 (Thermo
1143 Fisher, catalog no. A21428, 1:200). Subcapsular sinus macrophages were labeled using anti-
1144 sialoadhesin (CD169) antibody (Abcam, catalog no. ab53443, 1:600), followed by anti-rat
1145 secondary antibody conjugated with Alexa Fluor 488 (Abcam, catalog no. ab150165, 1:200). B
1146 cells were labeled using anti-B220 antibody (eBioscience, catalog no. 14-0452-82, 1:100),
1147 followed by anti-rat secondary antibody conjugated with Alexa Fluor 647 (Thermo Fisher, catalog
1148 no. A21247, 1:200). SUDV GPΔmuc trimer and SApNP-induced GC reactions were assessed by
1149 immunohistological study. GC B cells were stained using rat anti-GL7 antibody (FITC; BioLegend,
1150 catalog no. 144604, 1:250). T_{fh} cells were stained using anti-CD4 antibody (BioLegend, catalog
1151 no. 100402, 1:100), followed by anti-rat secondary antibody conjugated with Alexa Fluor 488
1152 (Abcam, catalog no. ab150165, 1:1000). GC cells were stained using Bcl6 antibody (Abcam,
1153 catalog no. ab220092, 1:300), followed by anti-rabbit secondary antibody conjugated with Alexa
1154 Fluor 555 (Thermo Fisher, catalog no. A21428, 1:1000). Cell nuclei were stained using 4',6-
1155 diamidino-2-phenylindole (DAPI; Sigma-Aldrich, catalog no. D9542, 100 ng/ml).

1156 The stained lymph node tissues were scanned using an Olympus VS-120 slide scanner with
1157 a Hamamatsu ORCA-R2 C10600 digital camera. The transport of SUDV GPΔmuc trimer and
1158 SApNP immunogens and their induced GCs in lymph nodes were quantified through bright-field
1159 and fluorescent images using ImageJ software (*169*).

1160 **Electron microscopy analysis of protein nanoparticles in lymph node tissues**

1161 To assess interactions between SUDV GPΔmuc immunogens and stromal and immune cells in
1162 lymph nodes, TEM analysis was conducted by the Core Microscopy Facility at The Scripps

1163 Research Institute (TSRI). The same protocol used for lymph node isolation, processing, and
1164 analysis was reported in our previous studies (*108, 121*). To visualize AP-adjuvanted SUDV
1165 GPΔmuc SApNPs (E2p and I3-01v9b) interacting with FDCs and phagocytic cells in lymph node
1166 tissues using TEM, mice were administered with 200 µl of antigen/adjuvant mix containing 100
1167 µg of SUDV immunogen and 100 µl of AP adjuvant into two hind footpads or 50 µg per footpad.
1168 Fresh popliteal lymph nodes were collected 2, 12, and 48 h after a single-dose injection. Lymph
1169 node tissues were then bisected and immersed in oxygenated 2.5% glutaraldehyde and 4%
1170 paraformaldehyde in 0.1 M sodium cacodylate buffer (pH 7.4) fixative overnight at 4°C. Next,
1171 lymph node samples were fixed and stained with 0.5% uranyl acetate overnight at 4°C. Lymph
1172 node tissues were infiltrated with LX-112 (Ladd) epoxy resin and polymerized at 60 °C. Ultrathin
1173 tissue slices (70 nm) were sectioned and placed on copper grids for TEM imaging. Tissue sections
1174 were imaged at 80 kV with a Talos L120C transmission electron microscope (Thermo Fisher).
1175 TEM images were acquired with a CETA 16M CMOS camera for further analysis.

1176 **Lymph node disaggregation, cell staining, and flow cytometry**

1177 To assess vaccine-induced humoral immune responses, the frequency and number of GC B cells
1178 ($GL7^+B220^+$) and T_{fh} cells ($CD3^+CD4^+CXCR5^+PD\text{-}1^+$) were used to quantify GC reactions by
1179 flow cytometry (**Fig. S9**). The same protocol used for lymph node tissue collection, processing,
1180 and analysis was reported in our previous studies (*108, 120, 121*). In brief, mice were administered
1181 with 80 µl of antigen/adjuvant mix containing 40 µg of vaccine immunogen (10 µg/injection,
1182 40 µg/mouse) into four footpads. The mice were euthanized 2, 5, and 8 weeks after a single-dose
1183 injection or 2 and 5 weeks after the boost. Fresh sentinel lymph nodes were isolated and
1184 immediately processed through mechanical disaggregation. Lymph node tissues were then merged
1185 in enzyme digestion solution. Upon incubation at 37°C for 30 min on a rotator, lymph node cells

1186 were filtered through a 70 μm cell strainer to achieve a single cell suspension. Anti-CD16/32
1187 antibody (BioLegend, catalog no. 101302, 1:50) was added to the cell samples to block the
1188 nonspecific binding of Fc receptors and kept on ice for 30 min. Next, cells were transferred to 96-
1189 well V-shaped-bottom microplates with preprepared cocktail antibodies that included Zombie NIR
1190 live/dead stain (BioLegend, catalog no. 423106, 1:100), Brilliant Violet 510 anti-mouse/human
1191 CD45R/B220 antibody (BioLegend, catalog no. 103247, 1:300), FITC anti-mouse CD3 antibody
1192 (BioLegend, catalog no. 100204, 1:300), Alexa Fluor 700 anti-mouse CD4 antibody (BioLegend,
1193 catalog no. 100536, 1:300), PE anti-mouse/human GL7 antibody (BioLegend, catalog no. 144608,
1194 1:500), Brilliant Violet 605 anti-mouse CD95 (Fas) antibody (BioLegend, catalog no. 152612,
1195 1:500), Brilliant Violet 421 anti-mouse CD185 (CXCR5) antibody (BioLegend, catalog no.
1196 145511, 1:500), and PE/Cyanine7 anti-mouse CD279 (PD-1) antibody (BioLegend, catalog no.
1197 135216, 1:500). Cells were mixed with cocktail antibodies on ice for 30 min and spun down at 400
1198 × *g* for 10 min. Cells were then fixed with 1.6% paraformaldehyde (Thermo Fisher Scientific,
1199 catalog no. 28906) in Hank's Balanced Salt Solution (HBSS) on ice for 30 min. Next, cells were
1200 spun down at 400 × *g* for 10 min and placed in HBSS blocking solution at 4 °C. Sample events
1201 were acquired by a 5-laser AZE5 flow cytometer (Yeti, Bio-Rad) with Everest software at the Core
1202 Facility of The Scripps Research Institute. The data were analyzed using FlowJo 10 software.

1203 **Pseudovirus production and neutralization assays**

1204 A filovirus-pseudoparticle (pp) neutralization assay (*95*) was performed to assess the neutralizing
1205 activity of vaccine-induced mouse sera and purified mouse IgG. Filovirus-pps were generated by
1206 the co-transfection of HEK293T cells with envelope-deficient HIV-1 pNL4-3.lucR^{-}E^{-} plasmid
1207 (NIH AIDS reagent program: https://www.aidsreagent.org/) and an expression plasmid encoding
1208 the GP gene of an EBOV Makona (GenBank accession no. KJ660346), SUDV Gulu (GenBank

1209 accession no. AY729654), BDBV Uganda (GenBank accession no. KR063673), or MARV
1210 Angola (GenBank accession no. DQ447653) strain at a 4:1 ratio using a Lipofectamine 3000
1211 transfection protocol (Thermo Fisher). After 72 h, pseudoviruses were collected from the
1212 supernatant by centrifugation at 3724 × g for 10 min, aliquoted, and stored at -80°C until use. For
1213 pseudovirus neutralization assays, mouse sera starting at a dilution of 100× or purified IgG at a
1214 starting concentration of 300 µg/ml were serially diluted 3-fold and incubated with pseudoviruses
1215 at 37°C for 1 h in white solid-bottom 96-half-well plates (Corning). Next, 0.8×10^4 Huh-7 cells
1216 were added to each well and the plates were incubated at 37°C for 60-72 h. After incubation, the
1217 supernatant was removed, and cells were lysed. Luciferase reporter gene expression was quantified
1218 through the addition of Bright-Glo Luciferase substrate (Promega) according to the manufacturer's
1219 instructions. Luciferase activity in relative light units (RLU) was measured on a BioTek microplate
1220 reader with Gen 5 software. Values from experimental wells were compared against virus-
1221 containing wells, with background luminescence from a series of uninfected wells subtracted from
1222 both. Dose-response neutralization curves were then fit by nonlinear regression with constraints
1223 (0-100%) in GraphPad Prism 10.3.1 software, from which IC_{50} and ID_{50} were calculated. The same
1224 protocols were used to produce and assay pseudoparticles displaying the envelope glycoprotein of
1225 lymphocytic choriomeningitis virus (LCMV-pps) as a negative control in IgG neutralization.

1226 **Statistical analysis**

1227 Data were collected from n = 8 mice per group in the immunization studies and n = 3-5 mice per
1228 group in the mechanistic study. All ELISA and pseudovirus neutralization assays were performed
1229 in duplicate. Different vaccine constructs, and adjuvant-formulated filovirus vaccine antigens,
1230 were compared using one-way analysis of variation (ANOVA), followed by Tukey's multiple
1231 comparison *post hoc* test. Statistical significance is indicated as the following in the figures: ns

1232 (not significant), *$p < 0.05$, **$p < 0.01$, ***$p < 0.001$, and ****$p < 0.0001$. The graphs were
1233 generated, and statistical analyses were performed using GraphPad Prism 10.3.1 software.

1234 **ACKNOWLEDGEMENTS**

1235 The authors acknowledge the facilities of the UC San Diego cryo-EM facility, part of the
1236 Goeddel Family Technology Sandbox, along with the scientific and technical assistance of Dr.
1237 Mariusz Matyszewski. We thank G. Ossetchkine, K. Duffin, M. Ganguly, and V. Bradaschia at
1238 The Centre for Phenogenomics for their expertise and technical support in immunohistology.
1239 We acknowledge K. Vanderpool, T. Fassel, and S. Henderson of the Core Microscopy Facility
1240 at The Scripps Research Institute for their expert assistance in the TEM analysis. We thank A.
1241 Saluk, B. Seegers, and B. Monteverde of the Flow Cytometry Core Facility at The Scripps
1242 Research Institute for their technical support in flow cytometry. Diffraction data were collected
1243 at the Stanford Synchrotron Radiation Lightsource (SSRL) beamlines 12-1. Use of the Stanford
1244 Synchrotron Radiation Lightsource and Stanford Linear Accelerator Center (SLAC), National
1245 Accelerator Laboratory, is supported by the U.S. Department of Energy, Office of Science,
1246 Office of Basic Energy Sciences under Contract No. DE-AC02-76SF00515. The SSRL
1247 Structural Molecular Biology Program is supported by the Department of Energy (DOE) Office
1248 of Biological and Environmental Research, and by the National Institutes of Health (NIH),
1249 National Institute of General Medical Sciences (NIGMS) (P30GM133894). The contents of this
1250 publication are solely the responsibility of the authors and do not necessarily represent the
1251 official views of NIGMS or NIH. We thank M. Arends for proofreading during the manuscript.
1252 **Funding:** This work was supported by Ufovax/SFP-2018-1013 and Uvax/SFP-2020-0111 (J.Z.).
1253 **Author contributions:** Project design by Y.-Z.L., Y.-N.Z., L.H., and J.Z.; protein design by
1254 J.Z.; protein expression and purification by Y.-Z.L., G.W., C.D., and L.H.; glycan analysis by

M.N., J.D.A., and M.C.; negative-stain EM and cryo-EM by Y.-Z.L., A.B.W., and J.Z.; x-ray crystallographic analysis by Y.-Z.L., R.L.S., and I.A.W; mouse immunization, lymph node isolation, immunohistology, TEM, flow cytometry, and serum ELISA by Y.-N.Z.; pseudovirus neutralization assays by G.W., K.B.G., C.D., and L.H.; manuscript written by Y.-Z.L., Y.-N.Z., M.N., K.B.G., S.A., L.H., M.C., and J.Z. All authors were asked to comment on the manuscript. **Competing interests:** Dr. Jiang Zhu serves as the Co-Founder, Interim Chief Scientific Officer, Consultant, and Scientific Advisory Board member of Uvax Bio, LLC, and holds associated financial interests. Other authors declare that they have no competing interests. **Data and material availability:** All data to understand and assess the conclusions of this research are available in the main text and Supplementary Materials. Structures obtained from x-ray crystallography and cryo-EM have been deposited in the Protein Data Bank (PDB, https://www.rcsb.org/) under accession codes 9N8E and 9N8F, respectively. Cryo-EM data were deposited in the Electron Microscopy Data Bank (EMDB, https://www.ebi.ac.uk/emdb/) under accession code EMD-49127. Mass spectrometry data has been deposited in the MassIVE server (https://massive.ucsd.edu) under accession code MassIVE MSV000097145. The authors declare that the data supporting the findings of this study are available within the article and its Supplementary Information files. Source data are provided with this paper.

1272 **References**:

1273 1. W. Slenczka, in *Marburg- and Ebolaviruses: From Ecosystems to Molecules,* E.
1274 Muhlberger, L. L. Hensley, J. S. Towner, Eds. (2017), vol. 411, pp. 3-21.
1275 2. K. M. Johnson, J. V. Lange, P. A. Webb, F. A. Murphy, Isolation and partial
1276 characterisation of a new virus causing acute haemorrhagic fever in Zaire. *Lancet* **1**, 569-
1277 571 (1977).
1278 3. E. T. Bowen *et al.*, Viral haemorrhagic fever in southern Sudan and northern Zaire.
1279 Preliminary studies on the aetiological agent. *Lancet* **1**, 571-573 (1977).
1280 4. C. E. M. Coltart, B. Lindsey, I. Ghinai, A. M. Johnson, D. L. Heymann, The Ebola
1281 outbreak, 2013-2016: old lessons for new epidemics. *Philos. Trans. R. Soc. B, Biol. Sci.*
1282 **372**, 20160297 (2017).
1283 5. S. Paessler, D. H. Walker, Pathogenesis of the viral hemorrhagic fevers. *Annu. Rev.*
1284 *Pathol.* **8**, 411-440 (2013).
1285 6. A. M. Marty, P. B. Jahrling, T. W. Gelsbert, Viral hemorrhagic fevers. *Clin. Lab. Med.*
1286 **26**, 345-386 (2006).
1287 7. J. H. Kuhn *et al.*, New filovirus disease classification and nomenclature. *Nat. Rev.*
1288 *Microbiol.* **17**, 261-263 (2019).
1289 8. J. H. Kuhn *et al.*, Virus nomenclature below the species level: a standardized
1290 nomenclature for filovirus strains and variants rescued from cDNA. *Arch. Virol.* **159**,
1291 1229-1237 (2014).
1292 9. S. C. Harrison, Viral membrane fusion. *Virol.* **479**, 498-507 (2015).
1293 10. M. Kielian, Mechanisms of virus membrane fusion proteins. *Annu. Rev. Virol.* **1**, 171-189
1294 (2014).
1295 11. J. M. White, S. E. Delos, M. Brecher, K. Schornberg, Structures and mechanisms of viral
1296 membrane fusion proteins: multiple variations on a common theme. *Crit. Rev. Biochem.*
1297 *Mol. Biol.* **43**, 189-219 (2008).
1298 12. S. C. Harrison, Viral membrane fusion. *Nat. Struct. Mol. Biol.* **15**, 690-698 (2008).
1299 13. J. E. Lee, E. O. Saphire, Ebolavirus glycoprotein structure and mechanism of entry.
1300 *Future Virol.* **4**, 621-635 (2009).
1301 14. T. R. W. Tipton *et al.*, Characterisation of the T-cell response to Ebola virus glycoprotein
1302 amongst survivors of the 2013-16 West Africa epidemic. *Nat. Commun.* **12**, 1153 (2021).
1303 15. A. I. Flyak *et al.*, Cross-reactive and potent neutralizing antibody responses in human
1304 survivors of natural ebolavirus infection. *Cell* **164**, 392-405 (2016).
1305 16. Z. A. Bornholdt *et al.*, Isolation of potent neutralizing antibodies from a survivor of the
1306 2014 Ebola virus outbreak. *Science* **351**, 1078-1083 (2016).
1307 17. X. Y. Yu, E. O. Saphire, Development and structural analysis of antibody therapeutics for
1308 filoviruses. *Pathog.* **11**, 374 (2022).
1309 18. L. B. King, B. R. West, S. L. Schendel, E. O. Saphire, The structural basis for filovirus
1310 neutralization by monoclonal antibodies. *Curr. Opin. Immunol.* **53**, 196-202 (2018).
1311 19. R. W. Cross, C. E. Mire, H. Feldmann, T. W. Geisbert, Post-exposure treatments for
1312 Ebola and Marburg virus infections. *Nat. Rev. Drug Discov.* **17**, 413-434 (2018).
1313 20. B. M. Friedrich *et al.*, Potential vaccines and post-exposure treatments for filovirus
1314 infections. *Viruses* **4**, 1619-1650 (2012).
1315 21. R. Burk *et al.*, Neglected filoviruses. *FEMS Microbiol. Rev.* **40**, 494-519 (2016).

1316 22. S. Mahanty, M. Bray, Pathogenesis of filoviral haemorrhagic fevers. *Lancet Infect. Dis.*
1317 **4**, 487-498 (2004).
1318 23. I. Messaoudi, G. K. Amarasinghe, C. F. Basler, Filovirus pathogenesis and immune
1319 evasion: insights from Ebola virus and Marburg virus. *Nat. Rev. Microbiol.* **13**, 663-676
1320 (2015).
1321 24. S. Moller-Tank, W. Maury, Ebola virus entry: a curious and complex series of events.
1322 *PLoS Pathog.* **11**, e1004731 (2015).
1323 25. M. Cote *et al.*, Small molecule inhibitors reveal Niemann-Pick C1 is essential for Ebola
1324 virus infection. *Nature* **477**, 344-348 (2011).
1325 26. I. Khan *et al.*, Tubeimosides are pan-coronavirus and filovirus inhibitors that can block
1326 their fusion protein binding to Niemann-Pick C1. *Nat. Commun.* **15**, 162 (2024).
1327 27. H. Wang *et al.*, Ebola viral glycoprotein bound to its endosomal receptor Niemann-Pick
1328 C1. *Cell* **164**, 258-268 (2016).
1329 28. A. P. Cardile, L. G. Downey, P. D. Wiseman, T. K. Warren, S. Bavari, Antiviral
1330 therapeutics for the treatment of Ebola virus infection. *Curr. Opin. Pharmacol.* **30**, 138-
1331 143 (2016).
1332 29. O. T. Mbaya, P. Mukumbayi, S. Mulangu, Review: insights on current FDA-approved
1333 monoclonal antibodies against Ebola virus infection. *Front. Immunol.* **12**, 721328 (2021).
1334 30. T. Hoenen, A. Groseth, H. Feldmann, Therapeutic strategies to target the Ebola virus life
1335 cycle. *Nat. Rev. Microbiol.* **17**, 593-606 (2019).
1336 31. Y. Gao *et al.*, Effects of therapies for Ebola virus disease: a systematic review and
1337 network meta-analysis. *Lancet Microbe* **3**, E683-E692 (2022).
1338 32. X. G. Qiu *et al.*, Reversion of advanced Ebola virus disease in nonhuman primates with
1339 ZMapp. *Nature* **514**, 47-53 (2014).
1340 33. R. T. Davey *et al.*, A randomized, controlled trial of ZMapp for Ebola virus infection. *N.*
1341 *Engl. J. Med.* **375**, 1448-1456 (2016).
1342 34. A. Markham, REGN-EB3: first approval. *Drugs* **81**, 175-178 (2021).
1343 35. D. Corti *et al.*, Protective monotherapy against lethal Ebola virus infection by a potently
1344 neutralizing antibody. *Science* **351**, 1339-1342 (2016).
1345 36. S. Mulangu *et al.*, A randomized, controlled trial of Ebola virus disease therapeutics. *N.*
1346 *Engl. J. Med.* **381**, 2293-2303 (2019).
1347 37. E. O. Saphire, M. J. Aman, Feverish quest for Ebola immunotherapy: straight or cocktail?
1348 *Trends Microbiol.* **24**, 684-686 (2016).
1349 38. C. D. Murin *et al.*, Structures of protective antibodies reveal sites of vulnerability on
1350 Ebola virus. *Proc. Natl. Acad. Sci. U. S. A.* **111**, 17182-17187 (2014).
1351 39. T. Hashiguchi *et al.*, Structural basis for Marburg virus neutralization by a cross-reactive
1352 human antibody. *Cell* **160**, 904-912 (2015).
1353 40. M. L. Fusco *et al.*, Protective mAbs and cross-reactive mAbs raised by immunization
1354 with engineered Marburg virus GPs. *PLoS Pathog.* **11**, e1005016 (2015).
1355 41. A. I. Flyak *et al.*, Mechanism of human antibody-mediated neutralization of Marburg
1356 virus. *Cell* **160**, 893-903 (2015).
1357 42. J. Pallesen *et al.*, Structures of Ebola virus GP and sGP in complex with therapeutic
1358 antibodies. *Nat. Microbiol.* **1**, 16128 (2016).
1359 43. Z. Y. Keck *et al.*, Macaque monoclonal antibodies targeting novel conserved epitopes
1360 within filovirus glycoprotein. *J. Virol.* **90**, 279-291 (2016).

1361 44. F. W. Holtsberg *et al.*, Pan-ebolavirus and pan-filovirus mouse monoclonal antibodies:
1362 protection against Ebola and Sudan viruses. *J. Virol.* **90**, 266-278 (2016).
1363 45. K. A. Howell *et al.*, Antibody treatment of Ebola and Sudan virus infection via a
1364 uniquely exposed epitope within the glycoprotein receptor-binding site. *Cell Rep.* **15**,
1365 1514-1526 (2016).
1366 46. X. L. Zhao *et al.*, Immunization-elicited broadly protective antibody reveals ebolavirus
1367 fusion loop as a site of vulnerability. *Cell* **169**, 891-904.e15 (2017).
1368 47. A. Z. Wec *et al.*, Antibodies from a human survivor define sites of vulnerability for broad
1369 protection against ebolaviruses. *Cell* **169**, 878-890.e15 (2017).
1370 48. L. B. King *et al.*, The marburgvirus-neutralizing human monoclonal antibody MR191
1371 targets a conserved site to block virus receptor binding. *Cell Host Microbe* **23**, 101-
1372 109.e4 (2018).
1373 49. P. Gilchuk *et al.*, Analysis of a therapeutic antibody cocktail reveals determinants for
1374 cooperative and broad ebolavirus neutralization. *Immunity* **52**, 388-403.e12 (2020).
1375 50. P. Gilchuk *et al.*, Multifunctional pan-ebolavirus antibody recognizes a site of broad
1376 vulnerability on the ebolavirus glycoprotein. *Immunity* **49**, 363-374.e10 (2018).
1377 51. C. D. Murin *et al.*, Convergence of a common solution for broad ebolavirus
1378 neutralization by glycan cap-directed human antibodies. *Cell Rep.* **35**, 108984 (2021).
1379 52. A. I. Flyak *et al.*, Broadly neutralizing antibodies from human survivors target a
1380 conserved site in the Ebola virus glycoprotein HR2-MPER region. *Nat. Microbiol.* **3**,
1381 670-677 (2018).
1382 53. K. A. Howell *et al.*, Cooperativity enables non-neutralizing antibodies to neutralize
1383 ebolavirus. *Cell Rep.* **19**, 413-424 (2017).
1384 54. E. O. Saphire *et al.*, Systematic analysis of monoclonal antibodies against Ebola virus GP
1385 defines features that contribute to protection. *Cell* **174**, 938-952.e13 (2018).
1386 55. Y. G. Zhao *et al.*, Toremifene interacts with and destabilizes the Ebola virus
1387 glycoprotein. *Nature* **535**, 169-172 (2016).
1388 56. F. Shaikh *et al.*, Structure-based in silico screening identifies a potent ebolavirus inhibitor
1389 from a traditional Chinese medicine library. *J. Med. Chem.* **62**, 2928-2937 (2019).
1390 57. J. S. Ren, Y. G. Zhao, E. E. Fry, D. I. Stuart, Target identification and mode of action of
1391 four chemically divergent drugs against ebolavirus infection. *J. Med. Chem.* **61**, 724-733
1392 (2018).
1393 58. J. M. Dias *et al.*, A shared structural solution for neutralizing ebolaviruses. *Nat. Struct.*
1394 *Mol. Biol.* **18**, 1424-1427 (2011).
1395 59. J. E. Lee *et al.*, Structure of the Ebola virus glycoprotein bound to an antibody from a
1396 human survivor. *Nature* **454**, 177-182 (2008).
1397 60. C. D. Murin, P. Gilchuk, J. E. Crowe, A. B. Ward, Structural biology illuminates
1398 molecular determinants of broad ebolavirus neutralization by human antibodies for pan-
1399 ebolavirus therapeutic development. *Front. Immunol.* **12**, 808047 (2022).
1400 61. A. Hargreaves *et al.*, Filovirus neutralising antibodies: mechanisms of action and
1401 therapeutic application. *Pathog.* **10**, 1201 (2021).
1402 62. A. M. Henao-Restrepo *et al.*, Efficacy and effectiveness of an rVSV-vectored vaccine in
1403 preventing Ebola virus disease: final results from the Guinea ring vaccination, open-label,
1404 cluster-randomised trial (Ebola Ca Suffit!). *Lancet* **389**, 505-518 (2017).

1405 63. I. D. Milligan *et al.*, Safety and immunogenicity of novel adenovirus type 26- and
1406 modified vaccinia Ankara-vectored Ebola vaccines: a randomized clinical trial. *J. Am.*
1407 *Med. Assoc.* **315**, 1610-1623 (2016).
1408 64. U. N. Sarwar *et al.*, Safety and immunogenicity of DNA vaccines encoding ebolavirus
1409 and marburgvirus wild-type glycoproteins in a phase I clinical trial. *J. Infect. Dis.* **211**,
1410 549-557 (2015).
1411 65. J. E. Ledgerwood *et al.*, Chimpanzee adenovirus vector Ebola vaccine. *N. Engl. J. Med.*
1412 **376**, 928-938 (2017).
1413 66. K. Ewer *et al.*, A monovalent chimpanzee adenovirus Ebola vaccine boosted with MVA.
1414 *N. Engl. J. Med.* **374**, 1635-1646 (2016).
1415 67. F. C. Zhu *et al.*, Safety and immunogenicity of a recombinant adenovirus type-5 vector-
1416 based Ebola vaccine in healthy adults in Sierra Leone: a single-centre, randomised,
1417 double-blind, placebo-controlled, phase 2 trial. *Lancet* **389**, 621-628 (2017).
1418 68. F. C. Zhu *et al.*, Safety and immunogenicity of a novel recombinant adenovirus type-5
1419 vector-based Ebola vaccine in healthy adults in China: preliminary report of a
1420 randomised, double-blind, placebo-controlled, phase 1 trial. *Lancet* **385**, 2272-2279
1421 (2015).
1422 69. M. J. Hamer *et al.*, Safety, tolerability, and immunogenicity of the chimpanzee
1423 adenovirus type 3-vectored Marburg virus (cAd3-Marburg) vaccine in healthy adults in
1424 the USA: a first-in-human, phase 1, open-label, dose-escalation trial. *Lancet* **401**, 294-
1425 302 (2023).
1426 70. M. D. Tapia *et al.*, Safety, reactogenicity, and immunogenicity of a chimpanzee
1427 adenovirus vectored Ebola vaccine in adults in Africa: a randomised, observer-blind,
1428 placebo-controlled, phase 2 trial. *Lancet Infect. Dis.* **20**, 707-718 (2020).
1429 71. A. To *et al.*, Thermostable bivalent filovirus vaccine protects against severe and lethal
1430 Sudan ebolavirus and marburgvirus infection. *Vaccine* **42**, 598-607 (2024).
1431 72. K. B. Preston *et al.*, Single-vial filovirus glycoprotein vaccines: biophysical
1432 characteristics and immunogenicity after co-lyophilization with adjuvant. *Vaccine* **39**,
1433 5650-5657 (2021).
1434 73. D. Xu *et al.*, Design of universal Ebola virus vaccine candidates via immunofocusing.
1435 *Proc. Natl. Acad. Sci. U. S. A.* **121**, e2316960121 (2024).
1436 74. M. Meyer *et al.*, Modified mRNA-based vaccines elicit robust immune responses and
1437 protect guinea pigs from Ebola virus disease. *J. Infect. Dis.* **217**, 451-455 (2018).
1438 75. L. A. Parish, E. J. Stavale, C. R. Houchens, D. N. Wolfe, Developing vaccines to
1439 improve preparedness for filovirus outbreaks: the perspective of the USA biomedical
1440 advanced research and development authority (BARDA). *Vaccines* **11**, 1120 (2023).
1441 76. M. Meyer, D. C. Malherbe, A. Bukreyev, Can Ebola virus vaccines have universal
1442 immune correlates of protection? *Trends Microbiol.* **27**, 8-16 (2019).
1443 77. S. A. Ehrhardt *et al.*, Polyclonal and convergent antibody response to Ebola virus vaccine
1444 rVSV-ZEBOV. *Nat. Med.* **25**, 1589-1600 (2019).
1445 78. H. Cohen-Dvashi *et al.*, Structural basis for a convergent immune response against Ebola
1446 virus. *Cell Host Microbe* **27**, 418-427.e4 (2020).
1447 79. B. F. Haynes, J. R. Mascola, The quest for an antibody-based HIV vaccine. *Immunol.*
1448 *Rev.* **275**, 5-10 (2017).
1449 80. P. D. Kwong, J. R. Mascola, G. J. Nabel, Broadly neutralizing antibodies and the search
1450 for an HIV-1 vaccine: the end of the beginning. *Nat. Rev. Immunol.* **13**, 693-701 (2013).

1451 81. B. F. Haynes, G. Kelsoe, S. C. Harrison, T. B. Kepler, B-cell-lineage immunogen design
1452 in vaccine development with HIV-1 as a case study. *Nat. Biotechnol.* **30**, 423-433 (2012).
1453 82. L. M. Walker, D. R. Burton, Rational antibody-based HIV-1 vaccine design: current
1454 approaches and future directions. *Curr. Opin. Immunol.* **22**, 358-366 (2010).
1455 83. B. S. Graham, M. S. A. Gilman, J. S. McLellan, Structure-based vaccine antigen design.
1456 *Annu. Rev. Med.* **70**, 91-104 (2019).
1457 84. R. W. Sanders *et al.*, A next-generation cleaved, soluble HIV-1 Env trimer, BG505
1458 SOSIP.664 gp140, expresses multiple epitopes for broadly neutralizing but not non-
1459 neutralizing antibodies. *PLoS Pathog.* **9**, e1003618 (2013).
1460 85. S. K. Sharma *et al.*, Cleavage-independent HIV-1 Env trimers engineered as soluble
1461 native spike mimetics for vaccine design. *Cell Rep.* **11**, 539-550 (2015).
1462 86. L. Kong *et al.*, Uncleaved prefusion-optimized gp140 trimers derived from analysis of
1463 HIV-1 envelope metastability. *Nat. Commun.* **7**, 12040 (2016).
1464 87. J. S. McLellan *et al.*, Structure-based design of a fusion glycoprotein vaccine for
1465 respiratory syncytial virus. *Science* **342**, 592-598 (2013).
1466 88. M. G. Joyce *et al.*, Iterative structure-based improvement of a fusion-glycoprotein
1467 vaccine against RSV. *Nat. Struct. Mol. Biol.* **23**, 811-820 (2016).
1468 89. A. Krarup *et al.*, A highly stable prefusion RSV F vaccine derived from structural
1469 analysis of the fusion mechanism. *Nat. Commun.* **6**, 8143 (2015).
1470 90. Y. Che *et al.*, Rational design of a highly immunogenic prefusion- stabilized F
1471 glycoprotein antigen for a respiratory syncytial virus vaccine. *Sci. Transl. Med.* **15**,
1472 eade6422 (2023).
1473 91. K. V. Houser *et al.*, Safety and immunogenicity of an HIV-1 prefusion-stabilized
1474 envelope trimer (Trimer 4571) vaccine in healthy adults: A first-in-human open-label,
1475 randomized, dose-escalation, phase 1 clinical trial. *Eclinicalmedicine* **48**, 101477 (2022).
1476 92. G. Papazisis *et al.*, Respiratory syncytial virus vaccines: analysis of pre-marketing
1477 clinical trials for immunogenicity in the population over 50 years of age. *Vaccines* **12**,
1478 353 (2024).
1479 93. M. Melgar *et al.*, Use of respiratory syncytial virus vaccines in older adults:
1480 recommendations of the advisory committee on immunization practices - United States,
1481 2023. *Morb. Mortal. Wkly. Rep.* **72**, 793-801 (2023).
1482 94. L. Rutten *et al.*, Structure-based design of prefusion-stabilized filovirus glycoprotein
1483 trimers. *Cell Rep.* **30**, 4540-4550.e3 (2020).
1484 95. L. He *et al.*, Single-component multilayered self-assembling nanoparticles presenting
1485 rationally designed glycoprotein trimers as Ebola virus vaccines. *Nat. Commun.* **12**, 2633
1486 (2021).
1487 96. J. J. Suschak, C. S. Schmaljohn, Vaccines against Ebola virus and Marburg virus: recent
1488 advances and promising candidates. *Hum. Vaccin. Immunother.* **15**, 2359-2377 (2019).
1489 97. O. Reynard *et al.*, Ebolavirus glycoprotein GP masks both its own epitopes and the
1490 presence of cellular surface proteins. *J. Virol.* **83**, 9596-9601 (2009).
1491 98. J. R. Francica *et al.*, Steric shielding of surface epitopes and impaired immune
1492 recognition induced by the Ebola virus glycoprotein. *PLoS Pathog.* **6**, e1001098 (2010).
1493 99. N. Chaudhary, D. Weissman, K. A. Whitehead, mRNA vaccines for infectious diseases:
1494 principles, delivery and clinical translation. *Nat. Rev. Drug Discov.* **20**, 817-838 (2021).
1495 100. D. S. Khoury *et al.*, Neutralizing antibody levels are highly predictive of immune
1496 protection from symptomatic SARS-CoV-2 infection. *Nat. Med.* **27**, 1205-1211 (2021).

1497 101. B. Nguyen, N. H. Tolia, Protein-based antigen presentation platforms for nanoparticle
1498 vaccines. *NPJ Vaccines* **6**, 70 (2021).
1499 102. D. J. Irvine, B. J. Read, Shaping humoral immunity to vaccines through antigen-
1500 displaying nanoparticles. *Curr. Opin. Immunol.* **65**, 1-6 (2020).
1501 103. R. Rappuoli, D. Serruto, Self-assembling nanoparticles usher in a new era of vaccine
1502 design. *Cell* **176**, 1245-1247 (2019).
1503 104. P. J. M. Brouwer, R. W. Sanders, Presentation of HIV-1 envelope glycoprotein trimers on
1504 diverse nanoparticle platforms. *Curr. Opin. HIV AIDS* **14**, 302-308 (2019).
1505 105. M. Brinkkemper, K. Sliepen, Nanoparticle vaccines for inducing HIV-1 neutralizing
1506 antibodies. *Vaccines* **7**, 76 (2019).
1507 106. B. Asbach, R. Wagner, Particle-based delivery of the HIV envelope protein. *Curr. Opin.*
1508 *HIV AIDS* **12**, 265-271 (2017).
1509 107. H. Y. Huang *et al.*, Vaccination with SARS-CoV-2 spike protein lacking glycan shields
1510 elicits enhanced protective responses in animal models. *Sci. Transl. Med.* **14**, eabm0899
1511 (2022).
1512 108. Y.-N. Zhang *et al.*, Single-component multilayered self-assembling protein nanoparticles
1513 presenting glycan-trimmed uncleaved prefusion optimized envelope trimers as HIV-1
1514 vaccine candidates. *Nat. Commun.* **14**, 1985 (2023).
1515 109. C. C. Wang *et al.*, Glycans on influenza hemagglutinin affect receptor binding and
1516 immune response. *Proc. Natl. Acad. Sci. U. S. A.* **106**, 18137-18142 (2009).
1517 110. S. C. Wang, H. Y. Liao, J. Y. Zhang, T. J. R. Cheng, C. H. Wong, Development of a
1518 universal influenza vaccine using hemagglutinin stem protein produced from Pichia
1519 pastoris. *Virol.* **526**, 125-137 (2019).
1520 111. B. R. West *et al.*, Structural basis of pan-ebolavirus neutralization by a human antibody
1521 against a conserved, yet cryptic epitope. *mBio* **9**, e01674-18 (2018).
1522 112. C. D. Murin *et al.*, Structural basis of pan-ebolavirus neutralization by an antibody
1523 targeting the glycoprotein fusion loop. *Cell Rep.* **24**, 2723-2732.e4 (2018).
1524 113. B. M. Janus *et al.*, Structural basis for broad neutralization of ebolaviruses by an antibody
1525 targeting the glycoprotein fusion loop. *Nat. Commun.* **9**, 3934 (2018).
1526 114. B. R. West *et al.*, Structural basis of broad ebolavirus neutralization by a human survivor
1527 antibody. *Nat. Struct. Mol. Biol.* **26**, 204-212 (2019).
1528 115. D. Lyumkis *et al.*, Cryo-EM structure of a fully glycosylated soluble cleaved HIV-1
1529 envelope trimer. *Science* **342**, 1484-1490 (2013).
1530 116. S. Bangaru *et al.*, Structural analysis of full-length SARS-CoV-2 spike protein from an
1531 advanced vaccine candidate. *Science* **370**, 1089-1094 (2020).
1532 117. H. L. Turner *et al.*, Potent anti-influenza H7 human monoclonal antibody induces
1533 separation of hemagglutinin receptor-binding head domains. *PLoS Biol.* **17**, e3000139
1534 (2019).
1535 118. S. Bale *et al.*, Structural basis for differential neutralization of ebolaviruses. *Viruses* **4**,
1536 447-470 (2012).
1537 119. A. Punjani, J. L. Rubinstein, D. J. Fleet, M. A. Brubaker, cryoSPARC: algorithms for
1538 rapid unsupervised cryo-EM structure determination. *Nat. Methods* **14**, 290-296 (2017).
1539 120. K. Braz Gomes *et al.*, Single-component multilayered self-assembling protein
1540 nanoparticles displaying extracellular domains of matrix protein 2 as a pan-influenza A
1541 vaccine. *ACS Nano* **17**, 23545-23567 (2023).

121. Y.-N. Zhang *et al.*, Mechanism of a COVID-19 nanoparticle vaccine candidate that elicits a broadly neutralizing antibody response to SARS-CoV-2 variants. *Sci. Adv.* **7**, eabj3107 (2021).
122. R. Rappuoli, Glycoconjugate vaccines: principles and mechanisms. *Sci. Transl. Med.* **10**, eaat4615 (2018).
123. J. G. Cyster, B cell follicles and antigen encounters of the third kind. *Nat. Immunol.* **11**, 989-996 (2010).
124. B. A. Heesters, R. C. Myers, M. C. Carroll, Follicular dendritic cells: dynamic antigen libraries. *Nat. Rev. Immunol.* **14**, 495-504 (2014).
125. J. G. Cyster, P. C. Wilson, Antibody modulation of B cell responses-Incorporating positive and negative feedback. *Immunity* **57**, 1466-1481 (2024).
126. J. Misasi *et al.*, Structural and molecular basis for Ebola virus neutralization by protective human antibodies. *Science* **351**, 1343-1346 (2016).
127. A. Martínez-Riaño *et al.*, Long-term retention of antigens in germinal centers is controlled by the spatial organization of the follicular dendritic cell network. *Nat. Immunol.* **24**, 1281-1294 (2023).
128. G. D. Victora, M. C. Nussenzweig, Germinal centers. *Annu. Rev. Immunol.* **30**, 429-457 (2012).
129. C. D. Allen, J. G. Cyster, Follicular dendritic cell networks of primary follicles and germinal centers: phenotype and function. *Semin. Immunol.* **20**, 14-25 (2008).
130. B. A. Heesters, C. E. van der Poel, A. Das, M. C. Carroll, Antigen presentation to B cells. *Trends Immunol.* **37**, 844-854 (2016).
131. M. E. M. El Shikh, R. M. El Sayed, S. Sukumar, A. K. Szakal, J. G. Tew, Activation of B cells by antigens on follicular dendritic cells. *Trends Immunol.* **31**, 205-211 (2010).
132. G. A. Roth *et al.*, Designing spatial and temporal control of vaccine responses. *Nat. Rev. Mater.* **7**, 174-195 (2022).
133. P. Yousefpour, K. Ni, D. J. Irvine, Targeted modulation of immune cells and tissues using engineered biomaterials. *Nat. Rev. Bioeng.* **1**, 107-124 (2023).
134. Y. R. Carrasco, F. D. Batista, B cells acquire particulate antigen in a macrophage-rich area at the boundary between the follicle and the subcapsular sinus of the lymph node. *Immunity* **27**, 160-171 (2007).
135. T. Junt *et al.*, Subcapsular sinus macrophages in lymph nodes clear lymph-borne viruses and present them to antiviral B cells. *Nature* **450**, 110-114 (2007).
136. T. G. Phan, I. Grigorova, T. Okada, J. G. Cyster, Subcapsular encounter and complement-dependent transport of immune complexes by lymph node B cells. *Nat. Immunol.* **8**, 992-1000 (2007).
137. T. G. Phan, J. A. Green, E. E. Gray, Y. Xu, J. G. Cyster, Immune complex relay by subcapsular sinus macrophages and noncognate B cells drives antibody affinity maturation. *Nat. Immunol.* **10**, 786-793 (2009).
138. S. F. Gonzalez *et al.*, Capture of influenza by medullary dendritic cells via SIGN-R1 is essential for humoral immunity in draining lymph nodes. *Nat. Immunol.* **11**, 427-434 (2010).
139. C. D. Allen, T. Okada, J. G. Cyster, Germinal-center organization and cellular dynamics. *Immunity* **27**, 190-202 (2007).
140. J. G. Cyster, C. D. C. Allen, B cell responses: cell interaction dynamics and decisions. *Cell* **177**, 524-540 (2019).

1588 141. F. D. Batista, N. E. Harwood, The who, how and where of antigen presentation to B cells.
1589 *Nat. Rev. Immunol.* **9**, 15-27 (2009).
1590 142. Z. Shulman *et al.*, T follicular helper cell dynamics in germinal centers. *Science* **341**,
1591 673-677 (2013).
1592 143. S. Crotty, T follicular helper cell differentiation, function, and roles in disease. *Immunity*
1593 **41**, 529-542 (2014).
1594 144. L. He *et al.*, Single-component, self-assembling, protein nanoparticles presenting the
1595 receptor binding domain and stabilized spike as SARS-CoV-2 vaccine candidates. *Sci.*
1596 *Adv.* **7**, eabf1591 (2021).
1597 145. L. He *et al.*, Proof of concept for rational design of hepatitis C virus E2 core nanoparticle
1598 vaccines. *Sci. Adv.* **6**, eaaz6225 (2020).
1599 146. R. W. Cross *et al.*, An introduction to the Marburg virus vaccine consortium, MARVAC.
1600 *PLoS Pathog.* **18**, e1010805 (2022).
1601 147. D. N. Wolfe *et al.*, Selection of filovirus isolates for vaccine development programs.
1602 *Vaccines* **9**, 1045 (2021).
1603 148. Y.-N. Zhang *et al.*, A single-component multilayered self-assembling protein
1604 nanoparticle vaccine based on extracellular domains of matrix protein 2 against both
1605 influenza A and B. *Vaccines* **12**, 975 (2024).
1606 149. Y. Z. Lee *et al.*, Rational design of uncleaved prefusion-closed trimer vaccines for human
1607 respiratory syncytial virus and metapneumovirus. *Nat. Commun.* **15**, 9939 (2024).
1608 150. L. He *et al.*, HIV-1 vaccine design through minimizing envelope metastability. *Sci. Adv.*
1609 **4**, aau6769 (2018).
1610 151. L. He *et al.*, Presenting native-like trimeric HIV-1 antigens with self-assembling
1611 nanoparticles. *Nat. Commun.* **7**, 12041 (2016).
1612 152. M. Gonzalez-Hernandez *et al.*, Preclinical immunogenicity and protective efficacy of a
1613 SARS-CoV-2 RBD-based vaccine produced with the thermophilic filamentous fungal
1614 expression system Thermothelomyces heterothallica C1. *Front. Immunol.* **14**, 1204834
1615 (2023).
1616 153. L. Lazo *et al.*, A recombinant SARS-CoV-2 receptor-binding domain expressed in an
1617 engineered fungal strain of Thermothelomyces heterothallica induces a functional
1618 immune response in mice. *Vaccine* **40**, 1162-1169 (2022).
1619 154. J. Korn *et al.*, Baculovirus-free insect cell expression system for high yield antibody and
1620 antigen production. *Sci. Rep.* **10**, 21393 (2020).
1621 155. M.-A. Elsliger *et al.*, The JCSG high-throughput structural biology pipeline. *Acta*
1622 *Crystallogr. Sect. F Struct. Biol. Cryst. Commun.* **66**, 1137-1142 (2010).
1623 156. Z. Otwinowski, W. Minor, Processing of X-ray diffraction data collected in oscillation
1624 mode. *Methods Enzymol.* **276**, 307-326 (1997).
1625 157. P. Emsley, B. Lohkamp, W. G. Scott, K. Cowtan, Features and development of Coot.
1626 *Acta Crystallogr. D Biol. Crystallogr.* **66**, 486-501 (2010).
1627 158. D. Liebschner *et al.*, Macromolecular structure determination using X-rays, neutrons and
1628 electrons: recent developments in Phenix. *Acta Crystallogr. D: Struct. Biol.* **75**, 861-877
1629 (2019).
1630 159. H. Berman, K. Henrick, H. Nakamura, Announcing the worldwide Protein Data Bank.
1631 *Nat. Struct. Biol.* **10**, 980 (2003).
1632 160. E. Potterton, P. Briggs, M. Turkenburg, E. Dodson, A graphical user interface to the
1633 CCP4 program suite. *Acta Crystallogr. D Biol. Crystallogr.* **59**, 1131-1137 (2003).

161. G. Tang *et al.*, EMAN2: An extensible image processing suite for electron microscopy. *J. Struct. Biol.* **157**, 38-46 (2007).
162. E. F. Pettersen *et al.*, UCSF chimera - A visualization system for exploratory research and analysis. *J. Comput. Chem.* **25**, 1605-1612 (2004).
163. E. C. Meng *et al.*, UCSF ChimeraX: Tools for structure building and analysis. *Protein Sci.* **32**, e4792 (2023).
164. E. F. Pettersen *et al.*, UCSF ChimeraX: Structure visualization for researchers, educators, and developers. *Protein Sci.* **30**, 70-82 (2021).
165. T. D. Goddard *et al.*, UCSF ChimeraX: Meeting modern challenges in visualization and analysis. *Protein Sci.* **27**, 14-25 (2018).
166. J. Zhu, L. Xie, B. Honig, Structural refinement of protein segments containing secondary structure elements: Local sampling, knowledge-based potentials, and clustering. *Proteins: Struct. Funct. Bioinf.* **65**, 463-479 (2006).
167. B. L. deGroot *et al.*, Prediction of protein conformational freedom from distance constraints. *Proteins: Struct. Funct. Genet.* **29**, 240-251 (1997).
168. R. Samudrala, J. Moult, An all-atom distance-dependent conditional probability discriminatory function for protein structure prediction. *J. Mol. Biol.* **275**, 895-916 (1998).
169. C. A. Schneider, W. S. Rasband, K. W. Eliceiri, NIH Image to ImageJ: 25 years of image analysis. *Nat. Methods* **9**, 671-675 (2012).

1655 **Figure Legends**

1656 **Fig. 1. Rational design and in vitro characterization of ebolavirus GP trimers.** (**a**) Schematic
1657 representation of GP construct design, including the MLD deletion (Δmuc) between G314 to N463,
1658 P^2 (T577P) or P^4 (L579P) mutation in HR1c, W615L mutation at the neck of the HR2 stalk, and
1659 C-terminal extension from D632 to D637. IFL: internal fusion loop. (**b**) Schematic representation
1660 of an ebolavirus GP trimer bound to NAb ADI-15878 (left) and SEC profiles of six ebolavirus
1661 GPΔmuc constructs following transient expression in 25 ml of ExpiCHO cells and IAC
1662 purification using an ADI-15878 column (right). Two major SEC peaks, aggregation (A) and
1663 trimer (T), are marked on the profile. (**c**) BN-PAGE of six ADI-15878/SEC-purified ebolaviruses
1664 GPΔmuc trimers. The gel bands are consistent with the expected trimer size and molecular weight.
1665 (**d**) DSC thermograms of six ADI-15878/SEC-purified ebolaviruses GPΔmuc trimers. The
1666 experimental data and Gaussian fitting are shown as black dots and red lines, respectively. Key
1667 parameters, such as thermal denaturation midpoint (T_m or T_{m1} and T_{m2}), onset temperature (T_{onset}),
1668 and half width of the peak ($\Delta T_{1/2}$) are labeled on the thermogram. (**e**) Site-specific glycan profiles
1669 for ADI-15878/SEC-purified EBOV, SUDV, and BDBV GPΔmuc-WL^2P^4 trimers. Glycan
1670 compositions are grouped into four types, including complex (solid pink), hybrid (pink lines),
1671 oligomannose (solid green), and unoccupied (solid gray). Glycan sites that could not be determined
1672 are denoted as "N.D." Sites that are not present are denoted as "N.P." (**f**) nsEM-derived 3D
1673 reconstructions of EBOV, SUDV, and BDBV GPΔmuc-WL^2P^4 trimers and their complexes with
1674 NAb ADI-15878. Crystal structures of EBOV GPΔmuc-WL^2P^2 (PDB ID: 7JPH) and ADI-15878
1675 (PDB ID: 6DZN) were used in the density fitting, with GP1, GP2, and ADI-15878 Fab in the
1676 resulting molecular model colored in cyan, green, and pink, respectively. (**e**) ELISA-derived EC_{50}
1677 (μg/ml) values of six ebolaviruses GPΔmuc trimers binding to four pan-ebolavirus NAbs and a

1678 marburgvirus NAb, MR-78. If absorbance at 450 nm is less than 0.5 at the starting and highest
1679 concentration (10 μg/ml), then the antigen has negligible binding to the tested antibody, and the
1680 EC_{50} value is set to 10 μg/ml. (**f**) BLI profiles of six ebolaviruses GPΔmuc trimers binding to the
1681 same NAbs. Sensorgrams were obtained from an Octet RED96 instrument using an antigen
1682 titration series of six concentrations (starting at 600 nM followed by 2-fold dilutions) and are
1683 shown in **Fig. S1i**. Peak values at the highest concentration are shown in a matrix, in which cells
1684 are colored in green (weak binding) to red (strong binding).

1685 **Fig. 2. Structural characterization of an unliganded EBOV GPΔmuc-WL^{2}P^4 trimer and a**
1686 **SUDV GPΔmuc-WL^{2}P^4 trimer in complex with NAb CA45.** (**a**) Left: crystal structure of a
1687 stabilized EBOV GPΔmuc-WL^{2}P^4 trimer determined at a resolution of 3.2 Å, with GP1 shown in
1688 cyan, glycan cap shown in gray, IFL shown in pink, and GP2 shown in gold. Structural details
1689 could not be determined for regions R200-P209, K294-I301, and C-terminus (T634-D637). Right:
1690 comparative analysis of the HR1c bend and its local structure for three rationally designed EBOV
1691 GPΔmuc constructs bearing the WL^2 mutation (PDB ID: 7JPI), WL^{2}P^2 mutation (PDB ID: 7JPH),
1692 and WL^{2}P^4 mutation. Sidechains are shown for amino acids that form cross-protomer interactions,
1693 including L95, R130, L573, and T576. A cutoff of 3.3 Å is used to define the donor-acceptor
1694 distance within a hydrogen bond. (**b**) Cryo-EM-derived 3D reconstruction of a SUDV GPΔmuc-
1695 WL^{2}P^4 trimer in complex with CA45 Fab determined at 3.13 Å, with GP1 shown in orange, GP2
1696 shown in green, CA45 heavy chain shown in blue, and CA45 light chain shown in pink. The glycan
1697 cap and HR2 stalk are missing in the density map at this resolution and can only be seen partially
1698 when the resolution is relaxed beyond 4.0 Å, as shown in **Fig. S2e**. (**c**) Ribbon representation of
1699 the cryo-EM structure of the SUDV GPΔmuc-WL^{2}P^4 trimer in complex with CA45 Fab. The same
1700 color-coding scheme is adopted for GP1, GP2, and CA45 heavy and light chains. Atomic details

1701 of the glycan cap and HR2 stalk cannot be reliably resolved due to low resolution of the density
1702 map for these regions. The left panel shows atomic details of hydrogen bonds and salt bridges
1703 between SUDV GPΔmuc and NAb CA45 heavy chain (top) and light chain (bottom), whereas the
1704 right panel overlaps the HR1c bend of SUDV GPΔmuc-WL^2P^4 with that of BDBV GPΔmuc (cryo-
1705 EM structure, top) and that of EBOV GPΔmuc-WL^2P^4 (crystal structure, bottom).

1706 **Fig. 3. Rational design and in vitro characterization of ebolaviruses GP-presenting SApNPs.**
1707 (**a**) Rational design of a 60-mer SApNP for the optimal surface display of trimeric antigens with a
1708 narrow stalk. Twenty I3-01v9a trimers assemble into an I3-01v9a SApNP (left), with the N-termini
1709 forming a triangle of 50.5 Å (middle). Using computational design, the *N*-terminus of I3-01v9a
1710 was extended by engineering a helix that packs against the protein core with the first residue
1711 forming a triangle of 12.9 Å, resulting in I3-01v9b/c. (**b**) nsEM analysis of EBOV GPΔmuc-
1712 WL^2P^4-I3-01v9b-T, in which I3-01v9b-T is a trimeric version of I3-01v9b with mutations to
1713 interrupt the particle-forming interface. Top: examples of 2D classification images; Bottom: side
1714 and top views of nsEM-derived 3D model. (**c**) Schematic representation of EBOV GPΔmuc-
1715 WL^2P^4-presenting I3-01v9b/c SApNP. The calculated particle size is 49.1 nm measured for GP1-
1716 T269. (**d**) SEC profiles of six ebolavirus GPΔmuc-WL^2P^4-presenting SApNPs following transient
1717 expression in ExpiCHO cells and IAC purification using an ADI-15878 column. The NP peak is
1718 labeled on the SEC profile, along with partially assembled NP (pNP) and trimer (T) peaks. (**e**)
1719 nsEM images of six SEC-purified ebolaviruses of GPΔmuc-WL^2P^4-presenting SApNPs. The scale
1720 (50 nm) is labeled on the nsEM images. (**f**) Particle size distribution of six SEC-purified ebolavirus
1721 GPΔmuc-WL^2P^4-presenting SApNPs. The hydrodynamic diameter (D_h) was measured by DLS.
1722 Three measurements are reported for each SUDV GPΔmuc SApNP, with the particle size range
1723 labeled on the plot. (**g**) Site-specific glycan profile of SUDV GPΔmuc-WL^2P^4-presenting E2p and

1724 I3-01v9b SApNPs, with the same labeling scheme of glycan types as in **Fig. 1e**. (**h**) ELISA-derived
1725 EC_{50} (μg/ml) values of six ebolaviruses GPΔmuc-WL^2P^4-presenting SApNPs binding to five
1726 NAbs, with the same cutoff (0.5) used for absorbance at 450 nm as in **Fig. 1f**. (**i**) BLI profiles of
1727 six ebolaviruses GPΔmuc-WL^2P^4-presenting SApNPs binding to five NAbs. Sensorgrams were
1728 obtained using the same protocol as in **Fig. 1g** and are shown in **Fig. S3k**. Peak values at the
1729 highest concentration are shown in a matrix, with the same color-coding as in **Fig. 1g**.

1730 **Fig. 4. Glycan modification of EBOV and SUDV GPΔmuc-WL^2P^4 trimers and SApNPs.** (**a**)
1731 SEC profiles of EBOV and SUDV GPΔmuc-WL^2P^4 constructs following transient expression in
1732 HEK293F cells and IAC purification using an ADI-15878 column, each construct with two glycan
1733 modifications: kifunensine (Kif) treatment and kifunensine plus endo H (Kif/endo H) treatment.
1734 While HEK293F expression in the presence of Kif produces oligomannose-type glycans, further
1735 treatment with endo H results in a monolayer of GlcNAc cores. The SEC peak around 14.7 ml
1736 corresponds to endo H. (**b**) DSC thermograms of ADI-15878/SEC-purified EBOV and SUDV
1737 GPΔmuc-WL^2P^4 trimers after glycan treatment. The experimental data and Gaussian fitting are
1738 shown as black dots and red lines, respectively. Key parameters, such as thermal denaturation
1739 midpoint (T_m or T_{m1} and T_{m2}), onset temperature (T_{onset}), and half width of the peak ($\Delta T_{1/2}$) are
1740 labeled on the thermogram. (**c**) ELISA-derived EC_{50} (μg/ml) values of glycan-modified EBOV
1741 and SUDV GPΔmuc-WL^2P^4 trimers binding to five NAbs, with the same cutoff (0.5) used for
1742 absorbance at 450 nm as in **Fig. 1f**. (**d**) BLI profiles of glycan-modified EBOV and SUDV
1743 GPΔmuc-WL^2P^4 trimers binding to five NAbs. Sensorgrams were obtained using the same
1744 protocol as in **Fig. 1g** and are shown in **Fig. S4c**. Peak values at the highest concentration are
1745 shown in a matrix, with the same color-coding as in **Fig. 1g**. (**e**) SEC profiles (top) and nsEM
1746 images (bottom) of glycan-modified EBOV and SUDV GPΔmuc-WL^2P^4-presenting SApNPs.

1747 Glycan modification was performed as described in **Fig. 4a**, with the results for EBOV GPΔmuc
1748 I3-01v9b not shown due to its low expression yield. The scale (50 nm) is labeled on the nsEM
1749 images. (**f**) Site-specific glycan profile of SUDV GPΔmuc-WL^{2}P^4-presenting E2p and I3-01v9b
1750 SApNPs after kifunensine treatment, with the same glycan type labeling as in **Fig. 1e**. (**g**) ELISA-
1751 derived EC_{50} (μg/ml) values of glycan-modified SUDV GPΔmuc-WL^{2}P^4-presenting E2p and I3-
1752 01v9b SApNPs binding to five NAbs, as in **Fig. 1f**. (**h**) BLI profiles of glycan-modified SUDV
1753 GPΔmuc-WL^{2}P^4-presenting E2p and I3-01v9b SApNPs binding to five NAbs. Sensorgrams were
1754 obtained using the same protocol as in **Fig. 1g** and are shown in **Fig. S4h**. Peak values at the
1755 highest concentration are shown in a matrix, with the same color-coding as in **Fig. 1g**.

1756 **Fig. 5. Rational design and in vitro characterization of marburgvirus GP trimers.** (**a**)
1757 Schematic representation of GP construct design, including MLD deletion (Δmuc) between T256
1758 to T424, P^2 (T578P) or P^4 (E580P) mutation in HR1c, and double mutation E631F/Q632V at the
1759 C-terminus, all based on the RAVV backbone. (**b**) SEC profiles of four RAVV GP constructs
1760 following transient expression in 16 ml of ExpiCHO cells and Nickel purification. Aggregation
1761 (A), trimer (T), and GP subunit (S) peaks are marked on the SEC profile. (**c**) BN-PAGE of RAVV
1762 GPΔmuc-P^{2}CT trimer fractions from SEC purification. (**d**) DSC thermograms of Nickel/SEC-
1763 purified RAVV GPΔmuc-P^2-foldon and GPΔmuc-P^{2}CT-foldon trimers. The experimental data and
1764 Gaussian fitting are shown as black dots and red lines, respectively. Thermal denaturation midpoint
1765 (T_{m1}, T_{m2}, and T_{m3}) values are labeled. (**e**) nsEM analysis of RAVV GPΔmuc-P^{2}CT-foldon/MR-
1766 78 Fab complex. Left: crystal structure (PDB ID: 5UQY) of RAVV GPΔmuc/MR-78 Fab complex
1767 fitted into the nsEM density map (left). Right: nsEM-derived 3D density map of RAVV
1768 GPΔmuc/MR-78 Fab complex (EMDB: 6233, shown in orange surface) overlaid with the nsEM
1769 density map. (**f**) Site-specific glycan profile of RAVV GPΔmuc-P^{2}CT trimer, with the same

1770 glycan type labeling as in **Fig. 1e**. (**g**) ELISA-derived EC_{50} (μg/ml) values of RAVV GPΔmuc-P^2
1771 and GPΔmuc-P^2CT trimer binding to marburgvirus NAbs MR-78 and MR-191, with the same
1772 cutoff (0.5) used for absorbance at 450 nm as in **Fig. 1f**. (**h**) BLI profiles of RAVV GPΔmuc-P^2
1773 and GPΔmuc-P^2CT trimer binding to marburgvirus NAbs MR-78 and MR-191. Sensorgrams were
1774 obtained using the same protocol as in **Fig. 1g** and are shown in **Fig. S5h**. Peak values at the
1775 highest concentration are shown in a matrix, with the same color-coding as in **Fig. 1g**.

1776 **Fig. 6. Retention of SUDV GPΔmuc-presenting SApNPs in lymph node follicles.** Distribution
1777 of (**a**) E2p and (**b**) I3-01v9b SApNPs displaying SUDV GPΔmuc-WL^2P^4 trimers in a lymph node
1778 12 h after a single-dose injection (10 μg/injection, 40 μg/mouse, left). A pan-ebolavirus NAb,
1779 CA45, was used to stain the sentinel lymph node tissue sections. Right: schematic illustration of
1780 SUDV SApNP accumulation in lymph node follicles. (**c**) Trafficking and retention of the SUDV
1781 GPΔmuc trimer and SApNPs in lymph node follicles 2 h to 8 weeks after a single-dose injection.
1782 Scale bar = 50 μm for each image. (**d**) Time-dependent curve and (**e**) Area under the curve (AUC)
1783 of the CA45-stained area in immunohistological images of SUDV vaccine retention in lymph node
1784 follicles over 8 weeks. (**f**) Quantification of SUDV vaccine accumulation in lymph node follicles
1785 48 h after a single-dose injection. Data were collected from more than 10 lymph node follicles (*n*
1786 = 3-5 mice/group). (**g**) Interaction of SUDV GPΔmuc trimer and trimer-presenting SApNPs with
1787 FDC networks in lymph node follicles 48 h after a single-dose injection. Both E2p and I3-01v9b
1788 SApNPs colocalized with FDC networks. Immunofluorescent images are pseudo-color-coded
1789 ($CD21^+$, green; $CD169^+$, red; CA45, white). Scale bars = 500 and 100 μm for a complete lymph
1790 node and the enlarged image of a follicle, respectively. The data points are expressed as the mean
1791 ± SEM for (d) and SD for (e and f). The data were analyzed using one-way ANOVA followed by
1792 Tukey's multiple comparison *post hoc* test. **$p < 0.01$, ****$p < 0.0001$.

1793 **Fig. 7. Interaction of SUDV GPΔmuc-presenting SApNPs with FDCs and phagocytic cells in**
1794 **lymph nodes. (a-c)** TEM images of (**a**) E2p SApNPs (yellow arrows) and (**b, c**) I3-01v9b SApNPs
1795 presenting SUDV GPΔmuc-WL^2P^4 trimers aligned on FDC dendrites in lymph node follicles (**a,**
1796 **b**) 12 h and (**c**) 48 h after a single-dose injection (2 footpads, 50 μg/footpad). The administered
1797 dose was 200 μl of antigen/aluminum phosphate (AP) adjuvant mix containing 100 μg of SApNP
1798 and 100 μl of AP adjuvant into two hind footpads. Fresh popliteal lymph nodes were collected. No
1799 AP adjuvant was observed on FDC dendrites. (**d, e**) TEM images of (**d**) E2p and (**e**) I3-01v9b
1800 SApNPs (yellow arrows) presenting SUDV GPΔmuc-WL^2P^4 trimers observed on the surface and
1801 inside endolysosomes of phagocytic cells 12 h after a single-dose injection. (**f**) TEM images of AP
1802 adjuvant (green arrows) aggregated in the extracellular matrix (ECM) 2 h after the injection. (**g**)
1803 TEM images of Sudan GPΔmuc-presenting I3-01v9b SApNPs and AP adjuvants observed inside
1804 endolysosomes of phagocytic cells 48 h after the injection.

1805 **Fig. 8. Induction of germinal center reactions by SUDV GPΔmuc-presenting SApNPs in**
1806 **lymph nodes**. (**a**) Top: representative immunofluorescent images of germinal centers (GCs)
1807 induced by the SUDV GPΔmuc-presenting SApNP vaccine 2 weeks after a single-dose injection
1808 (10 μg/injection, 40 μg/mouse). The administered dose was 80 μl of antigen/aluminum phosphate
1809 (AP) adjuvant mix. Bottom: robust GC formation with well-organized light zone (LZ) and dark
1810 zone (DZ) compartments in lymph node follicles. GC B cells ($GL7^+$, red) attached to FDCs ($CD21^+$,
1811 green) and T_{fh} cells located in LZ of GCs. Scale bars = 500 and 100 μm for a complete lymph node
1812 and the enlarged image of a follicle, respectively. (**b**, **c**) Assessment of GCs in immunofluorescent
1813 images 2, 5, and 8 weeks after a single-dose injection or 2 and 5 weeks after the boost, which
1814 occurred 3 weeks after the prime (n = 5 mice/group). The GC/FDC ratio and GC size were
1815 measured and plotted. (**d**, **e**) Representative GC immunofluorescent images generated by Sudan

1816 GP vaccine constructs at 8 weeks using a single-dose or prime-boost regimen. Scale bar = 50 μm
1817 for an enlarged lymph node follicle. (**f, g**) Quantification of GCs using flow cytometry after single-
1818 dose or prime-boost injections (*n* = 5 mice/group). Frequency and number of GC B cells and T_{fh}
1819 cells were characterized and plotted. The data points are shown as the mean ± SD. The data were
1820 analyzed using one-way ANOVA followed by Tukey's multiple comparison *post hoc* test for each
1821 timepoint. ns (not significant), *p < 0.05, **p < 0.01, ***p < 0.001, ****p < 0.0001.

1822 **Fig. 9**. **Antibody responses to rationally designed filovirus vaccines in mice.** (a) Schematic
1823 illustration of the mouse immunization regimen for EBOV, SUDV, and RAVV GPΔmuc vaccines
1824 (n = 8 mice/group). The administered dose was 200 μl of antigen/AH + CpG adjuvant mix
1825 containing 10 μg of immunogen and 100 μl of adjuvant. Mice were immunized at weeks 0, 3, 9
1826 and 15 with an extended interval of 6 weeks between the 2nd and 3rd doses and 3rd and 4th doses
1827 via the intraperitoneal route. (**b-d**) EBOV vaccine-induced binding antibody (bAb) responses
1828 against (**b**) EBOV GPΔmuc-WL^2P^4(1TD0), (**c**) SUDV GPΔmuc-WL^2P^4(1TD0), and (**d**) RAVV
1829 GPΔmuc-P^2CT(1TD0). (**e-g**) EBOV vaccine-induced NAb responses against (**e**) EBOV Makona,
1830 (**f**) SUDV Gulu, and (**g**) BDBV Uganda pseudoviruses. (**h-j**) SUDV vaccine-induced bAb
1831 responses against (**h**) SUDV GPΔmuc-WL^2P^4(1TD0), (**i**) EBOV GPΔmuc-WL^2P^4(1TD0), and (**j**)
1832 RAVV GPΔmuc-P^2CT(1TD0). (**k-m**) SUDV vaccine-induced NAb responses against (**k**) SUDV
1833 Gulu, (**l**) EBOV Makona, and (**m**) BDBV Uganda pseudoviruses. (**n-p**) RAVV vaccine-induced
1834 bAb responses against (**n**) RAVV GPΔmuc-P^2CT(1TD0), (**o**) EBOV GPΔmuc-WL^2P^4(1TD0), and
1835 (**p**) SUDV GPΔmuc-WL^2P^4(1TD0). (**q**) RAVV vaccine-induced NAb responses against MARV
1836 Angola pseudovirus and pseudotyped ebolaviruses using purified IgG and serum, respectively.
1837 Notably, EC_{50} titers were derived from serum ELISA against coating antigens, with geometric
1838 means labeled on the plots. ID_{50}/IC_{50} titers were derived from pseudovirus neutralization assays,

1839 with geometric means labeled on the plots. The ID_{50}/IC_{50} values were derived by setting %
1840 neutralization to be 0.0-100.0%. Color coding indicates the level of ID_{50} values (green to red: low
1841 to high neutralization). The data points are shown as the mean ± SD. The data were analyzed using
1842 one-way ANOVA, followed by Tukey's multiple comparison *post hoc* test for each timepoint.
1843 Statistical significance is indicated as the following: ns (not significant), *$p < 0.05$, **$p < 0.01$,
1844 ***$p < 0.001$, and ****$p < 0.0001$. The schematic illustration of the mouse immunization protocol
1845 was created with BioRender.com.

1846 **Fig. 10. Effect of glycan modification on antibody responses elicited by filovirus vaccines.**
1847 Schematic illustration of the mouse immunization regimen for glycan-modified EBOV, SUDV,
1848 and RAVV vaccines (n = 8 mice/group). The administered dose was 200 µl of antigen/AH + CpG
1849 adjuvant mix containing 10 µg of glycan-modified immunogen and 100 µl of adjuvant. Mice were
1850 injected at weeks 0, 3, 6 and 9 with an interval of 3 weeks between each immunization via the
1851 intraperitoneal route. The immunogenicity of filovirus vaccine antigens was compared between
1852 glycan modifications (expressed in the presence of kifunensine [Kif] *vs.* Kif treatment followed by
1853 glycan trimming using endo H) and wildtype. (**b**-**d**) Glycan-modified EBOV vaccine-induced bAb
1854 responses against EBOV GPΔmuc-WL^2P^4(1TD0). (**e-g**) Glycan-modified EBOV vaccine-induced
1855 NAb responses against EBOV Makona pseudovirus. (**h-j**) Glycan-modified SUDV vaccine-
1856 induced bAb responses against SUDV GPΔmuc-WL^2P^4(1TD0). (**k-m**) Glycan-modified SUDV
1857 vaccine-induced NAb responses against Gulu pseudovirus. (**n**) Glycan-trimmed RAVV vaccine-
1858 induced bAb responses against RAVV GPΔmuc-P^2CT(1TD0). (**o**) Glycan-trimmed RAVV
1859 vaccine-induced NAb responses against MARV Angola and pseudotyped ebolaviruses, both using
1860 purified IgG. EC_{50} titers were derived from serum ELISA against coating antigens, with geometric
1861 means labeled on the plots. ID_{50}/IC_{50} titers were derived from the pseudovirus neutralization assays,

1862 with geometric means labeled on the plots. The ID_{50}/IC_{50} values were derived by setting %
1863 neutralization to 0.0-100.0%. Color coding indicates the level of IC_{50} values (green to red: low to
1864 high neutralization). Of note, the immunogenicity data for wildtype EBOV GPΔmuc
1865 trimer/SApNPs, SUDV GPΔmuc trimer, and RAVV GPΔmuc trimer from the prior long-interval
1866 immunization study were included for comparison, for which the boost timepoints (W11 and W17)
1867 were labeled but not used for the statistical analysis. The data points are shown as the mean ± SD.
1868 The data were analyzed using one-way ANOVA, followed by Tukey's multiple comparison *post*
1869 *hoc* test for each timepoint. Statistical significance is indicated as the following: ns (not
1870 significant), $*p < 0.05$, $**p < 0.01$, $***p < 0.001$, and $****p < 0.0001$. The schematic illustration
1871 of the mouse immunization protocol was created with BioRender.com.

Figure 1

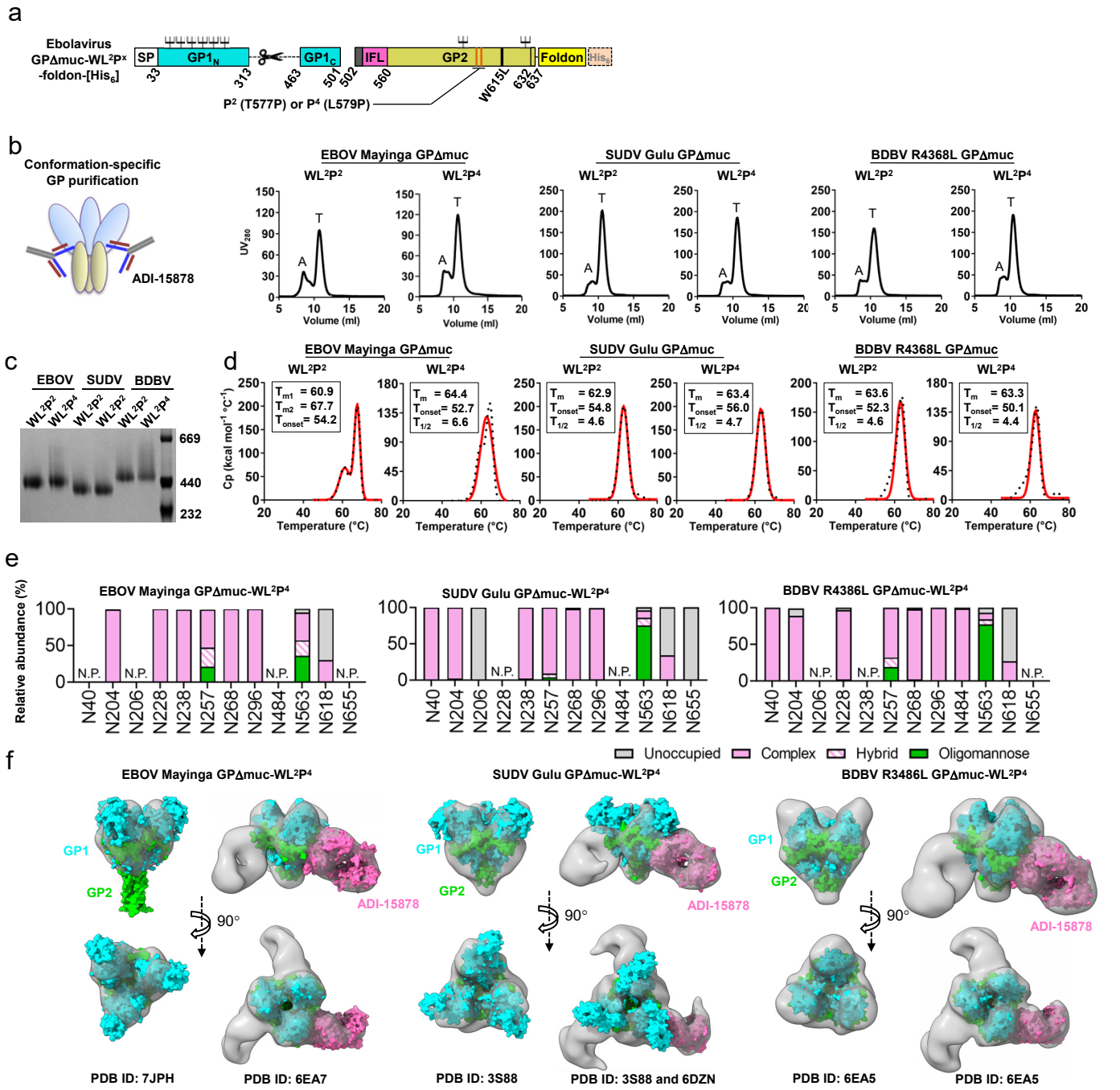

	CA45	ADI-15878	ADI-15946	BDBV-289	MR78
EBOV Mayinga GPΔmuc-WL²P²	0.68	0.58	0.38	0.41	0.00
EBOV Mayinga GPΔmuc-WL²P⁴	0.69	0.59	0.37	0.39	0.00
SUDV Gulu GPΔmuc-WL²P²	0.51	0.63	0.32	0.21	0.00
SUDV Gulu GPΔmuc-WL²P⁴	0.54	0.68	0.38	0.22	0.00
BDBV R4386L GPΔmuc-WL²P²	0.54	0.62	0.44	0.48	0.01
BDBV R4386L GPΔmuc-WL²P⁴	0.59	0.65	0.44	0.48	0.00

Figure 2

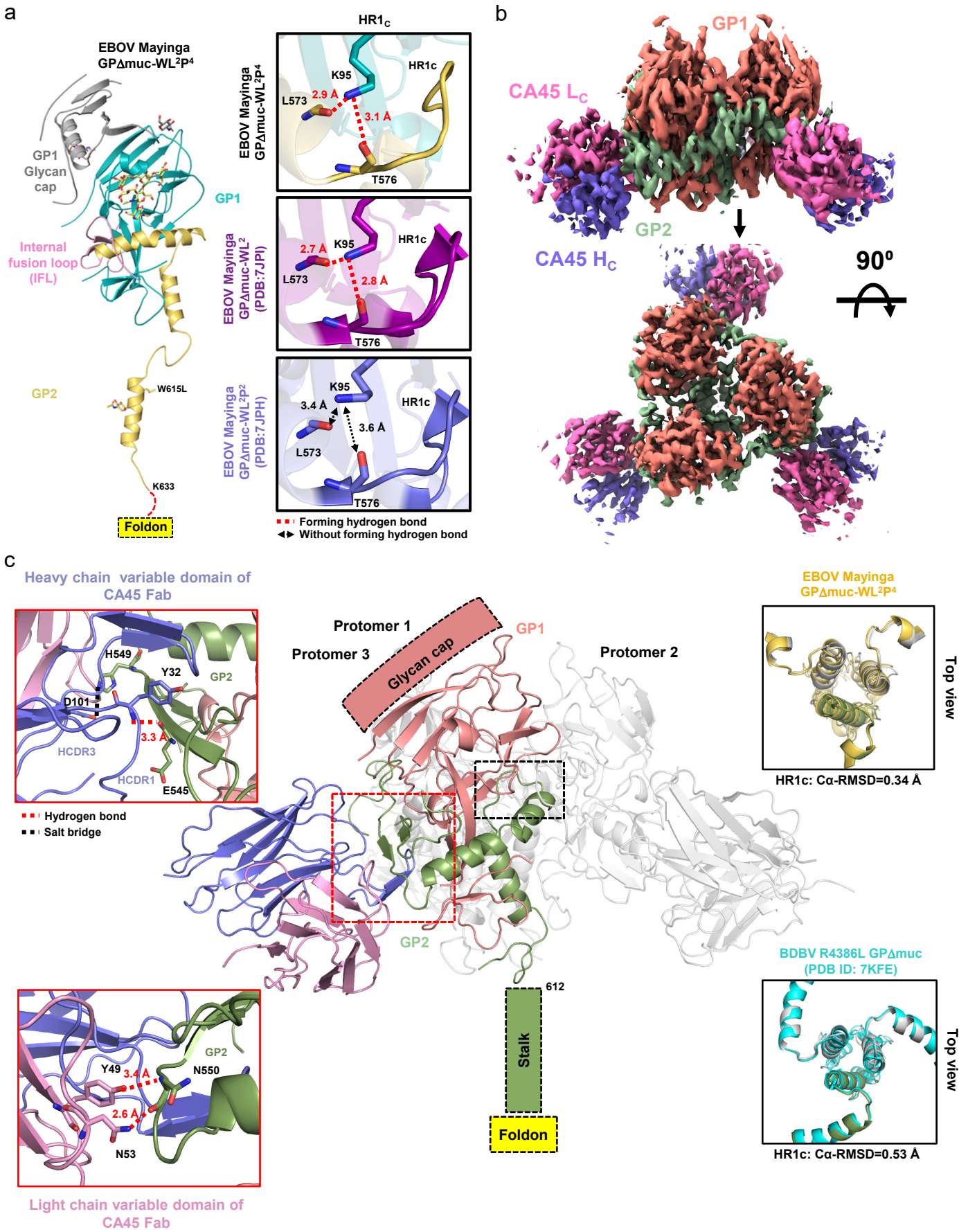
a
EBOV Mayinga GPΔmuc-WL²P⁴
GP1 Glycan cap
GP1
Internal fusion loop (IFL)
GP2
W615L
K633
Foldon
HR1c
EBOV Mayinga GPΔmuc-WL²P⁴
K95
HR1c
L573
2.9 Å
3.1 Å
T576
EBOV Mayinga GPΔmuc-WL² (PDB:7JPI)
2.7 Å
K95
HR1c
L573
2.8 Å
T576
EBOV Mayinga GPΔmuc-WL²P² (PDB:7JPH)
K95
3.4 Å
HR1c
3.6 Å
L573
T576
Forming hydrogen bond
Without forming hydrogen bond
b
GP1
CA45 L_C
GP2
CA45 H_C
90º
c
Heavy chain variable domain of CA45 Fab
H549
Y32
GP2
D101
3.3 Å
HCDR3
HCDR1
E545
Hydrogen bond
Salt bridge
Protomer 1
Protomer 3
Glycan cap
GP1
Protomer 2
GP2
612
Stalk
Foldon
EBOV Mayinga GPΔmuc-WL²P⁴
Top view
HR1c: Cα-RMSD=0.34 Å
BDBV R4386L GPΔmuc (PDB ID: 7KFE)
Top view
HR1c: Cα-RMSD=0.53 Å
GP2
Y49
3.4 Å
N550
2.6 Å
N53
Light chain variable domain of CA45 Fab

Figure 3

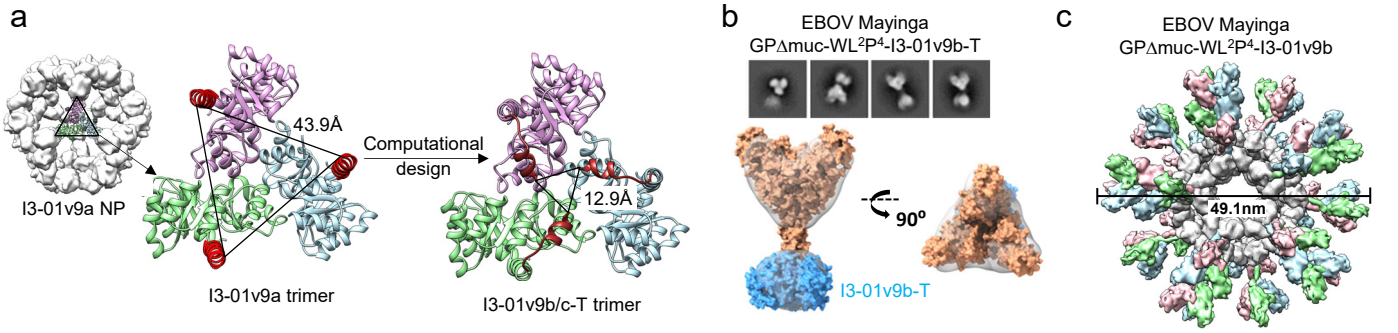

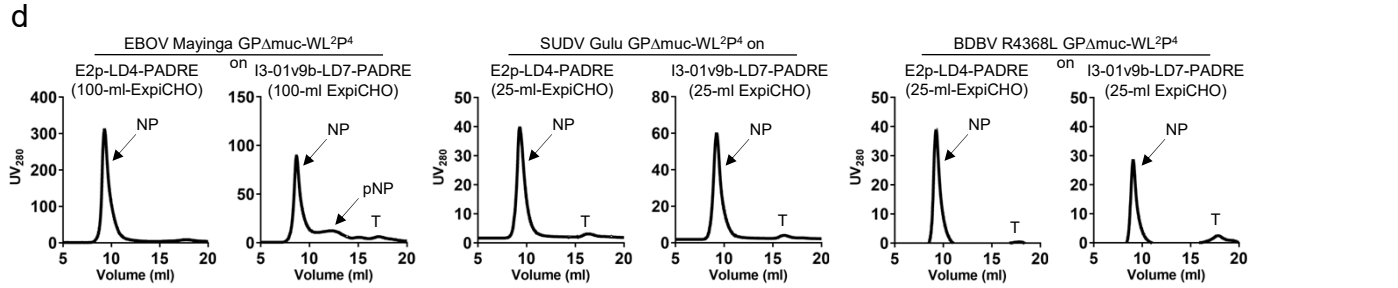

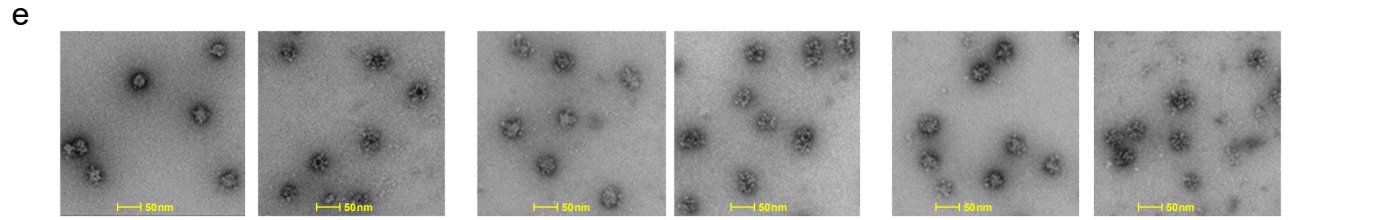

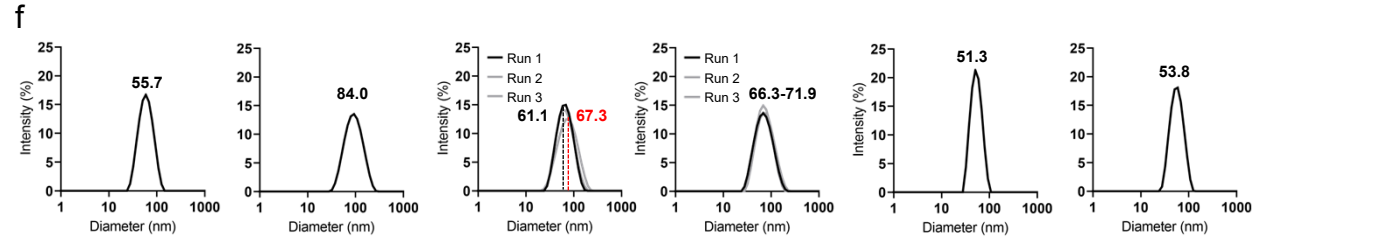

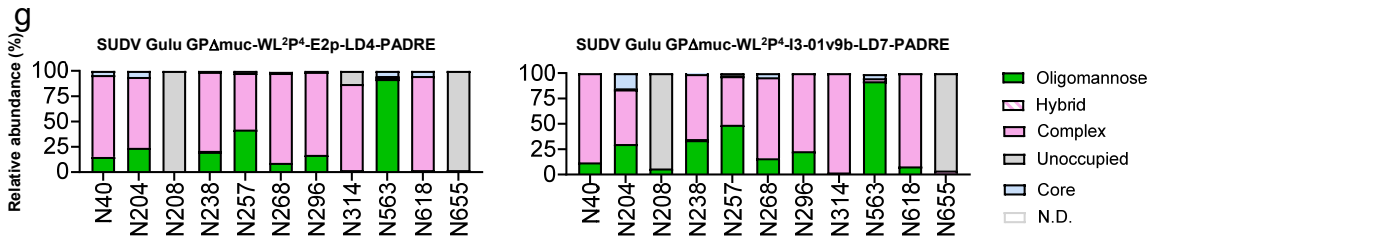

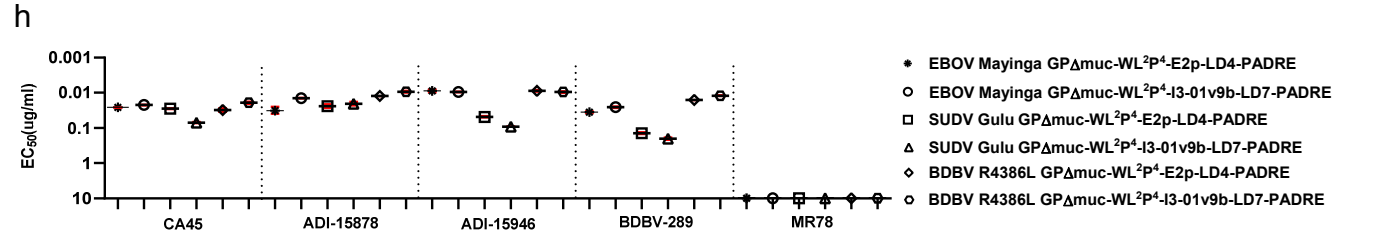

i

	CA45	ADI-15878	ADI-15946	BDBV-289	MR78
EBOV Mayinga GPΔmuc-WL^{2}P^4-E2p-LD4-PADRE	0.71	0.90	0.73	0.79	0.01
EBOV Mayinga GPΔmuc-WL^{2}P^4-I3-01v9b-LD7-PADRE	0.90	0.83	0.66	0.68	0.03
SUDV Gulu GPΔmuc-WL^{2}P^4-E2p-LD4-PADRE	1.37	1.60	1.37	0.51	0.00
SUDV Gulu GPΔmuc-WL^{2}P^4-I3-01v9b-LD7-PADRE	0.72	1.44	1.06	0.39	0.01
BDBV R4386L GPΔmuc-WL^{2}P^4-E2p-LD4-PADRE	0.95	1.68	1.24	2.03	0.01
BDBV R4386L GPΔmuc-WL^{2}P^4-I3-01v9b-LD7-PADRE	0.50	1.21	1.24	0.87	0.00

Figure 4

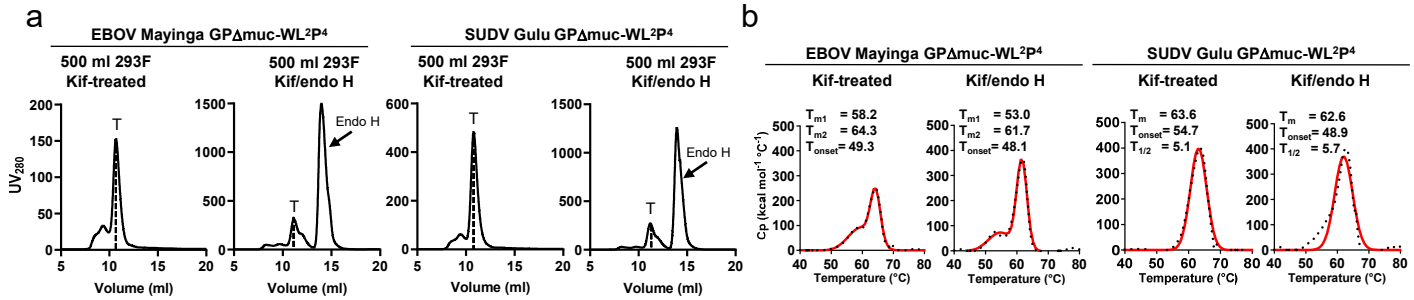

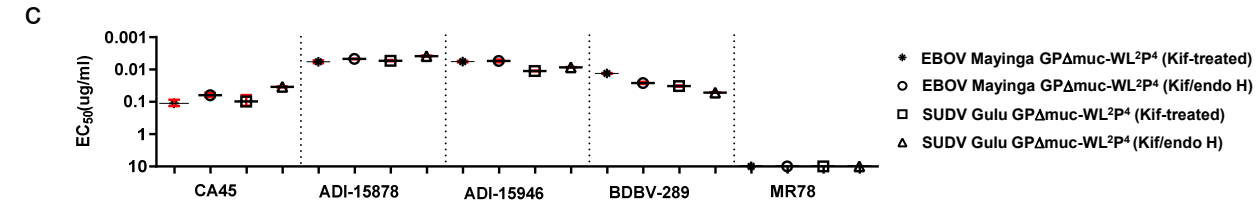

d

	CA45	ADI-15878	ADI-15946	BDBV-289	MR78
EBOV Mayinga GPΔmuc-WL^{2}P^4 (Kif-treated)	0.80	0.71	0.53	0.58	0.00
EBOV Mayinga GPΔmuc-WL^{2}P^4 (Kif/endo H)	0.74	0.62	0.45	0.51	0.00
SUDV Gulu GPΔmuc-WL^{2}P^4 (Kif-treated)	0.76	0.70	0.51	0.44	0.00
SUDV Gulu GPΔmuc-WL^{2}P^4 (Kif/endo H)	0.75	0.71	0.55	0.49	0.00

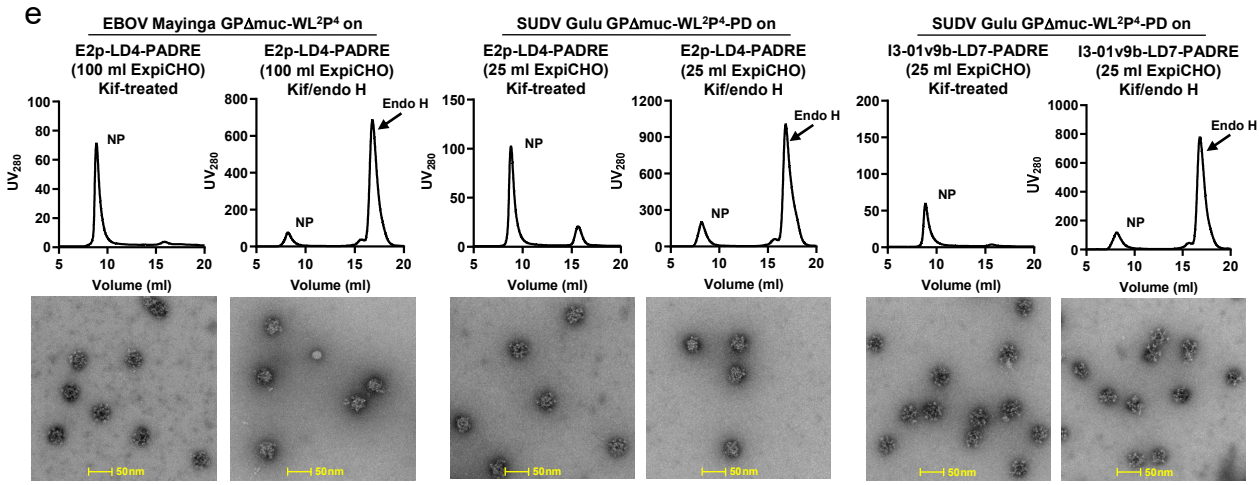

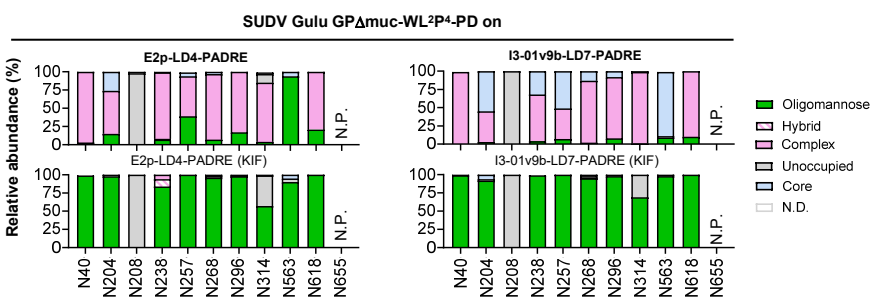

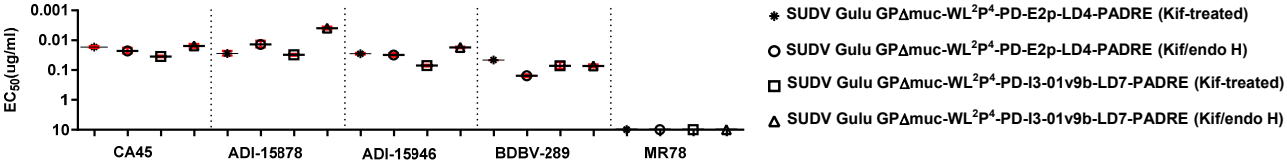

h

	CA45	ADI-15878	ADI-15946	BDBV-289	MR78
SUDV Gulu GPΔmuc-WL^{2}P^4-PD-E2p-LD4-PADRE (Kif-treated)	1.29	1.46	1.44	0.48	0.01
SUDV Gulu GPΔmuc-WL^{2}P^4-PD-E2p-LD4-PADRE (Kif/endo H)	1.63	2.23	1.78	0.58	0.00
SUDV Gulu GPΔmuc-WL^{2}P^4-PD-I3-01v9b-LD7-PADRE (Kif-treated)	0.89	1.43	1.20	0.42	0.01
SUDV Gulu GPΔmuc-WL^{2}P^4-PD-I3-01v9b-LD7-PADRE (Kif/endo H)	1.00	1.60	1.35	0.64	0.00

Figure 5

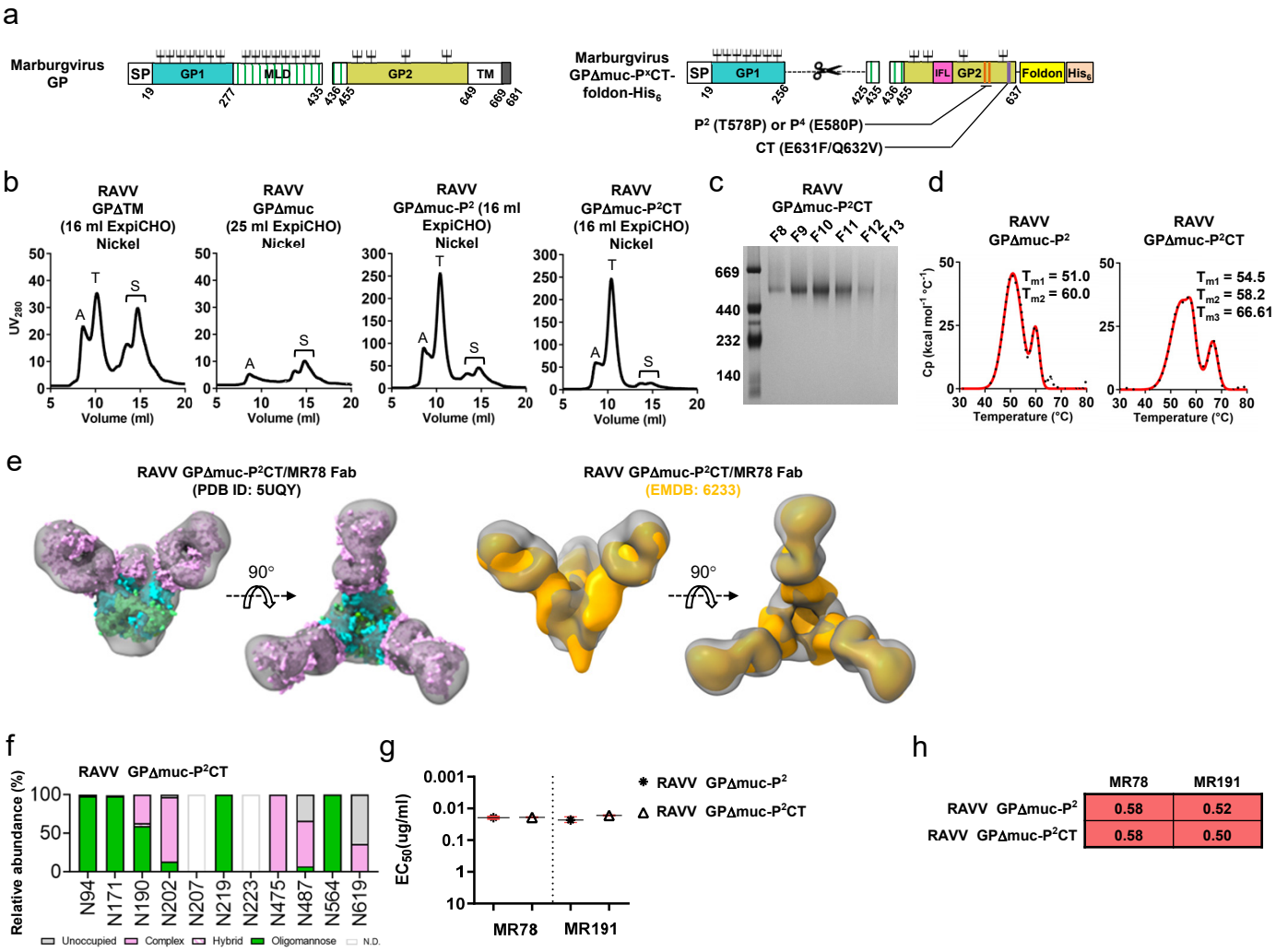

	MR78	MR191
RAVV GPΔmuc-P^2	0.58	0.52
RAVV GPΔmuc-P^{2}CT	0.58	0.50

Figure 6

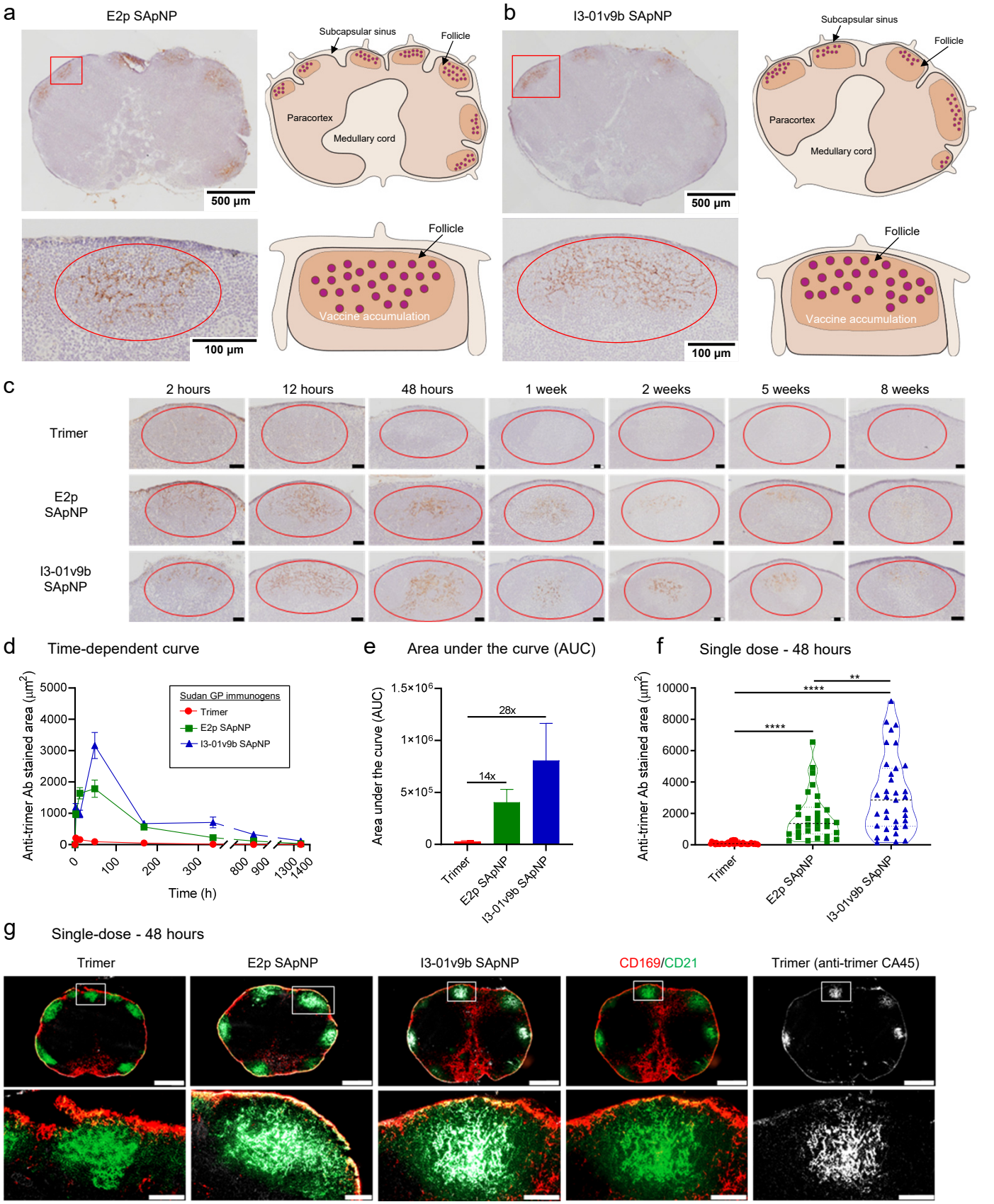
a
E2p SApNP
Subcapsular sinus
Follicle
Paracortex
Medullary cord
500 µm
Follicle
Vaccine accumulation
100 µm
b
I3-01v9b SApNP
Subcapsular sinus
Follicle
Paracortex
Medullary cord
500 µm
Follicle
Vaccine accumulation
100 µm
c
2 hours
12 hours
48 hours
1 week
2 weeks
5 weeks
8 weeks
Trimer
E2p SApNP
I3-01v9b SApNP
d
Time-dependent curve
Anti-trimer Ab stained area (µm²)
Sudan GP immunogens
Trimer
E2p SApNP
I3-01v9b SApNP
Time (h)
e
Area under the curve (AUC)
Area under the curve (AUC)
28x
14x
Trimer
E2p SApNP
I3-01v9b SApNP
f
Single dose - 48 hours
Anti-trimer Ab stained area (µm²)
****
****
**
Trimer
E2p SApNP
I3-01v9b SApNP
g
Single-dose - 48 hours
Trimer
E2p SApNP
I3-01v9b SApNP
CD169/CD21
Trimer (anti-trimer CA45)

Figure 7

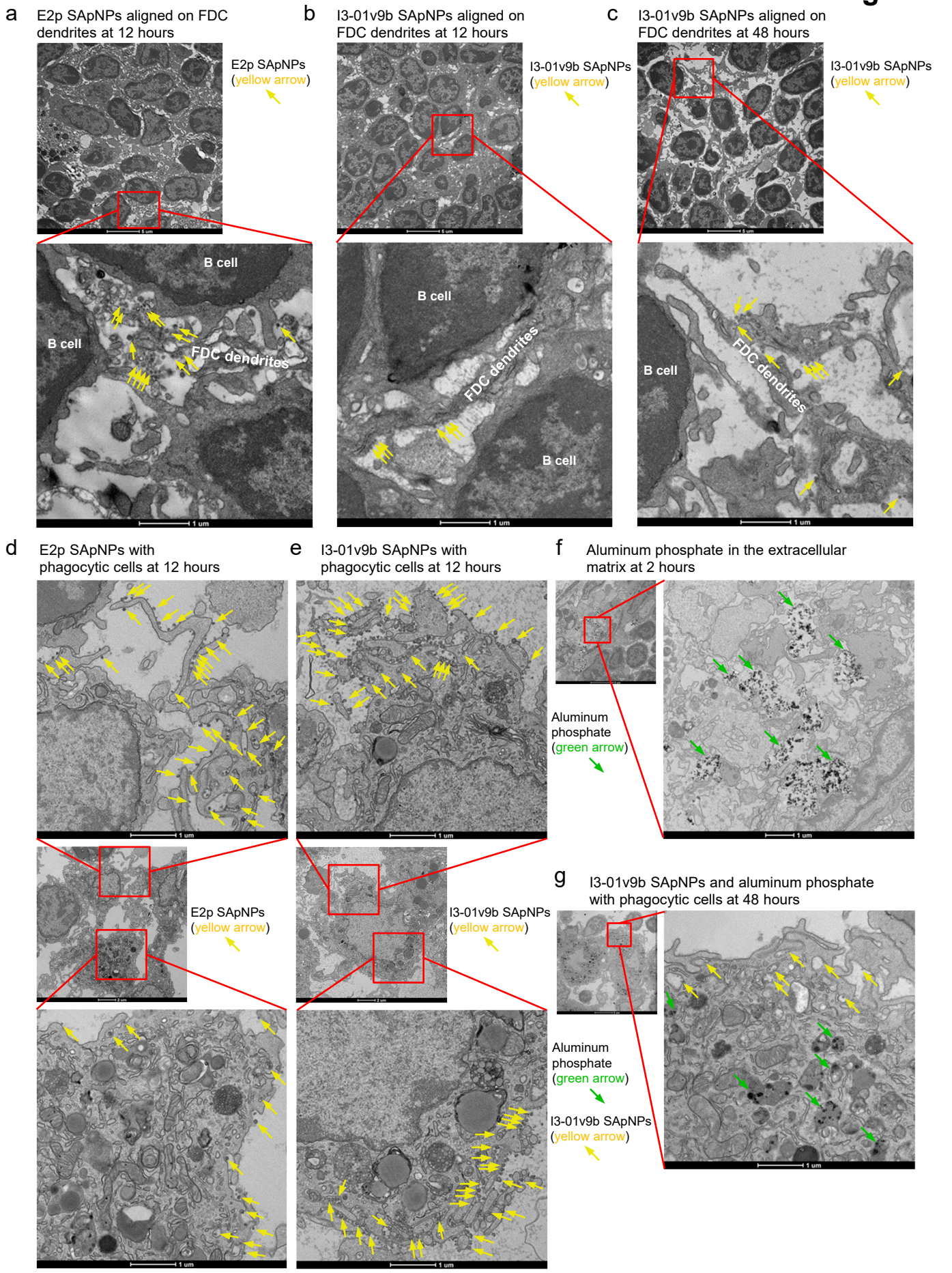
a
E2p SApNPs aligned on FDC dendrites at 12 hours
E2p SApNPs (yellow arrow)
B cell
B cell
FDC dendrites
b
I3-01v9b SApNPs aligned on FDC dendrites at 12 hours
I3-01v9b SApNPs (yellow arrow)
B cell
FDC dendrites
B cell
c
I3-01v9b SApNPs aligned on FDC dendrites at 48 hours
I3-01v9b SApNPs (yellow arrow)
B cell
FDC dendrites
d
E2p SApNPs with phagocytic cells at 12 hours
E2p SApNPs (yellow arrow)
e
I3-01v9b SApNPs with phagocytic cells at 12 hours
I3-01v9b SApNPs (yellow arrow)
f
Aluminum phosphate in the extracellular matrix at 2 hours
Aluminum phosphate (green arrow)
g
I3-01v9b SApNPs and aluminum phosphate with phagocytic cells at 48 hours
Aluminum phosphate (green arrow)
I3-01v9b SApNPs (yellow arrow)

Figure 8

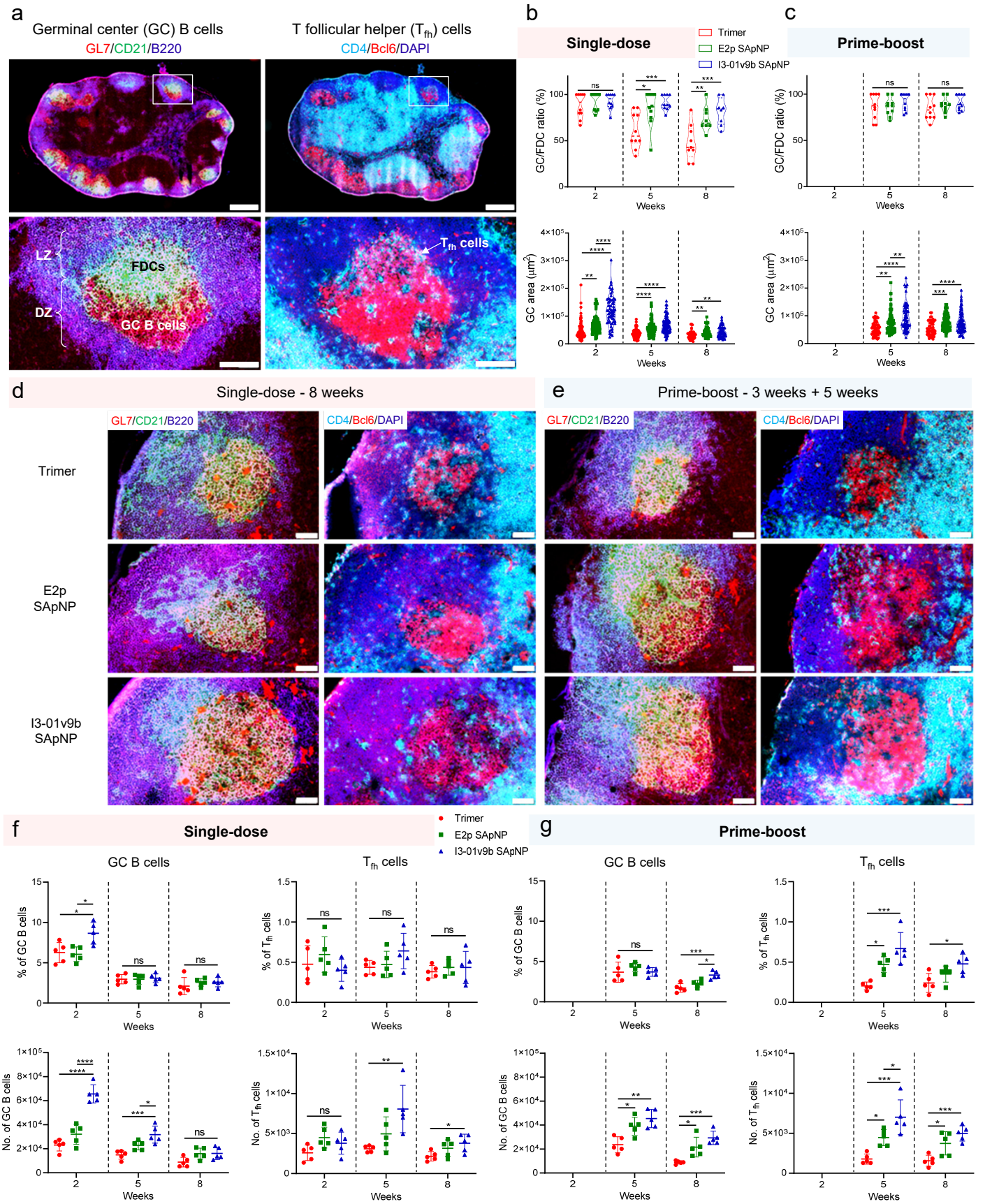
a
Germinal center (GC) B cells
GL7/CD21/B220
T follicular helper (T_{fh}) cells
CD4/Bcl6/DAPI
LZ
FDCs
DZ
GC B cells
T_{fh} cells
b
Single-dose
Trimer
E2p SApNP
I3-01v9b SApNP
GC/FDC ratio (%)
GC area (μm²)
Weeks
c
Prime-boost
d
Single-dose - 8 weeks
GL7/CD21/B220
CD4/Bcl6/DAPI
Trimer
E2p SApNP
I3-01v9b SApNP
e
Prime-boost - 3 weeks + 5 weeks
f
Single-dose
GC B cells
T_{fh} cells
% of GC B cells
% of T_{fh} cells
No. of GC B cells
No. of T_{fh} cells
g
Prime-boost

Figure 9

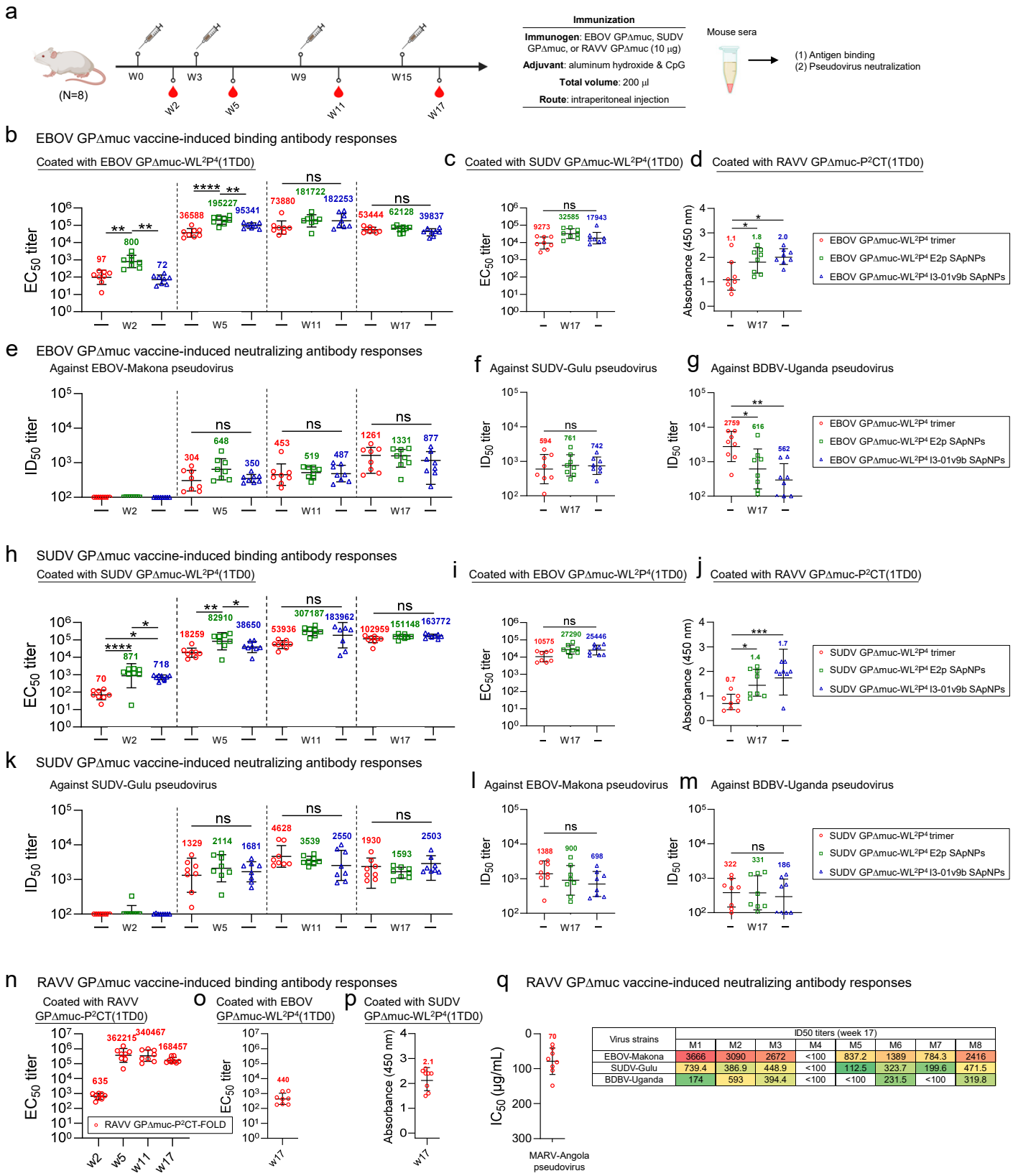

Virus strains	ID50 titers (week 17)							
	M1	M2	M3	M4	M5	M6	M7	M8
EBOV-Makona	3666	3090	2672	<100	837.2	1389	784.3	2416
SUDV-Gulu	739.4	386.9	448.9	<100	112.5	323.7	199.6	471.5
BDBV-Uganda	174	593	394.4	<100	<100	231.5	<100	319.8

Figure 10

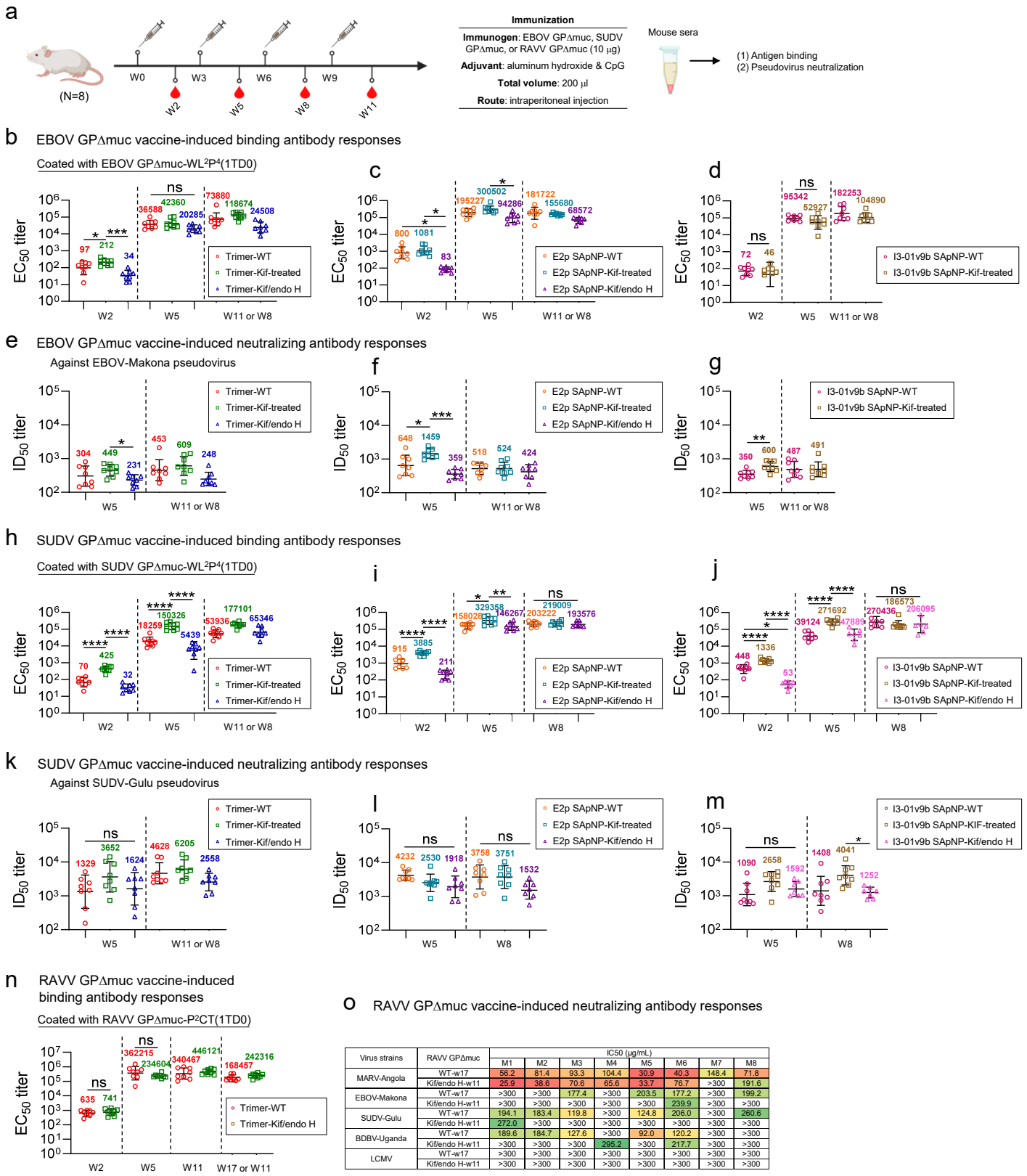

Virus strains	RAVV GPΔmuc	IC50 (μg/mL)							
		M1	M2	M3	M4	M5	M6	M7	M8
MARV-Angola	WT-w17	56.2	81.4	93.3	104.4	30.9	40.3	148.4	71.8
	Kif/endo H-w11	25.9	38.6	70.6	65.6	33.7	76.7	>300	191.6
EBOV-Makona	WT-w17	>300	>300	177.4	>300	203.5	177.2	>300	199.2
	Kif/endo H-w11	>300	>300	>300	>300	>300	239.9	>300	>300
SUDV-Gulu	WT-w17	194.1	183.4	119.8	>300	124.8	206.0	>300	260.6
	Kif/endo H-w11	272.0	>300	>300	>300	>300	>300	>300	>300
BDBV-Uganda	WT-w17	189.6	184.7	127.6	>300	92.0	120.2	>300	>300
	Kif/endo H-w11	>300	>300	>300	295.2	>300	217.7	>300	>300
LCMV	WT-w17	>300	>300	>300	>300	>300	>300	>300	>300
	Kif/endo H-w11	>300	>300	>300	>300	>300	>300	>300	>300

Fig. S1

a

>EBOV Mayinga GPΔmuc-WL²P²-foldon-[His$_6$]

MGVTGILQLPRDRFKRTSFFLWVIILFQRTFSIPLGVIHNSALQVSDVDKLVCRDKLSSTNQLRSVGLNLEGNGVATDVPSATKRWGFRSGVPPKVVNYEAGEWAENC
YNLEIKKPDGSECLPAAPDGIRGFPRCRYVHKVSGTGPCAGDFAFHKEGAFFLYDRLASTVIYRGTTFAEGVVAFLILPQAKKDFFSSHPLREPVNATEDPSSGYYST
TIRYQATGFGTNETEYLFEVDNLTYVQLESRFTPQFLLQLNETIYTSGKRSNTTGKLIWKVNPEIDTTIGEWAFWETKKNLTRKIRSEELSFTVVSTHHQDTGEESAS
SGKLGLITNTIAGVAGLITGGRRTRREAIVNAQPKCNPNLHYWTTQDEGAAIGLAWIPYFGPAAEGIYIEGLMHNQDGLICGLRQLANETTQALQLFLRATPELRTFS
ILNRKAIDFLLQRWGGTCHILGPDCCIEPHDLTKNITDKIDQIIHDFVDKTLPDASGYIPEAPRDGQAYVRKDGEWVLLSTFL[GSHHHHHH]

>EBOV Mayinga GPΔmuc-WL²P⁴-foldon-[His$_6$]

MGVTGILQLPRDRFKRTSFFLWVIILFQRTFSIPLGVIHNSALQVSDVDKLVCRDKLSSTNQLRSVGLNLEGNGVATDVPSATKRWGFRSGVPPKVVNYEAGEWAENC
YNLEIKKPDGSECLPAAPDGIRGFPRCRYVHKVSGTGPCAGDFAFHKEGAFFLYDRLASTVIYRGTTFAEGVVAFLILPQAKKDFFSSHPLREPVNATEDPSSGYYST
TIRYQATGFGTNETEYLFEVDNLTYVQLESRFTPQFLLQLNETIYTSGKRSNTTGKLIWKVNPEIDTTIGEWAFWETKKNLTRKIRSEELSFTVVSTHHQDTGEESAS
SGKLGLITNTIAGVAGLITGGRRTRREAIVNAQPKCNPNLHYWTTQDEGAAIGLAWIPYFGPAAEGIYIEGLMHNQDGLICGLRQLANETTQALQLFLRATTEPRTFS
ILNRKAIDFLLQRWGGTCHILGPDCCIEPHDLTKNITDKIDQIIHDFVDKTLPDASGYIPEAPRDGQAYVRKDGEWVLLSTFL[GSHHHHHH]

>SUDV Gulu GPΔmuc-WL²P²-foldon-[His$_6$]

MGILPSPGMPALLSLVSLLSVLLMGCVAEMPLGVVTNSTLEVTEIDQLVCKDHLASTDQLKSVGLNLEGSGVSTDIPSATKRWGFRSGVPPKVVSYEAGEWAENCYNL
EIKKPDGSECLPPPPDGVRGFPRCRYVHKAQGTGPCPGDYAFHKDGAFFLYDRLASTVIYRGVNFAEGVIAFLILAKPKETFLQSPPIREAVNYTENTSSYYATSYLE
YEIENFGAQHSTTLFKIDNNTFVRLDRPHTPQFLFQLNDTIHLHQQLSNTTGRLIWTLDANINADIGEWAFWENKKNLSEQLRGEELSFEALSLNETEDDDAASSSTS
NGLITSTVTGILGSLGLRKRSRRQTNTKATGKCNPNLHYWTAQEQHNAAGIAWIPYFGPGAEGIYTEGLMHNQNALVCGLRQLANETTQALQLFLRATPELRTYTILN
RKAIDFLLRRWGGTCRILGPDCCIEPHDLTKNITDKINQIIHDFIDNPLPNASGYIPEAPRDGQAYVRKDGEWVLLSTFL[GSHHHHHH]

>SUDV Gulu GPΔmuc-WL²P⁴-foldon-[His$_6$]

MGILPSPGMPALLSLVSLLSVLLMGCVAEMPLGVVTNSTLEVTEIDQLVCKDHLASTDQLKSVGLNLEGSGVSTDIPSATKRWGFRSGVPPKVVSYEAGEWAENCYNL
EIKKPDGSECLPPPPDGVRGFPRCRYVHKAQGTGPCPGDYAFHKDGAFFLYDRLASTVIYRGVNFAEGVIAFLILAKPKETFLQSPPIREAVNYTENTSSYYATSYLE
YEIENFGAQHSTTLFKIDNNTFVRLDRPHTPQFLFQLNDTIHLHQQLSNTTGRLIWTLDANINADIGEWAFWENKKNLSEQLRGEELSFEALSLNETEDDDAASSSTS
NGLITSTVTGILGSLGLRKRSRRQTNTKATGKCNPNLHYWTAQEQHNAAGIAWIPYFGPGAEGIYTEGLMHNQNALVCGLRQLANETTQALQLFLRATTEPRTYTILN
RKAIDFLLRRWGGTCRILGPDCCIEPHDLTKNITDKINQIIHDFIDNPLPNASGYIPEAPRDGQAYVRKDGEWVLLSTFL[GSHHHHHH]

>BDBV R4386L GPΔmuc-WL²P²-foldon-[His$_6$]

MGILPSPGMPALLSLVSLLSVLLMGCVAEIPLGVVHNNTLQVSDIDKLVCRDKLSSTSQLKSVGLNLEGNGVATDVPTATKRWGFRAGVPPKVVNYEAGEWAENCYNL
DIKKADGSECLPEAPEGVRGFPRCRYVHKVSGTGPCPEGYAFHKEGAFFLYDRLASTIIYRSTTFSEGVVAFLILPETKKDFFQSPPLHEPANMTTDPSSYYHTVTLN
YVADNFGTNMTNFLFQVDHLTYVQLEPRFTPQFLVQLNETIYTNGRRSNTTGTLIWKVNPTVDTGVGEWAFWENKKNFTKTLSSEELSVIFVPRAQDPGSNDISESTE
PGPLTNTTRGAANLLTGSRRTRREITLRTQAKCNPNLHYWTTQDEGAAIGLAWIPYFGPAAEGIYTEGIMHNQNGLICGLRQLANETTQALQLFLRATPELRTFSILN
RKAIDFLLQRWGGTCHILGPDCCIEPHDLTKNITDKIDQIIHDFIDKPLPDASGYIPEAPRDGQAYVRKDGEWVLLSTFL[GSHHHHHH]

>BDBV R4386L GPΔmuc-WL²P⁴-foldon-[His$_6$]

MGILPSPGMPALLSLVSLLSVLLMGCVAEIPLGVVHNNTLQVSDIDKLVCRDKLSSTSQLKSVGLNLEGNGVATDVPTATKRWGFRAGVPPKVVNYEAGEWAENCYNL
DIKKADGSECLPEAPEGVRGFPRCRYVHKVSGTGPCPEGYAFHKEGAFFLYDRLASTIIYRSTTFSEGVVAFLILPETKKDFFQSPPLHEPANMTTDPSSYYHTVTLN
YVADNFGTNMTNFLFQVDHLTYVQLEPRFTPQFLVQLNETIYTNGRRSNTTGTLIWKVNPTVDTGVGEWAFWENKKNFTKTLSSEELSVIFVPRAQDPGSNDISESTE
PGPLTNTTRGAANLLTGSRRTRREITLRTQAKCNPNLHYWTTQDEGAAIGLAWIPYFGPAAEGIYTEGIMHNQNGLICGLRQLANETTQALQLFLRATTEPRTFSILN
RKAIDFLLQRWGGTCHILGPDCCIEPHDLTKNITDKIDQIIHDFIDKPLPDASGYIPEAPRDGQAYVRKDGEWVLLSTFL[GSHHHHHH]

b **SEC profile of 6 ebolavirus GPΔmuc constructs expressed in HEK293F cells and purified by Nickel and IAC columns**

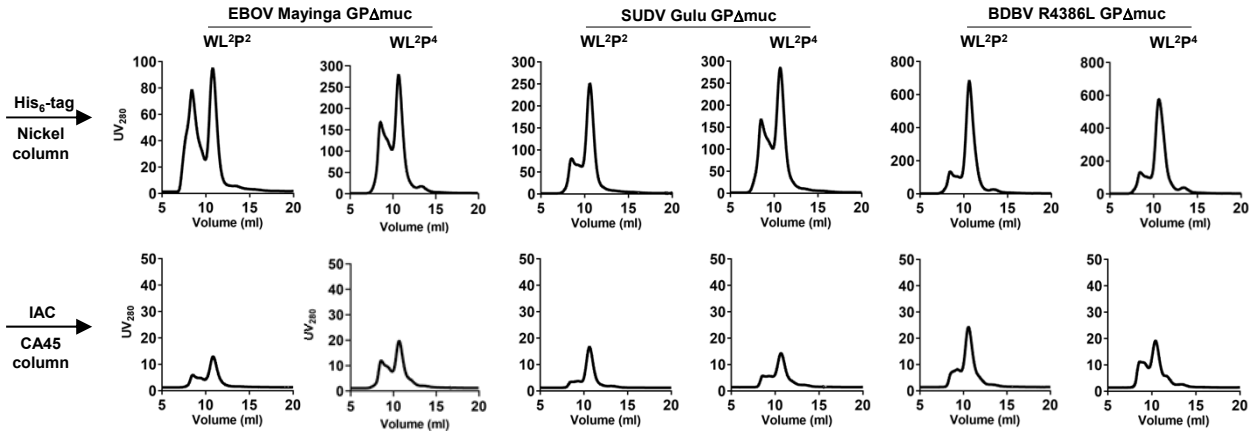

Fig. S1

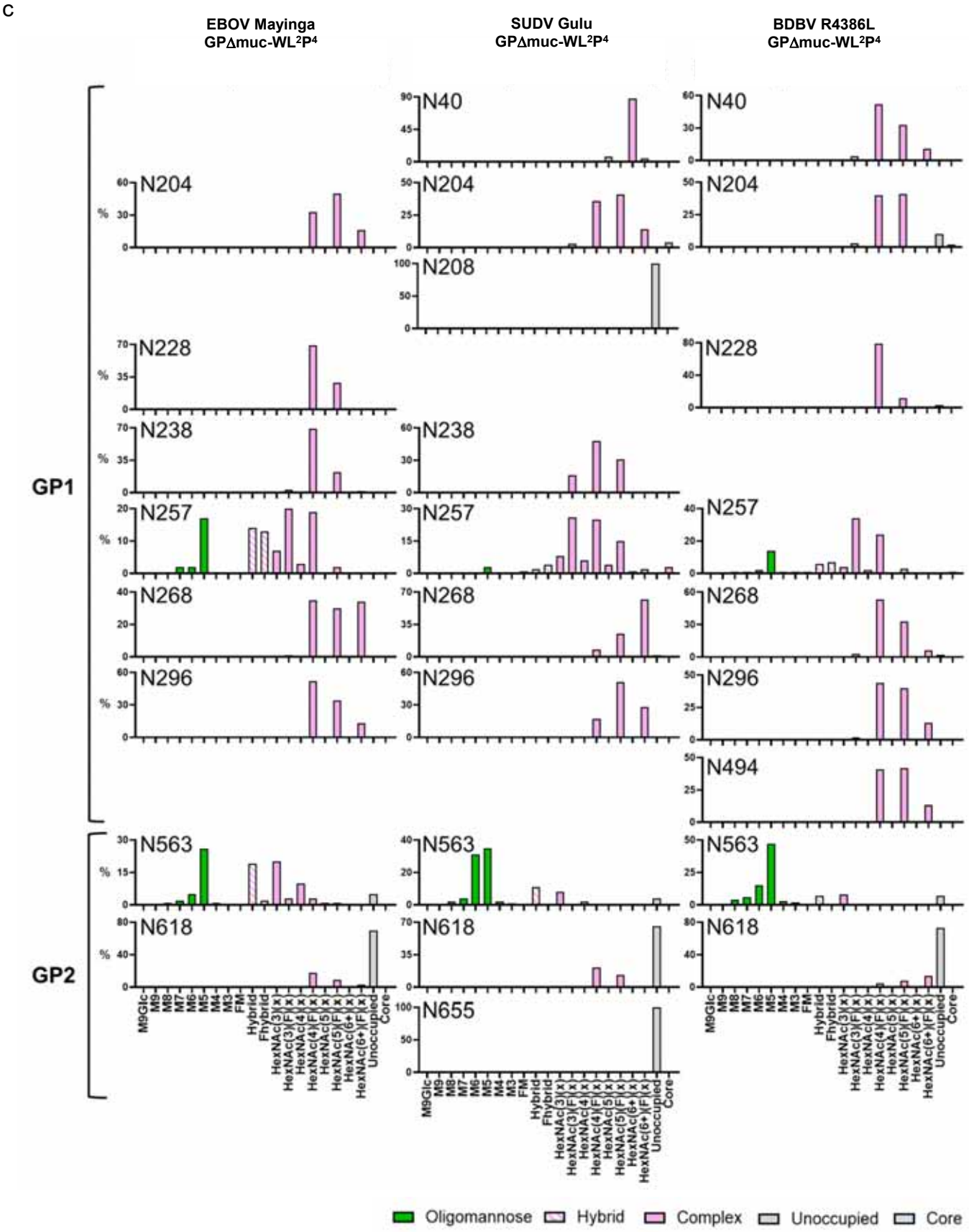
C
EBOV Mayinga GPΔmuc-WL2P4
SUDV Gulu GPΔmuc-WL2P4
BDBV R4386L GPΔmuc-WL2P4
GP1
GP2
N40
N204
N208
N228
N238
N257
N268
N296
N494
N563
N618
N655
%
M9Glc
M9
M8
M7
M6
M5
M4
M3
FM
Hybrid
Fhybrid
HexNAc(3)(x)
HexNAc(3)(F)(x)
HexNAc(4)(x)
HexNAc(4)(F)(x)
HexNAc(5)(x)
HexNAc(5)(F)(x)
HexNAc(6+)(x)
HexNAc(6+)(F)(x)
Unoccupied
Core
Oligomannose
Hybrid
Complex
Unoccupied
Core

Fig. S1

d Flowchart of image processing and model building protocol

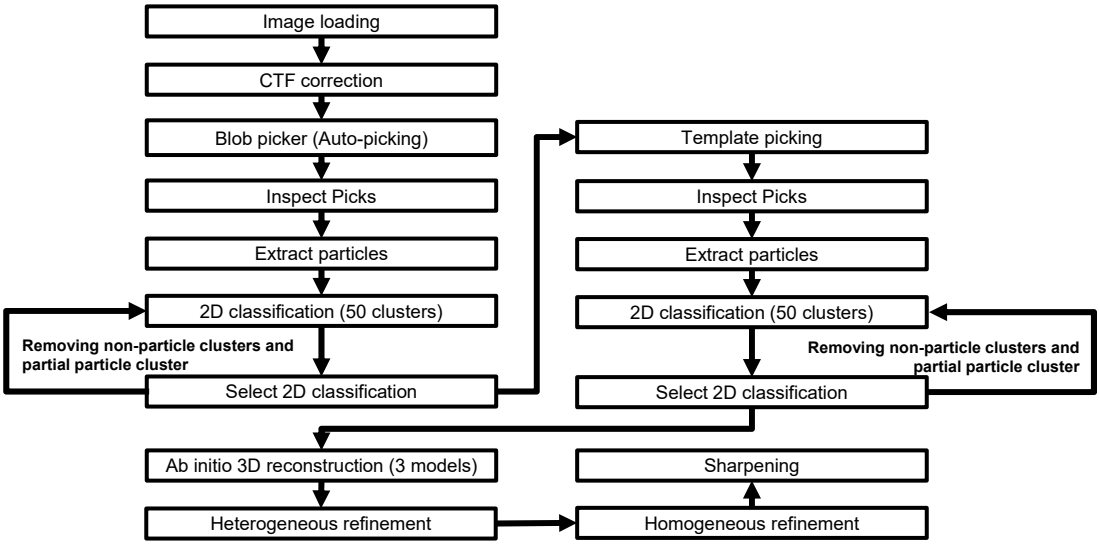

e **Selected 2D classifications for 3D modeling of EBOV Mayinga GPΔmuc**

GPΔmuc-WL^{2}P^4 trimer/ADI-15878 Fab complex

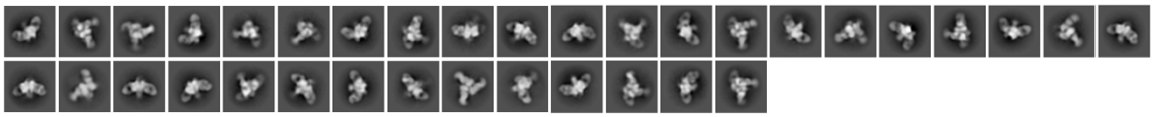

GPΔmuc-WL^{2}P^4 trimer

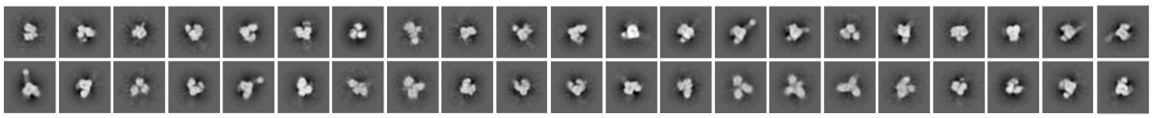

f **Selected 2D classifications for 3D modeling of SUDV Gulu GPΔmuc**

GPΔmuc-WL^{2}P^4 trimer/ADI-15878 Fab complex

GPΔmuc-WL^{2}P^4 trimer

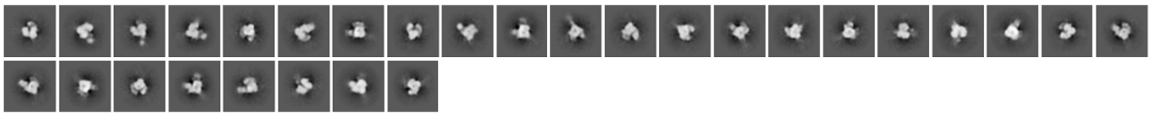

g **Selected 2D classifications for 3D modeling of BDBV R3486L GPΔmuc**

GPΔmuc-WL^{2}P^4 trimer/ADI-15878 Fab complex

GPΔmuc-WL^{2}P^4 trimer

h ELISA analysis of 6 rationally designed ebolavirus GPΔmuc trimers binding to 5 filovirus NAbs

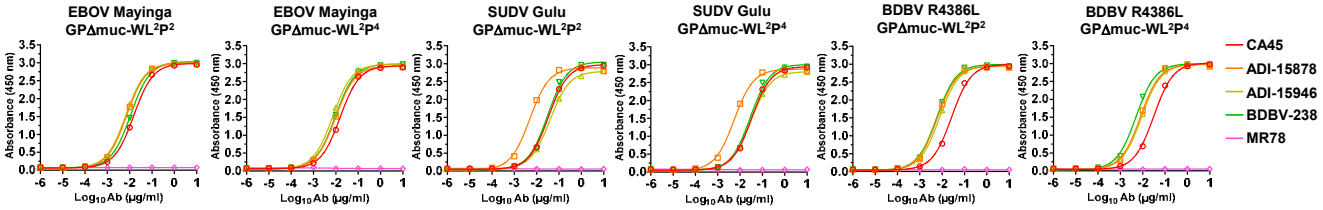

EBOV Mayinga GPΔmuc-WL^{2}P^2									
CA45		ADI-15878		ADI-15946		BDBV-289		MR78	
EC50	STD	EC50	STD	EC50	STD	EC50	STD	EC50	STD
0.01520	0.00023	0.00727	0.00072	0.00669	0.00017	0.01109	0.00029	N.D.	N.D.

EBOV Mayinga GPΔmuc-WL^{2}P^4									
CA45		ADI-15878		ADI-15946		BDBV-289		MR78	
EC50	STD	EC50	STD	EC50	STD	EC50	STD	EC50	STD
0.015639	0.000587	0.009683	0.001136	0.007233	0.000747	0.009632	0.00102	N.D.	N.D.

SUDV Gulu GPΔmuc-WL^{2}P^2									
CA45		ADI-15878		ADI-15946		BDBV-289		MR78	
EC50	STD	EC50	STD	EC50	STD	EC50	STD	EC50	STD
0.0338	2.83E-05	0.004959	7.07E-06	0.039574	0.002213	0.030734	0.000834	N.D.	N.D.

SUDV Gulu GPΔmuc-WL^{2}P^4									
CA45		ADI-15878		ADI-15946		BDBV-289		MR78	
EC50	STD	EC50	STD	EC50	STD	EC50	STD	EC50	STD
0.032764	0.001209	0.005461	0.000156	0.031179	0.002638	0.028805	0.000792	N.D.	N.D.

BDBV R4386L GPΔmuc-WL^{2}P^2									
CA45		ADI-15878		ADI-15946		BDBV-289		MR78	
EC50	STD	EC50	STD	EC50	STD	EC50	STD	EC50	STD
0.026339	0.001499	0.005969	0.000224	0.007626	0.000158	0.005773	3.39E-05	N.D.	N.D.

BDBV R4386L GPΔmuc-WL^{2}P^4									
CA45		ADI-15878		ADI-15946		BDBV-289		MR78	
EC50	STD	EC50	STD	EC50	STD	EC50	STD	EC50	STD
0.031360	0.000170	0.007866	0.000318	0.008934	0.000208	0.005026	0.000132	N.D.	N.D.

i BLI analysis of 6 rationally designed ebolavirus GPΔmuc trimers binding to 5 filovirus NAbs

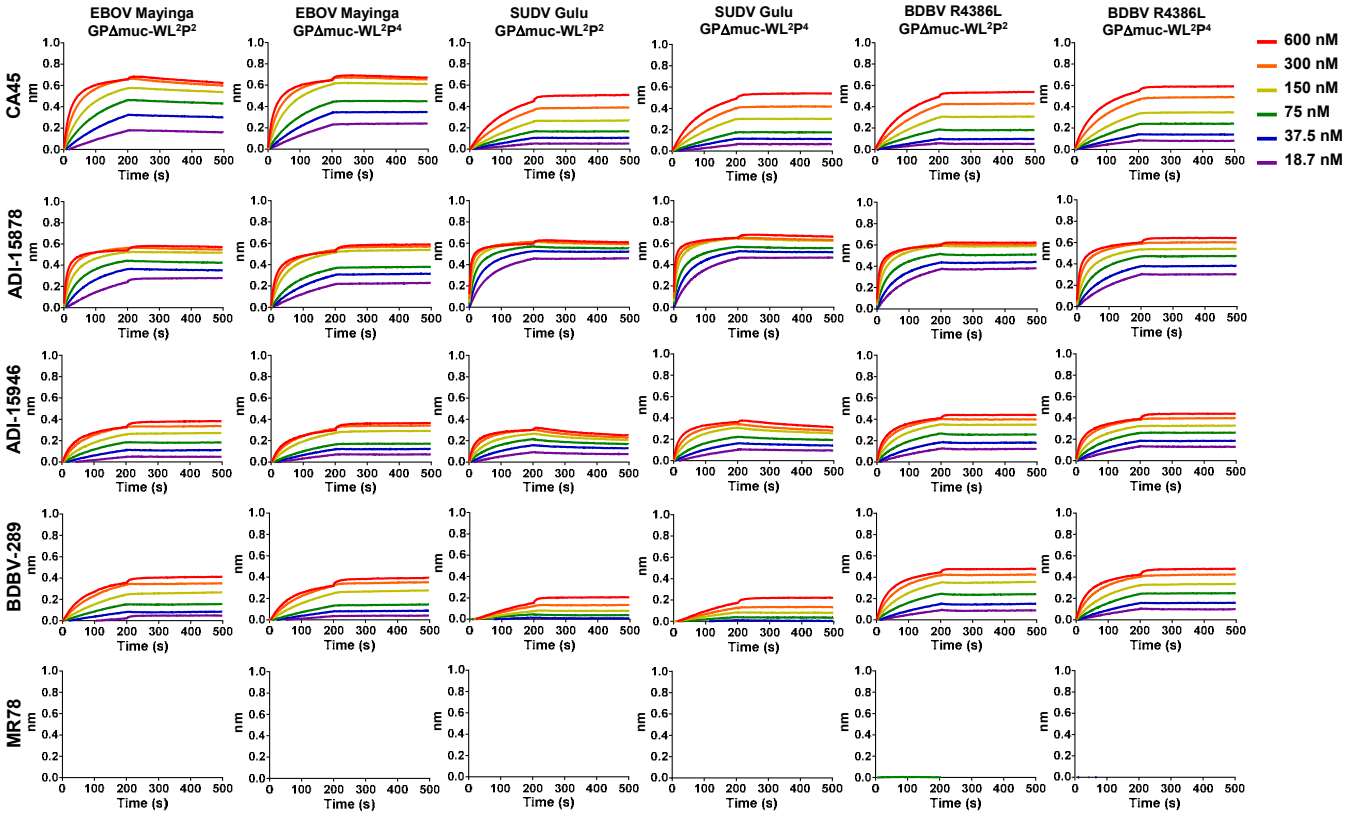

K_D values for 6 rationally designed ebolavirus GPΔmuc trimers binding to 5 filovirus NAbs (nM) [a]

	CA45	ADI-15878	ADI-15946	BDBV-289	MR78
EBOV Mayinga GPΔmuc-WL^{2}P^2	2.62	<1.0E-3	<1.0E-3	<1.0E-3	— [b]
EBOV Mayinga GPΔmuc-WL^{2}P^4	<1.0E-3	<1.0E-3	<1.0E-3	<1.0E-3	— [b]
SUDV Gulu GPΔmuc-WL^{2}P^2	<1.0E-3	<1.0E-3	7.22	<1.0E-3	— [b]
SUDV Gulu GPΔmuc-WL^{2}P^4	<1.0E-3	<1.0E-3	4.89	<1.0E-3	— [b]
BDBV R4386L GPΔmuc-WL^{2}P^2	<1.0E-3	<1.0E-3	<1.0E-3	<1.0E-3	— [b]
BDBV R4386L GPΔmuc-WL^{2}P^4	<1.0E-3	<1.0E-3	<1.0E-3	<1.0E-3	— [b]

[a] K_D values were derived from biolayer interferometry (BLI) using the binding equations describing a 1:1 interaction.
[b] "—" indicates cases where the peak signal value at the highest ebolavirus antigen concentration is 0.2 or lower.

Fig. S1. Construct design and in vitro characterization of ebolavirus GPΔmuc trimers. (**a**) Amino acid sequences of EBOV Mayinga , SUDV Gulu, and BDBV R3486L GPΔmuc-WL^2P^x-foldon-[His_6] constructs containing P^2 and P^4 mutations. Signal peptide, GP, restriction site (AS), foldon, linker (GS), and His_6 tag are highlighted in yellow, grey, green, orange, pink, and teal, respectively. The WL^2P^x mutations are colored in red. Notably, foldon is a C-terminal trimerization motif used in all ebolavirus GPΔmuc constructs and therefore will not be included in the construct names (except here in the sequence definition) to avoid redundancy. The GS linker and His_6 tag are shown in [ ] to indicate that they are only included in a set of GPΔmuc constructs generated for testing the Nickel purification method. (**b**) SEC profiles of EBOV Mayinga , SUDV Gulu, and BDBV R3486L GPΔmuc produced in 165 ml HEK293F cells and purified using either a Nickel column or a CA45 antibody column. (**c**) Compositional site-specific glycan analysis of three ebolavirus GPΔmuc-WL^2P^4 trimers. The graphs summarize quantitative mass spectrometric analysis of the glycan population present at individual N-linked glycosylation sites simplified into categories of glycans. The oligomannose-type glycan series (M9 to M5; $Man_9GlcNAc_2$ to $Man_5GlcNAc_2$) is colored green, afucosylated and fucosylated hybrid-type glycans (hybrid and F hybrid) are dashed pink, and complex glycans are grouped according to the number of antennae and presence of core fucosylation and are colored pink. Unoccupancy of an N-linked glycan site is represented in gray. Glycan sites that could not be determined are denoted as "N.D.". (**d**) Flowchart of image processing, 2D classification, and 3D reconstruction of negative stain EM (nsEM) data obtained for EBOV, SUDV, and BDBV GPΔmuc trimers and their complexes with ADI-15878 Fab using CryoSPARC. (**e**)-(**f**) Representative 2D classification images of EBOV, SUDV, and BDBV GPΔmuc-WL^2P^4 trimers and their complexes with ADI-15878 Fab. (**g**) ELISA analysis of EBOV, SUDV, and BDBV GPΔmuc trimers binding to 5 filovirus NAbs in the IgG form. Briefly, each well was coated with 0.1 μg of the appropriate antigen, and IgG was diluted in a 10-fold dilution series from a starting concentration of 10 μg/ml for all tested antibodies. Error bars represent the difference between these duplicate values at each concentration tested for each sample. (**h**) BLI analysis of EBOV, SUDV, and BDBV GPΔmuc trimers binding to 5 filovirus NAbs in the IgG form. Sensorgrams were obtained from an Octet RED96 instrument using the AHC biosensor. A two-fold concentration gradient of antigen, starting at 600 nM, was used in a dilution series of six. K_D values derived from a 1:1 fitting model are summarized in a table.

Fig. S2

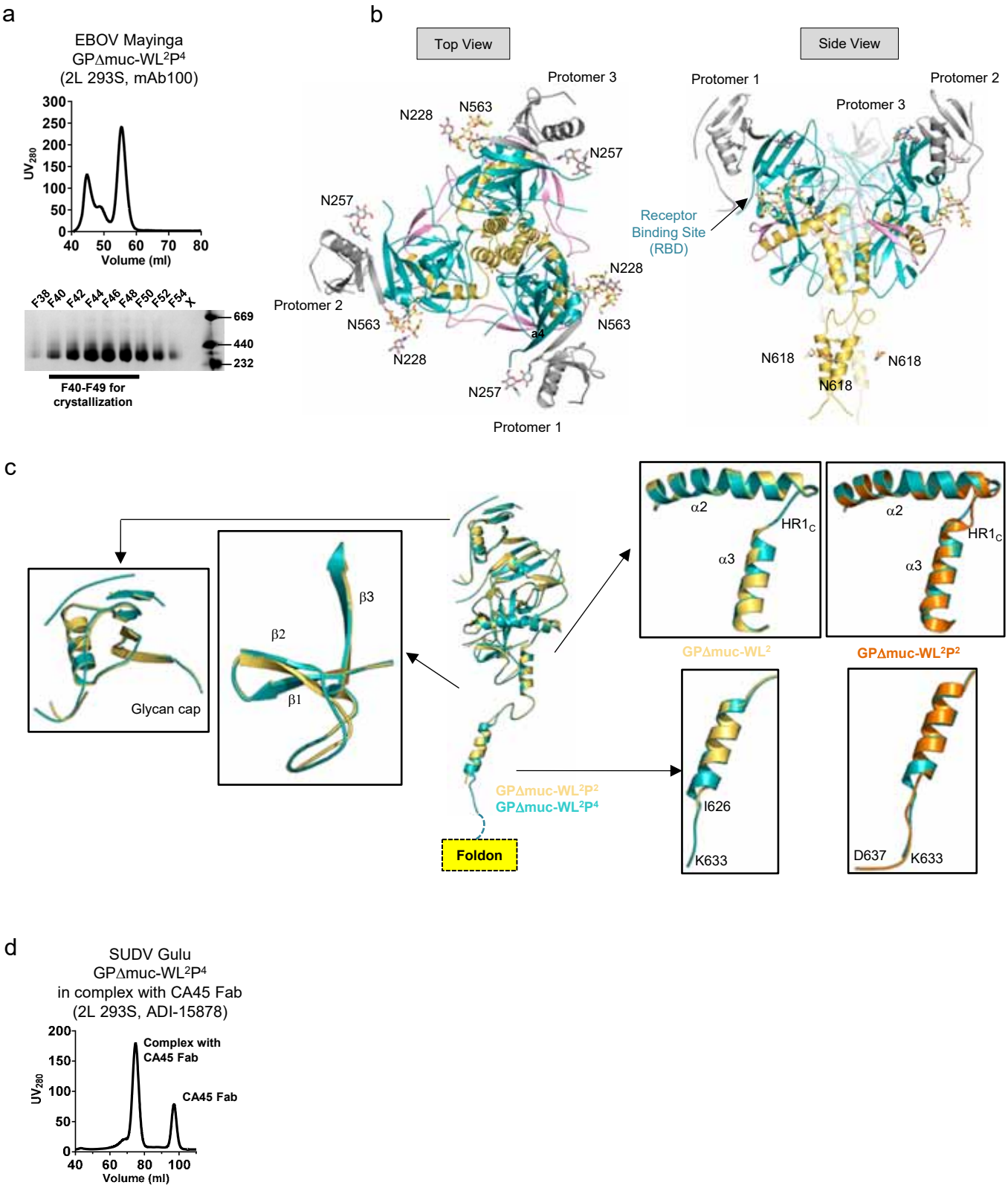
a
EBOV Mayinga
GPΔmuc-WL2P4
(2L 293S, mAb100)
UV280
Volume (ml)
F38 F40 F42 F44 F46 F48 F50 F52 F54 X
669
440
232
F40-F49 for crystallization
b
Top View
Side View
Protomer 3
Protomer 1
Protomer 2
N228
N563
N257
Receptor Binding Site (RBD)
α4
N618
c
Glycan cap
β1
β2
β3
α2
α3
HR1C
GPΔmuc-WL2
GPΔmuc-WL2P2
GPΔmuc-WL2P4
Foldon
I626
K633
D637
d
SUDV Gulu
GPΔmuc-WL2P4
in complex with CA45 Fab
(2L 293S, ADI-15878)
Complex with CA45 Fab
CA45 Fab

Fig. S2

e

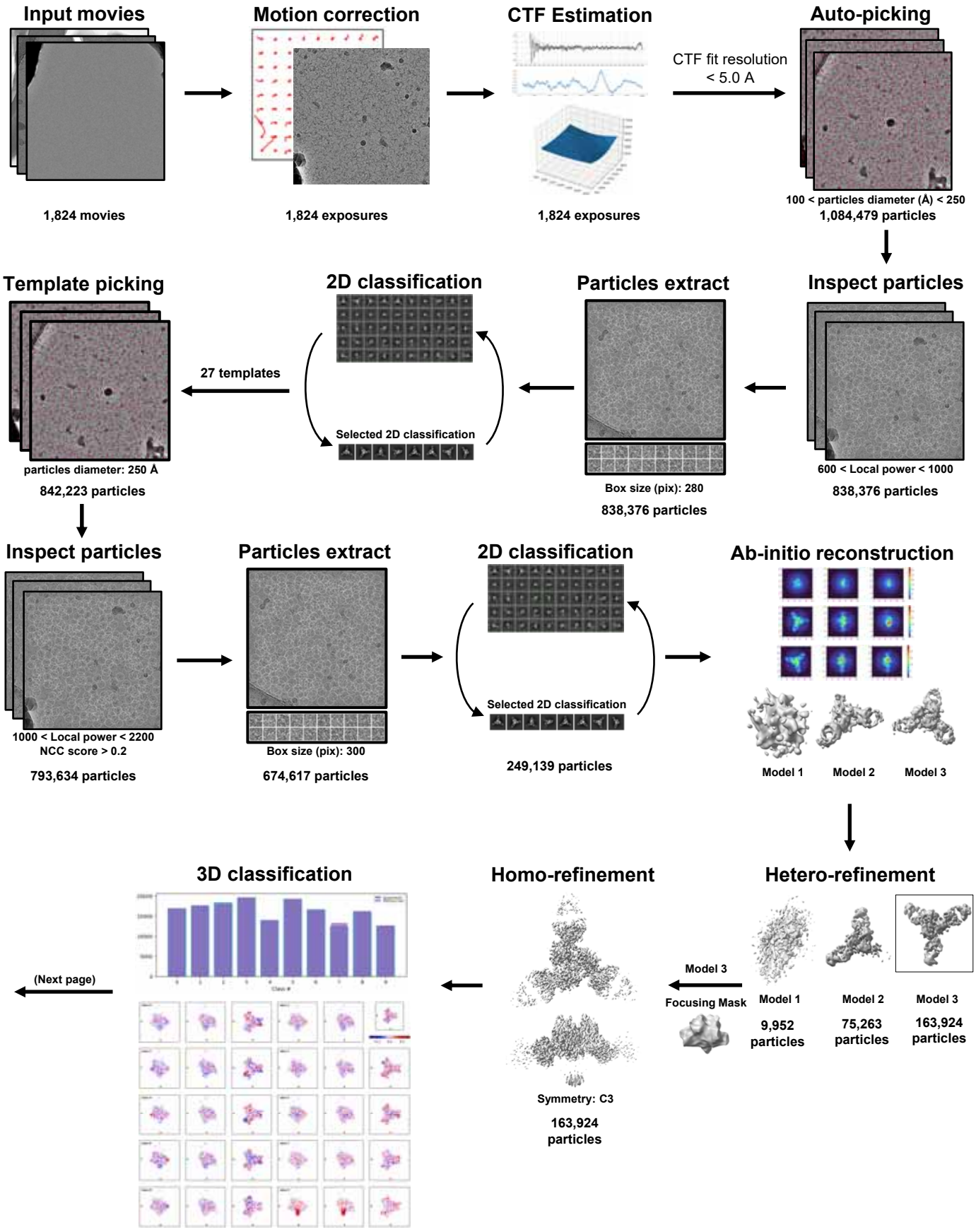
Input movies
1,824 movies
Motion correction
1,824 exposures
CTF Estimation
1,824 exposures
CTF fit resolution
< 5.0 A
Auto-picking
100 < particles diameter (Å) < 250
1,084,479 particles
Inspect particles
600 < Local power < 1000
838,376 particles
Particles extract
Box size (pix): 280
838,376 particles
2D classification
Selected 2D classification
27 templates
Template picking
particles diameter: 250 Å
842,223 particles
Inspect particles
1000 < Local power < 2200
NCC score > 0.2
793,634 particles
Particles extract
Box size (pix): 300
674,617 particles
2D classification
Selected 2D classification
249,139 particles
Ab-initio reconstruction
Model 1
Model 2
Model 3
Hetero-refinement
Model 1
9,952 particles
Model 2
75,263 particles
Model 3
163,924 particles
Model 3
Focusing Mask
Homo-refinement
Symmetry: C3
163,924 particles
3D classification
(Next page)

Fig. S2

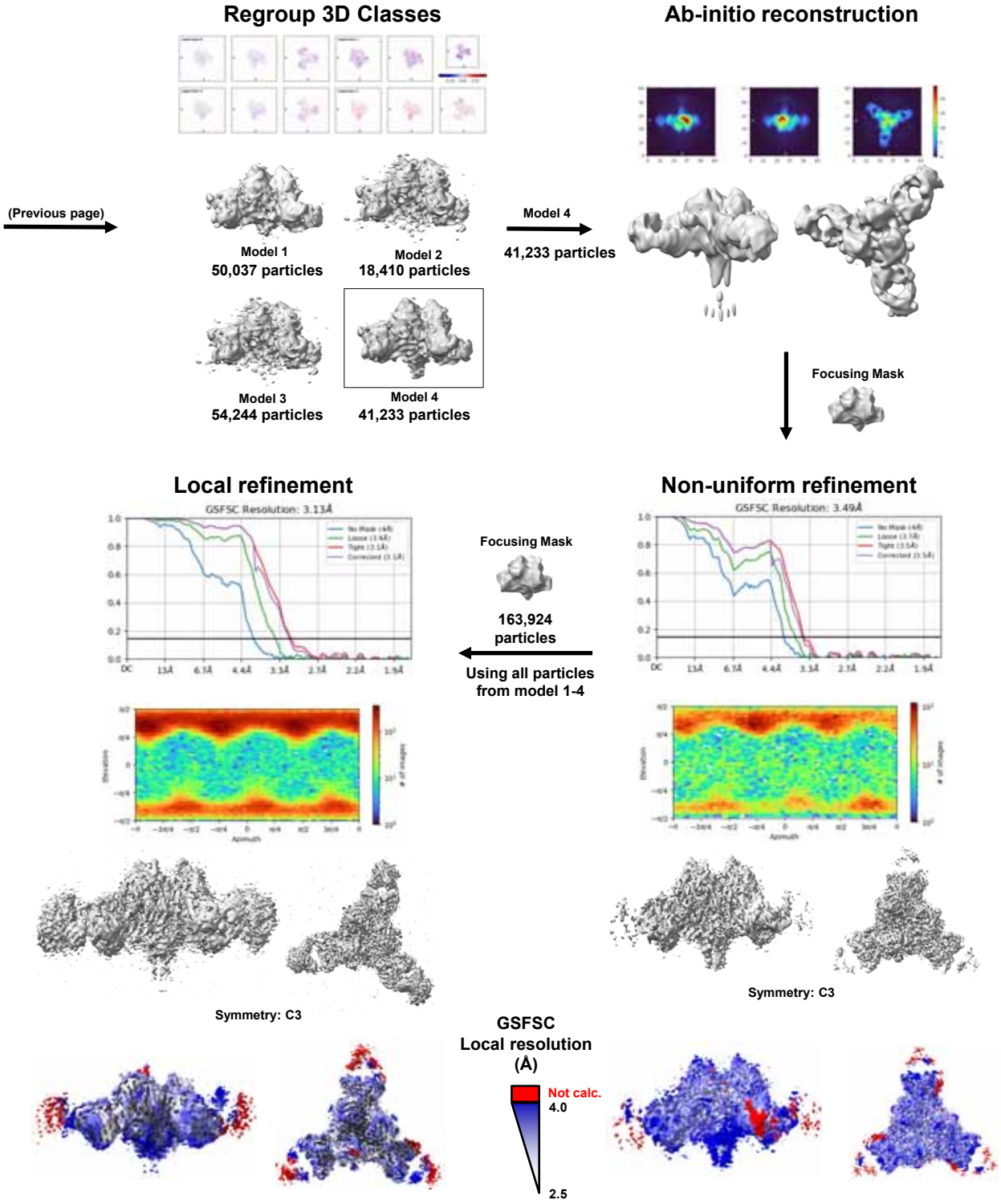
Regroup 3D Classes
Ab-initio reconstruction
(Previous page)
Model 1
50,037 particles
Model 2
18,410 particles
Model 3
54,244 particles
Model 4
41,233 particles
Model 4
41,233 particles
Focusing Mask
Local refinement
Non-uniform refinement
GSFSC Resolution: 3.13Å
GSFSC Resolution: 3.49Å
Focusing Mask
163,924
particles
Using all particles
from model 1-4
Symmetry: C3
Symmetry: C3
GSFSC
Local resolution
(Å)
Not calc.
4.0
2.5

f

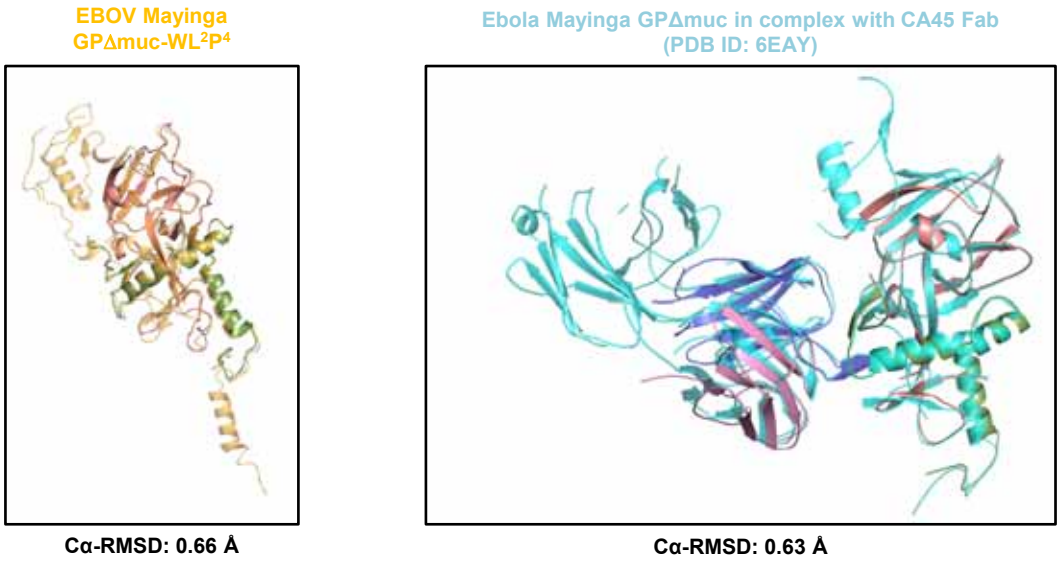

g

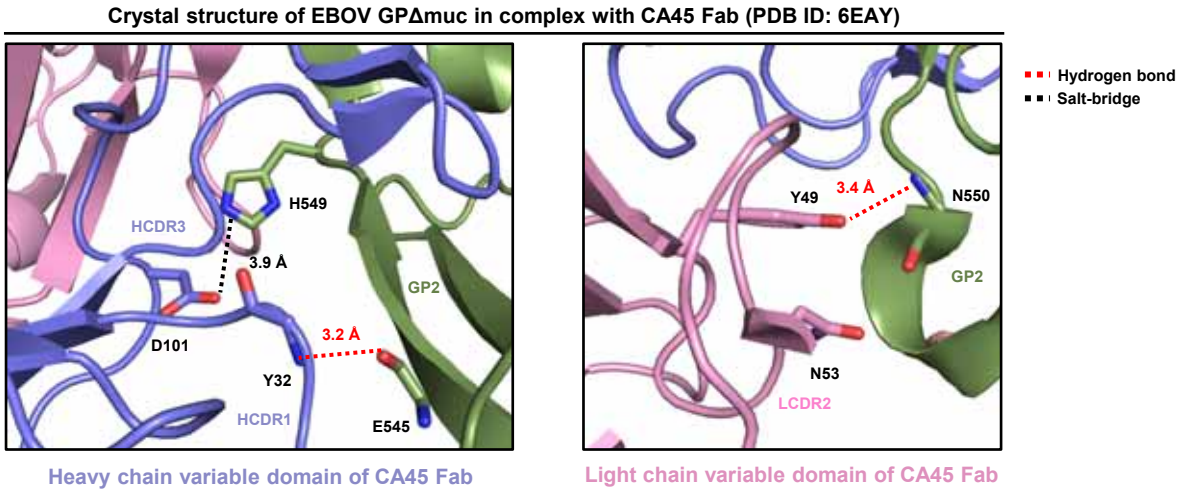

Fig. S2. Structural analysis for EBOV GPΔmuc-WL^{2}P^4 trimer and CA45 Fab-bound SUDV GPΔmuc-WL^{2}P^4 trimer. (**a**) SEC profile of EBOV GPΔmuc-WL^{2}P^4 trimer expressed in 2L HEK293S cells and BN-PAGE of ADI-15878/SEC-purified EBOV GPΔmuc-WL^{2}P^4 trimer. Fractions F40 to F49 were used for crystallization screening. The SEC profile was generated from a HiLoad Superdex 200 16/600 PG column (Cytiva). (**b**) Ribbon representation of EBOV GPΔmuc-WL^{2}P^4 trimer structure (Left: top view; Right: side view). The structure is colored as follows: glycan cap (gray), RBS (cyan), GP2 (yellow), and IFL (pink). *N*-linked glycans at N228, N257, N563, and N618 are shown as color-coded (by atom type) sticks. (**c**) Structural comparison of GPΔmuc-WL^{2}P^4 and previously reported GPΔmuc-WL^2 and GPΔmuc-WL^{2}P^2 trimers. The ribbon models of three GPΔmuc trimers containing WL^{2}P^4, WL^2, and WL^{2}P^2 mutations are shown in cyan, gold, and orange, respectively. Regions that are critical to the GP structure and exhibit appreciable differences in structure are superposed and shown as enlarged insects. (**d**) SEC profile of ADI-15878/SEC-purified SUDV GPΔmuc-WL^{2}P^4 trimer expressed in 2L HEK293S cells and complexed with ADI-15878 Fab. The SEC profile was generated from a Superose 6 10/300 increase column. (**e**) Schematic representation of image processing, 2D classification, and 3D reconstruction of cryo-EM data obtained for SUDV GPΔmuc-WL^{2}P^4 trimer in complex with ADI-15878 Fab using CryoSPARC. (**f**) Left: cryo-EM structure of SUDV GPΔmuc-WL^{2}P^4 superposed with the crystal structure of EBOV GPΔmuc-WL^{2}P^4 for comparison at the monomer level. The Cα root mean square deviation (Cα-RMSD) is 0.66 Å for 154 matching Cα atoms. Right: cryo-EM structure of SUDV GPΔmuc-WL^{2}P^4 in complex with ADI-15878 Fab superposed with the previously reported crystal structure of EBOV GPΔmuc in complex with CA45 Fab (PDB ID: 6EAY). Cα-RMSD is 0.63 Å for 149 matching Cα atoms. (**g**) Structural details illustrated for the GP-CA45 interface in the crystal structure of EBOV GPΔmuc in complex with CA45 Fab (PDB ID: 6EAY). Hydrogen bonds are shown in red dashed line and salt bridge shown in black dashed line with distances labeled.

Fig. S3

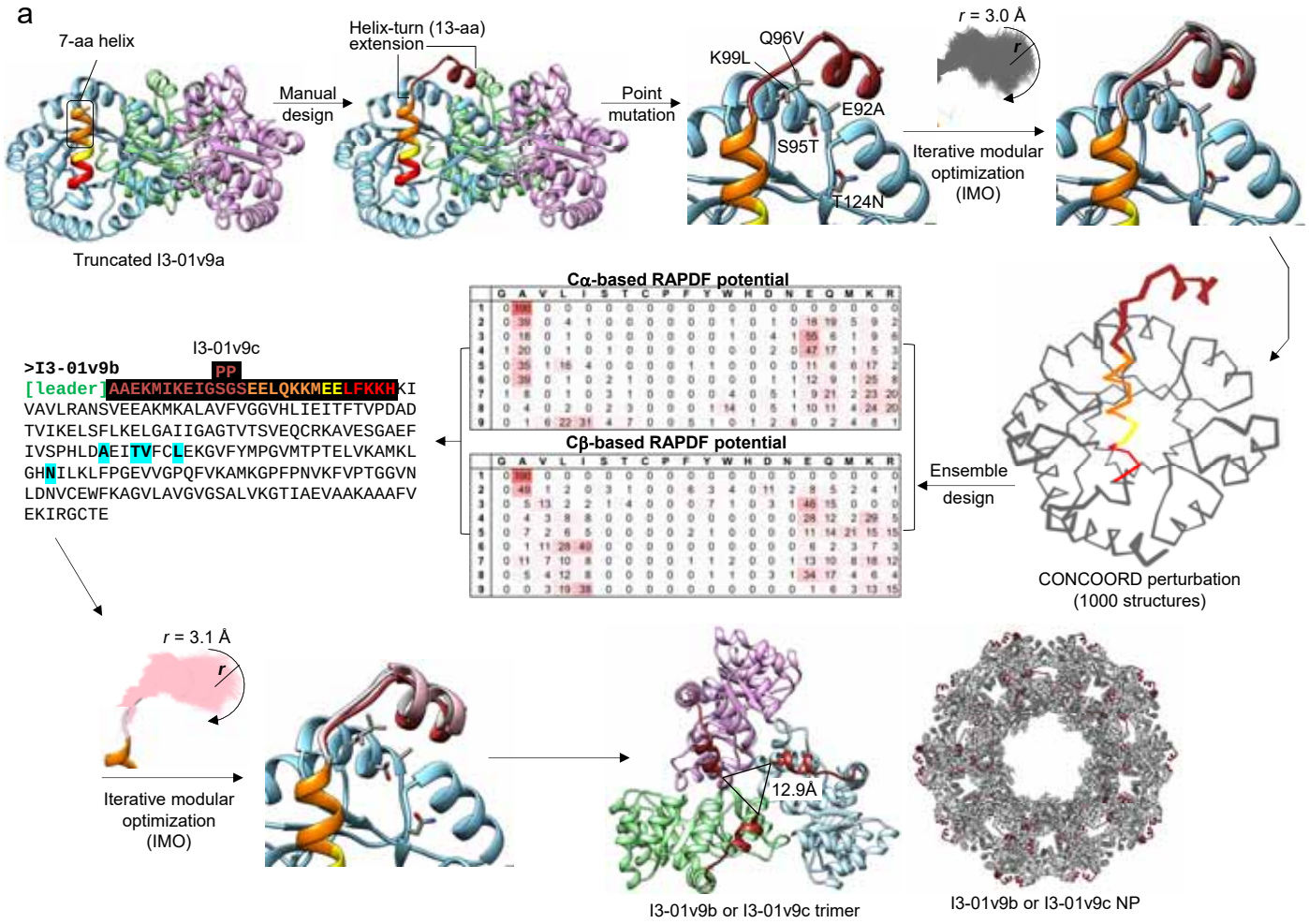
a
7-aa helix
Truncated I3-01v9a
Manual design
Helix-turn (13-aa) extension
Point mutation
Q96V
K99L
E92A
S95T
T124N
r = 3.0 Å
r
Iterative modular optimization (IMO)
Cα-based RAPDF potential
Cβ-based RAPDF potential
Ensemble design
CONCOORD perturbation (1000 structures)
I3-01v9c
>I3-01v9b
PP
[leader]AAEKMIKEIGSGSEELQKKMEELFKKHKI
VAVLRANSVEEAKMKALAVFVGGVHLIEITFTVPDAD
TVIKELSFLKELGAIIGAGTVTSVEQCRKAVESGAEF
IVSPHLDAEITVFCLEKGVFYMPGVMTPTELVKAMKL
GHNILKLFPGEVVGPQFVKAMKGPFPNVKFVPTGGVN
LDNVCEWFKAGVLAVGVGSALVKGTIAEVAAKAAAFV
EKIRGCTE
r = 3.1 Å
r
Iterative modular optimization (IMO)
12.9Å
I3-01v9b or I3-01v9c trimer
I3-01v9b or I3-01v9c NP

b

>EBOV Mayinga GPΔmuc-WL²P⁴-I3-01v9b-T

MGVTGILQLPRDRFKRTSFFLWVIILFQRTFSIPLGVIHNSALQVSDVDKLVCRDKLSSTNQLRSVGLNLEGNGVATDVPSATKRWGFRSGVPPKVVNYEAGEWAENCYNLEI
KKPDGSECLPAAPDGIRGFPRCRYVHKVSGTGPCAGDFAFHKEGAFFLYDRLASTVIYRGTTFAEGVVAFLILPQAKKDFFSSHPLREPVNATEDPSSGYYSTTIRYQATGFG
TNETEYLFEVDNLTYVQLESRFTPQFLLQLNETIYTSGKRSNTTGKLIWKVNPEIDTTIGEWAFWETKKNLTRKIRSEELSFTVVSTHHQDTGEESASSGKLGLITNTIAGVA
GLITGGRRTRREAIVNAQPKCNPNLHYWTTQDEGAAIGLAWIPYFGPAAEGIYIEGLMHNQDGLICGLRQLANETTQALQLFLRATTEPRTFSILNRKAIDFLLQRWGGTCHI
LGPDCCIEPHDLTKNITDKIDQIIHDFVDKTLPDASGAEKMIKEIG**SG**SEELQKKMEELFKKHKIVAVLRANSVEEAKEKALAVFEGGVHLIEITFTVPDADTVIKELSFLKE
KGAIIGAGTVTSVEQCRKAVESGAEFIVSPHLDAEITVFCLEKGVFYMPGVMTPTELVKAMKLGHNILKLFPGEVVGPQFVKAMKGPFPNVKFVPTGGVNLDNVCEWFKAGVL
AVGVGSALVKGTPDEVREKAKAFVEKIRGCTE

>EBOV Mayinga GPΔmuc-WL²P⁴-I3-01v9c-T

MGVTGILQLPRDRFKRTSFFLWVIILFQRTFSIPLGVIHNSALQVSDVDKLVCRDKLSSTNQLRSVGLNLEGNGVATDVPSATKRWGFRSGVPPKVVNYEAGEWAENCYNLEI
KKPDGSECLPAAPDGIRGFPRCRYVHKVSGTGPCAGDFAFHKEGAFFLYDRLASTVIYRGTTFAEGVVAFLILPQAKKDFFSSHPLREPVNATEDPSSGYYSTTIRYQATGFG
TNETEYLFEVDNLTYVQLESRFTPQFLLQLNETIYTSGKRSNTTGKLIWKVNPEIDTTIGEWAFWETKKNLTRKIRSEELSFTVVSTHHQDTGEESASSGKLGLITNTIAGVA
GLITGGRRTRREAIVNAQPKCNPNLHYWTTQDEGAAIGLAWIPYFGPAAEGIYIEGLMHNQDGLICGLRQLANETTQALQLFLRATTEPRTFSILNRKAIDFLLQRWGGTCHI
LGPDCCIEPHDLTKNITDKIDQIIHDFVDKTLPDASGAEKMIKEIG**PP**SEELQKKMEELFKKHKIVAVLRANSVEEAKEKALAVFEGGVHLIEITFTVPDADTVIKELSFLKE
KGAIIGAGTVTSVEQCRKAVESGAEFIVSPHLDAEITVFCLEKGVFYMPGVMTPTELVKAMKLGHNILKLFPGEVVGPQFVKAMKGPFPNVKFVPTGGVNLDNVCEWFKAGVL
AVGVGSALVKGTPDEVREKAKAFVEKIRGCTE

c

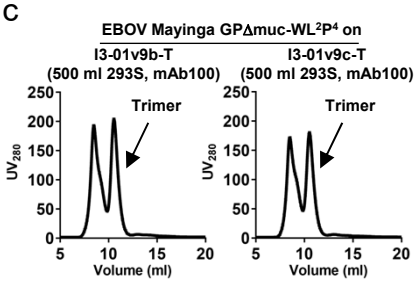

d

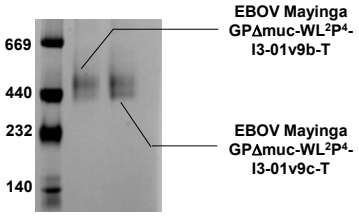

e

2D classes of EBOV Mayinga GPΔmuc-WL²P⁴-I3-01v9b-T

Selected 2D classification for modeling

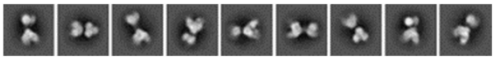

f

2D classes of EBOV Mayinga GPΔmuc-WL²P⁴-I3-01v9c-T

Selected 2D classification for modeling

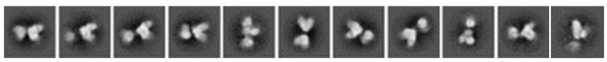

g

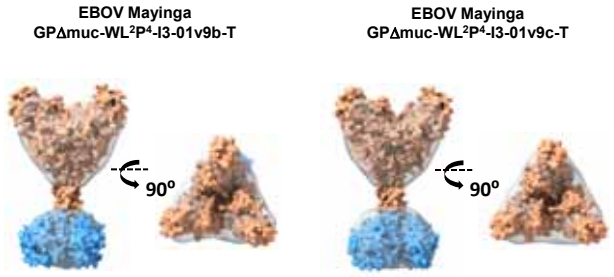

h

>EBOV Mayinga GPΔmuc-WL²P⁴-E2p-LD4-PADRE

MGVTGILQLPRDRFKRTSFFLWVIILFQRTFSIPLGVIHNSALQVSDVDKLVCRDKLSSTNQLRSVGLNLEGNGVATDVPSATKRWGFRSGVPPKVVNYEAGEWAENCYNLEI
KKPDGSECLPAAPDGIRGFPRCRYVHKVSGTGPCAGDFAFHKEGAFFLYDRLASTVIYRGTTFAEGVVAFLILPQAKKDFFSSHPLREPVNATEDPSSGYYSTTIRYQATGFG
TNETEYLFEVDNLTYVQLESRFTPQFLLQLNETIYTSGKRSNTTGKLIWKVNPEIDTTIGEWAFWETKKNLTRKIRSEELSFTVVSTHHQDTGEESASSGKLGLITNTIAGVA
GLITGGRRTRREAIVNAQPKCNPNLHYWTTQDEGAAIGLAWIPYFGPAAEGIYIEGLMHNQDGLICGLRQLANETTQALQLFLRATTEPRTFSILNRKAIDFLLQRWGGTCHI
LGPDCCIEPHDLTKNITDKIDQIIHDFVDKTLPDASGAAAKPATTEGEFPETREKMSGIRRAIAKAMVHSKHTAPHVTLMDEADVKLVAHRKKFKAIAAEKGIKLTFLPYVVK
ALVSALREYPVLNTAIDDETEEIIQKHYYNIGIAADTDRGLLVPVIKHADRKPIFALAQEINELAEKARDGKLTPGEMKGASCTITNIGSAGGQWFTPVINHPEVAILGIGRI
AEKPIVRDGEIVAAPMLALSLSFDHRMIDGATAQKALNHIKRLLSDPELLLMGGGGSFSEEQKKALDLAFYFDRRLTPEWRRYLSQRLGLNEEQIERWFRRKEQQIGWSHPQF
EKGSAKFVAAWTLKAAA

>EBOV Mayinga GPΔmuc-WL²P⁴-I3-01v9b-LD7-PADRE

MGVTGILQLPRDRFKRTSFFLWVIILFQRTFSIPLGVIHNSALQVSDVDKLVCRDKLSSTNQLRSVGLNLEGNGVATDVPSATKRWGFRSGVPPKVVNYEAGEWAENCYNLEI
KKPDGSECLPAAPDGIRGFPRCRYVHKVSGTGPCAGDFAFHKEGAFFLYDRLASTVIYRGTTFAEGVVAFLILPQAKKDFFSSHPLREPVNATEDPSSGYYSTTIRYQATGFG
TNETEYLFEVDNLTYVQLESRFTPQFLLQLNETIYTSGKRSNTTGKLIWKVNPEIDTTIGEWAFWETKKNLTRKIRSEELSFTVVSTHHQDTGEESASSGKLGLITNTIAGVA
GLITGGRRTRREAIVNAQPKCNPNLHYWTTQDEGAAIGLAWIPYFGPAAEGIYIEGLMHNQDGLICGLRQLANETTQALQLFLRATTEPRTFSILNRKAIDFLLQRWGGTCHI
LGPDCCIEPHDLTKNITDKIDQIIHDFVDKTLPDASGAEKMIKEIGSGSEELQKKMEELFKKHKIVAVLRANSVEEAKMKALAVFVGGVHLIEITFTVPDADTVIKELSFLKE
LGAIIGAGTVTSVEQCRKAVESGAEFIVSPHLDAEITVFCLEKGVFYMPGVMTPTELVKAMKLGHNILKLFPGEVVGPQFVKAMKGPFPNVKFVPTGGVNLDNVCEWFKAGVL
AVGVGSALVKGTIAEVAAKAAAFVEKIRGCTEGGGGSSPAVDIGDRLDELEKALEALSAEDGHDDVGQRLESLLRRWNSRRADGSAKFVAAWTLKAAA

>SUDV Gulu GPΔmuc-WL²P⁴-E2p-LD4-PADRE

MGILPSPGMPALLSLVSLLSVLLMGCVAEMPLGVVTNSTLEVTEIDQLVCKDHLASTDQLKSVGLNLEGSGVSTDIPSATKRWGFRSGVPPKVVSYEAGEWAENCYNLEIKKP
DGSECLPPPPDGVRGFPRCRYVHKAQGTGPCPGDYAFHKDGAFFLYDRLASTVIYRGVNFAEGVIAFLILAKPKETFLQSPPIREAVNYTENTSSYYATSYLEYEIENFGAQH
STTLFKIDNNTFVRLDRPHTPQFLFQLNDTIHLHQQLSNTTGRLIWTLDANINADIGEWAFWENKKNLSEQLRGEELSFEALSLNETEDDDAASSSTSNGLITSTVTGILGSL
GLRKRSRRQTNTKATGKCNPNLHYWTAQEQHNAAGIAWIPYFGPGAEGIYTEGLMHNQNALVCGLRQLANETTQALQLFLRATTEPRTYTILNRKAIDFLLRRWGGTCRILGP
DCCIEPHDLTKNITDKINQIIHDFIDNPLPNASGAAAKPATTEGEFPETREKMSGIRRAIAKAMVHSKHTAPHVTLMDEADVTKLVAHRKKFKAIAAEKGIKLTFLPYVVKAL
VSALREYPVLNTAIDDETEEIIQKHYYNIGIAADTDRGLLVPVIKHADRKPIFALAQEINELAEKARDGKLTPGEMKGASCTITNIGSAGGQWFTPVINHPEVAILGIGRIAE
KPIVRDGEIVAAPMLALSLSFDHRMIDGATAQKALNHIKRLLSDPELLLMGGGGSFSEEQKKALDLAFYFDRRLTPEWRRYLSQRLGLNEEQIERWFRRKEQQIGWSHPQFEK
GSAKFVAAWTLKAAA

>SUDV Gulu GPΔmuc-WL²P⁴-I3-01v9b-LD7-PADRE

MGILPSPGMPALLSLVSLLSVLLMGCVAEMPLGVVTNSTLEVTEIDQLVCKDHLASTDQLKSVGLNLEGSGVSTDIPSATKRWGFRSGVPPKVVSYEAGEWAENCYNLEIKKP
DGSECLPPPPDGVRGFPRCRYVHKAQGTGPCPGDYAFHKDGAFFLYDRLASTVIYRGVNFAEGVIAFLILAKPKETFLQSPPIREAVNYTENTSSYYATSYLEYEIENFGAQH
STTLFKIDNNTFVRLDRPHTPQFLFQLNDTIHLHQQLSNTTGRLIWTLDANINADIGEWAFWENKKNLSEQLRGEELSFEALSLNETEDDDAASSSTSNGLITSTVTGILGSL
GLRKRSRRQTNTKATGKCNPNLHYWTAQEQHNAAGIAWIPYFGPGAEGIYTEGLMHNQNALVCGLRQLANETTQALQLFLRATTEPRTYTILNRKAIDFLLRRWGGTCRILGP
DCCIEPHDLTKNITDKINQIIHDFIDNPLPNASGAEKMIKEIGSGSEELQKKMEELFKKHKIVAVLRANSVEEAKMKALAVFVGGVHLIEITFTVPDADTVIKELSFLKELGA
IIGAGTVTSVEQCRKAVESGAEFIVSPHLDAEITVFCLEKGVFYMPGVMTPTELVKAMKLGHNILKLFPGEVVGPQFVKAMKGPFPNVKFVPTGGVNLDNVCEWFKAGVLAVG
VGSALVKGTIAEVAAKAAAFVEKIRGCTEGGGGSSPAVDIGDRLDELEKALEALSAEDGHDDVGQRLESLLRRWNSRRADGSAKFVAAWTLKAAA

>BDBV R4386L GPΔmuc-WL^{2}P^4-E2p-LD4-PADRE

MGILPSPGMPALLSLVSLLSVLLMGCVAEIPLGVVHNNTLQVSDIDKLVCRDKLSSTSQLKSVGLNLEGNGVATDVPTATKRWGFRAGVPPKVVNYEAGEWAENCYNLDIKKA
DGSECLPEAPEGVRGFPRCRYVHKVSGTGPCPEGYAFHKEGAFFLYDRLASTIIYRSTTFSEGVVAFLILPETKKDFFQSPPLHEPANMTTDPSSYYHTVTLNYVADNFGTNM
TNFLFQVDHLTYVQLEPRFTPQFLVQLNETIYTNGRRSNTTGTLIWKVNPTVDTGVGEWAFWENKKNFTKTLSSEELSVIFVPRAQDPGSNDISESTEPGPLTNTTRGAANLL
TGSRRTRREITLRTQAKCNPNLHYWTTQDEGAAIGLAWIPYFGPAAEGIYTEGIMHNQNGLICGLRQLANETTQALQLFLRATTEPRTFSILNRKAIDFLLQRWGGTCHILGP
DCCIEPHDLTKNITDKIDQIIHDFIDKPLPDASGAAAKPATTEGEFPETREKMSGIRRAIAKAMVHSKHTAPHVTLMDEADVTKLVAHRKKFKAIAAEKGIKLTFLPYVVKAL
VSALREYPVLNTAIDDETEEIIQKHYYNIGIAADTDRGLLVPVIKHADRKPIFALAQEINELAEKARDGKLTPGEMKGASCTITNIGSAGGQWFTPVINHPEVAILGIGRIAE
KPIVRDGEIVAAPMLALSLSFDHRMIDGATAQKALNHIKRLLSDPELLLMGGGGSFSEEQKKALDLAFYFDRRLTPEWRRYLSQRLGLNEEQIERWFRRKEQQIGWSHPQFEK
GSAKFVAAWTLKAAA

>BDBV R4386L GPΔmuc-WL^{2}P^4-I3-01v9b-LD7-PADRE

MGILPSPGMPALLSLVSLLSVLLMGCVAEIPLGVVHNNTLQVSDIDKLVCRDKLSSTSQLKSVGLNLEGNGVATDVPTATKRWGFRAGVPPKVVNYEAGEWAENCYNLDIKKA
DGSECLPEAPEGVRGFPRCRYVHKVSGTGPCPEGYAFHKEGAFFLYDRLASTIIYRSTTFSEGVVAFLILPETKKDFFQSPPLHEPANMTTDPSSYYHTVTLNYVADNFGTNM
TNFLFQVDHLTYVQLEPRFTPQFLVQLNETIYTNGRRSNTTGTLIWKVNPTVDTGVGEWAFWENKKNFTKTLSSEELSVIFVPRAQDPGSNDISESTEPGPLTNTTRGAANLL
TGSRRTRREITLRTQAKCNPNLHYWTTQDEGAAIGLAWIPYFGPAAEGIYTEGIMHNQNGLICGLRQLANETTQALQLFLRATTEPRTFSILNRKAIDFLLQRWGGTCHILGP
DCCIEPHDLTKNITDKIDQIIHDFIDKPLPDASGAEKMIKEIGSGSEELQKKMEELFKKHKIVAVLRANSVEEAKMKALAVFVGGVHLIEITFTVPDADTVIKELSFLKELGA
IIGAGTVTSVEQCRKAVESGAEFIVSPHLDAEITVFCLEKGVFYMPGVMTPTELVKAMKLGHNILKLFPGEVVGPQFVKAMKGPFPNVKFVPTGGVNLDNVCEWFKAGVLAVG
VGSALVKGTIAEVAAKAAAFVEKIRGCTEGGGGSSPAVDIGDRLDELEKALEALSAEDGHDDVGQRLESLLRRWNSRRADGSAKFVAAWTLKAAA

i

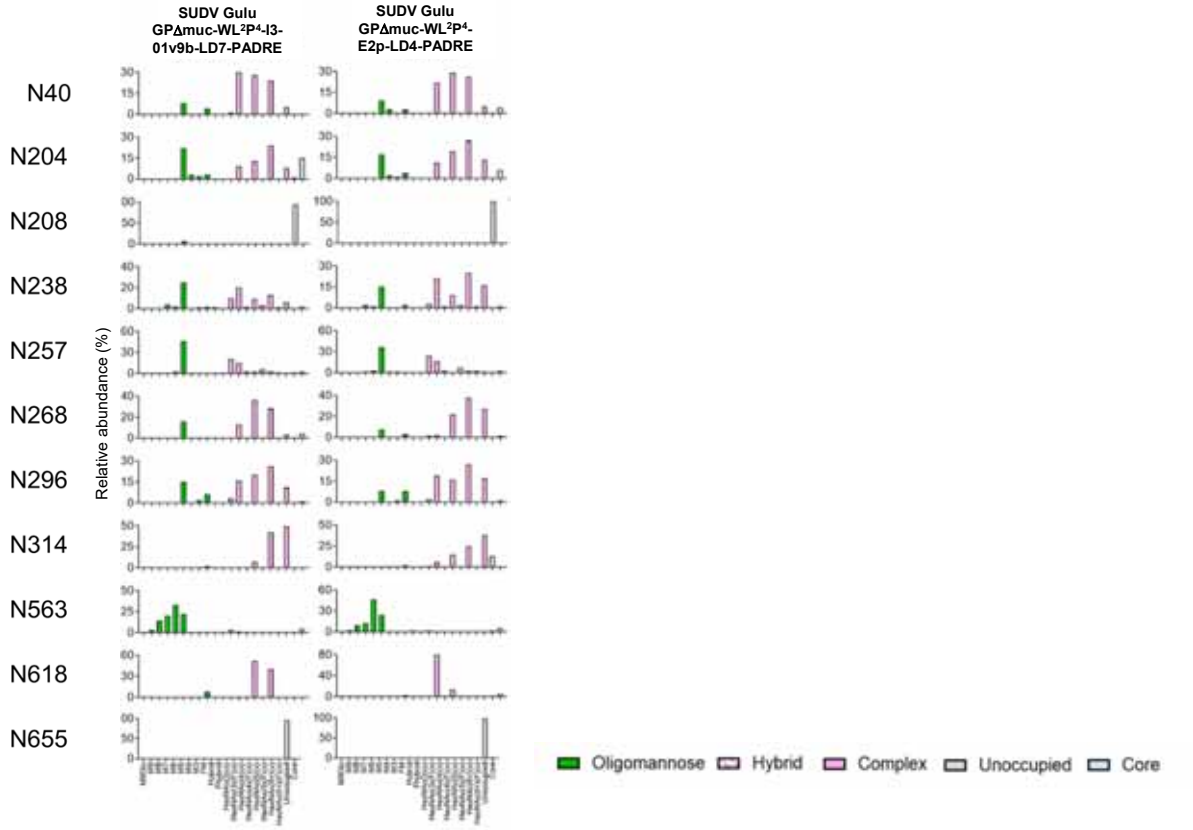

j **ELISA analysis of 6 rationally designed ebolavirus GPΔmuc SApNPs binding to 5 filovirus NAbs**

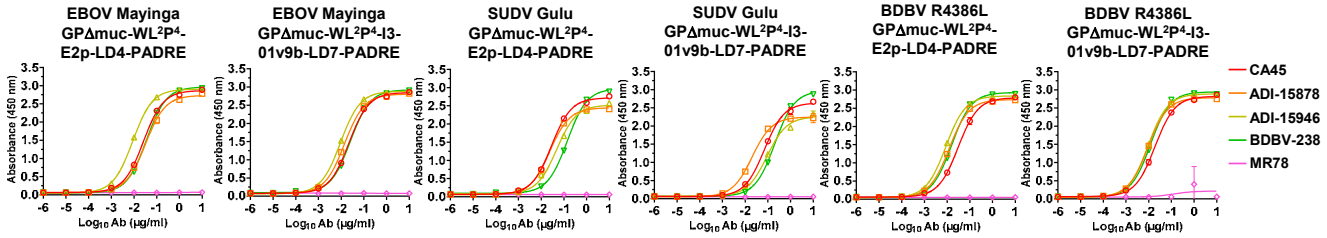

EBOV Mayinga GPΔmuc-WL^{2}P^4 E2p-LD4-PADRE									
CA45		ADI-15878		ADI-15946		BDBV-289		MR78	
EC50	STD	EC50	STD	EC50	STD	EC50	STD	EC50	STD
0.02593	0.00030	0.03197	0.00696	0.00879	0.00075	0.03550	0.00212	N.D.	N.D.

EBOV Mayinga GPΔmuc-WL^{2}P^4 I3-01v9b-LD7-PADRE									
CA45		ADI-15878		ADI-15946		BDBV-289		MR78	
EC50	STD	EC50	STD	EC50	STD	EC50	STD	EC50	STD
0.022141	0.000587	0.014095	0.000148	0.009384	0.000164	0.025555	0.00123	N.D.	N.D.

SUDV Gulu GPΔmuc-WL^{2}P^4 E2p-LD4-PADRE									
CA45		ADI-15878		ADI-15946		BDBV-289		MR78	
EC50	STD	EC50	STD	EC50	STD	EC50	STD	EC50	STD
0.02819	0.00070	0.02407	0.00284	0.04811	0.00204	0.14057	0.00849	N.D.	N.D.

SUDV Gulu GPΔmuc-WL^{2}P^4 I3-01v9b-LD7-PADRE									
CA45		ADI-15878		ADI-15946		BDBV-289		MR78	
EC50	STD	EC50	STD	EC50	STD	EC50	STD	EC50	STD
0.0699	0.0024	0.0204	0.0024	0.0910	0.0007	0.2017	0.0139	N.D.	N.D.

BDBV R4386L GPΔmuc-WL^{2}P^4 E2p-LD4-PADRE									
CA45		ADI-15878		ADI-15946		BDBV-289		MR78	
EC50	STD	EC50	STD	EC50	STD	EC50	STD	EC50	STD
0.0307	0.0035	0.0123	0.0002	0.0087	0.0004	0.0159	0.0002	N.D.	N.D.

BDBV R4386L GPΔmuc-WL^{2}P^4 I3-01v9b-LD7-PADRE									
CA45		ADI-15878		ADI-15946		BDBV-289		MR78	
EC50	STD	EC50	STD	EC50	STD	EC50	STD	EC50	STD
0.0191	0.0014	0.0093	0.0005	0.0095	0.0005	0.0120	0.0003	N.D.	N.D.

k **BLI analysis of 6 rationally designed ebolavirus GPΔmuc SApNPs binding to 5 filovirus NAbs**

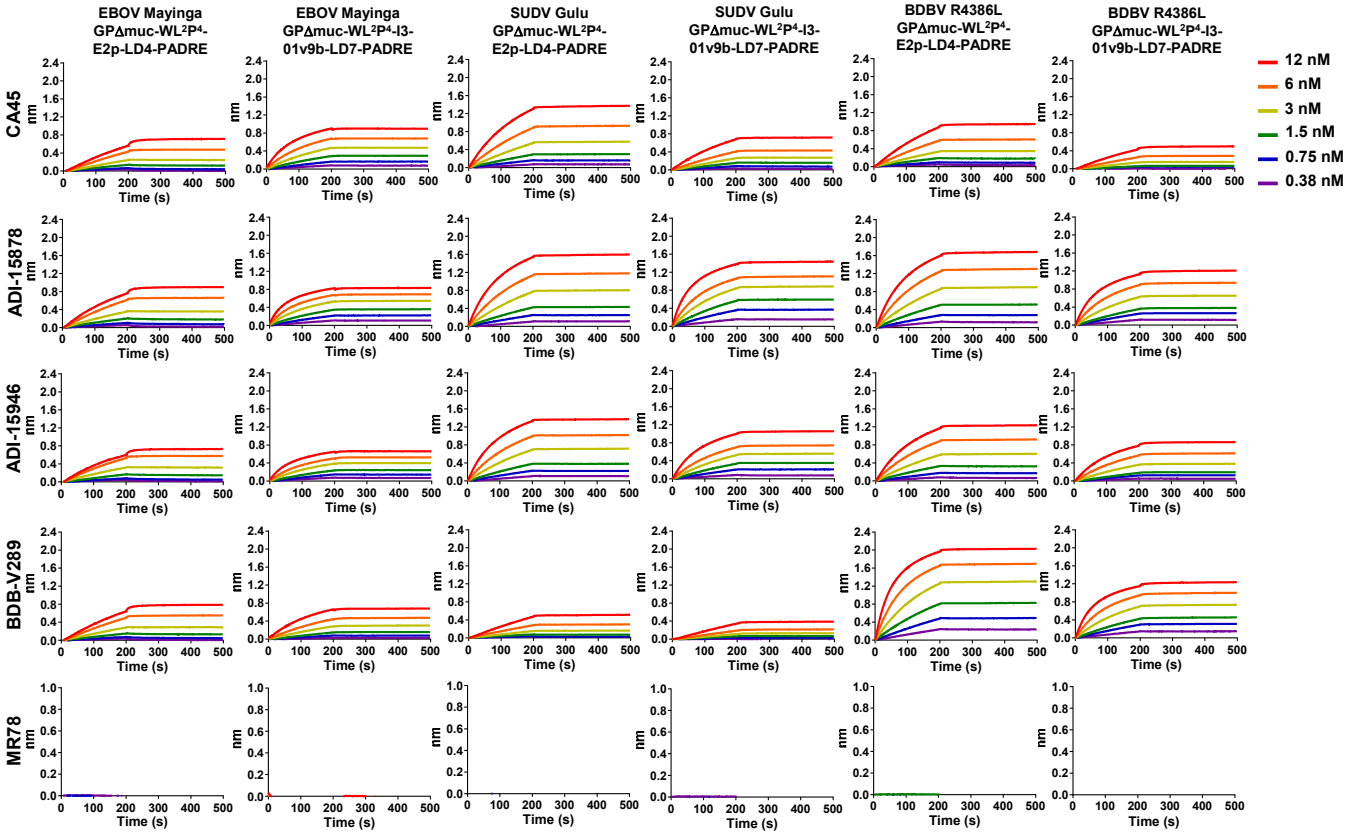

***K_D* values for 6 redesigned Filo-virus GP NP binding to 5 representative antibodies (nM) [a]**

	CA45	ADI-15878	ADI-15946	BDBV-289	MR78
EBOV Mayinga GPΔmuc-WL^{2}P^4-E2p-LD4-PADRE	<1.0E-3	<1.0E-3	<1.0E-3	<1.0E-3	— [b]
EBOV Mayinga GPΔmuc-WL^{2}P^4-I3-01v9b-LD7-PADRE	<1.0E-3	<1.0E-3	<1.0E-3	<1.0E-3	— [b]
SUDV Gulu GPΔmuc-WL^{2}P^4-E2p-LD4-PADRE	<1.0E-3	<1.0E-3	<1.0E-3	<1.0E-3	— [b]
SUDV Gulu GPΔmuc-WL^{2}P^4-I3-01v9b-LD7-PADRE	<1.0E-3	<1.0E-3	<1.0E-3	<1.0E-3	— [b]
BDBV R4386L GPΔmuc-WL^{2}P^4-E2p-LD4-PADRE	<1.0E-3	<1.0E-3	<1.0E-3	<1.0E-3	— [b]
BDBV R4386L GPΔmuc-WL^{2}P^4-I3-01v9b-LD7-PADRE	<1.0E-3	<1.0E-3	<1.0E-3	<1.0E-3	— [b]

[a] K_D values were derived from biolayer interferometry (BLI) using the binding equations describing a 1:1 interaction.
[b] "—" indicates cases where the peak signal value at the highest ebolavirus antigen concentration is 0.2 or lower.

Fig. S3. Rational design of I3-01v9b/c and in vitro characterization of ebolavirus GPΔmuc-presenting SApNPs. (**a**) Schematic representation of computational design of I3-01v9b/c. Top left: structural model of I3-01v9a with the 11-aa N-terminal helix truncated to 7 aa; Top middle left: a 13-aa helix-turn fragment (9-aa helix + 4-aa turn, all alanine) was fused to the 7-aa N-terminal helix of the truncated I3-01v9a in such a way the new 9-aa N-terminal helix from the fused fragment would pack within the groove of two helices that are part of the I3-01 core; Top middle right: four mutations, E92A, S95T, Q96V, and K99L, were introduced to the I3-01 core helices to remove their steric clashes with the new N-terminal helix; Top right: iterative modular optimization (IMO) of the helix-turn backbone, with a radius of 3.0 Å measured for the first amino acid at the N-terminus; Middle right: 1000 slightly perturbed backbone conformations generated by CONCOORD, a torsion-space sampling program; Middle middle: results from an ensemble-based protein design program used to predict the optimal sequence for the 9-aa N-terminal helix within the fragment using Cα and Cβ-based RAPDF potentials. The 4-aa turn was set to "GSGS"; Middle left: sequence of I3-01v9b designed by combining data from both RAPDF potentials, with the difference between I3-01v9b and I3-01v9c (the "PP" mutation) labeled on the sequence; Bottom left: further backbone relaxation using IMO with a minimum perturbation angle; Bottom right: a structural model of the trimeric I3-01v9b/c, termed I3-01v9b/c-T, in which the N-termini form a triangle of 12.9 Å, and a structural model of fully assembled I3-01v9b/c NP. (**b**) Amino acids sequences of EBOV GPΔmuc-WL2P4-I3-01v9b/c-T, which are EBOV Mayinga GPΔmuc-WL^{2}P^4 anchored to the trimeric I3-01v9b/c-T scaffolds. Signal peptide, GP, restriction site (AS), and I3-01v9b/c-T are highlighted in yellow, grey, green and pink, respectively. The double proline mutation in the N-terminus of I3-01v9c-T that differs from I3-01v9b-T is highlighted in red. (**c**) SEC profiles of EBOV GPΔmuc-WL2P4-I3-01v9b/c-T expressed in 500 ml HEK293S cells and purified using an ADI-15878 column. (**d**) BN-PAGE of ADI-15878/SEC-purified EBOV GPΔmuc-WL2P4-I3-01v9b/c-T. (**e**) and (**f**) Representative 2D classification images of ADI-15878/SEC-purified EBOV GPΔmuc-WL2P4-I3-01v9b/c-T trimers. (**g**) 3D reconstructions of ADI-15878/SEC-purified EBOV GPΔmuc-WL2P4-I3-01v9b/c-T trimers. Crystal structures of EBOV GPΔmuc-WL^{2}P^2 (PDB ID:7JPH) and the bacterial enzyme from which I3-01 was derived (PDB ID:1VLW) were fitted into the model and shown in orange and blue, respectively. (**h**) Amino acids sequences of EBOV, SUDV, and BDBV GPΔmuc-WL^{2}P^4-E2P-LD4-PADRE and -I3-01v9b-LD7-PADRE SApNP constructs. LD stands for locking domain (LD), which is fused to the C-terminus of the NP backbone and forms an inner layer to stabilize the NP shell from the inside. PADRE is a helper T-cell epitope and forms a hydrophobic core at the center of the assembled NP to further stabilize the NP structure and to induce a strong T-help response upon vaccination. (**i**) Compositional site-specific glycan analysis of SUDV GPΔmuc-WL^{2}P^4-E2P-LD4-PADRE and I3-01v9b-LD7-PADRE SApNPs, as in **Fig. S1c**. (**j**) ELISA analysis of EBOV, SUDV, and BDBV GPΔmuc-WL^{2}P^4-E2P-LD4-PADRE and I3-01v9b-LD7-PADRE SApNPs binding to 5 filovirus NAbs, as in **Fig. S1h**. (**k**) BLI analysis of EBOV, SUDV, and BDBV GPΔmuc-WL^{2}P^4-E2P-LD4-PADRE and I3-01v9b-LD7-PADRE SApNPs binding to 5 filovirus NAbs. A two-fold concentration gradient of antigen, starting at 12 nM, was used in a dilution series of six. K_D values derived from a 1:1 fitting model are summarized in a table.

Fig. S4

a

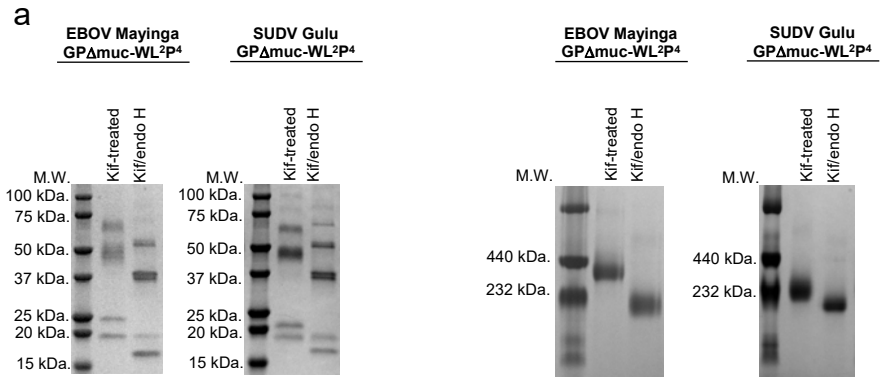

b **ELISA analysis of Kif-treated and glycan-trimmed EBOV and SUDV GPΔmuc-WL²P⁴ trimers binding to 5 filovirus NAbs**

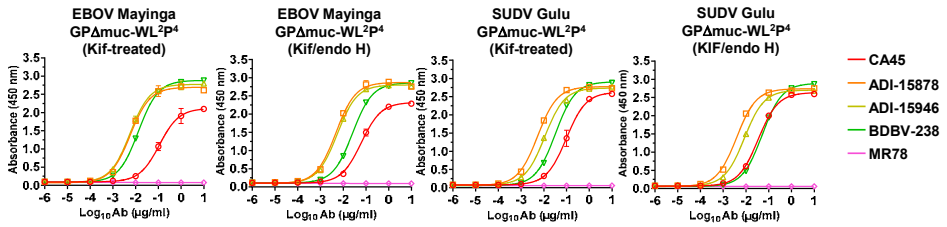

EBOV Mayinga GPΔmuc-WL²P⁴ (Kif-treated)									
CA45		ADI-15878		ADI-15946		BDBV-289		MR78	
EC50	STD	EC50	STD	EC50	STD	EC50	STD	EC50	STD
0.1110	0.0252	0.0058	0.0006	0.0057	0.0003	0.0133	0.0004	N.D.	N.D.

EBOV Mayinga GPΔmuc-WL²P⁴ (Kif/endo H)									
CA45		ADI-15878		ADI-15946		BDBV-289		MR78	
EC50	STD	EC50	STD	EC50	STD	EC50	STD	EC50	STD
0.0624	0.0093	0.0047	0.0001	0.0055	0.0006	0.0261	0.0021	N.D.	N.D.

SUDV Gulu GPΔmuc-WL²P⁴ (Kif-treated)									
CA45		ADI-15878		ADI-15946		BDBV-289		MR78	
EC50	STD	EC50	STD	EC50	STD	EC50	STD	EC50	STD
0.0973	0.0354	0.0054	0.0003	0.0111	0.0003	0.0325	0.0013	N.D.	N.D.

SUDV Gulu GPΔmuc-WL²P⁴ (Kif/endo H)									
CA45		ADI-15878		ADI-15946		BDBV-289		MR78	
EC50	STD	EC50	STD	EC50	STD	EC50	STD	EC50	STD
0.0347	0.0012	0.0039	0.0002	0.0086	0.0002	0.0518	0.0010	N.D.	N.D.

c **BLI analysis of Kif-treated and glycan-trimmed EBOV and SUDV GPΔmuc-WL²P⁴ trimers binding to 5 filovirus NAbs**

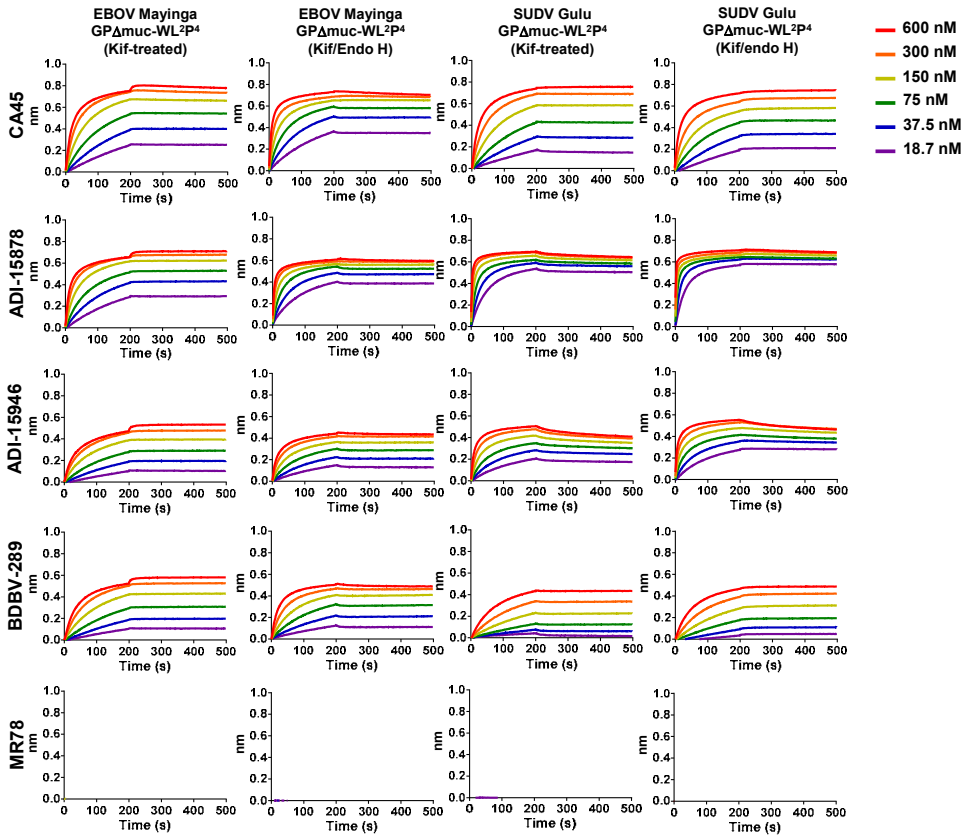

Fig. S4

K_D values for 4 glycan-modified ebolavirus GPΔmuc trimers binding to 5 filovirus NAbs (nM) [a]

	CA45	ADI-15878	ADI-15946	BDBV-289	MR78
EBOV Mayinga GPΔmuc-WL^{2}P^4 (Kif-treated)	<1.0E-3	<1.0E-3	<1.0E-3	<1.0E-3	— [b]
EBOV Mayinga GPΔmuc-WL^{2}P^4 (Kif/endo H)	<1.0E-3	<1.0E-3	<1.0E-3	<1.0E-3	— [b]
SUDV Gulu GPΔmuc-WL^{2}P^4 (Kif-treated)	<1.0E-3	2.99E-2	2.03	<1.0E-3	— [b]
SUDV Gulu GPΔmuc-WL^{2}P^4 (Kif/endo H)	<1.0E-3	<1.0E-3	9.52E-1	<1.0E-3	— [b]

[a] K_D values were derived from bio-layer interferometry (BLI) using the binding equations describing a 1:1 interaction.
[b] "—" indicates cases where the peak signal value at the highest ebolavirus antigen concentration is 0.2 or lower.

d

>SUDV Gulu GPΔmuc-WL^{2}P^4-PD-E2p-LD4-PADRE

MGILPSPGMPALLSLVSLLSVLLMGCVAEMPLGVVTNSTLEVTEIDQLVCKDHLASTDQLKSVGLNLEGSGVSTDIPSATKRWGFRSGVPPKVVSYEAGEWAENCYNLEIKKP
DGSECLPPPPDGVRGFPRCRYVHKAQGTGPCPGDYAFHKDGAFFLYDRLASTVIYRGVNFAEGVIAFLILAKPKETFLQSPPIREAVNYTENTSSYYATSYLEYEIENFGAQH
STTLFKIDNNTFVRLDRPHTPQFLFQLNDTIHLHQQLSNTTGRLIWTLDANINADIGEWAFWENKKNLSEQLRGEELSFEALSLNETEDDDAASSSTSNGLITSTVTGILGSL
GLRKRSRRQTNTKATGKCNPNLHYWTAQEQHNAAGIAWIPYFGPGAEGIYTEGLMHNQNALVCGLRQLANETTQALQLFLRATTEPRTYTILNRKAIDFLLRRWGGTCRILGP
DCCIEPHDLTKNITDKINQIIHDFIDNPLPDASGAAAKPATTEGEFPETREKMSGIRRAIAKAMVHSKHTAPHVTLMDEADVT
KLVAHRKKFKAIAAEKGIKLTFLPYVVKALVSALREYPVLNTAIDDETEEIIQKHYYNIGIAADTDRGLLVPVIKHADRKPIFALAQEINELAEKARDGKLTPGEMKGASCTI
TNIGSAGGQWFTPVINHPEVAILGIGRIAEKPIVRDGEIVAAPMLALSLSFDHRMIDGATAQKALNHIKRLLSDPELLLMGGGGSFSEEQKKALDLAFYFDRRLTPEWRRYLS
QRLGLNEEQIERWFRRKEQQIGWSHPQFEKGSAKFVAAWTLKAAA

>SUDV Gulu GPΔmuc-WL^{2}P^4-PD-I3-01v9b-LD7-PADRE

MGILPSPGMPALLSLVSLLSVLLMGCVAEMPLGVVTNSTLEVTEIDQLVCKDHLASTDQLKSVGLNLEGSGVSTDIPSATKRWGFRSGVPPKVVSYEAGEWAENCYNLEIKKP
DGSECLPPPPDGVRGFPRCRYVHKAQGTGPCPGDYAFHKDGAFFLYDRLASTVIYRGVNFAEGVIAFLILAKPKETFLQSPPIREAVNYTENTSSYYATSYLEYEIENFGAQH
STTLFKIDNNTFVRLDRPHTPQFLFQLNDTIHLHQQLSNTTGRLIWTLDANINADIGEWAFWENKKNLSEQLRGEELSFEALSLNETEDDDAASSSTSNGLITSTVTGILGSL
GLRKRSRRQTNTKATGKCNPNLHYWTAQEQHNAAGIAWIPYFGPGAEGIYTEGLMHNQNALVCGLRQLANETTQALQLFLRATTEPRTYTILNRKAIDFLLRRWGGTCRILGP
DCCIEPHDLTKNITDKINQIIHDFIDNPLPDASGAEKMIKEIGSGSEELQKKMEELFKKHKIVAVLRANSVEEAKEKALAVFEGGVHLIEITFTVPDADTVIKELSFLKEKGA
IIGAGTVTSVEQCRKAVESGAEFIVSPHLDAEITVFCLEKGVFYMPGVMTPTELVKAMKLGHNILKLFPGEVVGPQFVKAMKGPFPNVKFVPTGGVNLDNVCEWFKAGVLAVG
VGSALVKGTPDEVREKAKAFVEKIRGCTEGGGGSSPAVDIGDRLDELEKALEALSAEDGHDDVGQRLESLLRRWNSRRADGSAKFVAAWTLKAAA

e

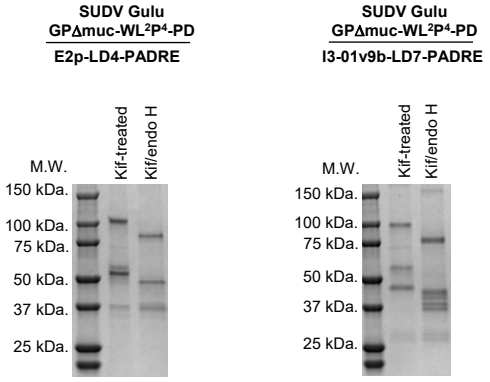

Fig. S4

f **Site-specific glycan profiles of wildtype and Kif-treated SUDV GPΔmuc-WL^{2}P^4-PD-presenting SApNPs**

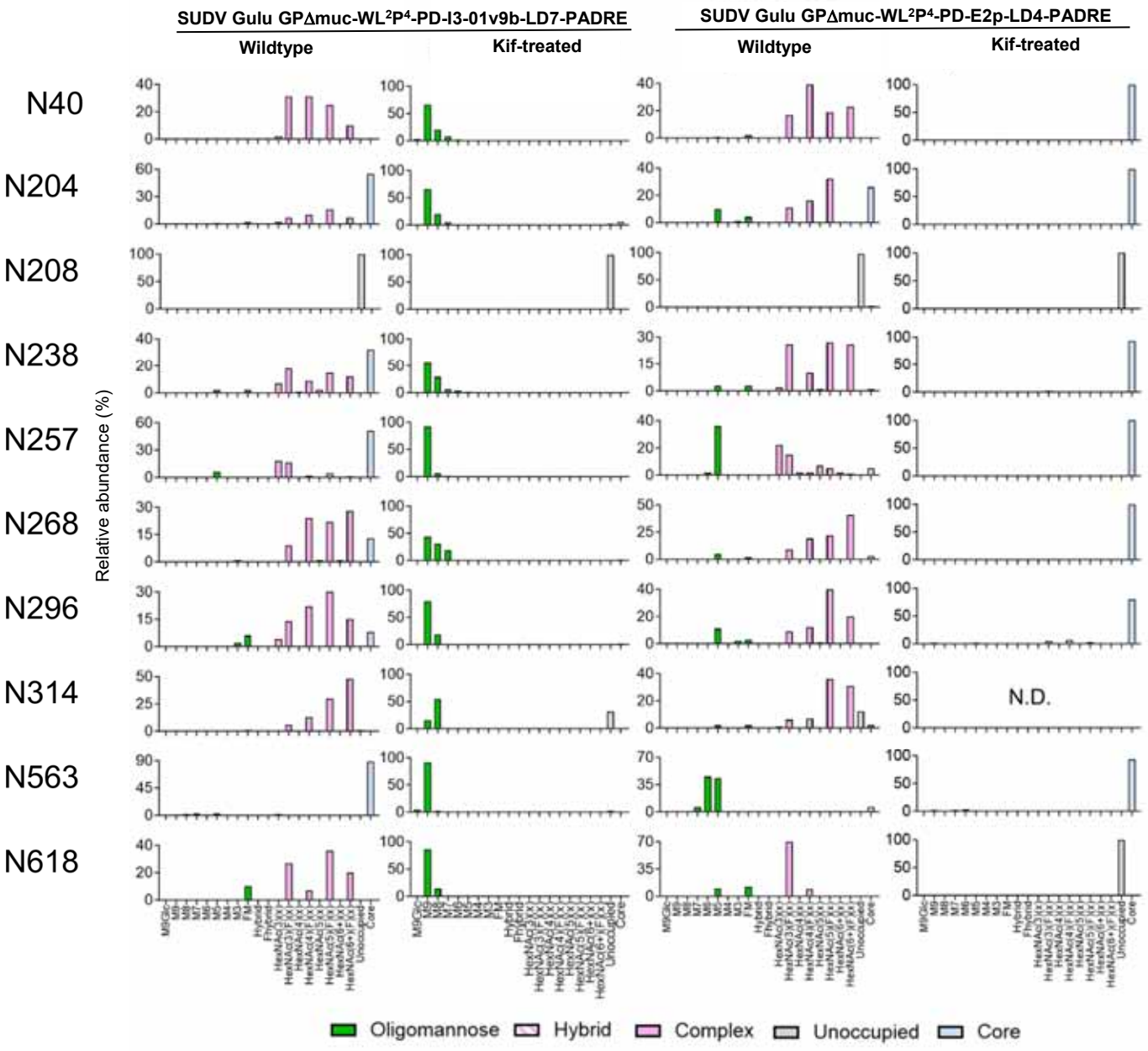

g

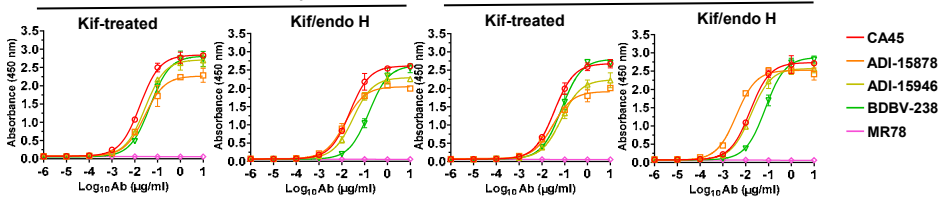

SUDV Gulu GPΔmuc-WL2P4-PD-E2p-LD4-PADRE (Kif-treated)									
CA45		ADI-15878		ADI-15946		BDBV-829		MR78	
EC50	STD	EC50	STD	EC50	STD	EC50	STD	EC50	STD
0.0168	0.0014	0.0277	0.0049	0.0283	0.0021	0.0462	0.0006	N.D.	N.D.

SUDV Gulu GPΔmuc-WL2P4-PD-E2p-LD4-PADRE (Kif/endo H)									
CA45		ADI-15878		ADI-15946		BDBV-829		MR78	
EC50	STD	EC50	STD	EC50	STD	EC50	STD	EC50	STD
0.0226	0.0048	0.0308	0.002	0.0312	0.0043	0.1550	0.0179	N.D.	N.D.

SUDV Gulu GPΔmuc-WL2P4-PD-I3-01v9b-LD7-PADRE (Kif-treated)									
CA45		ADI-15878		ADI-15946		BDBV-829		MR78	
EC50	STD	EC50	STD	EC50	STD	EC50	STD	EC50	STD
0.0348	0.0024	0.0254	0.0163	0.0708	0.0049	0.0718	0.0181	N.D.	N.D.

SUDV Gulu GPΔmuc-WL2P4-PD-I3-01v9b-LD7-PADRE (Kif/endo H)									
CA45		ADI-15878		ADI-15946		BDBV-829		MR78	
EC50	STD	EC50	STD	EC50	STD	EC50	STD	EC50	STD
0.0155	0.0023	0.0039	0.0004	0.0174	0.0011	0.0726	0.0083	N.D.	N.D.

h

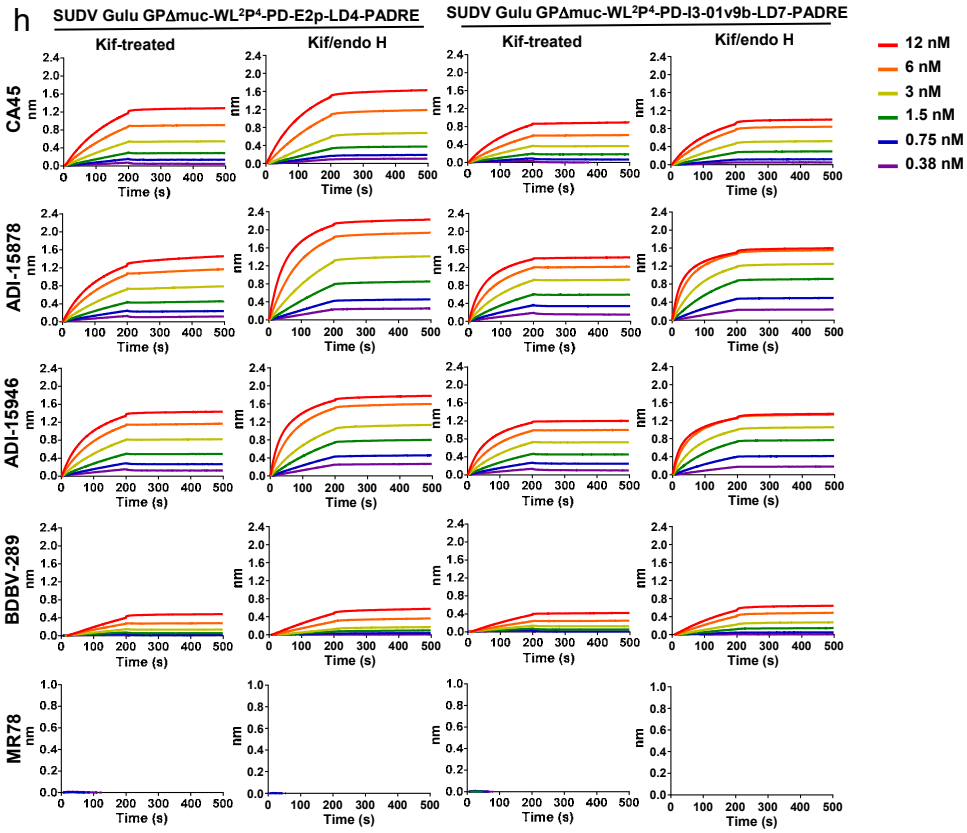

K_D values for 4 glycan-modified SUDVGPΔmuc-WL2P4-PD-presenting SApNPs binding to 5 filovirus NAbs (nM) [a]

	CA45	ADI-15878	ADI-15946	BDBV-289	MR78
SUDV Gulu GPΔmuc-WL2P4-PD-E2p-LD4-PADRE (Kif-treated)	<1.0E-3	<1.0E-3	<1.0E-3	<1.0E-3	— [b]
SUDV Gulu GPΔmuc-WL2P4-PD-E2p-LD4-PADRE (Kif/endo H)	<1.0E-3	<1.0E-3	<1.0E-3	<1.0E-3	— [b]
SUDV Gulu GPΔmuc-WL2P4-PD-I3-01v9b-LD7-PADRE (Kif-treated)	<1.0E-3	<1.0E-3	<1.0E-3	<1.0E-3	— [b]
SUDV Gulu GPΔmuc-WL2P4-PD-I3-01v9b-LD7-PADRE (Kif/endo H)	<1.0E-3	<1.0E-3	<1.0E-3	<1.0E-3	— [b]

[a] K_D values were derived from biolayer interferometry (BLI) using the binding equations describing a 1:1 interaction.
[b] "—" indicates cases where the peak signal value at the highest SUDV antigen concentration is 0.2 or lower.

Fig. S4. In vitro characterization for glycan-modified ebolavirus GPΔmuc trimers and SApNPs. (**a**) SDS-PAGE and BN-PAGE of glycan-modified EBOV Mayinga and SUDV Gulu GPΔmuc-WL^{2}P^4 trimers. They were either expressed in the presence of kifunensine (Kif-treated) to obtain oligomannose-only glycans or further trimmed using endo H (Kif/endo H) to obtain a mono-layer of GlcNAc stumps. (**b**) ELISA analysis of glycan-modified EBOV Mayinga and SUDV Gulu GPΔmuc-WL^{2}P^4 trimers binding to 5 filovirus NAbs in the IgG form, as in **Fig S1h.** (**c**) BLI analysis of glycan-modified EBOV Mayinga and SUDV Gulu GPΔmuc-WL^{2}P^4 trimers binding to 5 filovirus NAbs in the IgG form, as in **Fig S1i**. (**d**) Construct sequences for "multilayered" E2p (E2p-LD4-PADRE) and I3-01v9b (I3-0v9b-LD7-PADRE) SApNPs presenting 20 copies of a SUDV Gulu GPΔmuc-WL^{2}P^4-PD trimer, which contains a mutation (N637D) at the C-terminus to remove a potential glycosylation site between GP and NP. (**e**) SDS-PAGE of 3 glycan-modified SApNPs corresponding to EBOV Mayinga GPΔmuc-WL^{2}P^4 on the E2p-LD4-PADRE scaffold and SUDV Gulu GPΔmuc-WL^{2}P^4-PD on the E2p-LD4-PADRE and I3-01v9b-LD7-PADRE scaffolds. (**f**) Compositional site-specific glycan analysis of SUDV GPΔmuc-WL^{2}P^4-PD-presenting E2p and I3-01v9b SApNPs, as in **Fig. S1c**. (**g**) ELISA analysis of glycan-modified SUDV Gulu GPΔmuc-WL2P4-PD-presenting E2P and I3-01v9b SApNPs binding to 5 filovirus NAbs in the IgG form, as in **Fig S1h**. (**h**) BLI analysis of glycan-modified SUDV Gulu GPΔmuc-WL^{2}P^4-PD-presenting E2P and I3-01v9b SApNPs binding to 5 filovirus NAbs in the IgG form, as in **Fig S3k**.

Fig. S5

a

>RAVV GPΔTM-foldon-His$_6$

MGVTGILQLPRDRFKRTSFFLWVIILFQRTFSIKTLPVLEIASNSQPQDVDSVCSGTLQKTEDVHLMGFTLSGQKVADSPLEASKRWAFRTGVPPKNVEYTEGEEAKTCYNIS
VTDPSGKSLLLDPPSNIRDYPKCKTVHHIQGQNPHAQGIALHLWGAFFLYDRVASTTMYRGKVFTEGNIAAMIVNKTVHRMIFSRQGQGYRHMNLTSTNKYWTSSNETQRNDT
GCFGILQEYNSTNNQTCPPSLKPPSLPTVTPSIHSTNTQINTAK**SGT**MNPSSDDEDLMISGSGSGEQGPHTTLNVVTEQKQSSTILSTPSLHPSTSQHEQNSTNPSRHAVTEH
NGTDPTTQPATLLNNTNTTPTYNTLKYNLSTPSPPTRNITNNDTQRELAESEQTNAQLNTTLDPTENPTTGQDTNSTTNIIMTTSDITSKHPTNSSPDSSPTT**RPPI**YFRKKR
SIFWKEGDIFPFLDGLINTEIDFDPIPNTETIFDESPSFNTSTNEEQHTPPNISLTFSYFPDKNGDTAYSGENENDCDAELRIWSVQEDDLAAGLSWIPFFGPGIEGLYTAGL
IKNQNNLVCRLRRLANQTAKSLELLLRVTTEERTFSLINRHAIDFLLTRWGGTCKVLGPDCCIGIEDLSKNISEQIDKIRKDEQKEETGASGYIPEAPRDGQAYVRKDGEWVL
LSTFLGSHHHHHH

>RAVV GPΔmuc-foldon-His$_6$

MGVTGILQLPRDRFKRTSFFLWVIILFQRTFSIKTLPVLEIASNSQPQDVDSVCSGTLQKTEDVHLMGFTLSGQKVADSPLEASKRWAFRTGVPPKNVEYTEGEEAKTCYNIS
VTDPSGKSLLLDPPSNIRDYPKCKTVHHIQGQNPHAQGIALHLWGAFFLYDRVASTTMYRGKVFTEGNIAAMIVNKTVHRMIFSRQGQGYRHMNLTSTNKYWTSSNETQRNDT
GCFGILQEYNSTNNQTCPPSLKPPSLPTVTPSIHSTNTQINTAK**SGTRPP**IYFRKKRSIFWKEGDIFPFLDGLINTEIDFDPIPNTETIFDESPSFNTSTNEEQHTPPNISLT
FSYFPDKNGDTAYSGENENDCDAELRIWSVQEDDLAAGLSWIPFFGPGIEGLYTAGLIKNQNNLVCRLRRLANQTAKSLELLLRVTTEERTFSLINRHAIDFLLTRWGGTCKV
LGPDCCIGIEDLSKNISEQIDKIRKDEQKEETGASGYIPEAPRDGQAYVRKDGEWVLLSTFLGSHHHHHH

>RAVV GPΔmuc-P^2-foldon-His$_6$

MGVTGILQLPRDRFKRTSFFLWVIILFQRTFSIKTLPVLEIASNSQPQDVDSVCSGTLQKTEDVHLMGFTLSGQKVADSPLEASKRWAFRTGVPPKNVEYTEGEEAKTCYNIS
VTDPSGKSLLLDPPSNIRDYPKCKTVHHIQGQNPHAQGIALHLWGAFFLYDRVASTTMYRGKVFTEGNIAAMIVNKTVHRMIFSRQGQGYRHMNLTSTNKYWTSSNETQRNDT
GCFGILQEYNSTNNQTCPPSLKPPSLPTVTPSIHSTNTQINTAK**SGTRPP**IYFRKKRSIFWKEGDIFPFLDGLINTEIDFDPIPNTETIFDESPSFNTSTNEEQHTPPNISLT
FSYFPDKNGDTAYSGENENDCDAELRIWSVQEDDLAAGLSWIPFFGPGIEGLYTAGLIKNQNNLVCRLRRLANQTAKSLELLLRVTPEERTFSLINRHAIDFLLTRWGGTCKV
LGPDCCIGIEDLSKNISEQIDKIRKDEQKEETGASGYIPEAPRDGQAYVRKDGEWVLLSTFLGSHHHHHH

>RAVV GPΔmuc-P^4-foldon-His$_6$

MGVTGILQLPRDRFKRTSFFLWVIILFQRTFSIKTLPVLEIASNSQPQDVDSVCSGTLQKTEDVHLMGFTLSGQKVADSPLEASKRWAFRTGVPPKNVEYTEGEEAKTCYNIS
VTDPSGKSLLLDPPSNIRDYPKCKTVHHIQGQNPHAQGIALHLWGAFFLYDRVASTTMYRGKVFTEGNIAAMIVNKTVHRMIFSRQGQGYRHMNLTSTNKYWTSSNETQRNDT
GCFGILQEYNSTNNQTCPPSLKPPSLPTVTPSIHSTNTQINTAK**SGTRPP**IYFRKKRSIFWKEGDIFPFLDGLINTEIDFDPIPNTETIFDESPSFNTSTNEEQHTPPNISLT
FSYFPDKNGDTAYSGENENDCDAELRIWSVQEDDLAAGLSWIPFFGPGIEGLYTAGLIKNQNNLVCRLRRLANQTAKSLELLLRVTTEPRTFSLINRHAIDFLLTRWGGTCKV
LGPDCCIGIEDLSKNISEQIDKIRKDEQKEETGASGYIPEAPRDGQAYVRKDGEWVLLSTFLGSHHHHHH

>RAVV GPΔmuc-P^{2}CT-foldon-His$_6$

MGVTGILQLPRDRFKRTSFFLWVIILFQRTFSIKTLPVLEIASNSQPQDVDSVCSGTLQKTEDVHLMGFTLSGQKVADSPLEASKRWAFRTGVPPKNVEYTEGEEAKTCYNIS
VTDPSGKSLLLDPPSNIRDYPKCKTVHHIQGQNPHAQGIALHLWGAFFLYDRVASTTMYRGKVFTEGNIAAMIVNKTVHRMIFSRQGQGYRHMNLTSTNKYWTSSNETQRNDT
GCFGILQEYNSTNNQTCPPSLKPPSLPTVTPSIHSTNTQINTAK**SGTRPP**IYFRKKRSIFWKEGDIFPFLDGLINTEIDFDPIPNTETIFDESPSFNTSTNEEQHTPPNISLT
FSYFPDKNGDTAYSGENENDCDAELRIWSVQEDDLAAGLSWIPFFGPGIEGLYTAGLIKNQNNLVCRLRRLANQTAKSLELLLRVTPEERTFSLINRHAIDFLLTRWGGTCKV
LGPDCCIGIEDLSKNISEQIDKIRKD**FV**KEETGASGYIPEAPRDGQAYVRKDGEWVLLSTFLGSHHHHHH

b

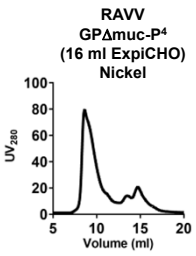

c

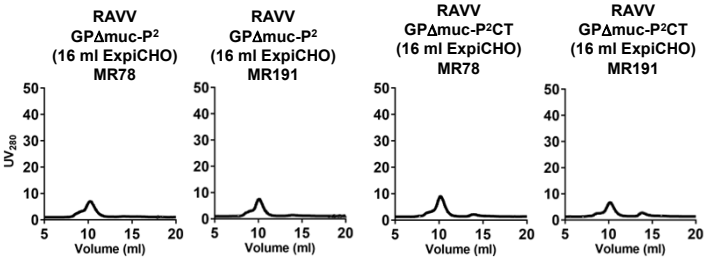

d

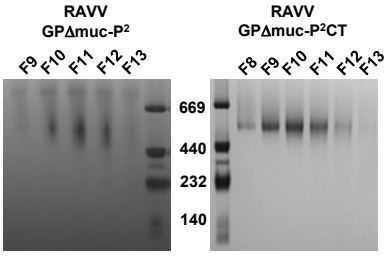

e

2D classes of RAVV GPΔmuc-P^{2}CT / MR78 Fab complex

Selected 2D classifications for 3D modeling

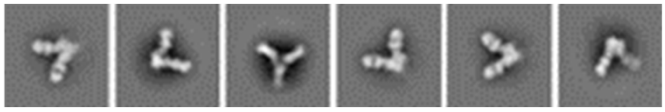

Fig. S5

f

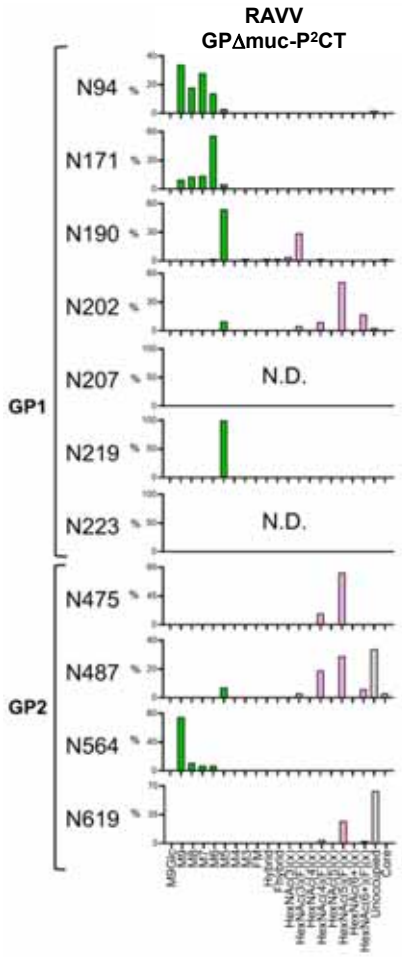

g

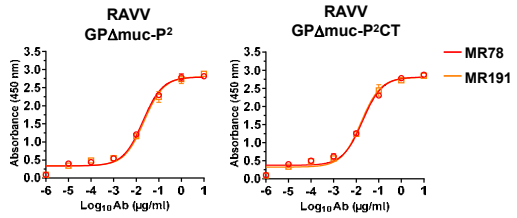

RAVV GPΔmuc-P²			
MR78		MR191	
EC50	STD	EC50	STD
0.0191	0.0007	0.0166	0.0007

RAVV GPΔmuc-P²CT			
MR78		MR191	
EC50	STD	EC50	STD
0.0196	0.0015	0.0230	0.0046

h

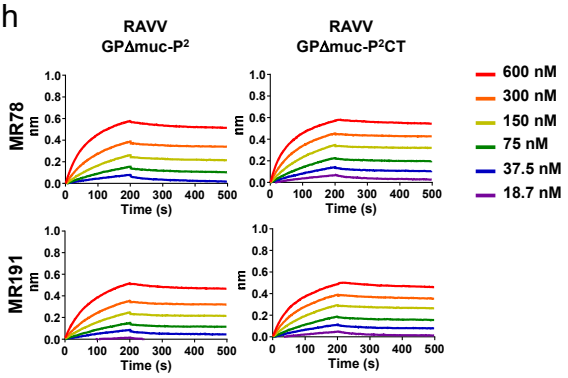

***K_D* values for two RAVV GPΔmuc trimers binding to 2 marburgvirus NAbs in the IgG form (nM)** [a]

	MR78	MR191
RAVV GPΔmuc-P²	6.61E-1	1.55E+1
RAVV GPΔmuc-P²CT	8.06	1.30E+1

[a] K_D values were derived from bio-layer interferometry (BLI) using the binding equations describing a 1:1 interaction.
[b] "—" indicates cases where the peak signal value at the highest RSV-F concentration is 0.2 or lower.

i

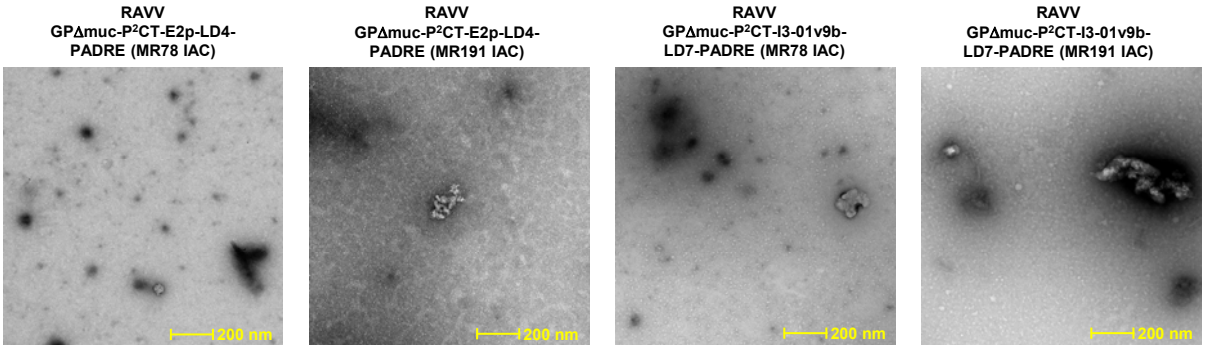

Fig. S5. Construct design and in vitro characterization of RAVV GP trimers. (**a**) Constructs sequences of RAVV GP designs. Signal peptide, mucin-like domain (MLD), HR1c, restriction site (AS), foldon, linker (GS), and His_6-tag are highlighted in yellow, gray, cyan, green, orange, light pink, and light sea green, respectively. The proline mutation on HR1c and CT are shown in red. Notably, the foldon motif, GS linker, and His_6 tag are present in all RAVV GP trimers tested in this study and will not be included in the construct names to avoid redundancy. (**b**) SEC profile of Nickel-purified RAVV GPΔmuc-P^4 expressed in 16 ml ExpiCHO cells. (**c**) SECs profile of NAb MR78/MR191-purified RAVV GPΔmuc-P^2 and GPΔmuc-P^2CT each expressed in 16 ml ExpiCHO cells. (**d**) BN-PAGE of the trimer fractions from the SEC analysis of Nickel-purified RAVV GPΔmuc-P^2 and GPΔmuc-P^2CT. (**e**) Representative 2D classification images of the RAVV GPΔmuc-P^2CT trimer in complex with MR78 Fab. (**f**) Compositional site-specific glycan analysis for RAVV GPΔmuc-P^2CT trimer, as in **Fig. S1c**. (**g**) ELISA analysis of RAVV GPΔmuc-P^2 and GPΔmuc-P^2CT trimers binding to NAbs MR78 and MR191 in the IgG form. Briefly, each well was coated with 0.1 μg of the appropriate antigen and IgG antibodies were diluted in a 10-fold dilution series from a starting concentration of 10 μg/ml for all antibodies. Error bars represent the difference between these duplicate values at each concentration tested for each sample. (**h**) BLI analysis of RAVV GPΔmuc-P^2 and GPΔmuc-P^2CT trimers binding to NAbs MR78 and MR191 in the IgG form, as in **Fig. S1i**. (i) nsEM analysis of RAVV GPΔmuc-P^2CT E2p and I3-01v9b constructs following ExpiCHO expression and MR78- or MR191-based IAC purification. Scale bar is labeled in yellow on the EM micrographs. No discernible protein NPs are shown in any of the EM micrographs.

Fig. S6

a

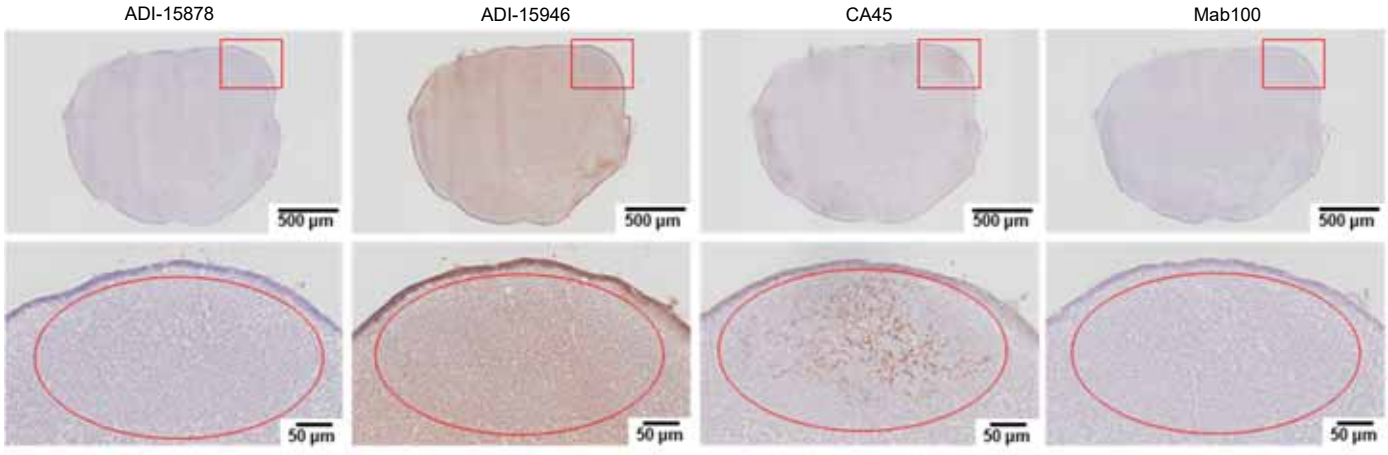

b Single-dose - 2 hours

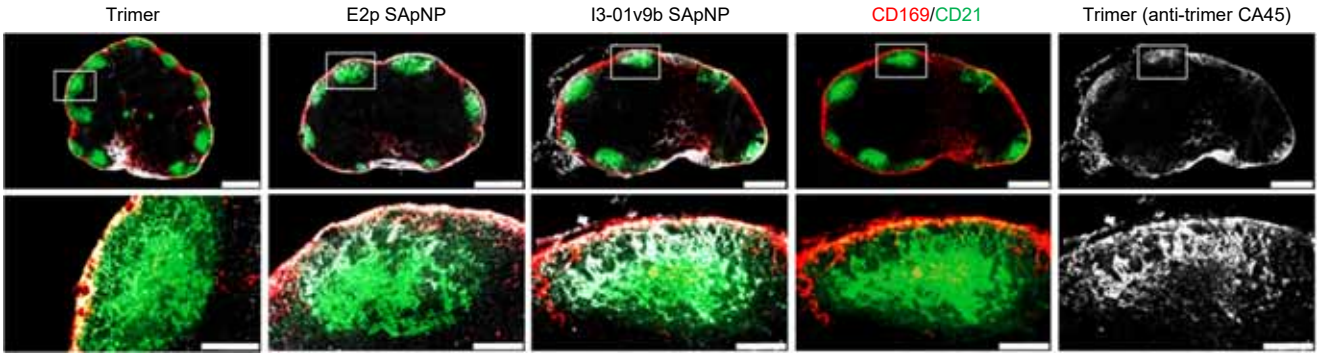

c Single-dose - 12 hours

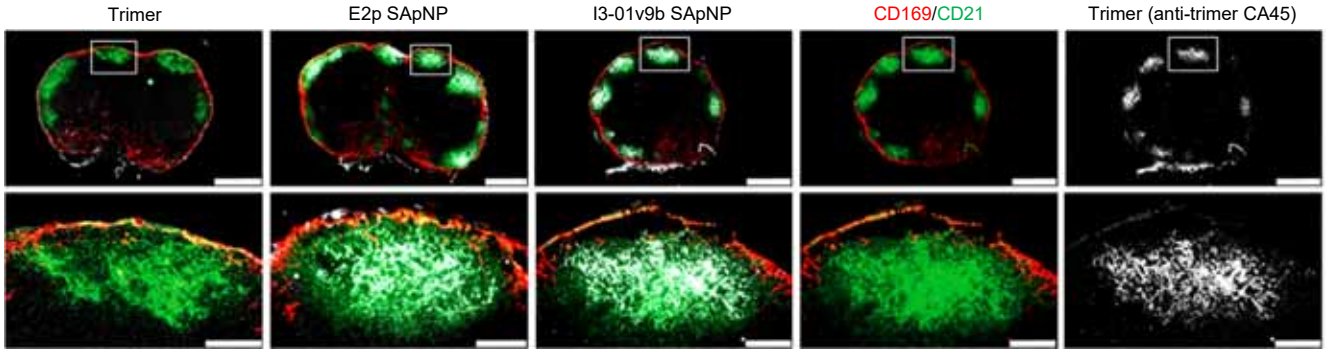

d Single-dose - 1 week

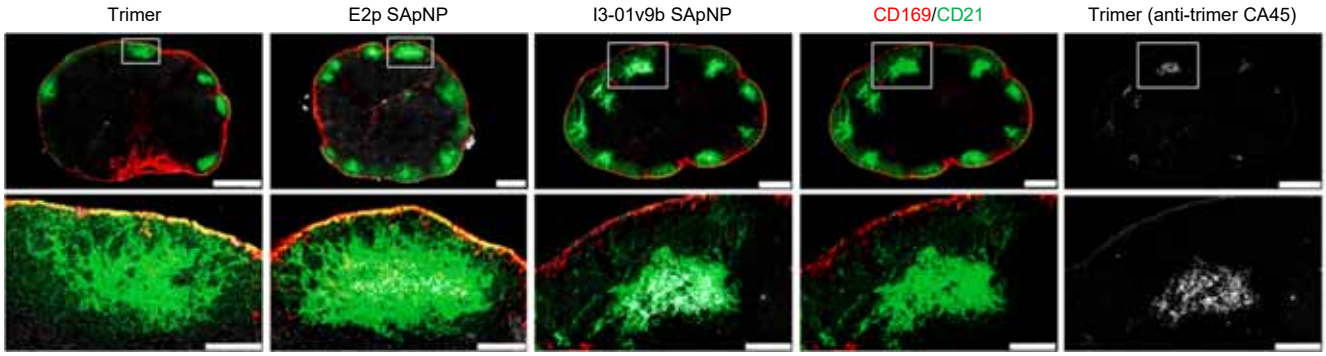

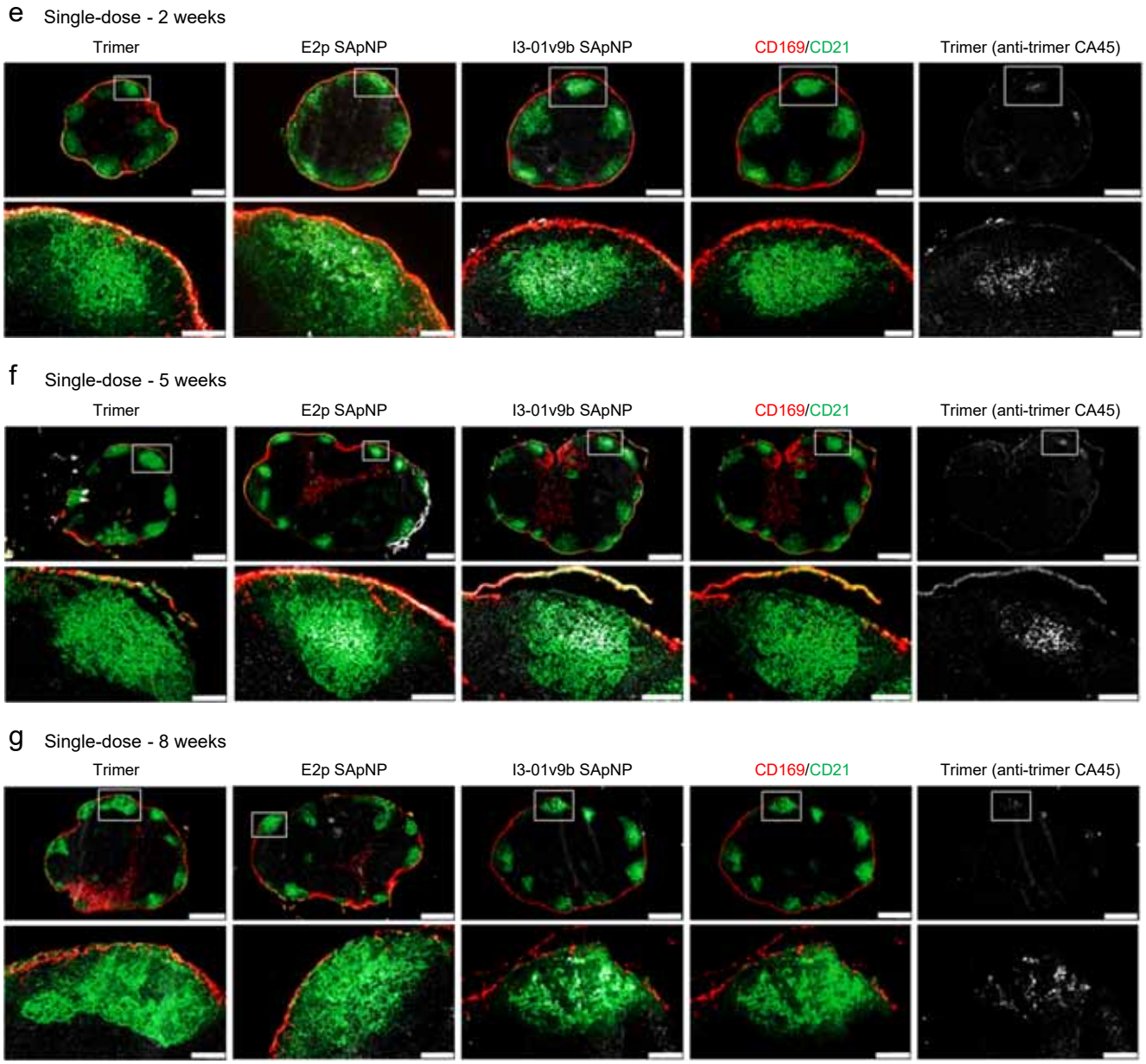

Fig. S6. Immunohistological images of SUDV GPΔmuc trimer and SApNPs in lymph nodes. (**a**) Immunostaining images of lymph node tissues from SUDV GPΔmuc trimer-presenting SApNP injected mice stained with four anti-trimer antibody ADI-15878, ADI-15946, CA45 and Mab100. SUDV vaccine constructs of GPΔmuc trimer and GPΔmuc trimer-presenting E2p and I3-01v9b SApNPs interaction with FDC networks in lymph node follicles (**b**) 2 hours, (**c**) 12 hours, (**d**) 1 week, (**e**) 2 weeks, (**f**) 5 weeks, and (**g**) 8 weeks after a single-dose injection (10 μg per injection, totaling 40 μg per mouse). Immunofluorescent images are pseudo color coded (CD21+, green; CD169+, red; anti-trimer CA45, white). Scale bars = 500 and 100 μm for complete lymph node and enlarged image of a follicle, respectively. Data were collected from more than 10 lymph node follicles (n = 3-5 mice/group).

Fig. S7

a E2p SApNPs (yellow arrow) are aligned on FDC dendrites after 2 hours of injection

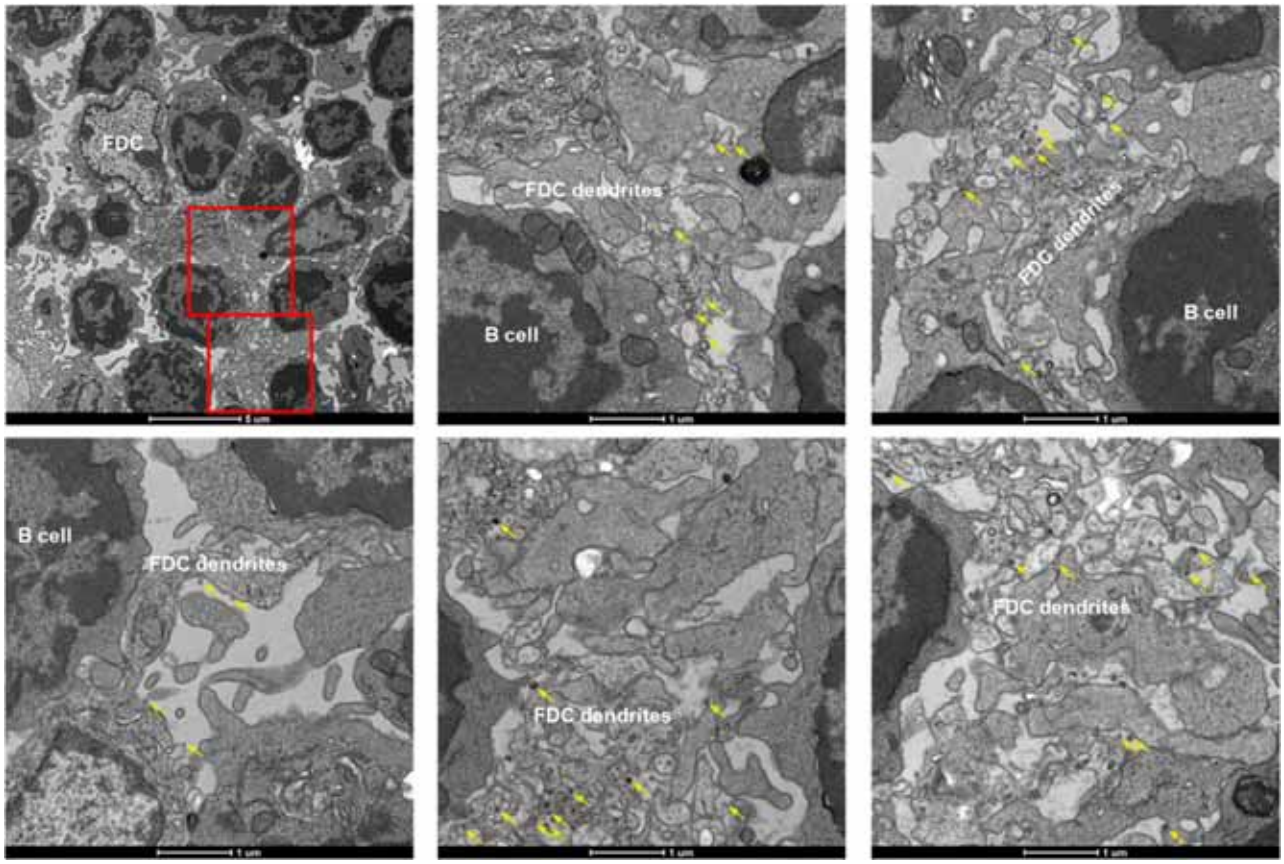

b E2p SApNPs (yellow arrow) are aligned on FDC dendrites after 12 hours of injection

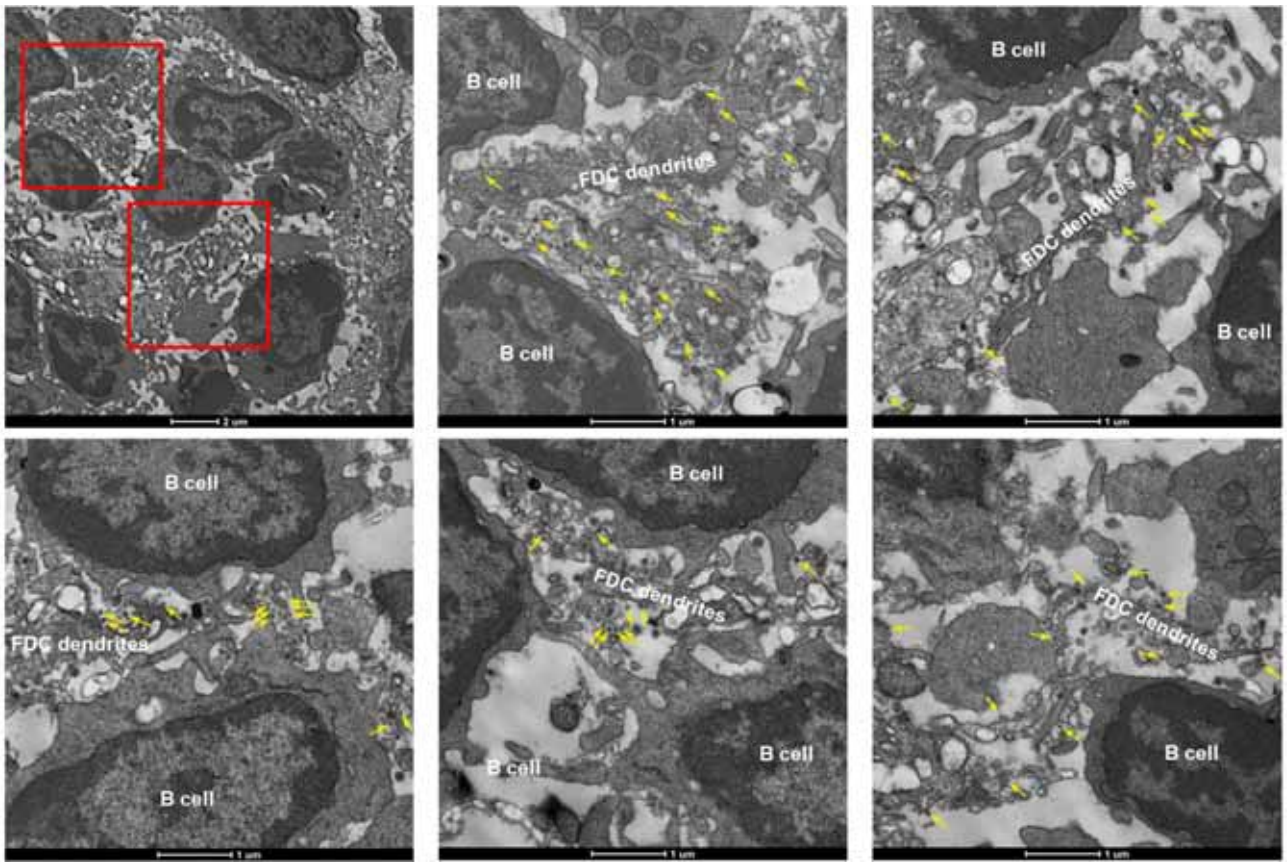

Fig. S7

c E2p SApNPs (yellow arrow) are aligned on FDC dendrites or taken up by B cells after 48 hours of injection

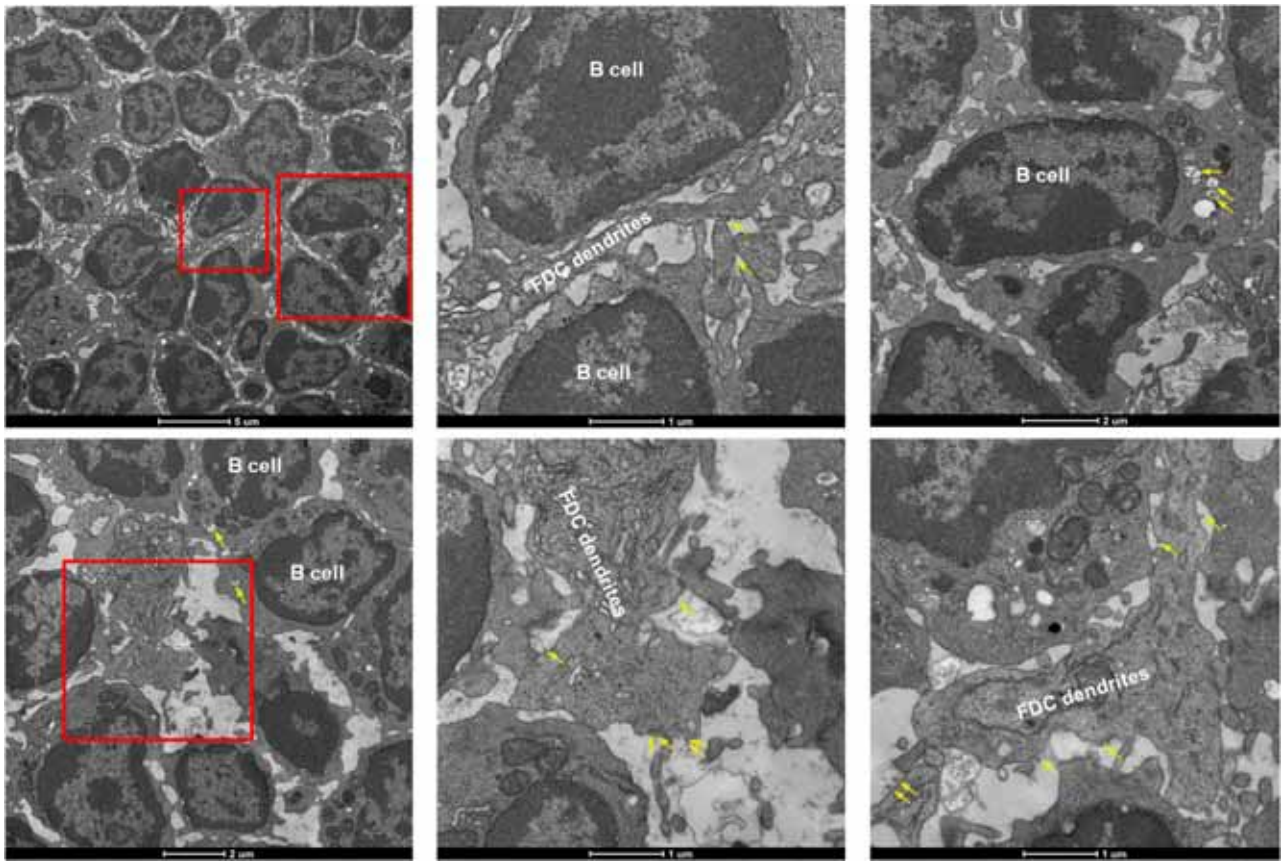

d I3-01v9b SApNPs (yellow arrow) are aligned on FDC dendrites or inside endolysosomes of FDC dendrities after 2 hours of injection

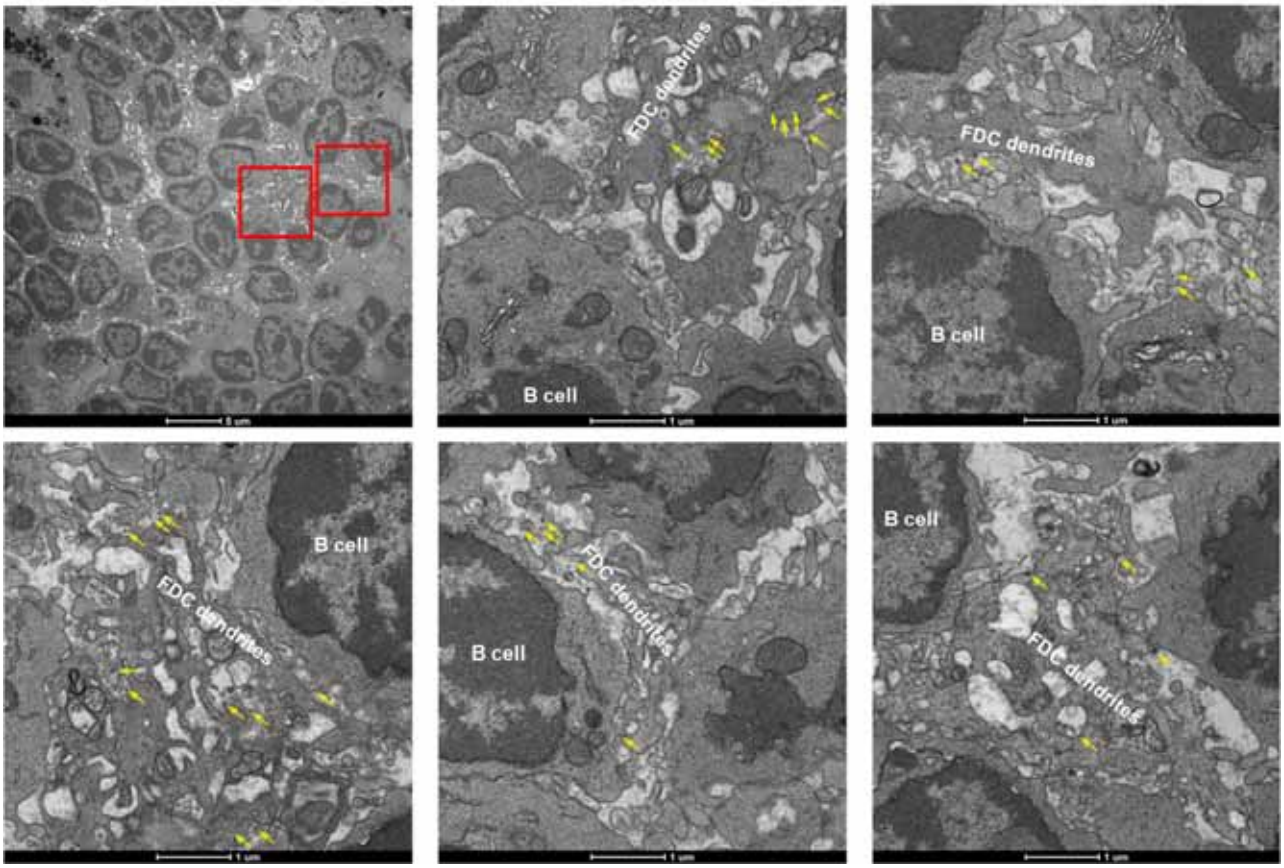

Fig. S7

e I3-01v9b SApNPs (yellow arrow) are aligned on FDC dendrites or taken up by B cells after 12 hours of injection

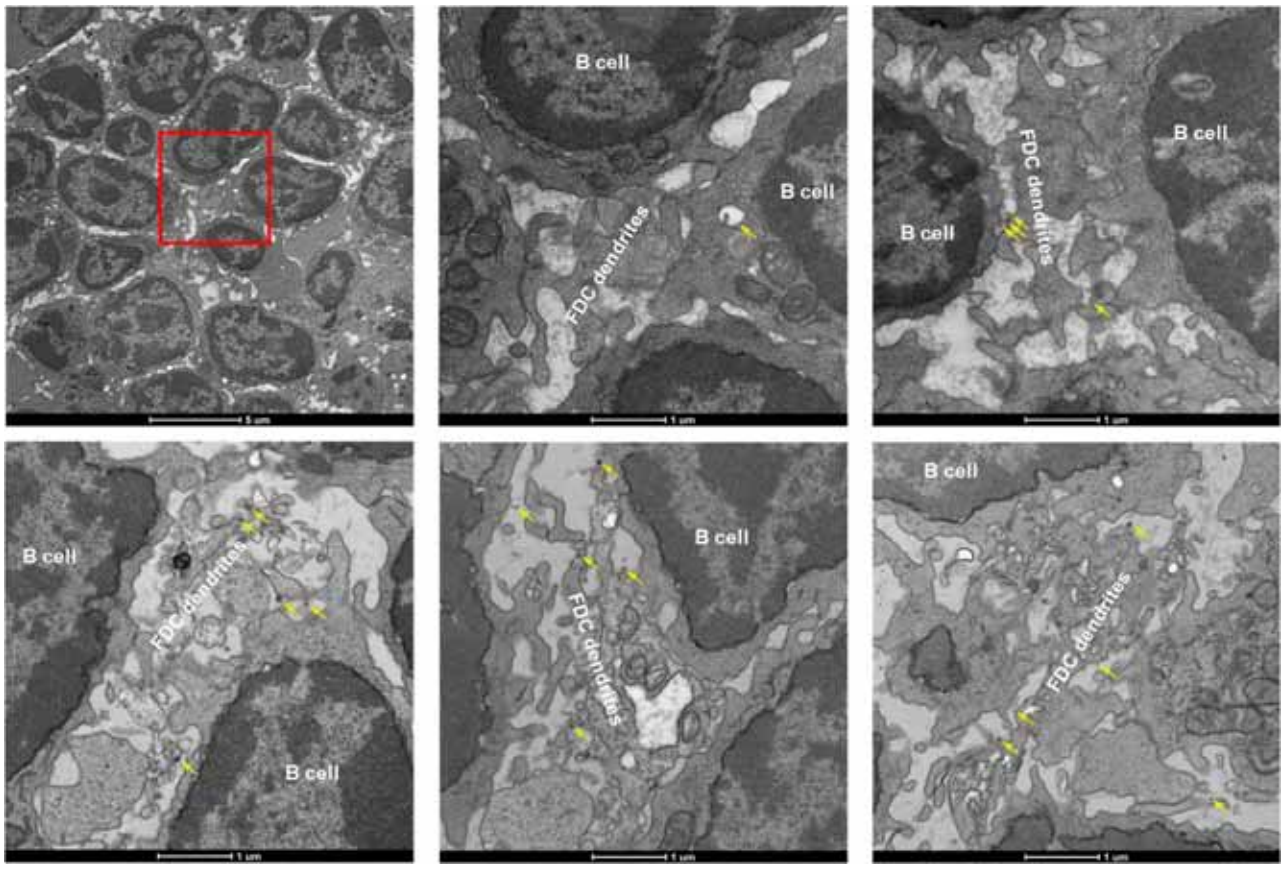

f I3-01v9b SApNPs (yellow arrow) are aligned on FDC dendrites after 48 hours of injection

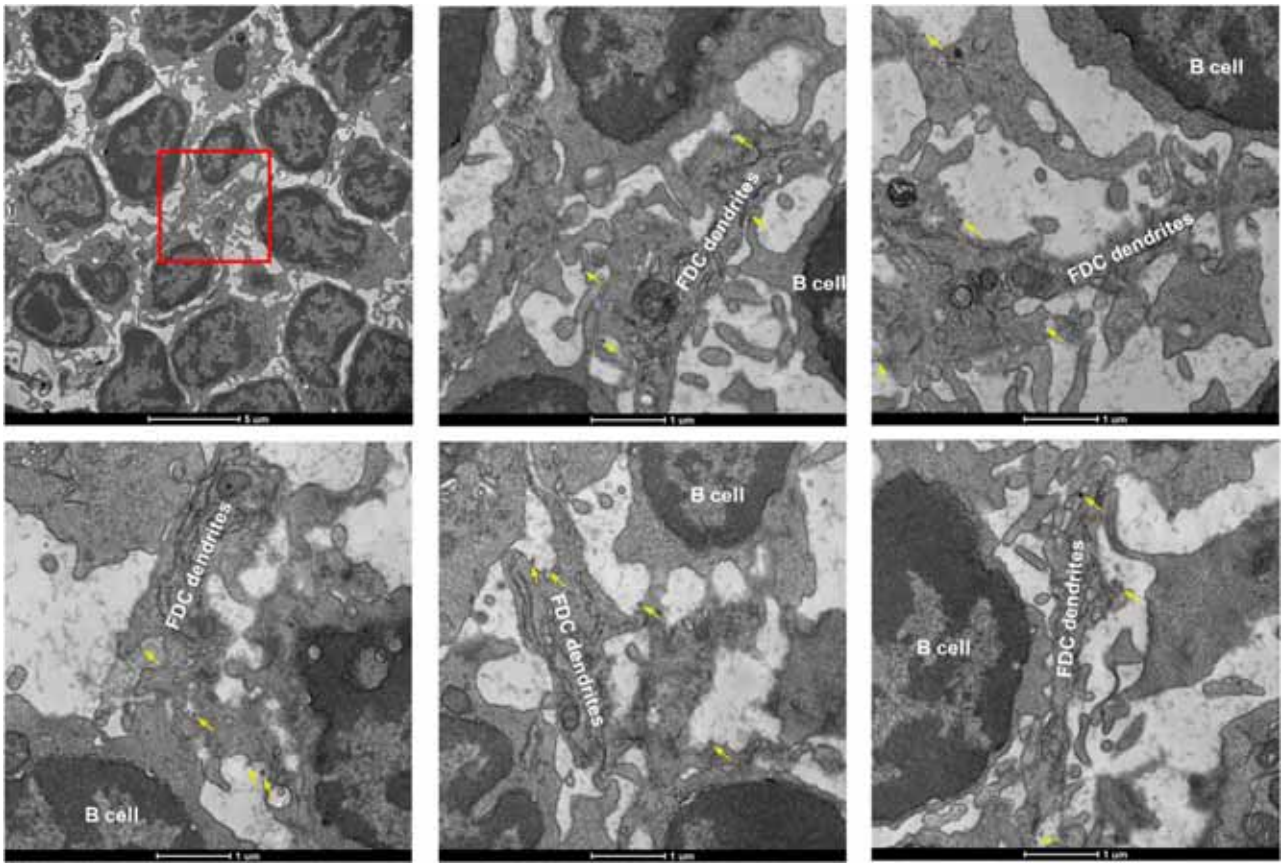

Fig. S7

g E2p SApNPs (yellow arrow) are associated with phagocytic cells after 2 hours of injection

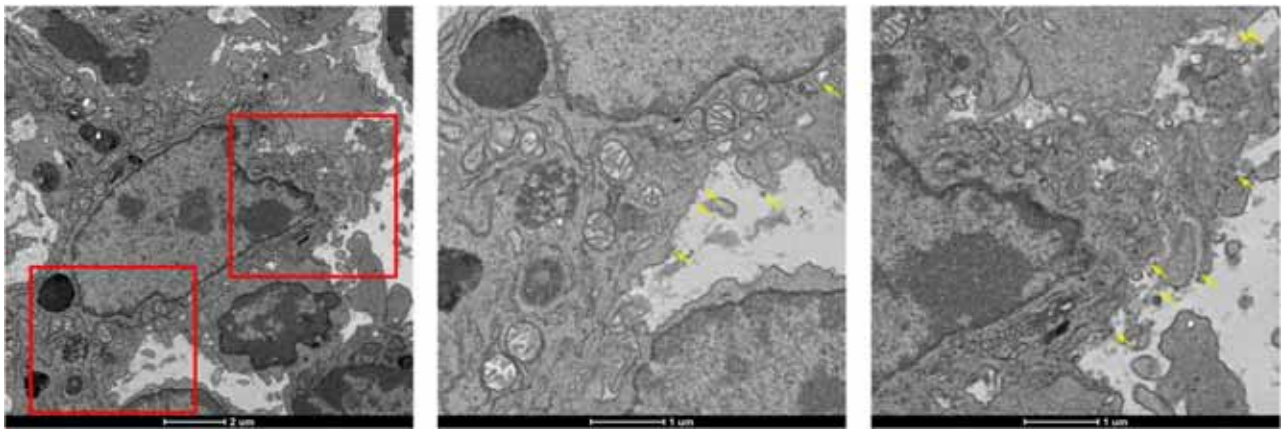

h E2p SApNPs (yellow arrow) are associated with phagocytic cells after 12 hours of injection

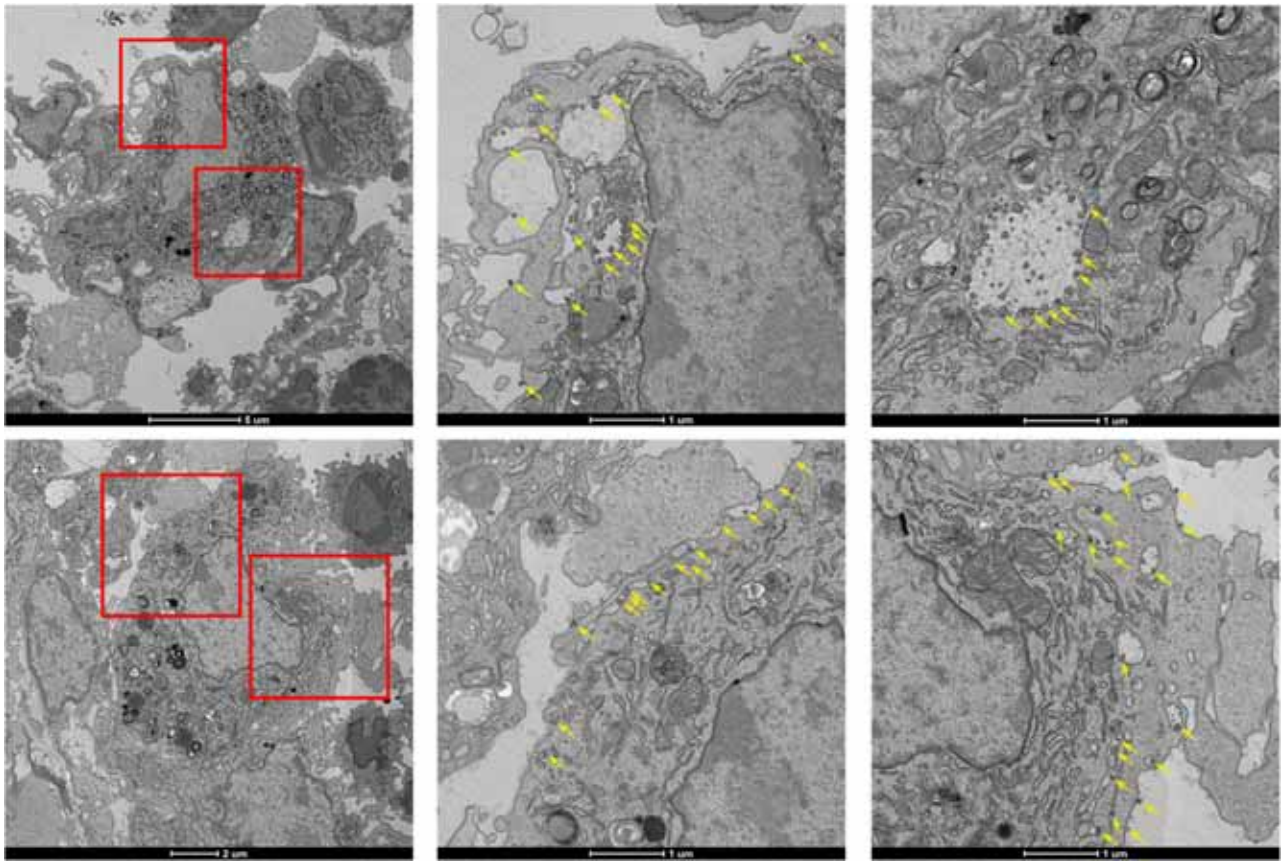

Fig. S7

i E2p SApNPs (yellow arrow) are associated with phagocytic cells after 48 hours of injection

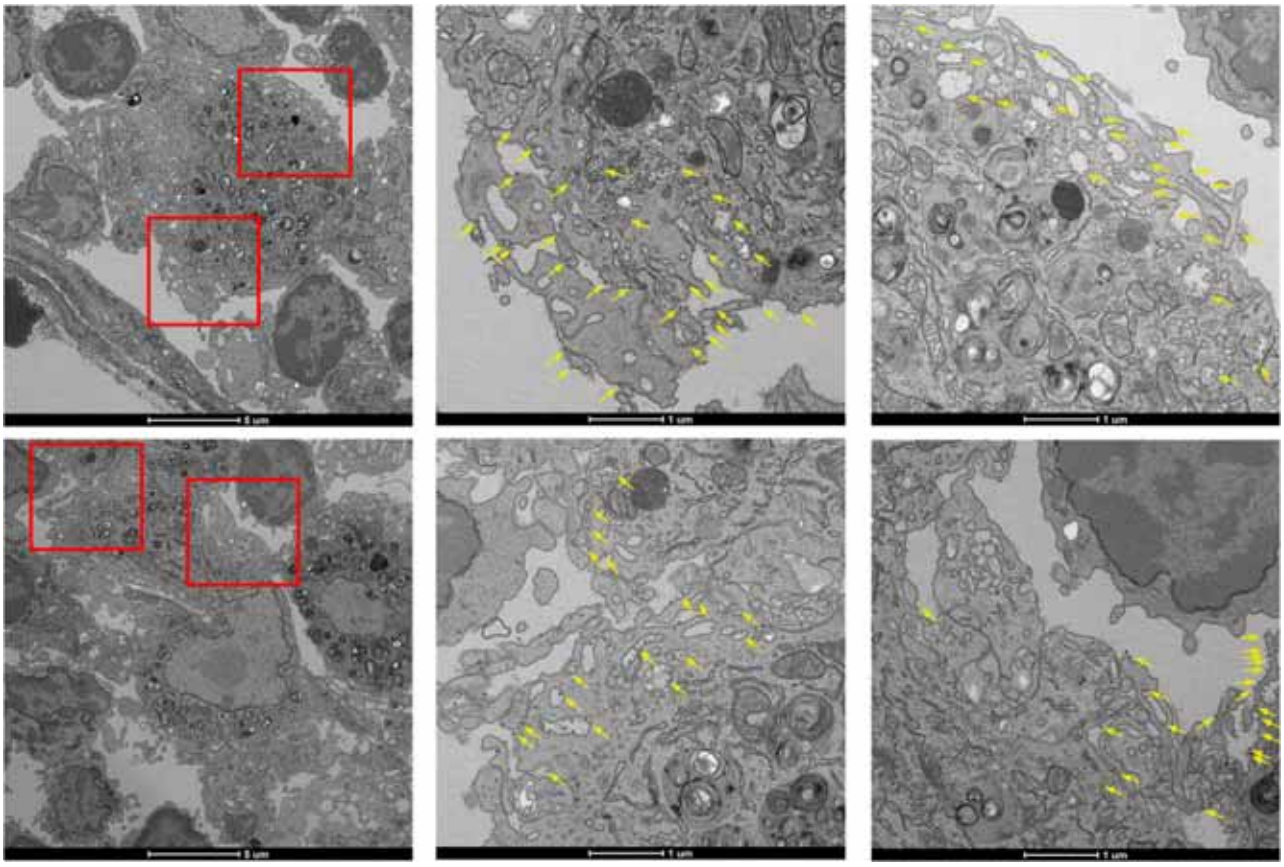

j I3-01v9b SApNPs (yellow arrow) are associated with phagocytic cells after 2 hours of injection

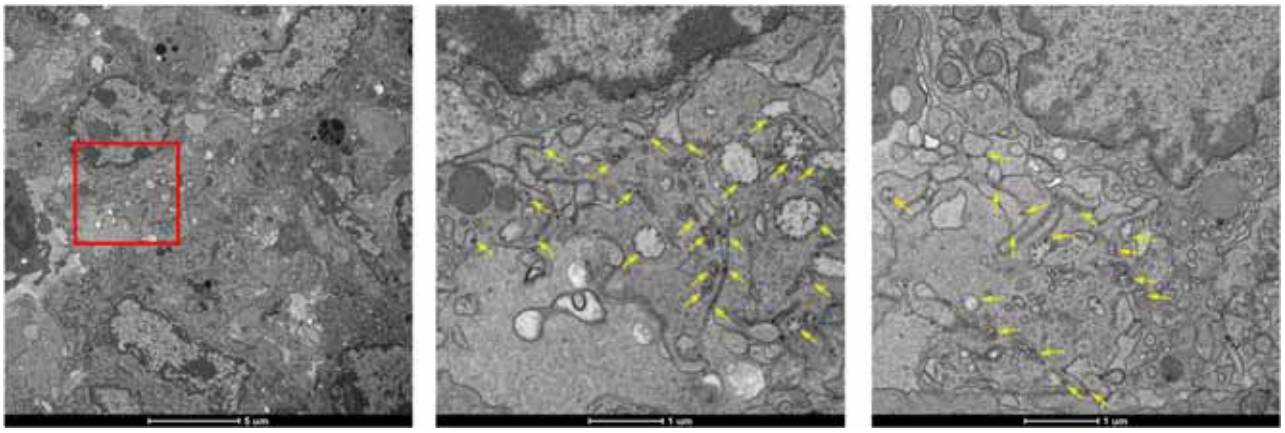

Fig. S7

k I3-01v9b SApNPs (yellow arrow) are associated with phagocytic cells after 12 hours of injection

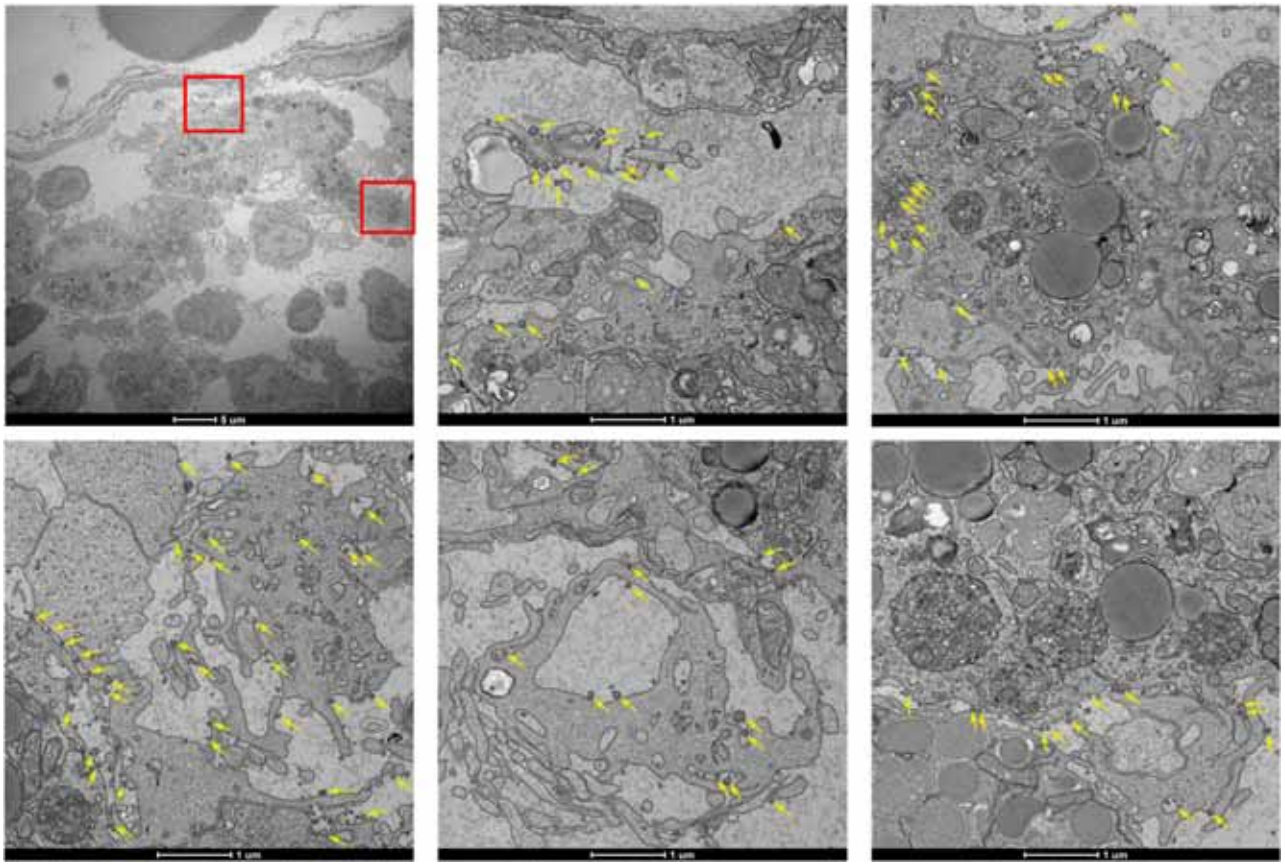

l I3-01v9b SApNPs (yellow arrow) are associated with phagocytic cells after 48 hours of injection

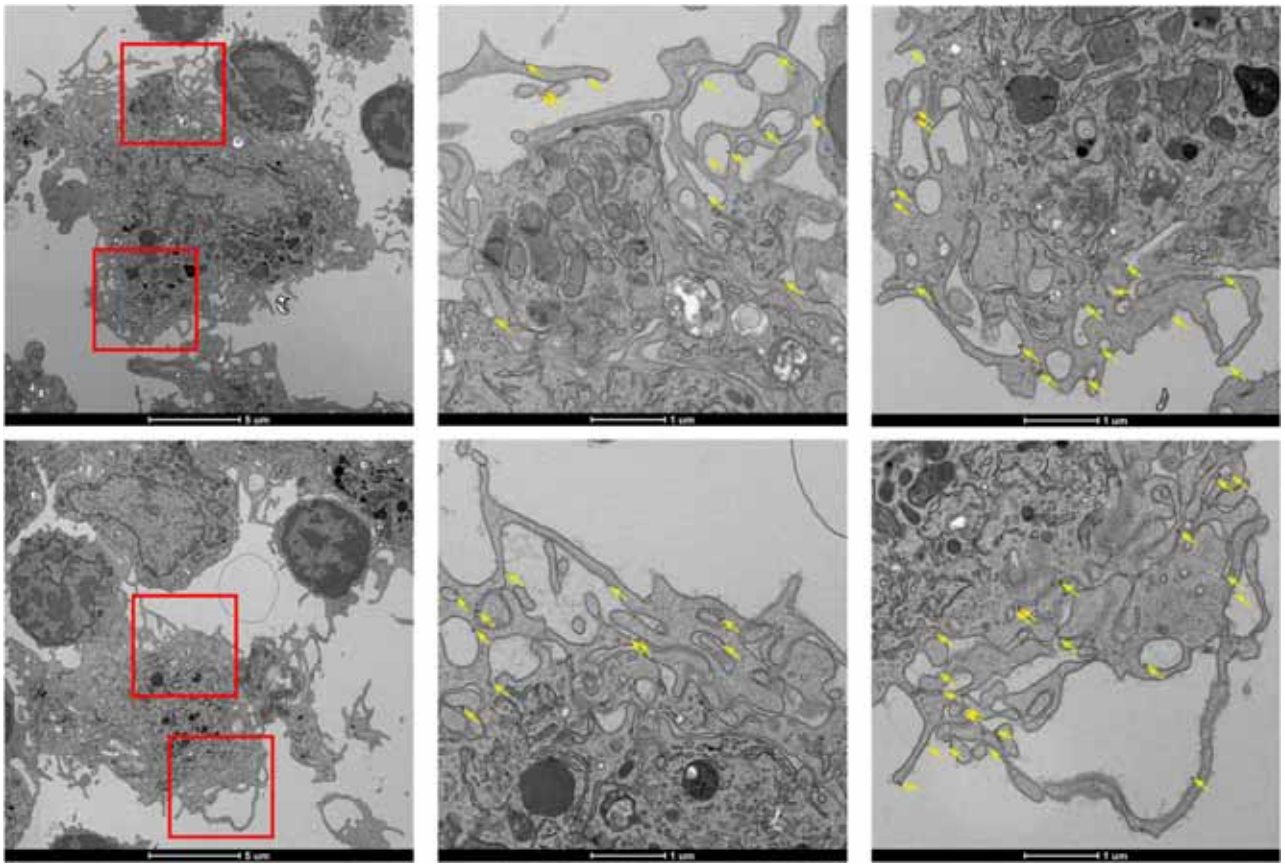

Fig. S7

m Aluminum phosphate (green arrow) tends to aggregate in the ECM after 2 hours of injection

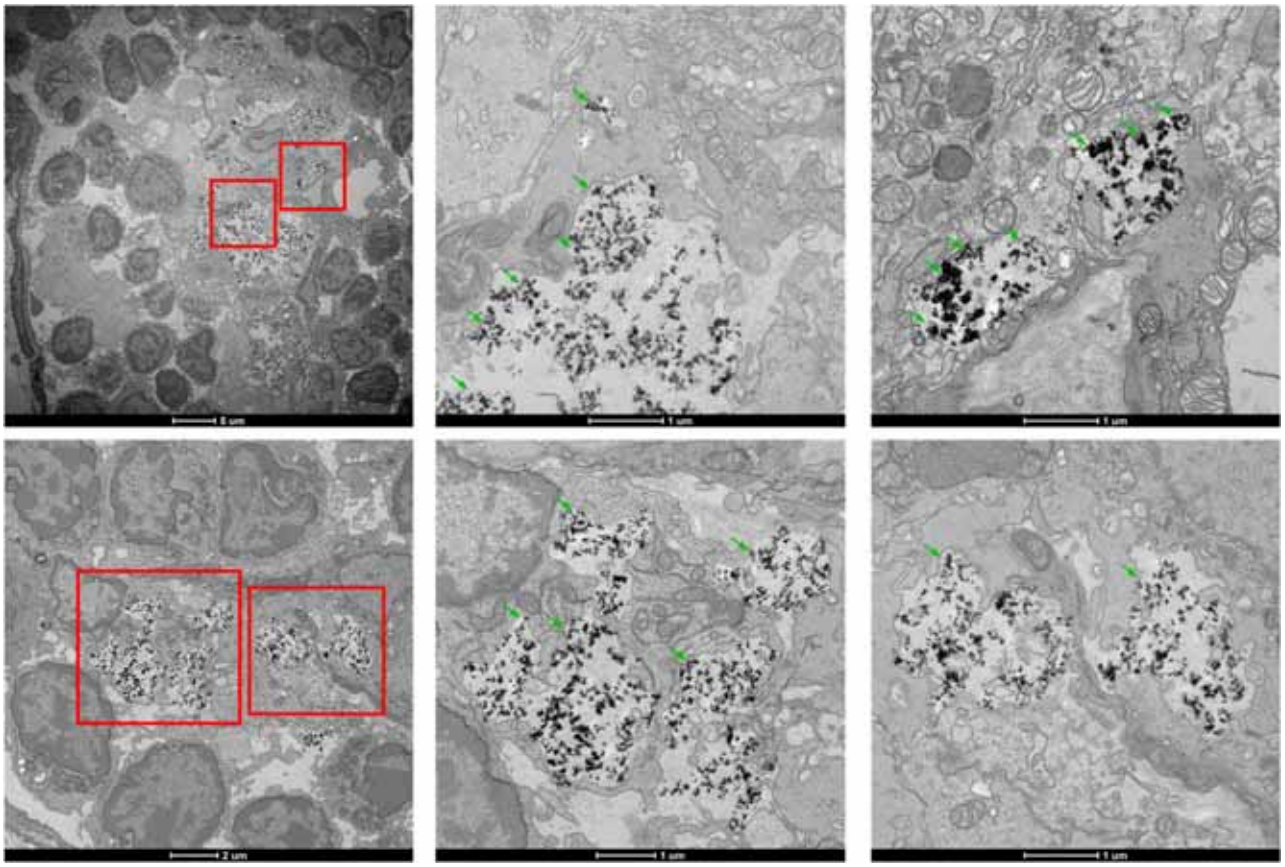

n I3-01v9b SApNPs (yellow arrow) and aluminum phosphate (green arrow) with phagocytic cells at 2 hours

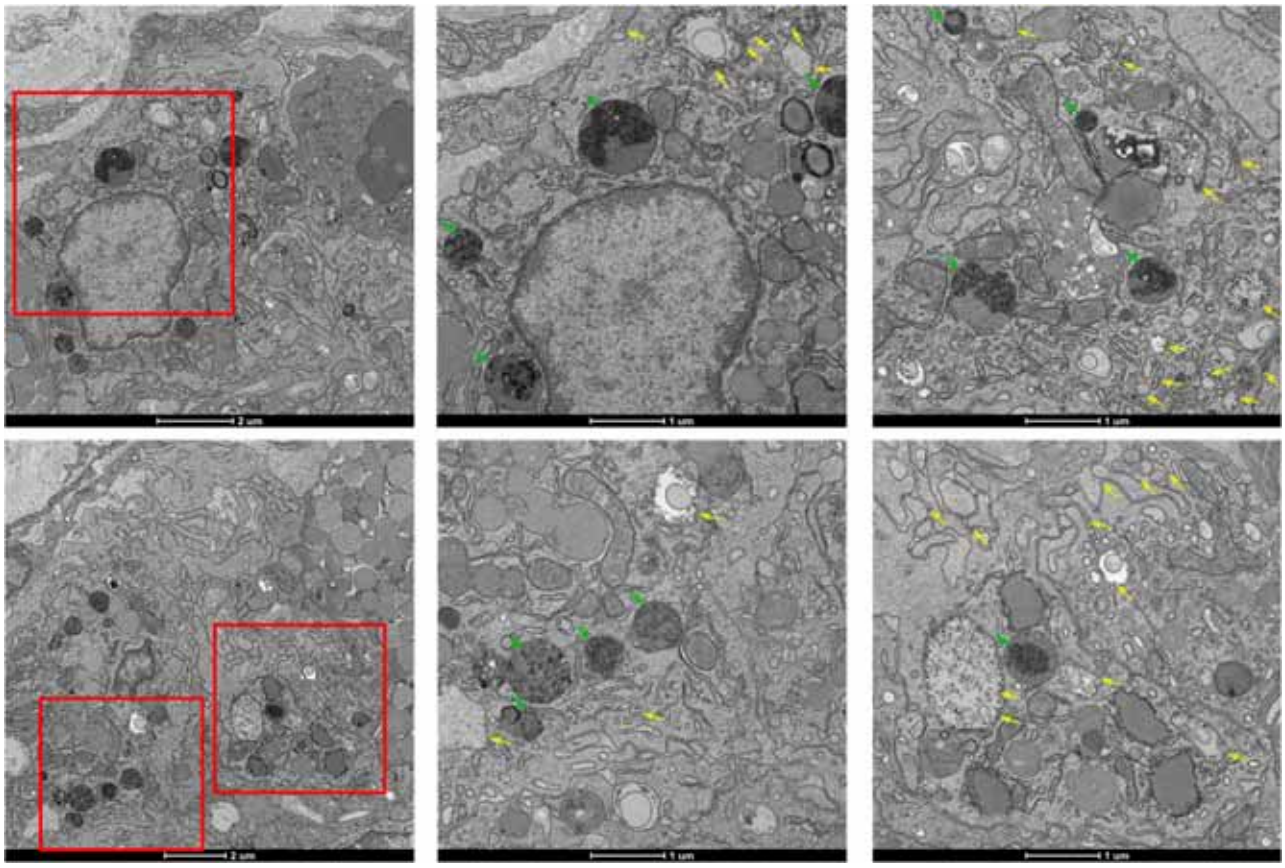

Fig. S7

o I3-01v9b SApNPs (yellow arrow) and aluminum phosphate (green arrow) with phagocytic cells at 12 hours

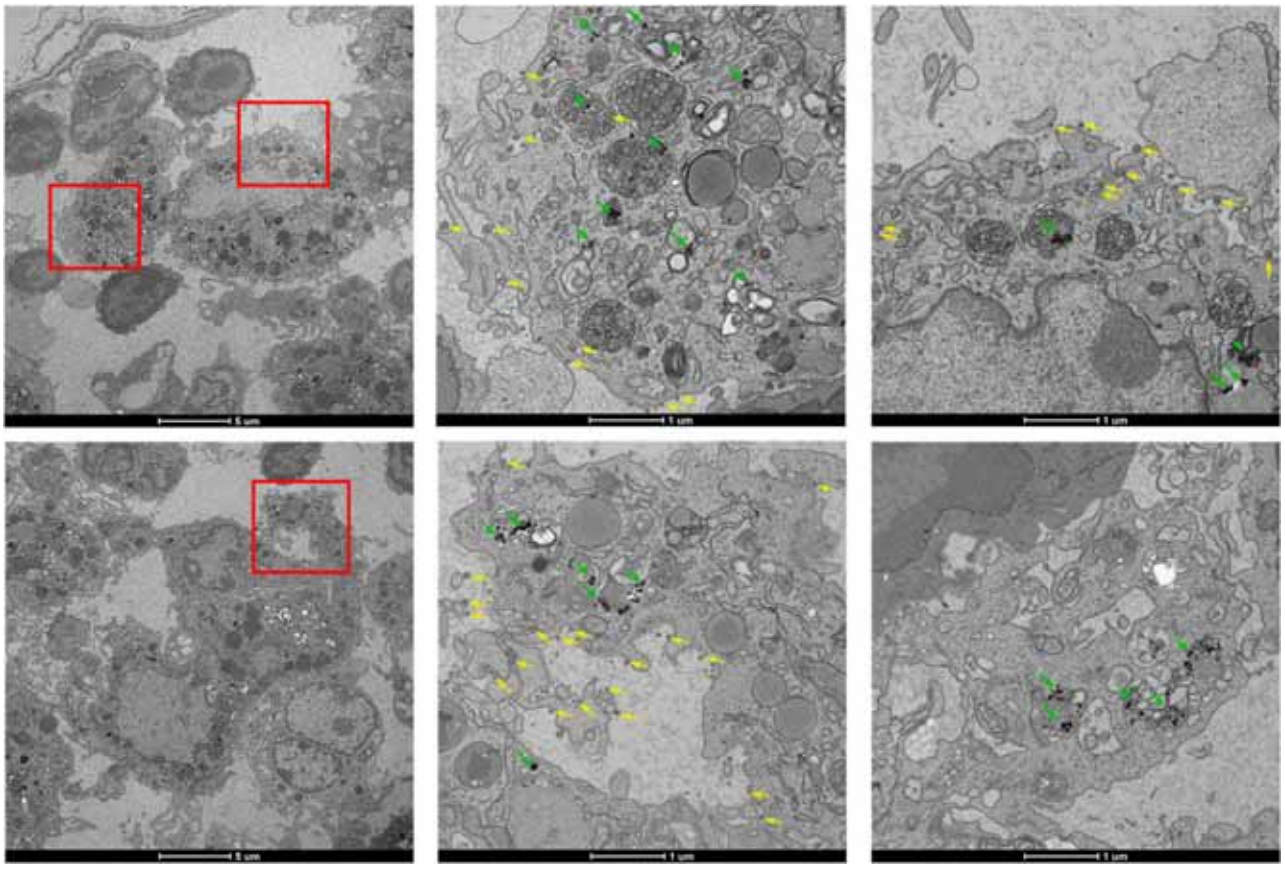

p I3-01v9b SApNPs (yellow arrow) and aluminum phosphate (green arrow) with phagocytic cells at 48 hours

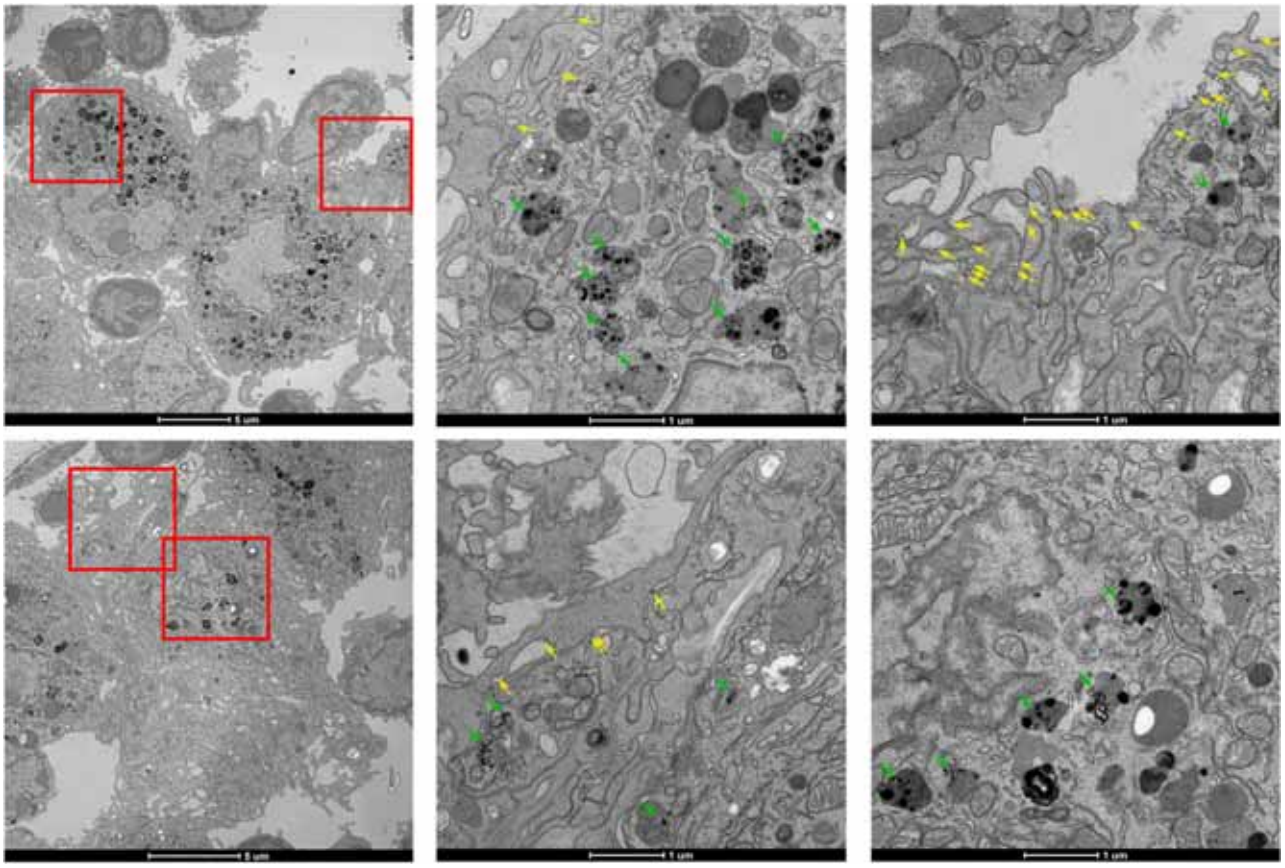

Fig. S7. TEM images of Sudan GPΔmuc-presenting SApNPs interacting with FDCs and phagocytic cells in a lymph node. SUDV GPΔmuc trimer-presenting E2p SApNPs are aligned on FDC dendrites at (**a**) 2 hours, (**b**) 12 hours, and (**c**) 48 hours after a single-dose injection (2 footpads, 50 µg/footpad). SUDV GPΔmuc trimer-presenting I3-01v9b SApNPs are aligned on FDC dendrites at (**d**) 2 hours, (**e**) 12 hours, and (**f**) 48 hours after a single-dose injection. Aluminum phosphate (AP) particles are not associated with SApNPs on FDC dendrites. SUDV GPΔmuc trimer-presenting E2p SApNPs are aligned on the surface or inside endolysosomes of phagocytic cells at (**g**) 2 hours, (**h**) 12 hours, and (**i**) 48 hours after an injection. SUDV GPΔmuc trimer-presenting I3-01v9b SApNPs are associated with phagocytic cells after (**j**) 2 hours, (**k**) 12 hours, and (**l**) 48 hours after the injection. (**m**) AP particles aggregate in the extracellular matrix 2 hours after the injection. SUDV GPΔmuc trimer-presenting I3-01v9b SApNPs formulated with AP are associated with phagocytic cells at (**n**) 2 hours, (**o**) 12 hours, and (**p**) 48 hours after an injection. TEM images were performed on 2 popliteal lymph nodes for each SApNP construct. E2p or I3-01v9b SApNPs are pointed to by yellow arrows and AP adjuvants are pointed to by green arrows.

Fig. S8

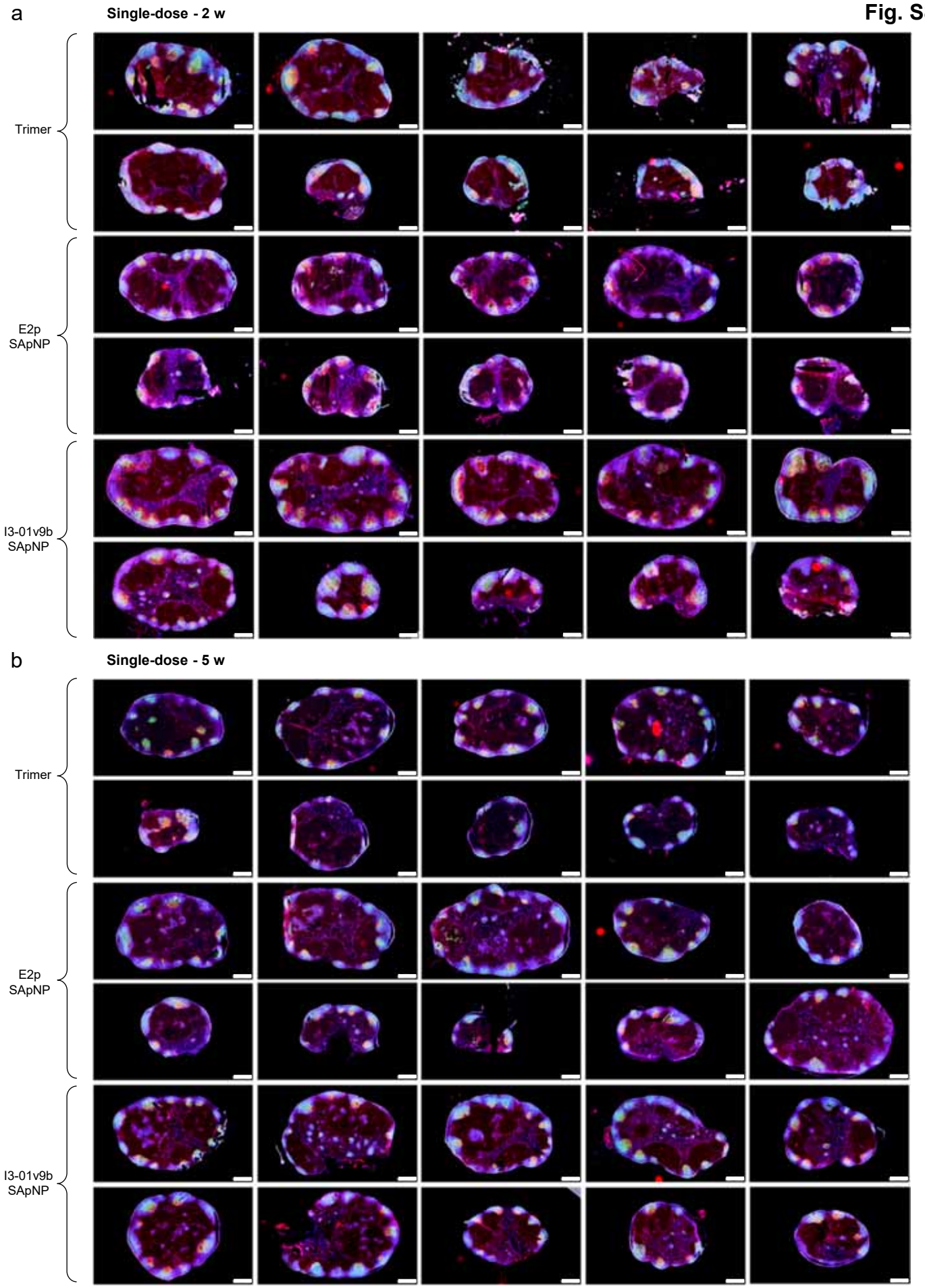
a
Single-dose - 2 w
Trimer
E2p SApNP
I3-01v9b SApNP
b
Single-dose - 5 w
Trimer
E2p SApNP
I3-01v9b SApNP

Fig. S8

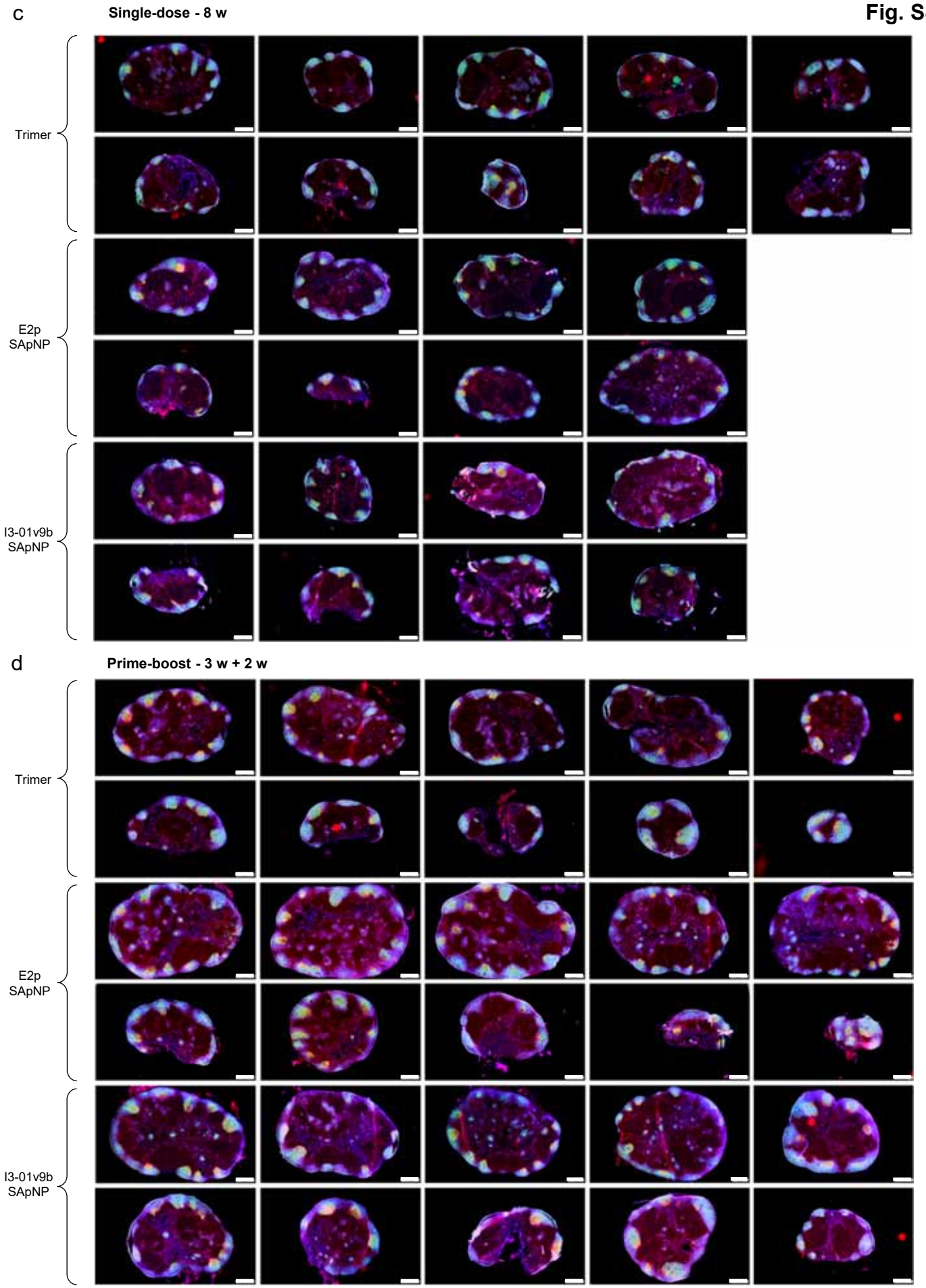
c
Single-dose - 8 w
Trimer
E2p SApNP
I3-01v9b SApNP
d
Prime-boost - 3 w + 2 w
Trimer
E2p SApNP
I3-01v9b SApNP

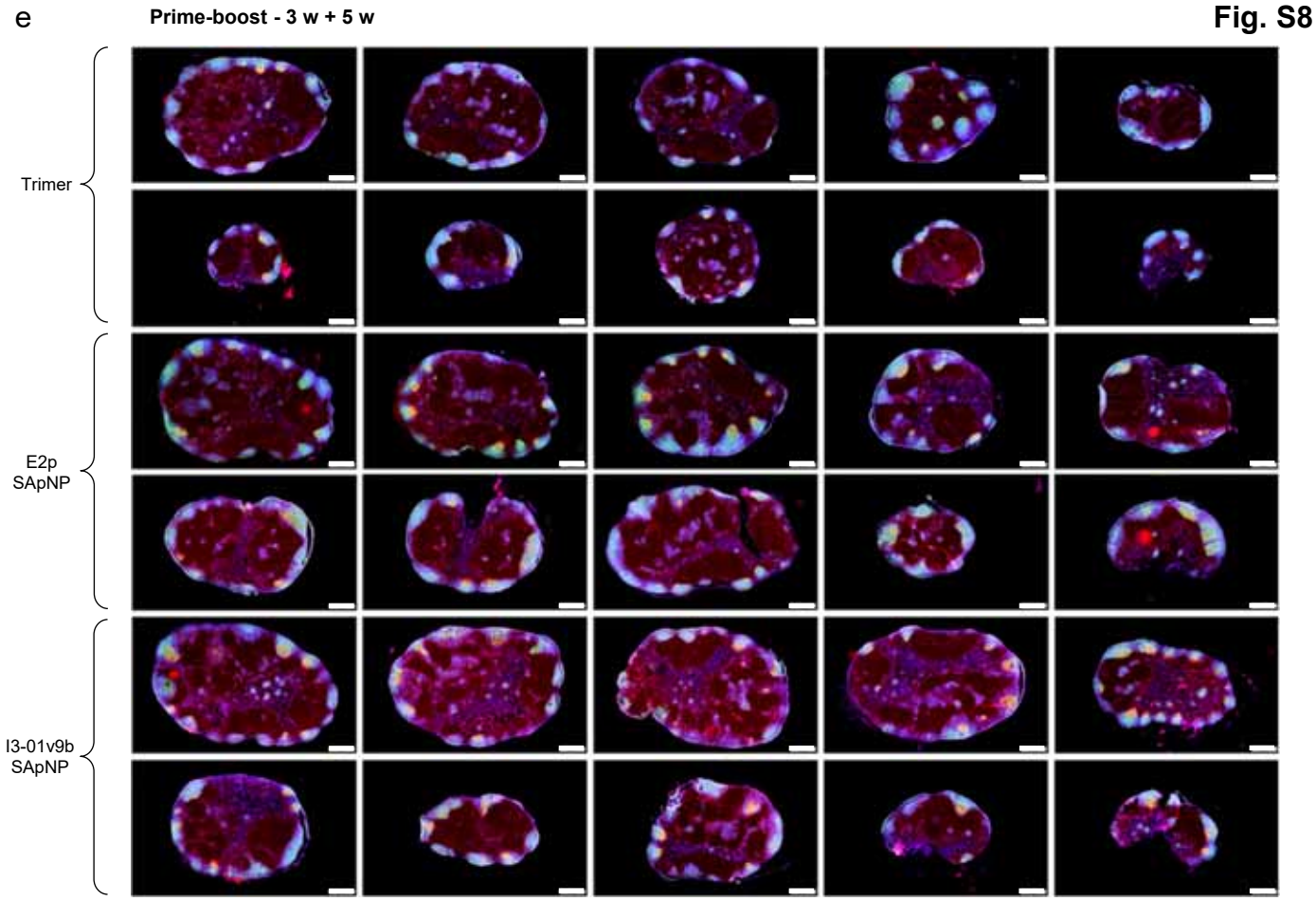

Fig. S8. Immunohistological analysis of SUDV GPΔmuc trimer and SApNP vaccine-induced GCs. Immunohistological images of GCs at (**a**) 2, (**b**) 5, and (**c**) 8 weeks after a single-dose injection of GPΔmuc trimer and GPΔmuc trimer-presenting E2p and I3-01v9b SApNPs (10 μg per injection, totaling 40 μg per mouse). Images of GCs at (**d**) 2 and (**e**) 5 weeks after the boost, which occurred at 3 weeks after the first dose (n = 5 mice/group). Immunofluorescent images are pseudo color coded (GL7+, red; CD21+, green; B220, blue). Scale bars = 500 μm for each image of a lymph node.

Fig. S9

a

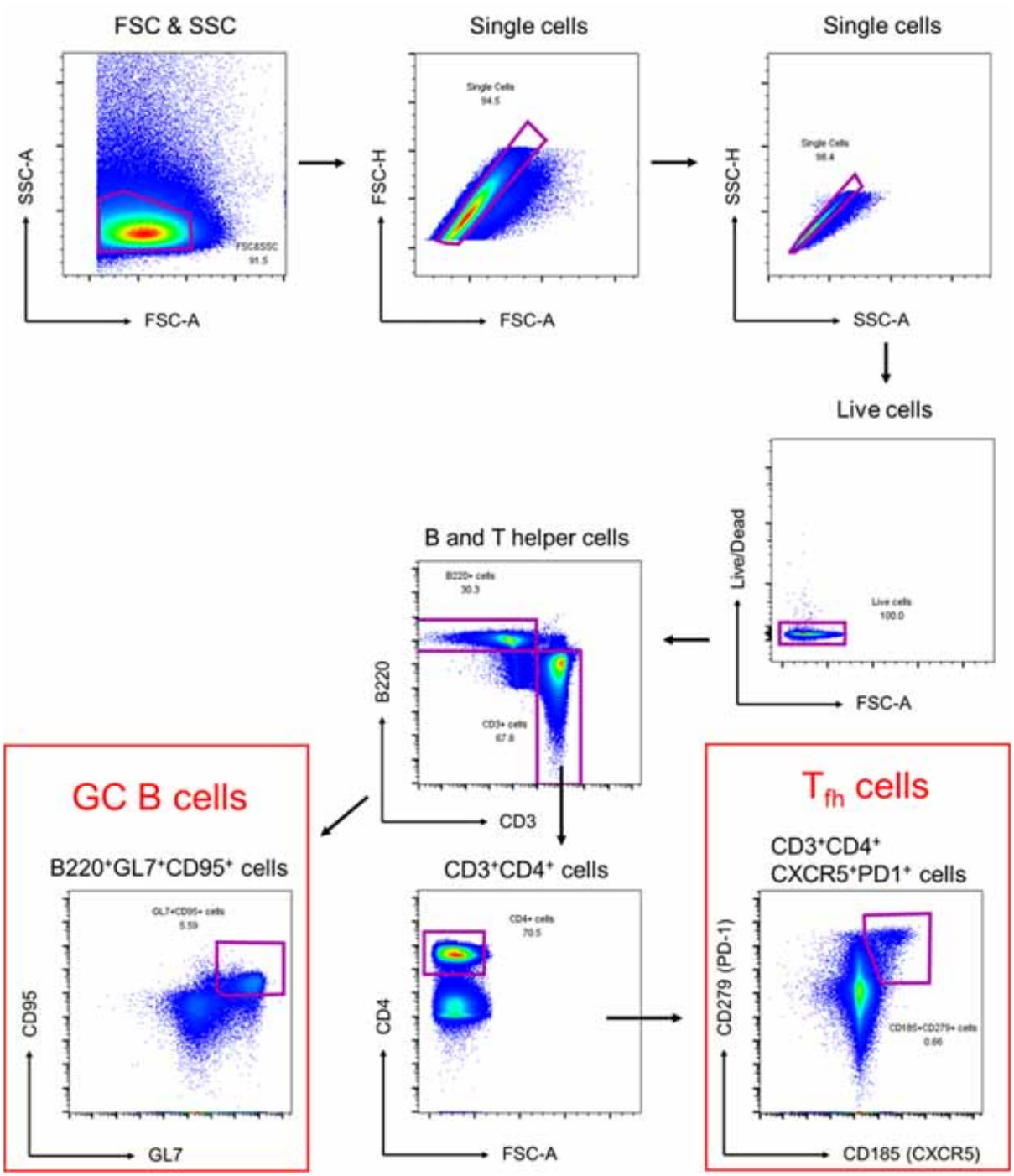

Fig. S9. Flow cytometry analysis of SUDV GPΔmuc trimer and SApNPs vaccine-induced GCs. Gating strategy for analyzing GCs (GC B cells and T follicular helper cells) using flow cytometry (*n* = 5 mice/group).

Fig. S10

a Sera of individual mice immunized with EBOV vaccines binding to EBOV GPΔmuc-WL^{2}P^4(1TD0) trimer

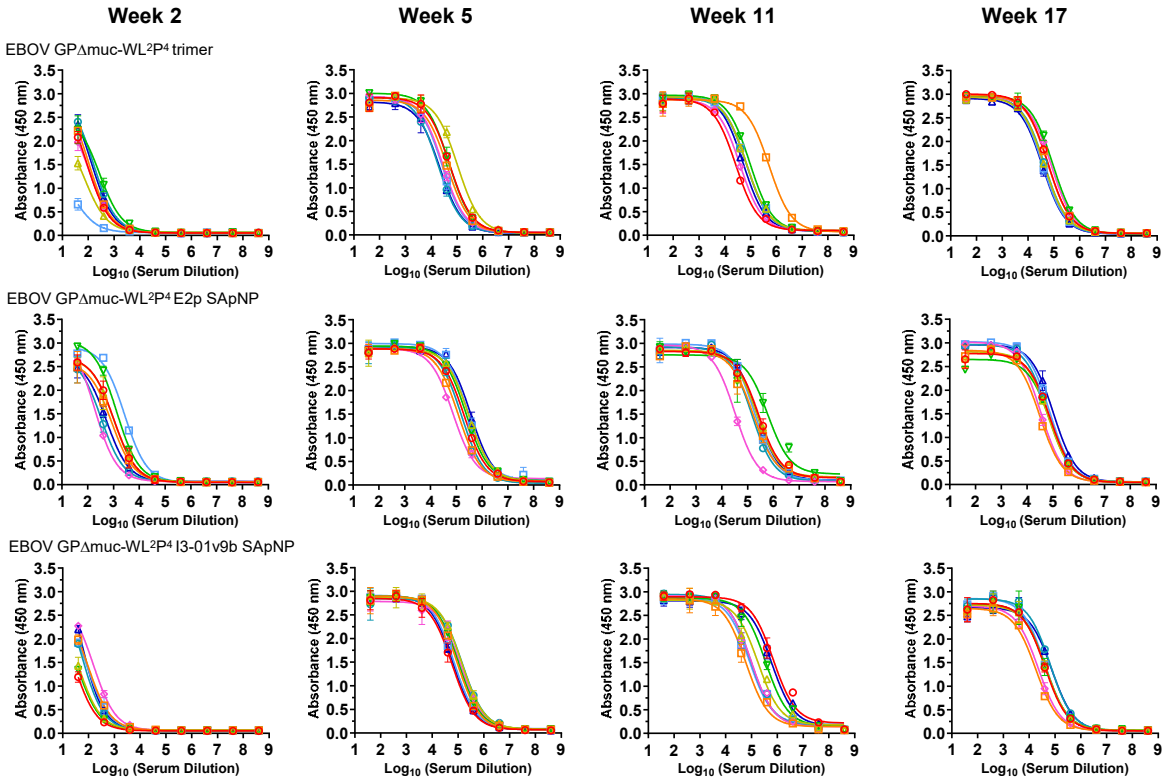

b Mouse serum ELISA EC_{50} titers

Week 2

Antigen	EC50 titers (week 2)								Geometric Mean
	M1	M2	M3	M4	M5	M6	M7	M8	
EBOV GPΔmuc-WL^{2}P^4 trimer	111.7	136.3	51.3	227.2	103.0	200.2	12.6	173.3	97.3
EBOV GPΔmuc-WL^{2}P^4 E2p SApNP	985.3	706.4	970.8	1772.0	271.5	336.1	3145.0	486.4	799.6
EBOV GPΔmuc-WL^{2}P^4 I3-01v9b SApNP	30.1	101.8	43.0	37.9	172.4	80.7	91.5	115.6	72.1

Week 5

Antigen	EC50 titers (week 5)								Geometric Mean
	M1	M2	M3	M4	M5	M6	M7	M8	
EBOV GPΔmuc-WL^{2}P^4 trimer	52545	41735	104914	48787	27947	18271	26144	21434	36588.3
EBOV GPΔmuc-WL^{2}P^4 E2p SApNP	199849	120954	303168	237335	74446	156667	282413	368341	195227.1
EBOV GPΔmuc-WL^{2}P^4 I3-01v9b SApNP	58458	93275	140476	104463	128829	148277	70114	63709	95341.8

Week 11

Antigen	EC50 titers (week 11)								Geometric Mean
	M1	M2	M3	M4	M5	M6	M7	M8	
EBOV GPΔmuc-WL^{2}P^4 trimer	26545	524033	69054	94400	39464	69865	68351	51944	73880.6
EBOV GPΔmuc-WL^{2}P^4 E2p SApNP	267135	163352	223491	606328	32762	143908	182928	233182	181721.7
EBOV GPΔmuc-WL^{2}P^4 I3-01v9b SApNP	703967	60730	178784	354031	97482	91294	82827	610293	182253.3

Week 17

Antigen	EC50 titers (week 17)								Geometric Mean
	M1	M2	M3	M4	M5	M6	M7	M8	
EBOV GPΔmuc-WL^{2}P^4-FOLD	59703	59841	42414	92526	80033	44111	36894	36448	53444.3
EBOV GPΔmuc-WL^{2}P^4 E2p SApNP	78072	31500	66659	79702	33830	63116	75359	105584	62128.2
EBOV GPΔmuc-WL^{2}P^4 I3-01v9b SApNP	40965	18206	43559	42711	22529	65820	41237	74760	39837.1

Statistical analysis

One-way ANOVA with Tukey's multiple comparisons test (w2)	Statistics	Adjusted P Value
EBOV GPΔmuc-WL^{2}P^4 trimer vs. EBOV GPΔmuc-WL^{2}P^4 E2p SApNP	**	0.0067
EBOV GPΔmuc-WL^{2}P^4 trimer vs. EBOV GPΔmuc-WL^{2}P^4 I3-01v9b SApNP	ns	0.9871
EBOV GPΔmuc-WL^{2}P^4 E2p SApNP vs. EBOV GPΔmuc-WL^{2}P^4 I3-01v9b SApNP	**	0.0047

One-way ANOVA with Tukey's multiple comparisons test (w5)	Statistics	Adjusted P Value
EBOV GPΔmuc-WL^{2}P^4 trimer vs. EBOV GPΔmuc-WL^{2}P^4 E2p SApNP	****	<0.0001
EBOV GPΔmuc-WL^{2}P^4 trimer vs. EBOV GPΔmuc-WL^{2}P^4 I3-01v9b SApNP	ns	0.1769
EBOV GPΔmuc-WL^{2}P^4 E2p SApNP vs. EBOV GPΔmuc-WL^{2}P^4 I3-01v9b SApNP	**	0.0034

One-way ANOVA with Tukey's multiple comparisons test (w11)	Statistics	Adjusted P Value
EBOV GPΔmuc-WL^{2}P^4 trimer vs. EBOV GPΔmuc-WL^{2}P^4 E2p SApNP	ns	0.5058
EBOV GPΔmuc-WL^{2}P^4 trimer vs. EBOV GPΔmuc-WL^{2}P^4 I3-01v9b SApNP	ns	0.2942
EBOV GPΔmuc-WL^{2}P^4 E2p SApNP vs. EBOV GPΔmuc-WL^{2}P^4 I3-01v9b SApNP	ns	0.9135

One-way ANOVA with Tukey's multiple comparisons test (w17)	Statistics	Adjusted P Value
EBOV GPΔmuc-WL^{2}P^4 trimer vs. EBOV GPΔmuc-WL^{2}P^4 E2p SApNP	ns	0.6171
EBOV GPΔmuc-WL^{2}P^4 trimer vs. EBOV GPΔmuc-WL^{2}P^4 I3-01v9b SApNP	ns	0.4761
EBOV GPΔmuc-WL^{2}P^4 E2p SApNP vs. EBOV GPΔmuc-WL^{2}P^4 I3-01v9b SApNP	ns	0.1078

C Week-7 sera of individual mice immunized with EBOV vaccines binding to SUDV GPΔmuc-WL^{2}P^4(1TD0) trimer

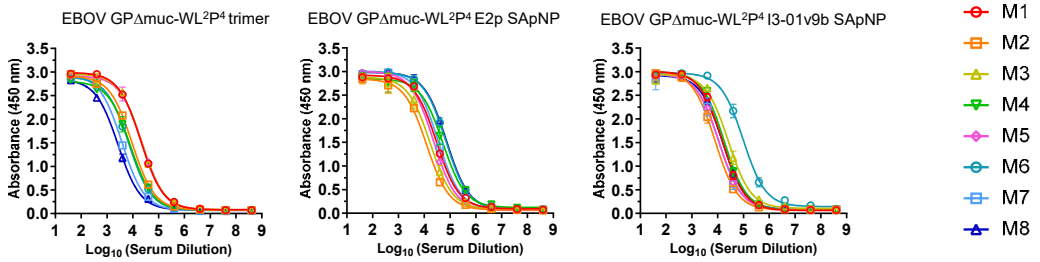

Mouse serum ELISA EC_{50} titers

Week 17

Antigen	EC50 titers (week 17)								Geometric Mean
	M1	M2	M3	M4	M5	M6	M7	M8	
EBOV GPΔmuc-WL^{2}P^4 trimer	20545	9375	21603	8039	22891	7014	3805	2676	9273.3
EBOV GPΔmuc-WL^{2}P^4 E2p SApNP	29973	12206	17018	52874	22735	68558	33997	72867	32585.3
EBOV GPΔmuc-WL^{2}P^4 I3-01v9b SApNP	15023	7900	26186	17813	11241	97786	11184	15787	17943.0

Statistical analysis

One-way ANOVA with Tukey's multiple comparisons test (w17)	Statistics	Adjusted P Value
EBOV GPΔmuc-WL^{2}P^4 trimer vs. EBOV GPΔmuc-WL^{2}P^4 E2p SApNP	ns	0.0641
EBOV GPΔmuc-WL^{2}P^4 trimer vs. EBOV GPΔmuc-WL^{2}P^4 I3-01v9b SApNP	ns	0.4678
EBOV GPΔmuc-WL^{2}P^4 E2p SApNP vs. EBOV GPΔmuc-WL^{2}P^4 I3-01v9b SApNP	ns	0.4656

d Week-17 sera of individual mice immunized with EBOV vaccines binding to RAVV GPΔmuc-P^{2}CT(1TD0) trimer

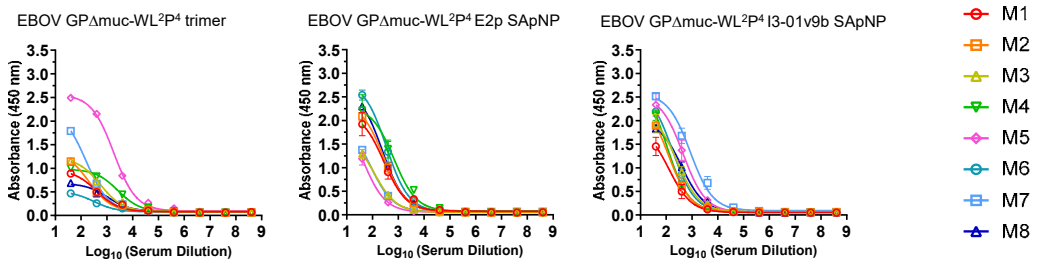

Mouse serum ELISA EC_{50} titers

Week 17

Antigen	Absorbance (450 nm) (week 17)								Geometric Mean
	M1	M2	M3	M4	M5	M6	M7	M8	
EBOV GPΔmuc-WL^{2}P^4 trimer	0.9	1.1	1.2	1.0	2.5	0.5	1.8	0.7	1.1
EBOV GPΔmuc-WL^{2}P^4 E2p SApNP	1.9	2.1	1.3	2.2	1.2	2.5	1.4	2.3	1.8
EBOV GPΔmuc-WL^{2}P^4 I3-01v9b SApNP	1.5	1.9	1.9	2.1	2.3	2.2	2.5	1.8	2.0

Statistical analysis

One-way ANOVA with Tukey's multiple comparisons test (w17)	Statistics	Adjusted P Value
EBOV GPΔmuc-WL^{2}P^4 trimer vs. EBOV GPΔmuc-WL^{2}P^4 E2p SApNP	*	0.0449
EBOV GPΔmuc-WL^{2}P^4 trimer vs. EBOV GPΔmuc-WL^{2}P^4 I3-01v9b SApNP	*	0.0111
EBOV GPΔmuc-WL^{2}P^4 E2p SApNP vs. EBOV GPΔmuc-WL^{2}P^4 I3-01v9b SApNP	ns	0.7982

Fig. S10

e Sera of individual mice immunized with EBOV vaccines neutralizing an EBOV Makona strain

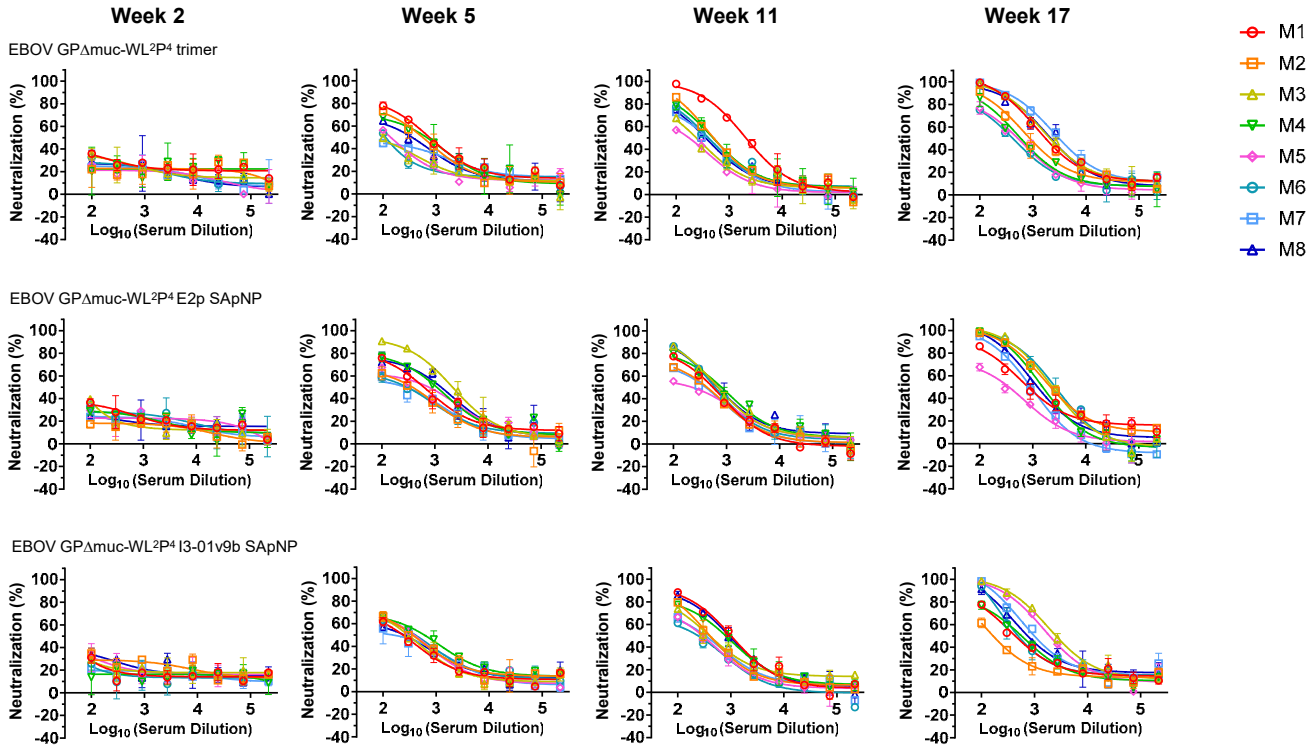

f Mouse serum neutralizing ID_{50} titers

Week 2

Antigen	ID50 titers (week 2)								Geometric Mean
	M1	M2	M3	M4	M5	M6	M7	M8	
EBOV GPΔmuc-WL^{2}P^4 trimer	<100	<100	<100	<100	<100	<100	<100	<100	N/A
EBOV GPΔmuc-WL^{2}P^4 E2p SApNP	<100	<100	<100	<100	<100	<100	<100	<100	N/A
EBOV GPΔmuc-WL^{2}P^4 I3-01v9b SApNP	<100	<100	<100	<100	<100	<100	<100	<100	N/A

Week 5

Antigen	ID50 titers (week 5)								Geometric Mean
	M1	M2	M3	M4	M5	M6	M7	M8	
EBOV GPΔmuc-WL^{2}P^4 trimer	805.4	559.3	149.3	588.2	174.1	145.1	203.2	360.5	304.1
EBOV GPΔmuc-WL^{2}P^4 E2p SApNP	636.9	358.8	2178.0	1002.0	555.2	322.9	299.4	1167.0	648.4
EBOV GPΔmuc-WL^{2}P^4 I3-01v9b SApNP	267.9	390.2	313.1	575.8	378.9	413.4	258.7	296.7	350.3

Week 11

Antigen	ID50 titers (week 11)								Geometric Mean
	M1	M2	M3	M4	M5	M6	M7	M8	
EBOV GPΔmuc-WL^{2}P^4 trimer	2117.0	560.6	254.4	521.5	188.7	430.2	369.3	377.3	453.2
EBOV GPΔmuc-WL^{2}P^4 E2p SApNP	494.5	392.0	734.2	747.4	275.3	643.8	365.2	759.9	518.6
EBOV GPΔmuc-WL^{2}P^4 I3-01v9b SApNP	1006.0	434.9	454.1	766.3	289.4	237.7	327.0	928.5	487.3

Week 17

Antigen	ID50 titers (week 17)								Geometric Mean
	M1	M2	M3	M4	M5	M6	M7	M8	
EBOV GPΔmuc-WL^{2}P^4 trimer	2106.0	1038.0	2482.0	641.1	505.0	437.0	3537.0	2352.0	1260.8
EBOV GPΔmuc-WL^{2}P^4 E2p SApNP	1000.0	2501.0	2393.0	1580.0	329.2	2587.0	875.5	1415.0	1333.1
EBOV GPΔmuc-WL^{2}P^4 I3-01v9b SApNP	513.1	205.2	2961.0	592.6	2154.0	693.4	1272.0	994.0	876.7

Statistical analysis

One-way ANOVA with Tukey's multiple comparisons test (w5)	Statistics	Adjusted P Value
EBOV GPΔmuc-WL^{2}P^4 trimer vs. EBOV GPΔmuc-WL^{2}P^4 E2p SApNP	ns	0.0919
EBOV GPΔmuc-WL^{2}P^4 trimer vs. EBOV GPΔmuc-WL^{2}P^4 I3-01v9b SApNP	ns	0.9982
EBOV GPΔmuc-WL^{2}P^4 E2p SApNP vs. EBOV GPΔmuc-WL^{2}P^4 I3-01v9b SApNP	ns	0.0824

One-way ANOVA with Tukey's multiple comparisons test (w11)	Statistics	Adjusted P Value
EBOV GPΔmuc-WL^{2}P^4 trimer vs. EBOV GPΔmuc-WL^{2}P^4 E2p SApNP	ns	0.9676
EBOV GPΔmuc-WL^{2}P^4 trimer vs. EBOV GPΔmuc-WL^{2}P^4 I3-01v9b SApNP	ns	0.9724
EBOV GPΔmuc-WL^{2}P^4 E2p SApNP vs. EBOV GPΔmuc-WL^{2}P^4 I3-01v9b SApNP	ns	0.9998

One-way ANOVA with Tukey's multiple comparisons test (w17)	Statistics	Adjusted P Value
EBOV GPΔmuc-WL^{2}P^4 trimer vs. EBOV GPΔmuc-WL^{2}P^4 E2p SApNP	ns	0.9938
EBOV GPΔmuc-WL^{2}P^4 trimer vs. EBOV GPΔmuc-WL^{2}P^4 I3-01v9b SApNP	ns	0.618
EBOV GPΔmuc-WL^{2}P^4 E2p SApNP vs. EBOV GPΔmuc-WL^{2}P^4 I3-01v9b SApNP	ns	0.6831

g Week-17 sera of individual mice immunized with EBOV vaccines neutralizing a SUDV Gulu strain

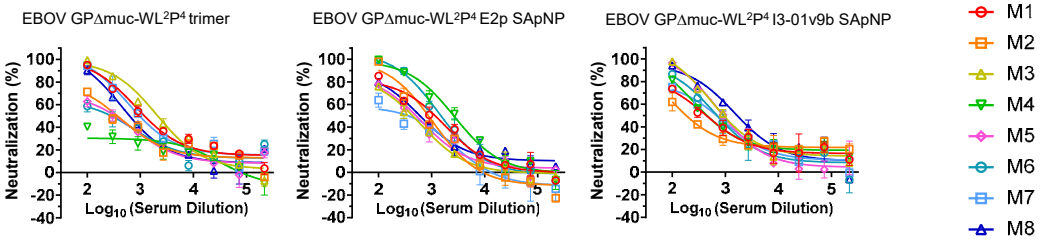

Mouse serum neutralizing ID_{50} titers

	Antigen	ID50 titers (week 17)								Geometric Mean
		M1	M2	M3	M4	M5	M6	M7	M8	
Week 17	EBOV GPΔmuc-WL^{2}P^4 trimer	1530.0	407.3	2200.0	113.8	341.2	323.2	1236.0	726.5	593.8
	EBOV GPΔmuc-WL^{2}P^4 E2p SApNP	956.0	759.0	403.8	2580.0	489.0	1564.0	301.3	647.6	761.3
	EBOV GPΔmuc-WL^{2}P^4 I3-01v9b SApNP	512.3	265.2	1198.0	608.8	1006.0	765.2	662.5	1824.0	742.3

Statistical analysis

One-way ANOVA with Tukey's multiple comparisons test (w17)	Statistics	Adjusted P Value
EBOV GPΔmuc-WL^{2}P^4 trimer vs. EBOV GPΔmuc-WL^{2}P^4 E2p SApNP	ns	0.9497
EBOV GPΔmuc-WL^{2}P^4 trimer vs. EBOV GPΔmuc-WL^{2}P^4 I3-01v9b SApNP	ns	>0.9999
EBOV GPΔmuc-WL^{2}P^4 E2p SApNP vs. EBOV GPΔmuc-WL^{2}P^4 I3-01v9b SApNP	ns	0.9453

h Week-17 sera of individual mice immunized with EBOV vaccines neutralizing a BDBV Uganda strain

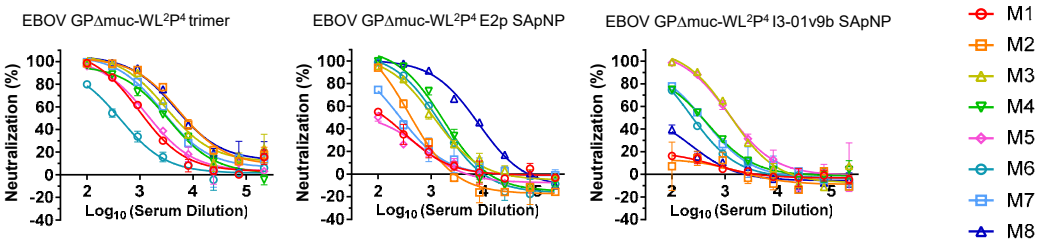

Mouse serum neutralizing ID_{50} titers

	Antigen	ID50 titers (week 17)								Geometric Mean
		M1	M2	M3	M4	M5	M6	M7	M8	
Week 17	EBOV GPΔmuc-WL^{2}P^4 trimer	1344.0	7809.0	5137.0	3217.0	1631.0	411.3	3729.0	7747.0	2759.4
	EBOV GPΔmuc-WL^{2}P^4 E2p SApNP	149.6	394.3	1109.0	1525.0	115.1	1174.0	261.1	5895.0	616.1
	EBOV GPΔmuc-WL^{2}P^4 I3-01v9b SApNP	<100	<100	1332.0	356.1	1397.0	240.1	352.0	<100	561.9

Statistical analysis

One-way ANOVA with Tukey's multiple comparisons test (w17)	Statistics	Adjusted P Value
EBOV GPΔmuc-WL^{2}P^4 trimer vs. EBOV GPΔmuc-WL^{2}P^4 E2p SApNP	*	0.0469
EBOV GPΔmuc-WL^{2}P^4 trimer vs. EBOV GPΔmuc-WL^{2}P^4 I3-01v9b SApNP	**	0.0076
EBOV GPΔmuc-WL^{2}P^4 E2p SApNP vs. EBOV GPΔmuc-WL^{2}P^4 I3-01v9b SApNP	ns	0.6882

Fig. S10

i Sera of individual mice immunized with SUDV vaccines binding to SUDV GPΔmuc-WL^{2}P^4(1TD0) trimer

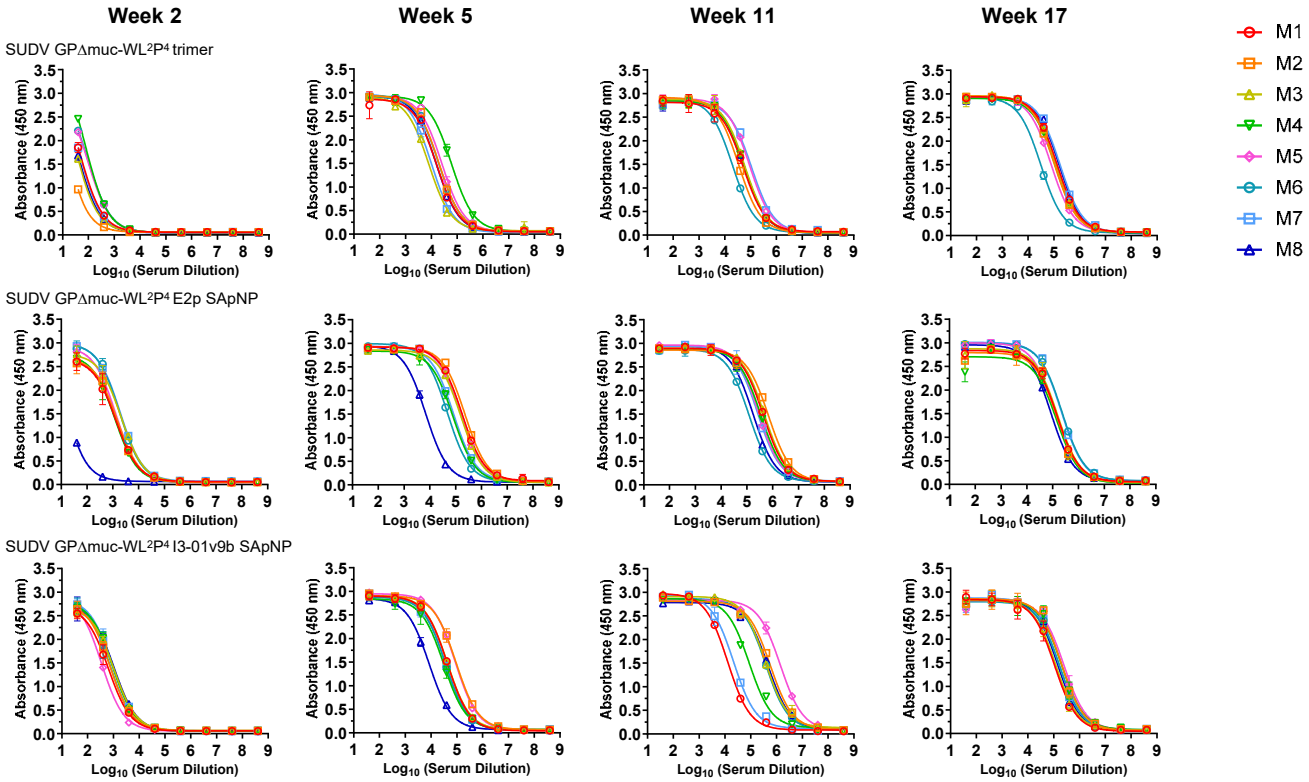

j Mouse serum ELISA EC_{50} titers

Week 2

Antigen	EC50 titers (week 2)								Geometric Mean
	M1	M2	M3	M4	M5	M6	M7	M8	
SUDV GPΔmuc-WL^{2}P^4 trimer	69.8	20.2	50.0	149.7	116.9	122.4	68.1	55.0	69.8
SUDV GPΔmuc-WL^{2}P^4 E2p SApNP	1058.0	1223.0	1977.0	1062.0	1419.0	2123.0	2262.0	17.9	871.0
SUDV GPΔmuc-WL^{2}P^4 I3-01v9b SApNP	550.3	700.2	876.2	893.5	373.7	741.1	903.2	940.0	718.4

Week 5

Antigen	EC50 titers (week 5)								Geometric Mean
	M1	M2	M3	M4	M5	M6	M7	M8	
SUDV GPΔmuc-WL^{2}P^4 trimer	16436	19941	7907	60277	25656	19754	9992	15619	18259.2
SUDV GPΔmuc-WL^{2}P^4 E2p SApNP	177305	230404	159220	79353	157784	47895	82714	6921	82910.4
SUDV GPΔmuc-WL^{2}P^4 I3-01v9b SApNP	42731	93470	42715	31125	87027	36180	35115	8482	38650.3

Week 11

Antigen	EC50 titers (week 11)								Geometric Mean
	M1	M2	M3	M4	M5	M6	M7	M8	
SUDV GPΔmuc-WL^{2}P^4 trimer	51852	34819	59219	58035	92570	20182	108658	56856	53935.6
SUDV GPΔmuc-WL^{2}P^4 E2p SApNP	427238	688825	479499	349324	289258	121660	264183	173015	307186.5
SUDV GPΔmuc-WL^{2}P^4 I3-01v9b SApNP	12804	573418	373590	88061	1405850	379235	21591	471753	183962.3

Week 17

Antigen	EC50 titers (week 17)								Geometric Mean
	M1	M2	M3	M4	M5	M6	M7	M8	
SUDV GPΔmuc-WL^{2}P^4 trimer	132375	104284	117314	112501	78562	31328	174100	161747	102958.9
SUDV GPΔmuc-WL^{2}P^4 E2p SApNP	150503	150658	156743	142867	124345	229353	218325	86164	151148.0
SUDV GPΔmuc-WL^{2}P^4 I3-01v9b SApNP	108351	204158	120591	200895	248727	170555	157838	144221	163771.7

Statistical analysis

One-way ANOVA with Tukey's multiple comparisons test (w2)	Statistics	Adjusted P Value
SUDV GPΔmuc-WL^{2}P^4 trimer vs. SUDV GPΔmuc-WL^{2}P^4 E2p SApNP	****	<0.0001
SUDV GPΔmuc-WL^{2}P^4 trimer vs. SUDV GPΔmuc-WL^{2}P^4 I3-01v9b SApNP	*	0.0169
SUDV GPΔmuc-WL^{2}P^4 E2p SApNP vs. SUDV GPΔmuc-WL^{2}P^4 I3-01v9b SApNP	*	0.0207

One-way ANOVA with Tukey's multiple comparisons test (w5)	Statistics	Adjusted P Value
SUDV GPΔmuc-WL^{2}P^4 trimer vs. SUDV GPΔmuc-WL^{2}P^4 E2p SApNP	**	0.0016
SUDV GPΔmuc-WL^{2}P^4 trimer vs. SUDV GPΔmuc-WL^{2}P^4 I3-01v9b SApNP	ns	0.5472
SUDV GPΔmuc-WL^{2}P^4 E2p SApNP vs. SUDV GPΔmuc-WL^{2}P^4 I3-01v9b SApNP	*	0.0187

One-way ANOVA with Tukey's multiple comparisons test (w11)	Statistics	Adjusted P Value
SUDV GPΔmuc-WL^{2}P^4 trimer vs. SUDV GPΔmuc-WL^{2}P^4 E2p SApNP	ns	0.1259
SUDV GPΔmuc-WL^{2}P^4 trimer vs. SUDV GPΔmuc-WL^{2}P^4 I3-01v9b SApNP	ns	0.0502
SUDV GPΔmuc-WL^{2}P^4 E2p SApNP vs. SUDV GPΔmuc-WL^{2}P^4 I3-01v9b SApNP	ns	0.885

One-way ANOVA with Tukey's multiple comparisons test (w17)	Statistics	Adjusted P Value
SUDV GPΔmuc-WL^{2}P^4 trimer vs. SUDV GPΔmuc-WL^{2}P^4 E2p SApNP	ns	0.1724
SUDV GPΔmuc-WL^{2}P^4 trimer vs. SUDV GPΔmuc-WL^{2}P^4 I3-01v9b SApNP	ns	0.0653
SUDV GPΔmuc-WL^{2}P^4 E2p SApNP vs. SUDV GPΔmuc-WL^{2}P^4 I3-01v9b SApNP	ns	0.8627

k Week-17 sera of individual mice immunized with SUDV vaccines binding to EBOV GPΔmuc-WL^{2}P^4(1TD0) trimer

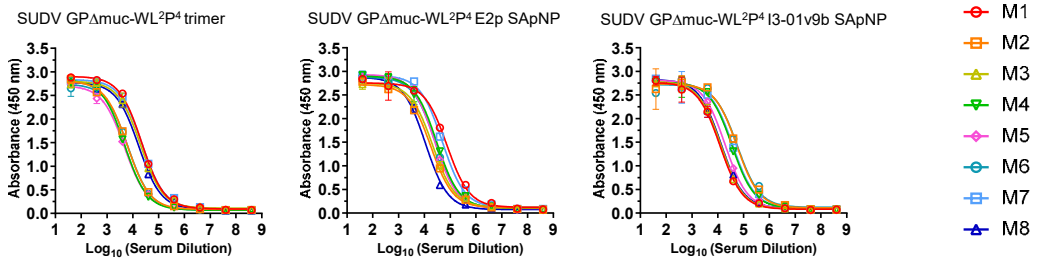

Mouse serum ELISA EC_{50} titers

	Antigen	EC50 titers (week 17)								Geometric Mean
		M1	M2	M3	M4	M5	M6	M7	M8	
Week 17	SUDV GPΔmuc-WL^{2}P^4 trimer	22131	6105	19939	4814	4809	6529	22832	16822	10574.9
	SUDV GPΔmuc-WL^{2}P^4 E2p SApNP	74857	17696	20913	30182	25142	26898	49408	11012	27290.2
	SUDV GPΔmuc-WL^{2}P^4 I3-01v9b SApNP	12210	55319	13273	35138	19190	57302	38054	13336	25446.4

Statistical analysis

One-way ANOVA with Tukey's multiple comparisons test (w17)	Statistics	Adjusted P Value
SUDV GPΔmuc-WL^{2}P^4 trimer vs. SUDV GPΔmuc-WL^{2}P^4 E2p SApNP	ns	0.0832
SUDV GPΔmuc-WL^{2}P^4 trimer vs. SUDV GPΔmuc-WL^{2}P^4 I3-01v9b SApNP	ns	0.1177
SUDV GPΔmuc-WL^{2}P^4 E2p SApNP vs. SUDV GPΔmuc-WL^{2}P^4 I3-01v9b SApNP	ns	0.9817

l Week-17 sera of individual mice immunized with SUDV vaccines binding to RAVV GPΔmuc-P^{2}CT(1TD0) trimer

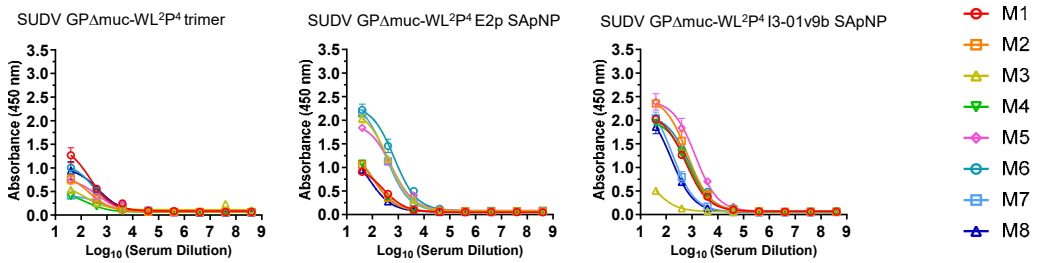

Mouse serum ELISA EC_{50} titers

	Antigen	Absorbance (450 nm) (week 17)								Geometric Mean
		M1	M2	M3	M4	M5	M6	M7	M8	
Week 17	SUDV GPΔmuc-WL^{2}P^4 trimer	1.3	0.8	0.5	0.4	0.7	1.0	0.4	0.9	0.7
	SUDV GPΔmuc-WL^{2}P^4 E2p SApNP	0.9	1.1	2.0	1.1	1.8	2.2	2.1	1.0	1.4
	SUDV GPΔmuc-WL^{2}P^4 I3-01v9b SApNP	2.0	2.4	0.5	1.9	2.4	2.0	2.0	1.9	1.7

Statistical analysis

One-way ANOVA with Tukey's multiple comparisons test (w17)	Statistics	Adjusted P Value
SUDV GPΔmuc-WL^{2}P^4 trimer vs. SUDV GPΔmuc-WL^{2}P^4 E2p SApNP	*	0.0149
SUDV GPΔmuc-WL^{2}P^4 trimer vs. SUDV GPΔmuc-WL^{2}P^4 I3-01v9b SApNP	***	0.0005
SUDV GPΔmuc-WL^{2}P^4 E2p SApNP vs. SUDV GPΔmuc-WL^{2}P^4 I3-01v9b SApNP	ns	0.338

m Sera of individual mice immunized with SUDV vaccines neutralizing a SUDV Gulu strain

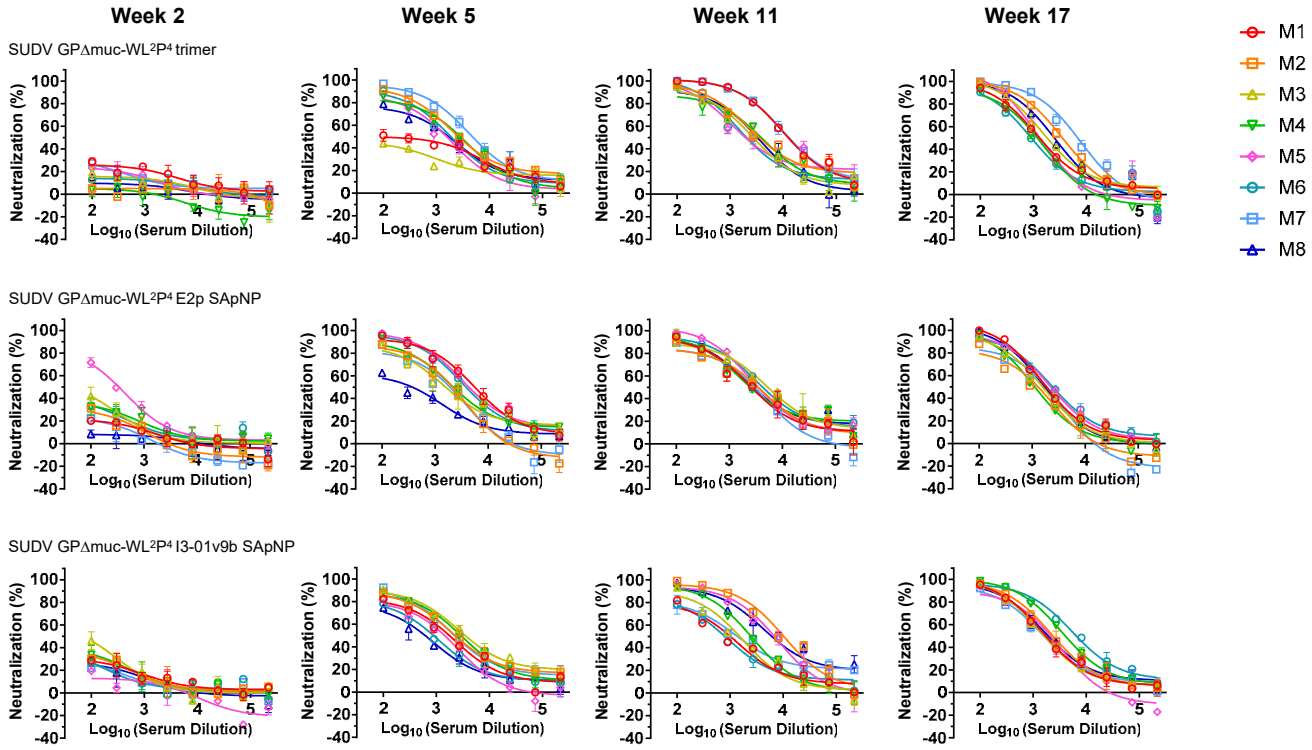

n Mouse serum neutralizing ID_{50} titers

Week 2

Antigen	ID50 titers (week 2)								Geometric Mean
	M1	M2	M3	M4	M5	M6	M7	M8	
SUDV GPΔmuc-WL^{2}P^4 trimer	<100	<100	<100	<100	<100	<100	<100	<100	N/A
SUDV GPΔmuc-WL^{2}P^4 E2p SApNP	<100	<100	<100	<100	331.1	<100	<100	<100	N/A
SUDV GPΔmuc-WL^{2}P^4 I3-01v9b SApNP	<100	<100	107.2	<100	<100	<100	<100	<100	N/A

Week 5

Antigen	ID50 titers (week 5)								Geometric Mean
	M1	M2	M3	M4	M5	M6	M7	M8	
SUDV GPΔmuc-WL^{2}P^4 trimer	420	3076	156.6	2417	1377	1896	5149	1477	1328.6
SUDV GPΔmuc-WL^{2}P^4 E2p SApNP	5677	1634	1754	2420	5081	4212	1332	355.5	2114.1
SUDV GPΔmuc-WL^{2}P^4 I3-01v9b SApNP	1582	2485	4102	2862	1119	843.6	2506	584.4	1681.2

Week 11

Antigen	ID50 titers (week 11)								Geometric Mean
	M1	M2	M3	M4	M5	M6	M7	M8	
SUDV GPΔmuc-WL^{2}P^4 trimer	13810	4694	2805	3670	2858	2497	14410	3069	4628.4
SUDV GPΔmuc-WL^{2}P^4 E2p SApNP	2835	3130	5528	3311	3940	4935	2323	3352	3538.7
SUDV GPΔmuc-WL^{2}P^4 I3-01v9b SApNP	889.3	10154	1391	2424	6257	808.9	1524	7608	2549.8

Week 17

Antigen	ID50 titers (week 17)								Geometric Mean
	M1	M2	M3	M4	M5	M6	M7	M8	
SUDV GPΔmuc-WL^{2}P^4 trimer	1389	3550	2017	1006	1354	931.1	6329	2409	1929.8
SUDV GPΔmuc-WL^{2}P^4 E2p SApNP	2035	928.9	1546	1147	2291	2536	1215	1753	1593.1
SUDV GPΔmuc-WL^{2}P^4 I3-01v9b SApNP	1853	2507	1746	4395	1648	7166	1695	2160	2503.1

Statistical analysis

One-way ANOVA with Tukey's multiple comparisons test (w5)	Statistics	Adjusted P Value
SUDV GPΔmuc-WL^{2}P^4 trimer vs. SUDV GPΔmuc-WL^{2}P^4 E2p SApNP	ns	0.5769
SUDV GPΔmuc-WL^{2}P^4 trimer vs. SUDV GPΔmuc-WL^{2}P^4 I3-01v9b SApNP	ns	0.9998
SUDV GPΔmuc-WL^{2}P^4 E2p SApNP vs. SUDV GPΔmuc-WL^{2}P^4 I3-01v9b SApNP	ns	0.5879

One-way ANOVA with Tukey's multiple comparisons test (w11)	Statistics	Adjusted P Value
SUDV GPΔmuc-WL^{2}P^4 trimer vs. SUDV GPΔmuc-WL^{2}P^4 E2p SApNP	ns	0.4294
SUDV GPΔmuc-WL^{2}P^4 trimer vs. SUDV GPΔmuc-WL^{2}P^4 I3-01v9b SApNP	ns	0.4956
SUDV GPΔmuc-WL^{2}P^4 E2p SApNP vs. SUDV GPΔmuc-WL^{2}P^4 I3-01v9b SApNP	ns	0.9925

One-way ANOVA with Tukey's multiple comparisons test (w17)	Statistics	Adjusted P Value
SUDV GPΔmuc-WL^{2}P^4 trimer vs. SUDV GPΔmuc-WL^{2}P^4 E2p SApNP	ns	0.6592
SUDV GPΔmuc-WL^{2}P^4 trimer vs. SUDV GPΔmuc-WL^{2}P^4 I3-01v9b SApNP	ns	0.7862
SUDV GPΔmuc-WL^{2}P^4 E2p SApNP vs. SUDV GPΔmuc-WL^{2}P^4 I3-01v9b SApNP	ns	0.2916

O Week-17 sera of individual mice immunized with SUDV vaccines neutralizing an EBOV Makona strain

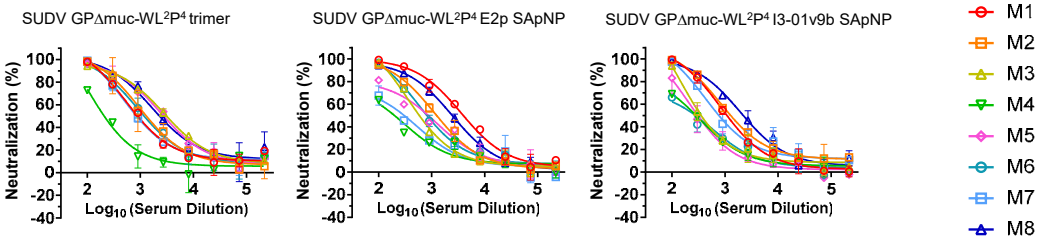

Mouse serum neutralizing ID_{50} titers

	Antigen	ID50 titers (week 17)								Geometric Mean
		M1	M2	M3	M4	M5	M6	M7	M8	
Week 17	SUDV GPΔmuc-WL^{2}P^4 trimer	1073	1510	3312	230.5	2932	1345	1075	2621	1387.6
	SUDV GPΔmuc-WL^{2}P^4 E2p SApNP	4144	1304	687.5	217	758.8	964.7	297	2453	899.9
	SUDV GPΔmuc-WL^{2}P^4 I3-01v9b SApNP	1214	1567	467.4	296.9	336.4	271	990.7	2370	698.3

Statistical analysis

One-way ANOVA with Tukey's multiple comparisons test (w17)	Statistics	Adjusted P Value
SUDV GPΔmuc-WL^{2}P^4 trimer vs. SUDV GPΔmuc-WL^{2}P^4 E2p SApNP	ns	0.7312
SUDV GPΔmuc-WL^{2}P^4 trimer vs. SUDV GPΔmuc-WL^{2}P^4 I3-01v9b SApNP	ns	0.2983
SUDV GPΔmuc-WL^{2}P^4 E2p SApNP vs. SUDV GPΔmuc-WL^{2}P^4 I3-01v9b SApNP	ns	0.7257

P Week-17 sera of individual mice immunized with SUDV vaccines neutralizing a BDBV Uganda strain

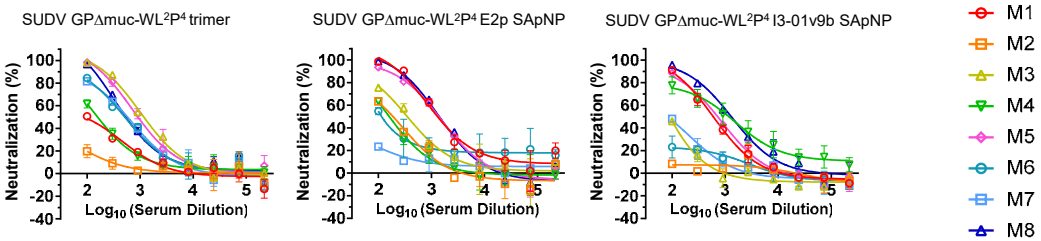

Mouse serum neutralizing ID_{50} titers

	Antigen	ID50 titers (week 17)								Geometric Mean
		M1	M2	M3	M4	M5	M6	M7	M8	
Week 17	SUDV GPΔmuc-WL^{2}P^4 trimer	126.7	26.1	1237.0	165.3	985.6	518.9	543.9	613.3	322.0
	SUDV GPΔmuc-WL^{2}P^4 E2p SApNP	1504.0	174.5	356.0	156.5	1298.0	151.8	35.5	1393.0	330.6
	SUDV GPΔmuc-WL^{2}P^4 I3-01v9b SApNP	580.4	9.7	69.0	1085.0	656.4	<100	<100	1280.0	185.5

Statistical analysis

One-way ANOVA with Tukey's multiple comparisons test (w17)	Statistics	Adjusted P Value
SUDV GPΔmuc-WL^{2}P^4 trimer vs. SUDV GPΔmuc-WL^{2}P^4 E2p SApNP	ns	0.913
SUDV GPΔmuc-WL^{2}P^4 trimer vs. SUDV GPΔmuc-WL^{2}P^4 I3-01v9b SApNP	ns	0.9893
SUDV GPΔmuc-WL^{2}P^4 E2p SApNP vs. SUDV GPΔmuc-WL^{2}P^4 I3-01v9b SApNP	ns	0.8492

q Sera of individual mice immunized with RAVV vaccines binding to RAVV GPΔmuc-P²CT(1TD0) trimer

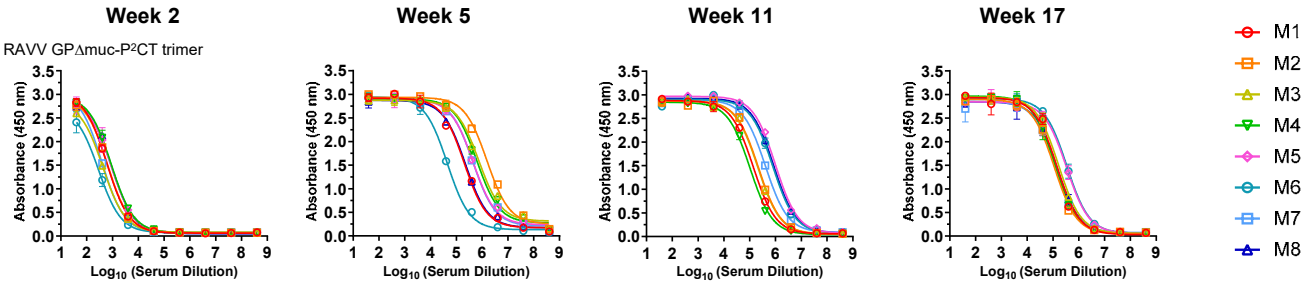

Mouse serum ELISA EC_{50} titers

Antigen	EC50 titers								Geometric Mean
	M1	M2	M3	M4	M5	M6	M7	M8	
RAVV GPΔmuc-P²CT trimer-w2	718.9	721.9	432.3	1030.0	946.3	262.3	481.5	958.5	635.1
RAVV GPΔmuc-P²CT trimer-w5	202735	1544554	746406	628189	447117	44771	446178	225949	362215.2
RAVV GPΔmuc-P²CT trimer-w11	139135	218951	208199	104125	998580	786127	408247	853062	340466.6
RAVV GPΔmuc-P²CT trimer-w17	140811	110900	164905	119990	336478	344895	127509	141835	168457.1

r Week-17 sera of individual mice immunized with RAVV vaccines binding to EBOV GPΔmuc-WL²P⁴(1TD0) trimer

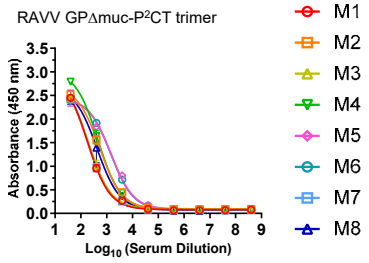

Mouse serum ELISA EC_{50} titers

Antigen	EC50 titers (week 17)								Geometric Mean
	M1	M2	M3	M4	M5	M6	M7	M8	
RAVV GPΔmuc-P²CT trimer	177.5	537.5	197.8	459.9	1477.0	1430.0	182.7	422.8	440.4

s Week-17 sera of individual mice immunized with RAVV vaccines binding to SUDV GPΔmuc-WL²P⁴(1TD0) trimer

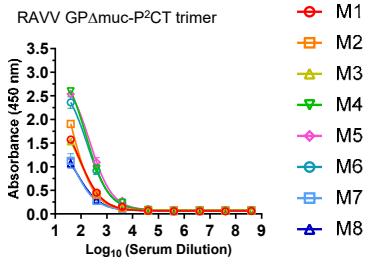

Mouse serum ELISA EC_{50} titers

Antigen	Absorbance (450 nm) (week 17)								Geometric Mean
	M1	M2	M3	M4	M5	M6	M7	M8	
RAVV GPΔmuc-P²CT trimer	1.6	1.9	1.5	2.6	2.5	2.4	2.4	2.4	2.1

t Week-17 IgG samples of individual mice immunized with RAVV vaccines neutralizing a MARV Angola strain

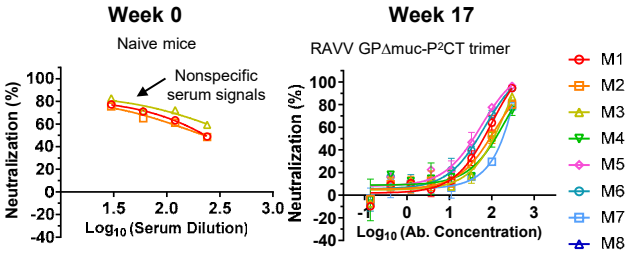

Week 17 mouse IgG neutralization

Virus strains	IC50 (μg/mL)								Geometric Mean
	M1	M2	M3	M4	M5	M6	M7	M8	
MARV-Angola	56.2	81.4	93.3	104.4	30.9	40.3	148.4	71.8	70.2

u Week-17 sera of individual mice immunized with RAVV vaccines neutralizing three ebolavirus strains

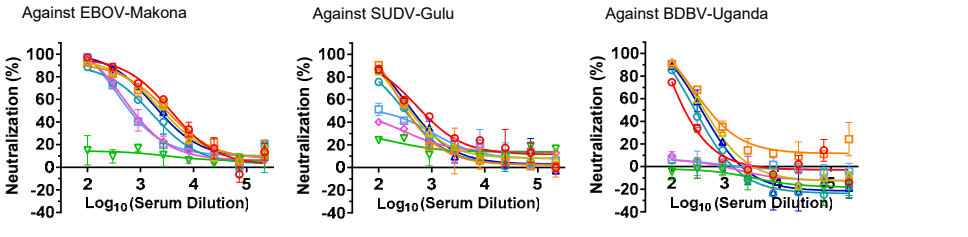

Fig. S10. Immunogenicity of EBOV, SUDV, and RAVV GPΔmuc vaccines in mice. (**a**) ELISA curves of mouse sera from EBOV GPΔmuc trimer and SApNP vaccine groups (n = 8 mice/group) binding to the coating antigen, EBOV GPΔmuc-WL^2P^4(1TD0) trimer (**b**) (Top) Summary of geometric means of EC_{50} titers measured for Ebola GPΔmuc vaccine groups against EBOV GPΔmuc-WL^2P^4(1TD0) trimer. Color coding indicates the level of EC_{50} titers (green to red: low to high binding). (Bottom) Summary of statistical analysis performed for each timepoint. Of note, the EC_{50} values at week 2 were derived by setting the minimum/maximum OD_{450} values to 0.0/2.8. (**c**) ELISA curves of mouse sera from EBOV GPΔmuc vaccine groups at week 17 after four immunizations binding to SUDV GPΔmuc-WL^2P^4(1TD0) trimer. Summary of geometric means of EC_{50} titers and statistical analysis. (**d**) ELISA curves of mouse sera from Ebola GPΔmuc vaccine groups at week 17 after four immunizations binding to RAVV GPΔmuc-P^2CT(1TD0) trimer. Summary of absorbance at 450 nm (A450) values was included. (**e**) Neutralization curves of mouse sera from EBOV GPΔmuc trimer and SApNP vaccine groups against EBOV Makona pseudovirus. (**f**) (Top) Summary of geometric means of ID_{50} titers measured for EBOV GPΔmuc vaccine groups against EBOV Makona pseudovirus. Color coding indicates the level of ID_{50} titers (white: no neutralization; green to red: low to high neutralization). Of note, the ID_{50} values were derived by setting the minimum/maximum %neutralization to 0.0/100.0 as constraints. (Bottom) Summary of statistical analysis as in (**b**). (**g**) Neutralization curves of mouse sera from EBOV GPΔmuc vaccine groups at week 17 against SUDV Gulu pseudovirus. Summary of geometric means of ID_{50} values and statistical analysis. (**h**) Neutralization curves of mouse sera from EBOV GPΔmuc vaccine groups at week 17 against BDBV Uganda pseudovirus. Summary of geometric means of ID_{50} values and statistical analysis. (**i**) ELISA curves of mouse sera from SUDV GPΔmuc trimer and SApNP vaccine groups binding to SUDV GPΔmuc-WL^2P^4(1TD0) trimer. (**j**) (Top) Summary of geometric means of EC_{50} titers measured for SUDV GPΔmuc vaccine groups against SUDV GPΔmuc-WL^2P^4(1TD0) trimer. (Bottom) Summary of statistical analysis as in (**b**). Of note, the EC_{50} values at week 2 were derived by setting the minimum/maximum OD_{450} values to 0.0/2.9. (**k**) ELISA curves of mouse sera from SUDV GPΔmuc vaccine groups at week 17 after four immunizations binding to EBOV GPΔmuc-WL^2P^4(1TD0) trimer. Summary of geometric means of EC_{50} titers and statistical analysis. (**l**) ELISA curves of mouse sera from SUDV GPΔmuc vaccine groups at week 17 after four immunizations binding to RAVV GPΔmuc-P^2CT(1TD0) trimer. Summary of A450 values was included. (**m**) Neutralization curves of mouse sera from SUDV GPΔmuc trimer and SApNP vaccine groups against SUDV Gulu pseudovirus. (**n**) (Top) Summary of geometric means of ID_{50} titers measured for EBOV GPΔmuc vaccine groups against EBOV Makona pseudovirus. (Bottom) Summary of statistical analysis as in (**b**). (**o**) Neutralization curves of mouse sera from EBOV GPΔmuc vaccine groups at week 17 against EBOV Makona pseudovirus. Summary of geometric means of ID_{50} values and statistical analysis. (**p**) Neutralization curves of mouse sera from EBOV GPΔmuc vaccine groups at week 17 against BDBV Uganda pseudovirus. Summary of geometric means of ID_{50} values and statistical analysis. (**q**) (Top) ELISA curves of mouse sera from RAVV GPΔmuc trimer vaccine groups binding to RAVV GPΔmuc-P^2CT(1TD0) trimer. (Bottom) Summary of geometric means of EC_{50} values. Of note, the EC_{50} values at week 2 were derived by setting the minimum/maximum OD_{450} values to 0.0/2.9. (**r**) ELISA curves of mouse sera from RAVV GPΔmuc vaccine groups at week 17 after four immunizations binding to EBOV GPΔmuc-WL^2P^4(1TD0) trimer. Summary of geometric means of EC_{50} titers. (**s**) ELISA curves of mouse sera from RAVV GPΔmuc vaccine groups at week 17 after four immunizations binding to SUDV GPΔmuc-WL^2P^4(1TD0) trimer. Summary of A450 values was included. (**t**) Neutralization curves of purified IgG from RAVV GPΔmuc vaccine groups at week 17 against MARV Angola pseudovirus. Summary of IC_{50} values. Left panel: sera from three naive mice showed nonspecific background in MARV Angola pseudovirus assays, suggesting that IgG purification is required to eliminate the nonspecific serum reactivity. (**u**) Neutralization curves of mouse sera from RAVV GPΔmuc vaccine groups at week 17 against various ebolavirus strains. Error bars represent the difference between these duplicate values at each concentration tested for each sample. EC_{50}, ID_{50}, and IC_{50} values were calculated in GraphPad Prism 10.3.1. Data were analyzed using one-way ANOVA, followed by Tukey's multiple comparison post hoc test for each timepoint. For significance, ns (not significant), $^*p < 0.05$, $^{**}p < 0.01$, $^{***}p < 0.001$, and $^{****}p < 0.0001$.

Figure S11

a **Sera of individual mice immunized with glycan-modified EBOV vaccines binding to EBOV GPΔmuc-WL^{2}P^4(1TD0) trimer**

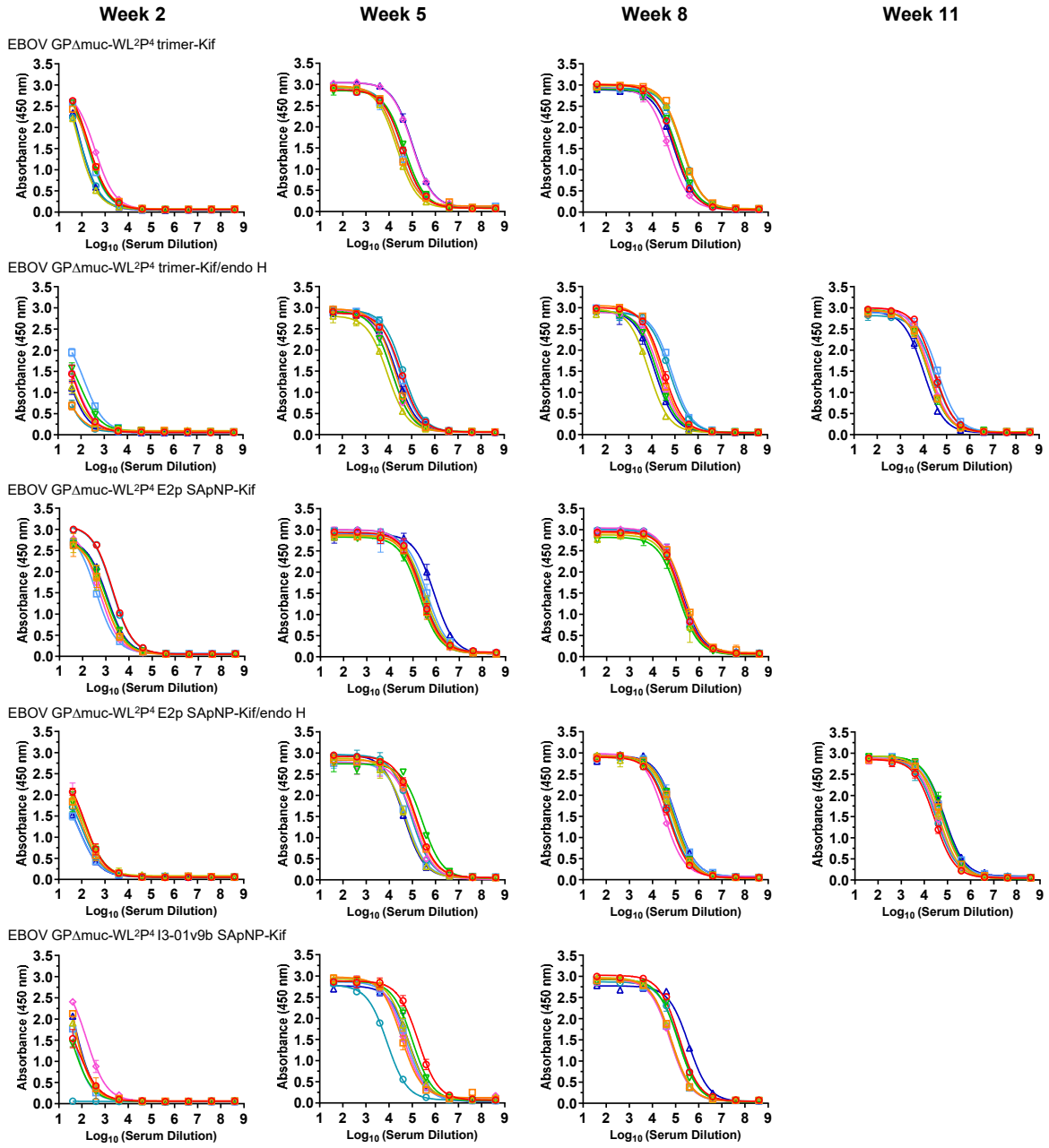

Figure S11

b Mouse serum ELISA EC_{50} titers

Week 2

Antigen	EC50 titers (week 2)								Geometric Mean
	M1	M2	M3	M4	M5	M6	M7	M8	
EBOV GPΔmuc-WL^{2}P^4 trimer	111.7	136.3	51.3	227.2	103.0	200.2	12.6	173.3	97.3
EBOV GPΔmuc-WL^{2}P^4 trimer-Kif	283.7	255.1	119.5	248.0	423.8	133.4	239.1	141.3	212.1
EBOV GPΔmuc-WL^{2}P^4 trimer-Kif/endo H	43.1	13.4	28.4	56.2	46.5	14.1	106.9	26.8	33.8
EBOV GPΔmuc-WL^{2}P^4 E2p SApNP	985.3	706.4	970.8	1772.0	271.5	336.1	3145.0	486.4	799.6
EBOV GPΔmuc-WL^{2}P^4 E2p SApNP-Kif	2721.0	813.3	815.7	1046.0	678.3	2584.0	482.5	1166.0	1080.8
EBOV GPΔmuc-WL^{2}P^4 E2p SApNP-Kif/endo H	126.0	84.5	104.9	95.8	122.8	69.1	50.0	51.4	83.4
EBOV GPΔmuc-WL^{2}P^4 I3-01v9b SApNP	30.1	101.8	43.0	37.9	172.4	80.7	91.5	115.6	72.1
EBOV GPΔmuc-WL^{2}P^4 I3-01v9b SApNP-Kif	51.8	97.6	80.2	41.8	201.5	0.9	62.9	95.3	45.5

Week 5

Antigen	EC50 titers (week 5)								Geometric Mean
	M1	M2	M3	M4	M5	M6	M7	M8	
EBOV GPΔmuc-WL^{2}P^4 trimer	52545	41735	104914	48787	27947	18271	26144	21434	36588
EBOV GPΔmuc-WL^{2}P^4 trimer-Kif	38706	25086	21695	47634	99875	36855	27014	103907	42360
EBOV GPΔmuc-WL^{2}P^4 trimer-Kif/endo H	35186	18238	8909	13634	13630	41752	29227	22113	20285
EBOV GPΔmuc-WL^{2}P^4 E2p SApNP	199849	120954	303168	237335	74446	156667	282413	368341	195227
EBOV GPΔmuc-WL^{2}P^4 E2p SApNP-Kif	241215	224657	335618	192147	216173	258075	406613	838779	300502
EBOV GPΔmuc-WL^{2}P^4 E2p SApNP-Kif/endo H	141920	136153	48617	265817	117352	88543	56725	42434	94286
EBOV GPΔmuc-WL^{2}P^4 I3-01v9b SApNP	58458	93275	140476	104463	128829	148277	70114	63709	95342
EBOV GPΔmuc-WL^{2}P^4 I3-01v9b SApNP-Kif	180905	34224	63566	102618	42941	8255	57374	74974	52927

Week 11 or 8

Antigen	EC50 titers (week 11 or 8)								Geometric Mean
	M1	M2	M3	M4	M5	M6	M7	M8	
EBOV GPΔmuc-WL^{2}P^4 trimer-w11	26545	524033	69054	94400	39464	69865	68351	51944	73881
EBOV GPΔmuc-WL^{2}P^4 trimer-Kif-w8	93214	195305	183599	116631	50918	193472	114590	89398	118674
EBOV GPΔmuc-WL^{2}P^4 trimer-Kif/endo H-w8	31571	25030	7454	16954	21834	59045	72580	13927	24508
EBOV GPΔmuc-WL^{2}P^4 E2p SApNP-w11	267135	163352	223491	606328	32762	143908	182928	233182	181722
EBOV GPΔmuc-WL^{2}P^4 E2p SApNP-Kif-w8	153387	211525	149619	126857	158759	131151	152440	176520	155680
EBOV GPΔmuc-WL^{2}P^4 E2p SApNP-Kif/endo H-w8	50455	81205	73372	89472	32112	55202	99817	102711	68571
EBOV GPΔmuc-WL^{2}P^4 I3-01v9b SApNP-w11	703967	60730	178784	354031	97482	91294	82827	610293	182253
EBOV GPΔmuc-WL^{2}P^4 I3-01v9b SApNP-Kif-w8	146649	66233	62594	129059	58475	142777	61089	366113	104890

Statistical analysis

One-way ANOVA with Tukey's multiple comparisons test (w2)	Statistics	Adjusted P Value
EBOV GPΔmuc-WL^{2}P^4 trimer vs. EBOV GPΔmuc-WL^{2}P^4 trimer-Kif	*	0.0276
EBOV GPΔmuc-WL^{2}P^4 trimer vs. EBOV GPΔmuc-WL^{2}P^4 trimer-Kif/endo H	ns	0.0775
EBOV GPΔmuc-WL^{2}P^4 trimer-Kif vs. EBOV GPΔmuc-WL^{2}P^4 trimer-Kif/endo H	***	0.0001

One-way ANOVA with Tukey's multiple comparisons test (w5)	Statistics	Adjusted P Value
EBOV GPΔmuc-WL^{2}P^4 trimer vs. EBOV GPΔmuc-WL^{2}P^4 trimer-Kif	ns	0.8381
EBOV GPΔmuc-WL^{2}P^4 trimer vs. EBOV GPΔmuc-WL^{2}P^4 trimer-Kif/endo H	ns	0.2962
EBOV GPΔmuc-WL^{2}P^4 trimer-Kif vs. EBOV GPΔmuc-WL^{2}P^4 trimer-Kif/endo H	ns	0.1137

One-way ANOVA with Tukey's multiple comparisons test (w2)	Statistics	Adjusted P Value
EBOV GPΔmuc-WL^{2}P^4 E2p SApNP vs. EBOV GPΔmuc-WL^{2}P^4 E2p SApNP-Kif	ns	0.8496
EBOV GPΔmuc-WL^{2}P^4 E2p SApNP vs. EBOV GPΔmuc-WL^{2}P^4 E2p SApNP-Kif/endo H	*	0.0371
EBOV GPΔmuc-WL^{2}P^4 E2p SApNP-Kif vs. EBOV GPΔmuc-WL^{2}P^4 E2p SApNP-Kif/endo H	*	0.0112

One-way ANOVA with Tukey's multiple comparisons test (w5)	Statistics	Adjusted P Value
EBOV GPΔmuc-WL^{2}P^4 E2p SApNP vs. EBOV GPΔmuc-WL^{2}P^4 E2p SApNP-Kif	ns	0.2278
EBOV GPΔmuc-WL^{2}P^4 E2p SApNP vs. EBOV GPΔmuc-WL^{2}P^4 E2p SApNP-Kif/endo H	ns	0.3186
EBOV GPΔmuc-WL^{2}P^4 E2p SApNP-Kif vs. EBOV GPΔmuc-WL^{2}P^4 E2p SApNP-Kif/endo H	*	0.0119

Unpaired t test (w2)	Statistics	P Value
EBOV GPΔmuc-WL^{2}P^4 I3-01v9b SApNP vs. EBOV GPΔmuc-WL^{2}P^4 I3-01v9b SApNP-Kif	ns	0.8507

Unpaired t test (w5)	Statistics	P Value
EBOV GPΔmuc-WL^{2}P^4 I3-01v9b SApNP vs. EBOV GPΔmuc-WL^{2}P^4 I3-01v9b SApNP-Kif	ns	0.1978

Figure S11

C Sera of individual mice immunized with EBOV vaccines neutralizing an EBOV Makona strain

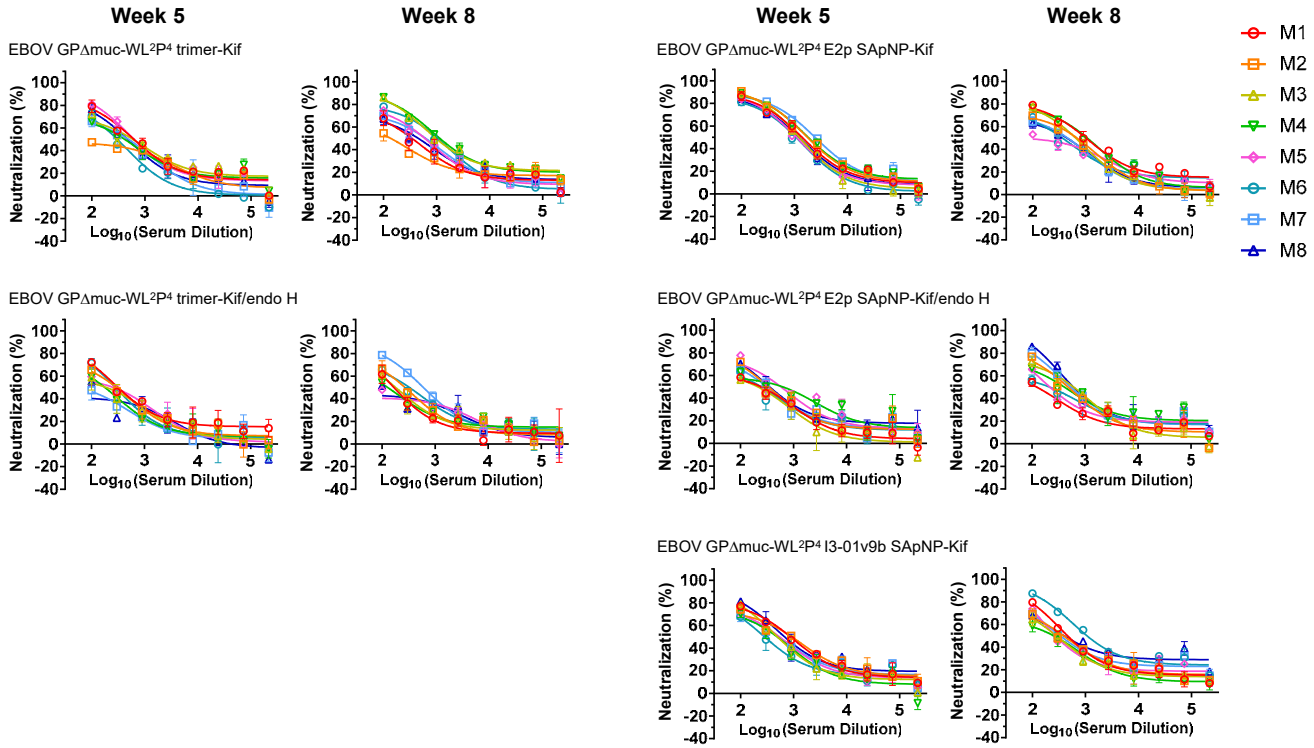

d Mouse serum neutralizing ID_{50} titers

Week 5

Antigen	ID50 titers (week 5)								Geometric Mean
	M1	M2	M3	M4	M5	M6	M7	M8	
EBOV GPΔmuc-WL^{2}P^4 trimer	805.4	559.3	149.3	588.2	174.1	145.1	203.2	360.5	304.1
EBOV GPΔmuc-WL^{2}P^4 trimer-Kif	685.5	234.7	577.4	443.0	708.5	285.4	407.7	489.1	449.3
EBOV GPΔmuc-WL^{2}P^4 trimer-Kif/endo H	383.7	299.7	227.6	199.9	271.6	298.0	132.4	145.5	231.2
EBOV GPΔmuc-WL^{2}P^4 E2p SApNP	636.9	358.8	2178.0	1002.0	555.2	322.9	299.4	1167.0	648.4
EBOV GPΔmuc-WL^{2}P^4 E2p SApNP-Kif	1414.0	1867.0	1249.0	1961.0	1107.0	963.3	2480.0	1201.0	1459.0
EBOV GPΔmuc-WL^{2}P^4 E2p SApNP-Kif/endo H	263.2	376.3	232.9	513.0	559.4	273.6	353.0	430.4	358.9
EBOV GPΔmuc-WL^{2}P^4 I3-01v9b SApNP	881.2	850.8	555.5	452.4	550.2	340.8	548.8	865.0	599.9
EBOV GPΔmuc-WL^{2}P^4 I3-01v9b SApNP-Kif	267.9	390.2	313.1	575.8	378.9	413.4	258.7	296.7	350.3

Week 11 or 8

Antigen	ID50 titers (week 11 or 8)								Geometric Mean
	M1	M2	M3	M4	M5	M6	M7	M8	
EBOV GPΔmuc-WL^{2}P^4 trimer-w11	2117.0	560.6	254.4	521.5	188.7	430.2	369.3	377.3	453.2
EBOV GPΔmuc-WL^{2}P^4 trimer-Kif-w8	370.3	204.5	1305	1425	578	911.8	569.1	448.8	609.1
EBOV GPΔmuc-WL^{2}P^4 trimer-Kif/endo H-w8	192.8	287.4	217.4	178.6	171.6	351.1	636.2	175.4	248.3
EBOV GPΔmuc-WL^{2}P^4 E2p SApNP-w11	494.5	392.0	734.2	747.4	275.3	643.8	365.2	759.9	518.6
EBOV GPΔmuc-WL^{2}P^4 E2p SApNP-Kif-w8	1031	562.3	594.7	902.2	273	393.9	416.3	408.9	524.1
EBOV GPΔmuc-WL^{2}P^4 E2p SApNP-Kif/endo H-w8	179.2	499.6	538.7	486.6	301.2	292.4	649.2	772.1	423.6
EBOV GPΔmuc-WL^{2}P^4 I3-01v9b SApNP-w11	1006.0	434.9	454.1	766.3	289.4	237.7	327.0	928.5	487.3
EBOV GPΔmuc-WL^{2}P^4 I3-01v9b SApNP-Kif-w8	562.9	429.3	326.9	281.2	376.1	1462	459.4	603.8	491.2

Statistical analysis

One-way ANOVA with Tukey's multiple comparisons test (w5)	Statistics	Adjusted P Value
EBOV GPΔmuc-WL^{2}P^4 trimer vs. EBOV GPΔmuc-WL^{2}P^4 trimer-Kif	ns	0.489
EBOV GPΔmuc-WL^{2}P^4 trimer vs. EBOV GPΔmuc-WL^{2}P^4 trimer-Kif/endo H	ns	0.3549
EBOV GPΔmuc-WL^{2}P^4 trimer-Kif vs. EBOV GPΔmuc-WL^{2}P^4 trimer-Kif/endo H	*	0.0453

One-way ANOVA with Tukey's multiple comparisons test (w5)	Statistics	Adjusted P Value
EBOV GPΔmuc-WL^{2}P^4 E2p SApNP vs. EBOV GPΔmuc-WL^{2}P^4 E2p SApNP-Kif	*	0.02
EBOV GPΔmuc-WL^{2}P^4 E2p SApNP vs. EBOV GPΔmuc-WL^{2}P^4 E2p SApNP-Kif/endo H	ns	0.1792
EBOV GPΔmuc-WL^{2}P^4 E2p SApNP-Kif vs. EBOV GPΔmuc-WL^{2}P^4 E2p SApNP-Kif/endo H	***	0.0003

Unpaired t test (w5)	Statistics	P Value
EBOV GPΔmuc-WL^{2}P^4 I3-01v9b SApNP vs. EBOV GPΔmuc-WL^{2}P^4 I3-01v9b SApNP-Kif	**	0.0055

Figure S11

e **Sera of individual mice immunized with wildtype/glycan-modified SUDV vaccines binding to SUDV GPΔmuc-WL^{2}P^4(1TD0) trimer**

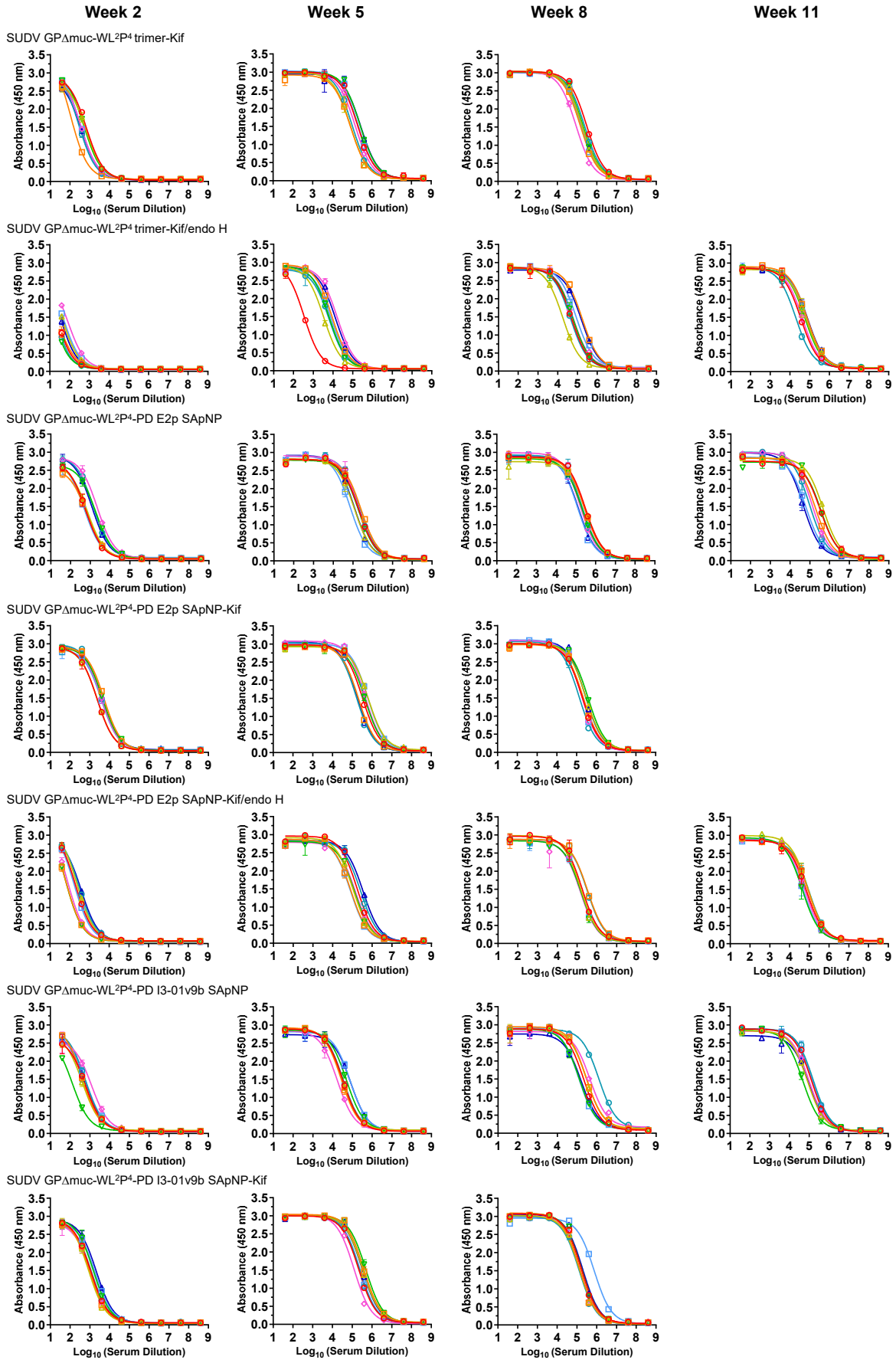

Figure S11

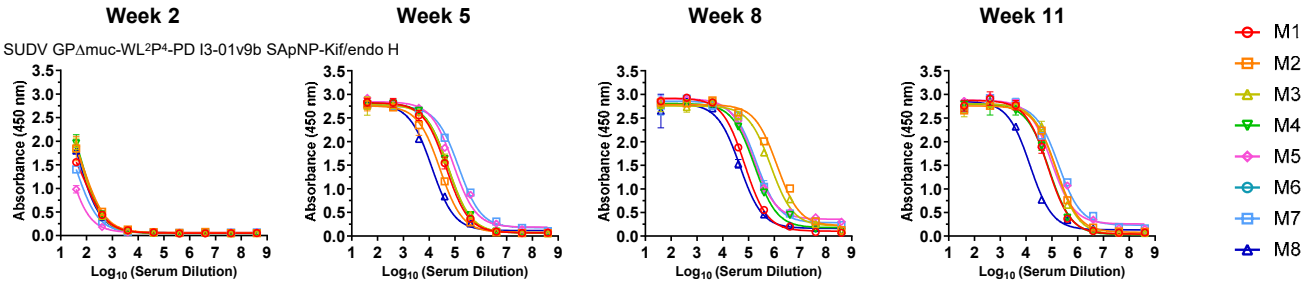

f Mouse serum ELISA EC_{50} titers

Week 2

Antigen	EC50 titers (week 2)								Geometric Mean
	M1	M2	M3	M4	M5	M6	M7	M8	
SUDV GPΔmuc-WL^{2}P^4 trimer	69.8	20.2	50.0	149.7	116.9	122.4	68.1	55.0	69.8
SUDV GPΔmuc-WL^{2}P^4 trimer-Kif	714.8	192.9	605.3	591.0	412.8	343.0	419.8	362.8	425.0
SUDV GPΔmuc-WL^{2}P^4 trimer-Kif/endo H	23.3	24.5	44.7	15.7	72.2	19.6	50.5	36.9	31.8
SUDV GPΔmuc-WL^{2}P^4-PD E2p SApNP	527.1	474.8	583.8	1483.0	2336.0	1545.0	475.4	1316.0	914.5
SUDV GPΔmuc-WL^{2}P^4-PD E2p SApNP-Kif	2482.0	5568.0	2483.0	4798.0	4273.0	4408.0	3878.0	4312.0	3884.6
SUDV GPΔmuc-WL^{2}P^4-PD E2p SApNP-Kif/endo H	271.0	99.3	330.9	99.8	124.0	375.7	234.7	410.6	211.4
SUDV GPΔmuc-WL^{2}P^4-PD I3-01v9b SApNP	469.6	479.9	387.3	115.2	890.0	616.4	586.8	503.1	448.2
SUDV GPΔmuc-WL^{2}P^4-PD I3-01v9b SApNP-Kif	1206.0	1067.0	961.1	1644.0	1098.0	1237.0	1839.0	2248.0	1355.8
SUDV GPΔmuc-WL^{2}P^4-PD I3-01v9b SApNP-Kif/endo H	49.8	73.8	77.8	80.5	20.8	N/A	38.4	65.2	53.1

Week 5

Antigen	EC50 titers (week 5)								Geometric Mean
	M1	M2	M3	M4	M5	M6	M7	M8	
SUDV GPΔmuc-WL^{2}P^4 trimer	16436	19941	7907	60277	25656	19754	9992	15619	18259.2
SUDV GPΔmuc-WL^{2}P^4 trimer-Kif	187796	83838	82374	256237	143796	100245	199748	272537	150326.2
SUDV GPΔmuc-WL^{2}P^4 trimer-Kif/endo H	337	8926	3406	6542	16601	6364	8124	13307	5439.3
SUDV GPΔmuc-WL^{2}P^4-PD E2p SApNP	194403	254967	120302	189915	195340	209194	72385	116111	158028.4
SUDV GPΔmuc-WL^{2}P^4-PD E2p SApNP-Kif	328808	203797	637646	429942	440079	160965	596309	178438	329358.5
SUDV GPΔmuc-WL^{2}P^4-PD E2p SApNP-Kif/endo H	174902	82685	108551	129398	143808	261848	79238	345641	146267.1
SUDV GPΔmuc-WL^{2}P^4-PD I3-01v9b SApNP	32933	27405	30608	50359	17406	34313	79188	83439	39124.1
SUDV GPΔmuc-WL^{2}P^4-PD I3-01v9b SApNP-Kif	213630	375263	331165	484567	123702	233165	246351	324809	271692.3
SUDV GPΔmuc-WL^{2}P^4-PD I3-01v9b SApNP-Kif/endo H	45679	26310	57270	55138	87196	N/A	138210	12630	47889.1

Week 11 or 8

Antigen	EC50 titers (week 11,8)								Geometric Mean
	M1	M2	M3	M4	M5	M6	M7	M8	
SUDV GPΔmuc-WL^{2}P^4 trimer-w11	51852	34819	59219	58035	92570	20182	108658	56856	53935.6
SUDV GPΔmuc-WL^{2}P^4 trimer-Kif-w8	302797	144377	177306	198140	88084	235081	164275	185242	177101.1
SUDV GPΔmuc-WL^{2}P^4 trimer-Kif/endo H-w8	50453	172980	18107	59100	58943	44125	87452	156514	65346.1
SUDV GPΔmuc-WL^{2}P^4-PD E2p SApNP-w8	299781	269350	317854	207812	165230	208403	120522	131427	203221.8
SUDV GPΔmuc-WL^{2}P^4-PD E2p SApNP-Kif-w8	192720	218683	292392	372944	179861	130425	179178	274004	219008.7
SUDV GPΔmuc-WL^{2}P^4-PD E2p SApNP-Kif/endo H-w8	180099	336638	152272	156367	145160	325977	149103	N/A	193576.0
SUDV GPΔmuc-WL^{2}P^4-PD I3-01v9b SApNP-w8	219021	293708	296644	131589	450528	1270551	122274	162786	270436.4
SUDV GPΔmuc-WL^{2}P^4-PD I3-01v9b SApNP-Kif-w8	166508	138485	135652	171299	143035	129149	754862	196507	186573.4
SUDV GPΔmuc-WL^{2}P^4-PD I3-01v9b SApNP-Kif/endo H-w8	71039	1261224	728092	170130	156138	N/A	198137	45999	206095.4

Statistical analysis

One-way ANOVA with Tukey's multiple comparisons test (w2)	Statistics	Adjusted P Value
SUDV GPΔmuc-WL^{2}P^4 trimer vs. SUDV GPΔmuc-WL^{2}P^4 trimer-Kif	****	<0.0001
SUDV GPΔmuc-WL^{2}P^4 trimer vs. SUDV GPΔmuc-WL^{2}P^4 trimer-Kif/endo H	ns	0.6485
SUDV GPΔmuc-WL^{2}P^4 trimer-Kif vs. SUDV GPΔmuc-WL^{2}P^4 trimer-Kif/endo H	****	<0.0001

One-way ANOVA with Tukey's multiple comparisons test (w5)	Statistics	Adjusted P Value
SUDV GPΔmuc-WL^{2}P^4 trimer vs. SUDV GPΔmuc-WL^{2}P^4 trimer-Kif	****	<0.0001
SUDV GPΔmuc-WL^{2}P^4 trimer vs. SUDV GPΔmuc-WL^{2}P^4 trimer-Kif/endo H	ns	0.8066
SUDV GPΔmuc-WL^{2}P^4 trimer-Kif vs. SUDV GPΔmuc-WL^{2}P^4 trimer-Kif/endo H	****	<0.0001

One-way ANOVA with Tukey's multiple comparisons test (w2)	Statistics	Adjusted P Value
SUDV GPΔmuc-WL^{2}P^4-PD E2p SApNP vs. SUDV GPΔmuc-WL^{2}P^4-PD E2p SApNP-Kif	****	<0.0001
SUDV GPΔmuc-WL^{2}P^4-PD E2p SApNP vs. SUDV GPΔmuc-WL^{2}P^4-PD E2p SApNP-Kif/endo H	ns	0.0778
SUDV GPΔmuc-WL^{2}P^4-PD E2p SApNP-Kif vs. SUDV GPΔmuc-WL^{2}P^4-PD E2p SApNP-Kif/endo H	****	<0.0001

One-way ANOVA with Tukey's multiple comparisons test (w5)	Statistics	Adjusted P Value
SUDV GPΔmuc-WL^{2}P^4-PD E2p SApNP vs. SUDV GPΔmuc-WL^{2}P^4-PD E2p SApNP-Kif	*	0.0103
SUDV GPΔmuc-WL^{2}P^4-PD E2p SApNP vs. SUDV GPΔmuc-WL^{2}P^4-PD E2p SApNP-Kif/endo H	ns	0.9984
SUDV GPΔmuc-WL^{2}P^4-PD E2p SApNP-Kif vs. SUDV GPΔmuc-WL^{2}P^4-PD E2p SApNP-Kif/endo H	**	0.0091

One-way ANOVA with Tukey's multiple comparisons test (w2)	Statistics	Adjusted P Value
SUDV GPΔmuc-WL^{2}P^4-PD I3-01v9b SApNP vs. SUDV GPΔmuc-WL^{2}P^4-PD I3-01v9b SApNP-Kif	****	<0.0001
IDV GPΔmuc-WL^{2}P^4-PD I3-01v9b SApNP vs. SUDV GPΔmuc-WL^{2}P^4-PD I3-01v9b SApNP-Kif/endo H	*	0.0224
V GPΔmuc-WL^{2}P^4-PD I3-01v9b SApNP-Kif vs. SUDV GPΔmuc-WL^{2}P^4-PD I3-01v9b SApNP-Kif/endo H	****	<0.0001

One-way ANOVA with Tukey's multiple comparisons test (w5)	Statistics	Adjusted P Value
SUDV GPΔmuc-WL^{2}P^4-PD I3-01v9b SApNP vs. SUDV GPΔmuc-WL^{2}P^4-PD I3-01v9b SApNP-Kif	****	<0.0001
SUDV GPΔmuc-WL^{2}P^4-PD I3-01v9b SApNP vs. SUDV GPΔmuc-WL^{2}P^4-PD I3-01v9b SApNP-Kif/endo H	ns	0.903
SUDV GPΔmuc-WL^{2}P^4-PD I3-01v9b SApNP-Kif vs. SUDV GPΔmuc-WL^{2}P^4-PD I3-01v9b SApNP-Kif/endo H	****	<0.0001

Figure S11

g Sera of individual mice immunized with wildtype/glycan-modified SUDV vaccines neutralizing a SUDV Gulu strain

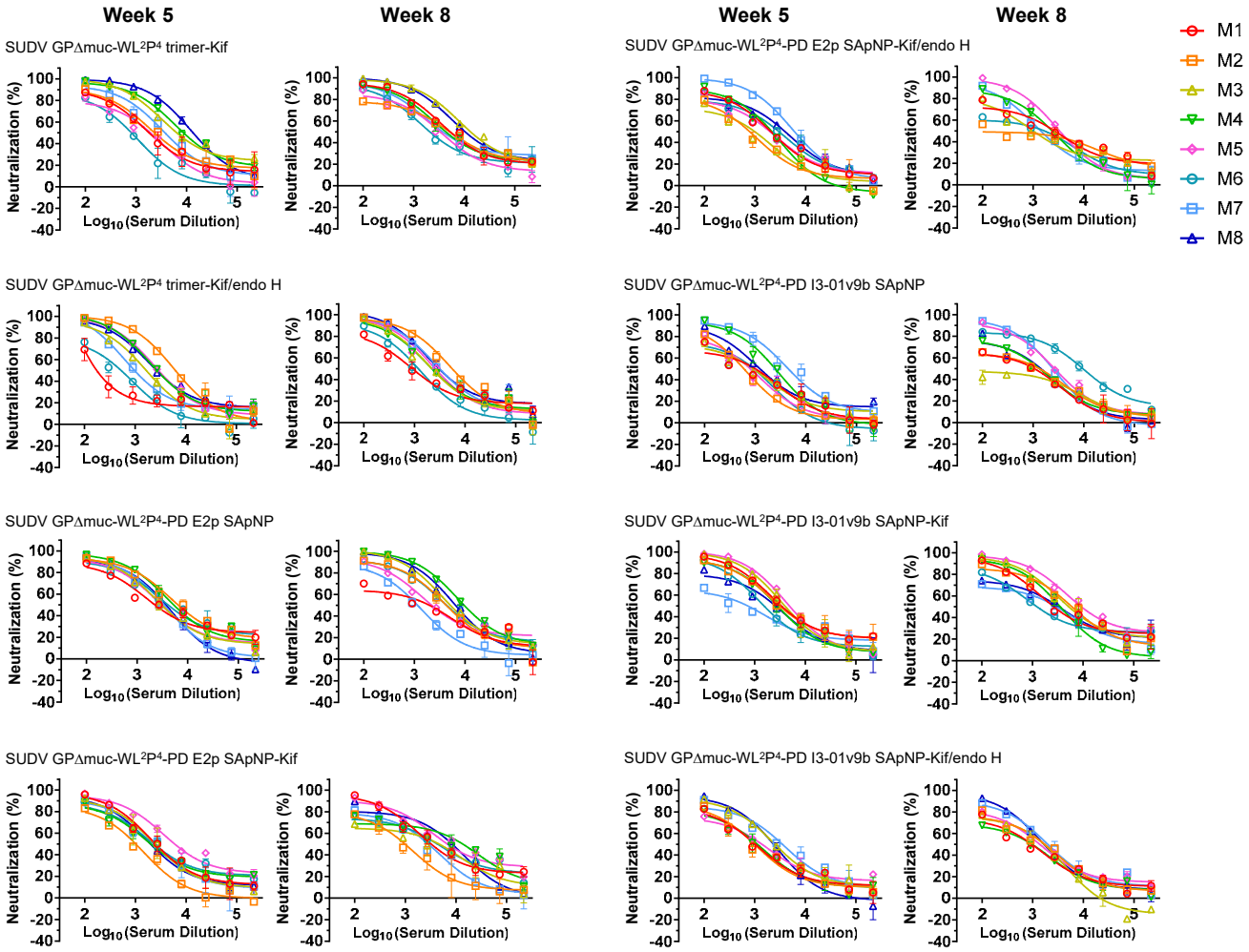

h Mouse serum neutralizing ID_{50} titers

Week 5

Antigen	ID50 titers (week 5)								Geometric Mean
	M1	M2	M3	M4	M5	M6	M7	M8	
SUDV GPΔmuc-WL²P⁴ trimer	420	3076	156.6	2417	1377	1896	5149	1477	1328.6
SUDV GPΔmuc-WL²P⁴ trimer-Kif	1986	2709	8760	10520	1522	736.6	4016	14183	3652.3
SUDV GPΔmuc-WL²P⁴ trimer-Kif/endo H	243.4	6460	1691	3127	3197.0	463.3	1201.0	3265.0	1623.6
SUDV GPΔmuc-WL²P⁴-PD E2p SApNP	3142	7835	3520	6205	3431	5382	3249	3187	4231.6
SUDV GPΔmuc-WL²P⁴-PD E2p SApNP-Kif	2877	873.4	2512	2311	7871	2706	2473	2186	2530.2
SUDV GPΔmuc-WL²P⁴-PD E2p SApNP-Kif/endo H	2075	721.3	713.9	1791	1742	2481	6384	3462	1917.5
SUDV GPΔmuc-WL²P⁴-PD I3-01v9b SApNP	662.4	592.3	758.7	2268	682.9	642.8	4778	1402	1089.5
SUDV GPΔmuc-WL²P⁴-PD I3-01v9b SApNP-Kif	4252	3819	4262	2863	5193	1734	651.4	2141	2657.6
SUDV GPΔmuc-WL²P⁴-PD I3-01v9b SApNP-Kif/endo H	1023	1000	2652	1043	1287	N/A	3262	2177	1591.5

Week 11 or 8

Antigen	ID50 titers (week 11,8)								Geometric Mean
	M1	M2	M3	M4	M5	M6	M7	M8	
SUDV GPΔmuc-WL²P⁴ trimer-w11	13810	4694	2805	3670	2858	2497	14410	3069	4628.4
SUDV GPΔmuc-WL²P⁴ trimer-Kif-w8	6582	5258	16937	5674	3316	2649	5681	13235	6204.7
SUDV GPΔmuc-WL²P⁴ trimer-Kif/endo H-w8	1035	6006	2560	2543	2847	1139	3639	3835	2557.7
SUDV GPΔmuc-WL²P⁴-PD E2p SApNP-w8	1224	4430	6202	11133	2887	4953	1083	6855	3757.6
SUDV GPΔmuc-WL²P⁴-PD E2p SApNP-Kif-w8	4414	880.9	2466	7047	10493	4060	2235	6092	3751.0
SUDV GPΔmuc-WL²P⁴-PD E2p SApNP-Kif/endo H-w8	2234	555.2	1224	2211	3512	1040	1615	N/A	1531.9
SUDV GPΔmuc-WL²P⁴-PD I3-01v9b SApNP-w8	739.1	911.5	343.7	1130	2675	9196	2305	1040	1407.8
SUDV GPΔmuc-WL²P⁴-PD I3-01v9b SApNP-Kif-w8	3830	5923	6805	3469	12386	1653	2090	3103	4041.0
SUDV GPΔmuc-WL²P⁴-PD I3-01v9b SApNP-Kif/endo H-w8	810.8	1367	1095	777.2	1388	N/A	2057	1791	1252.0

Statistical analysis

One-way ANOVA with Tukey's multiple comparisons test (w5)	Statistics	Adjusted P Value
SUDV GPΔmuc-WL²P⁴ trimer vs. SUDV GPΔmuc-WL²P⁴ trimer-Kif	ns	0.0934
SUDV GPΔmuc-WL²P⁴ trimer vs. SUDV GPΔmuc-WL²P⁴ trimer-Kif/endo H	ns	0.9563
SUDV GPΔmuc-WL²P⁴ trimer-Kif vs. SUDV GPΔmuc-WL²P⁴ trimer-Kif/endo H	ns	0.1577

One-way ANOVA with Tukey's multiple comparisons test (w5)	Statistics	Adjusted P Value
SUDV GPΔmuc-WL²P⁴-PD E2p SApNP vs. SUDV GPΔmuc-WL²P⁴-PD E2p SApNP-Kif	ns	0.2678
SUDV GPΔmuc-WL²P⁴-PD E2p SApNP vs. SUDV GPΔmuc-WL²P⁴-PD E2p SApNP-Kif/endo H	ns	0.0973
SUDV GPΔmuc-WL²P⁴-PD E2p SApNP-Kif vs. SUDV GPΔmuc-WL²P⁴-PD E2p SApNP-Kif/endo H	ns	0.8296

One-way ANOVA with Tukey's multiple comparisons test (w8)	Statistics	Adjusted P Value
SUDV GPΔmuc-WL²P⁴-PD E2p SApNP vs. SUDV GPΔmuc-WL²P⁴-PD E2p SApNP-Kif	ns	0.9947
SUDV GPΔmuc-WL²P⁴-PD E2p SApNP vs. SUDV GPΔmuc-WL²P⁴-PD E2p SApNP-Kif/endo H	ns	0.1006
SUDV GPΔmuc-WL²P⁴-PD E2p SApNP-Kif vs. SUDV GPΔmuc-WL²P⁴-PD E2p SApNP-Kif/endo H	ns	0.1201

One-way ANOVA with Tukey's multiple comparisons test (w5)	Statistics	Adjusted P Value
SUDV GPΔmuc-WL²P⁴-PD I3-01v9b SApNP vs. SUDV GPΔmuc-WL²P⁴-PD I3-01v9b SApNP-Kif	ns	0.0604
SUDV GPΔmuc-WL²P⁴-PD I3-01v9b SApNP vs. SUDV GPΔmuc-WL²P⁴-PD I3-01v9b SApNP-Kif/endo H	ns	0.9009
SUDV GPΔmuc-WL²P⁴-PD I3-01v9b SApNP-Kif vs. SUDV GPΔmuc-WL²P⁴-PD I3-01v9b SApNP-Kif/endo H	ns	0.1599

One-way ANOVA with Tukey's multiple comparisons test (w8)	Statistics	Adjusted P Value
SUDV GPΔmuc-WL²P⁴-PD I3-01v9b SApNP vs. SUDV GPΔmuc-WL²P⁴-PD I3-01v9b SApNP-Kif	ns	0.1544
SUDV GPΔmuc-WL²P⁴-PD I3-01v9b SApNP vs. SUDV GPΔmuc-WL²P⁴-PD I3-01v9b SApNP-Kif/endo H	ns	0.7712
SUDV GPΔmuc-WL²P⁴-PD I3-01v9b SApNP-Kif vs. SUDV GPΔmuc-WL²P⁴-PD I3-01v9b SApNP-Kif/endo H	*	0.0468

Figure S11

i Sera of individual mice immunized with glycan-modified RAVV vaccines binding to RAVV GPΔmuc-P²CT(1TD0) trimer

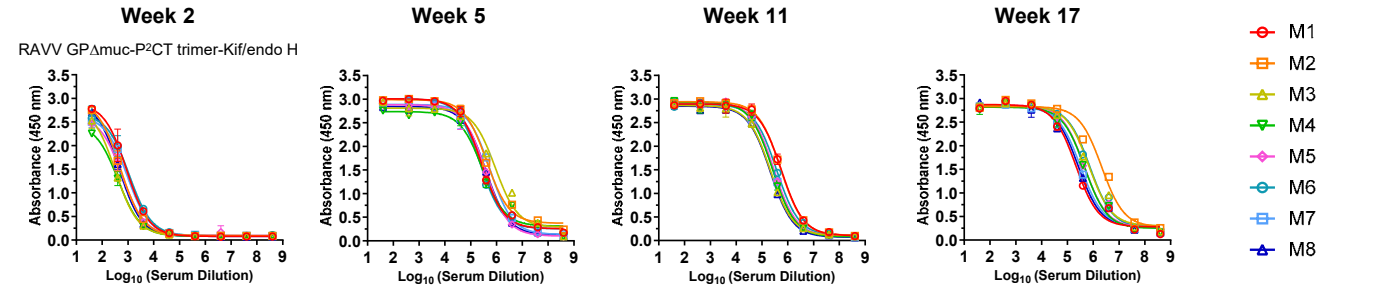

j Mouse serum ELISA EC_{50} titers

Week 2

Antigen	EC50 titers (week 2)								Geometric Mean
	M1	M2	M3	M4	M5	M6	M7	M8	
RAVV GPΔmuc-P²CT trimer	718.9	721.9	432.3	1030.0	946.3	262.3	481.5	958.5	635.1
RAVV GPΔmuc-P²CT trimer-Kif/endo H	1088.0	842.6	372.8	326.6	773.6	1455.0	1260.0	571.6	740.6

Week 5

Antigen	EC50 titers (week 5)								Geometric Mean
	M1	M2	M3	M4	M5	M6	M7	M8	
RAVV GPΔmuc-P²CT trimer	202735	1544554	746406	628189	447117	44771	446178	225949	362215.2
RAVV GPΔmuc-P²CT trimer-Kif/endo H	208318	261241	222068	150370	267446	198233	450054	211636	234603.9

Week 11 or 8

Antigen	EC50 titers (week 11,8)								Geometric Mean
	M1	M2	M3	M4	M5	M6	M7	M8	
RAVV GPΔmuc-P²CT trimer-w11	139135	218951	208199	104125	998580	786127	408247	853062	340466.6
RAVV GPΔmuc-P²CT trimer-Kif/endo H-w8	770620	683058	388118	292655	294767	621323	524297	273292	446120.6

Week 17 or 11

Antigen	EC50 titers (week 17,11)								Geometric Mean
	M1	M2	M3	M4	M5	M6	M7	M8	
RAVV GPΔmuc-P²CT trimer-w17	140811	110900	164905	119990	336478	344895	127509	141835	168457
RAVV GPΔmuc-P²CT trimer-Kif/endo H-w11	125144	295308	212027	173036	313400	398840	295603	237268	242316

Statistical analysis

Unpaired t test (w2)	Statistics	P Value
RAVV GPΔmuc-P²CT trimer vs. RAVV GPΔmuc-P²CT trimer-Kif/endo H	ns	0.4307

Unpaired t test (w5)	Statistics	P Value
RAVV GPΔmuc-P²CT trimer vs. RAVV GPΔmuc-P²CT trimer-Kif/endo H	ns	0.1079

k Purified IgG of individual mice immunized with RAVV vaccines neutralizing a MARV Angola strain

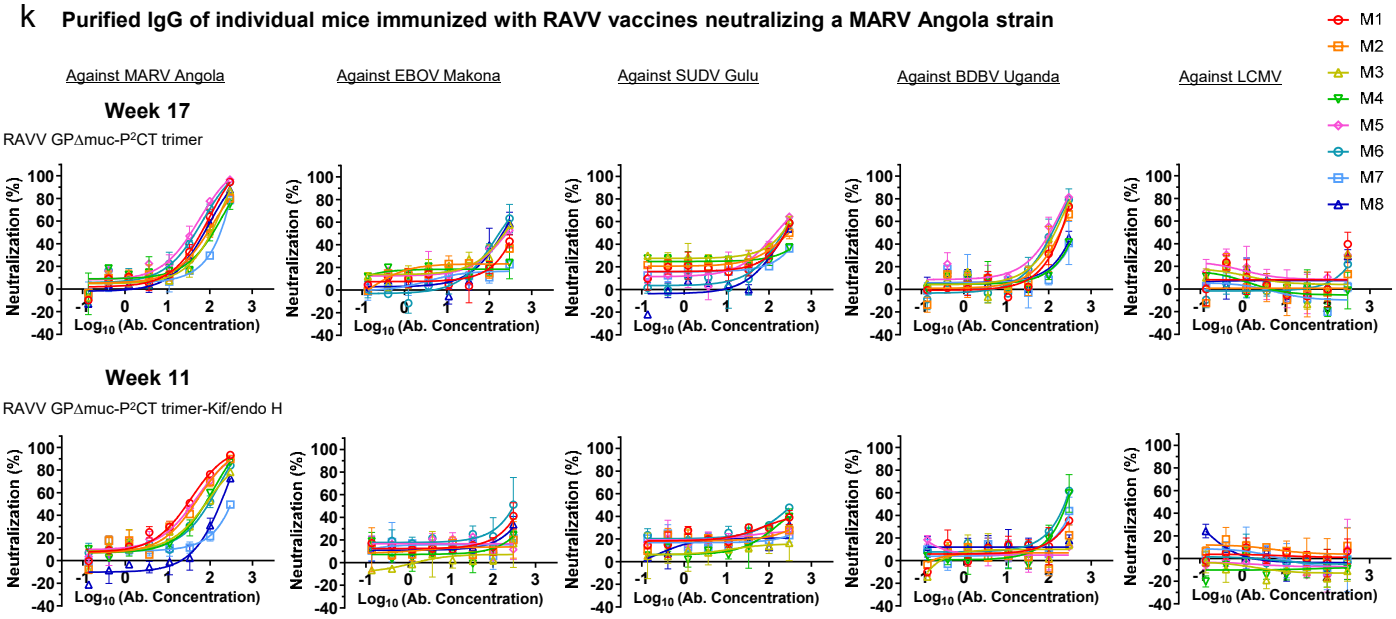

Figure S11

Fig. S11. Immunogenicity of glycan-modified EBOV, SUDV, and RAVV GPΔmuc vaccines in mice. (**a**) ELISA curves of mouse sera from glycan-modified EBOV GPΔmuc trimer and SApNP vaccine groups (n = 8 mice/group) binding to EBOV GPΔmuc-WL^{2}P^4(1TD0) trimer. (**b**) (Top) Summary of geometric means of EC_{50} titers measured for glycan-modified EBOV GPΔmuc vaccine groups against EBOV GPΔmuc-WL^{2}P^4(1TD0) trimer. Color coding indicates the level of EC_{50} titers (green to red: low to high binding). (Bottom) Summary of statistical analysis performed for each timepoint. Of note, the EC_{50} values at week 2 were derived by setting the minimum/maximum OD_{450} values to 0.0/2.8. (**c**) Neutralization curves of mouse sera from glycan-modified EBOV GPΔmuc trimer and SApNP vaccine groups against EBOV Makona pseudovirus. (**d**) (Top) Summary of geometric means of ID_{50} titers measured for EBOV GPΔmuc vaccine groups against EBOV Makona pseudovirus. Color coding indicates the level of ID_{50} titers (white: no neutralization; green to red: low to high neutralization). Of note, the ID_{50} values were derived by setting the minimum/maximum %neutralization to 0.0/100.0 as constraints. (Bottom) Summary of statistical analysis. (**e**) ELISA curves of mouse sera from glycan-modified SUDV GPΔmuc trimer and SApNP vaccine groups binding to SUDV GPΔmuc-WL^{2}P^4(1TD0) trimer. (**f**) (Top) Summary of geometric means of EC_{50} titers measured for glycan-modified SUDV GPΔmuc vaccine groups against SUDV GPΔmuc-WL^{2}P^4(1TD0) trimer. (Bottom) Summary of statistical analysis. Of note, the EC_{50} values at week 2 were derived by setting the minimum/maximum OD_{450} values to 0.0/2.9. (**g**) Neutralization curves of mouse sera from glycan-modified SUDV GPΔmuc trimer and SApNP vaccine groups against SUDV Gulu pseudovirus. (**h**) (Top) Summary of geometric means of ID_{50} titers measured for SUDV GPΔmuc vaccine groups against SUDV Gulu pseudovirus. (Bottom) Summary of statistical analysis. (**i**) ELISA curves of mouse sera from glycan modified RAVV GPΔmuc trimer vaccine groups binding to RAVV GPΔmuc-P^{2}CT(1TD0) trimer. (**j**) (Top) Summary of geometric means of EC_{50} titers measured for glycan-modified RAVV GPΔmuc vaccine groups against RAVV GPΔmuc-P^{2}CT(1TD0) trimer. (Bottom) Summary of statistical analysis. Of note, the EC_{50} values at week 2 were derived by setting the minimum/maximum OD_{450} values to 0.0/2.9. (**k**) Neutralization curves of purified mouse IgG from glycan-modified RAVV GPΔmuc vaccine groups after four immunizations at week 17 or week 11 against MARV Angola or various ebolavirus strains. Lymphocytic choriomeningitis virus (LCMV) was included as a negative control to confirm the cross-NAb responses measured using purified IgG. Error bars represent the difference between these duplicate values at each concentration tested for each sample. EC_{50} and ID_{50} values were calculated in GraphPad Prism 10.3.1. Data were analyzed using one-way ANOVA, followed by Tukey's multiple comparison post hoc test for each timepoint. For significance, ns (not significant), *$p < 0.05$, **$p < 0.01$, ***$p < 0.001$, and ****$p < 0.0001$.

Table S1. Data collection and refinement statistics for EBOV Mayinga GPΔmuc-WL^{2}P^4.

Data Collection	**EBOV Mayinga GPΔmuc-WL^{2}P^4**
Beamline	SSRL 12-1
Wavelength (Å)	0.97946
Resolution (Å)[a]	40.6 - 3.20 (3.29 - 3.20)
Space group	P321
Unit cell (Å)	114.47,114.47,133.38
(°)	90 90 120
Total reflections	189,316 (12,886)
Unique reflections	17,104 (815)
Multiplicity	11.1 (9.6)
Completeness (%)	99.8 (98.2)
Mean (I)/ σ_I	22.2 (1.2)
R_{merge} (%)	6.1 (>100)
R_{meas}[c] (%)	12.3 (>100)
R_{pim}[d] (%)	3.7 (69.3)
$CC_{1/2}$[e] (%)	99.8 (30.3)
Refinement	
Refinement resolution (Å)[a]	40.6 - 3.20 (3.29 - 3.20)
# reflections in refinement (work/free)	17,082 (1,323)
R_{work} (%)	21.5 (36.1)
R_{free} (%)	22.2 (33.0)
# Protein atoms	3,119
# Carbohydrate atoms	128
# Waters	0
# Protein residues	398
Bond r.m.s. deviation (Å)	0.013
Angle r.m.s. deviation (º)	1.60
Wilson B (Å^2)	114
Average B protein (Å^2)	119
carbohydrate (Å^2)	156
Ramachandran favored, allowed, outliers (%)	96.1, 3.9, 0.0, 0.0
Clashscore[f]	8.2
PDB ID	9N8E

[a]Numbers in parentheses are for highest resolution shell
[b]$R_{merge} = \Sigma_{hkl} \Sigma_{i=1,n}|I_i(hkl) - \langle I(hkl)\rangle| / \Sigma_{hkl} \Sigma_{i=1,n} I_i(hkl)$
[c]$R_{meas} = \Sigma_{hkl} \sqrt{(n/n-1)} \Sigma_{i=1,n}|I_i(hkl) - \langle I(hkl)\rangle| / \Sigma_{hkl} \Sigma_{i=1,n} I_i(hkl)$
[d]$R_{pim} = \Sigma_{hkl} \sqrt{(1/n-1)} \Sigma_{i=1,n}|I_i(hkl) - \langle I(hkl)\rangle| / \Sigma_{hkl} \Sigma_{i=1,n} I_i(hkl)$
[e]$CC_{1/2}$ = Pearson correlation coefficient between two random half datasets
[f] Number of unfavorable all-atom steric overlaps ≥ 0.4 Å per 1000 atoms

Table S2. Cryo-EM data collection information, model building, and refinement statistics.

Data collection information	**SUDV Gulu GPΔmuc-WL^{2}P^4/CA45 Fab**
Microscope	Titan Krios G4
Voltage (keV)	200
Detector	Falcon 4 camera with a Selectris-X energy filter
Recording mode	Counting
Magnification	130,000 x
Movie micrograph pixel size	0.89
Total dose (e−/Å^2)	50
Under focus range (µm)	-1.0 to -2.0 um
Number of movie micrographs	1,824
Model building and refinement statistics	
Map Resolution (Å)	3.13
Residues	
Amino-acids	1473
Carbohydrates	9
RMSD Bonds (Å)	0.003
RMSD Angles (º)	0.746
Ramachandran	
Outliers (%)	0.00
Allowed (%)	7.21
Favored (%)	92.8
Rotamer outliers	1.67
Clash score	8.98
Molprobity score	2.10
PDB ID	9N8F
EMDB ID	EMD-49127